

ABSTRACT

Title of Thesis: INFLUENCE OF GAS FLOW RATES ON TRACE QUALITY
AND RELIABILITY IN A SELECTED CONDUCTOR INK
PRINTED WITH AN AEROSOL JET PRINTER

Neil Dalal, Master of Science, 2018

Thesis Directed By: Professors Abhijit Dasgupta and Siddhartha Das
Department of Mechanical Engineering

Preliminary comparisons conducted between two aerosol jet printed samples, an interconnect-over-fillet specimen and baseline test coupons, revealed strong differences in surface agglomeration characteristics. These differences were subsequently found to be strongly correlated with differences in thermal cycling durability. One potential cause could be the differences in the carrier and sheath gas flow rates at which the nanoparticle ink was deposited onto the substrate during the AJP process. A parametric study was conducted to explore any relationship between gas flow rates and print quality. Serpentine test structures were aerosol jet printed at parametrically varied carrier and sheath gas flow rates. For each serpentine, its macroscale and micromorphological features were assessed as quality metrics and investigated for a potential relationship with gas flow rates. Future studies will subject these printed serpentine test structures of

varying quality to thermal cycling to establish possible correlations between gas flow rate and thermal cycling durability.

INFLUENCE OF GAS FLOW RATES ON TRACE QUALITY AND RELIABILITY IN
A SELECTED CONDUCTOR INK PRINTED WITH AN AEROSOL JET PRINTER

by

Neil Dalal

Thesis submitted to the Faculty of the Graduate School of the
University of Maryland, College Park, in partial fulfillment
of the requirements for the degree of
Master of Science
2018

Thesis Committee:

Professor Abhijit Dasgupta, Mechanical Engineering, Chair

Professor Siddhartha Das, Mechanical Engineering, Co-Chair

Professor Hugh Bruck, Mechanical Engineering

Dr. Daniel Hines, Laboratory for Physical Sciences

Professor Patrick McCluskey, Mechanical Engineering

© Copyright by

Neil Dalal

2018

Acknowledgements

I would like to thank Dr. Abhijit Dasgupta, my advisor, for allowing me to join his group three years ago as an undergraduate and transition into the B.S./M.S. program. He along with Dr. Siddhartha Das, my co-advisor, have been essential in the research I have conducted as a part of this thesis. I would like to thank the Laboratory for Physical Sciences (LPS) and particularly Dr. Yuan Gu, Dr. Daniel Hines, Dr. Daniel Hinkel, Dr. Guang Chen, and Mr. Peng Chen for helping on this project by providing and analyzing specimens. I am also grateful to NextFlex for providing me financial support during my M.S. Through the years, I am also grateful to have received assistance from many others including Dr. Jiancun Rao, Dr. Bob Utter and Mr. Majid Aroom.

I appreciate the help from professors and staff within the University of Maryland, College Park Mechanical Engineering department and in particular within the Center for Advanced Life Cycle Engineering (CALCE) who supported me during this project. Many thanks to my Thesis Defense Committee of Dr. Patrick McCluskey and Dr. Hugh Bruck in addition to Drs. Dasgupta, Das, and Hines. I was also assisted throughout my research by fellow lab colleagues Daniel Breu, Deng Chen, Subramani Manoharan, Jose Romero, Hao Huang, Jonathan Kordell, Abhishek Deshpande, Qian Jiang, David Leslie, and Mark Mifsud.

Table of Contents

Acknowledgements.....	ii
Table of Contents.....	iii
Table of Tables.....	v
Table of Figures.....	vi
List of Abbreviations.....	xii
Chapter 1 – Introduction.....	1
Section 1.1: Problem Statement.....	1
Section 1.2: Background and Motivation.....	1
Section 1.3: Literature Review.....	7
Section 1.3.1: Printed Hybrid Electronics.....	7
Section 1.3.2: Gaps in the Literature.....	10
Section 1.4: Research Objectives.....	11
Chapter 2 – Ink A Reliability Studies.....	12
Section 2.1: Introduction.....	12
Section 2.2: Test Specimens.....	13
Section 2.2.1: Interconnect over Fillet (IoF) Specimen.....	14
Section 2.2.2: Baseline Test Coupons.....	17
Section 2.2.3: Macroscale Geometry.....	20
Section 2.2.4: Microscale Morphology.....	20
Section 2.2.5: Effective Conductivity.....	23
Section 2.3: Test Plan.....	24
Section 2.4: Results.....	27
Section 2.4.1: Resistance Profiles.....	28
Section 2.4.2: Failure Analysis.....	33
Section 2.5: Summary.....	39
Chapter 3 – Effect of Gas Flow Rate on Trace Quality.....	41
Section 3.1: Introduction.....	41
Section 3.2: Approach.....	45
Section 3.2.1: Test Coupon.....	45
Section 3.2.2: Test Plan.....	47
Section 3.3: Results.....	48

Section 3.3.1: Deposition Rate	48
Section 3.3.2: Profilometry.....	50
Section 3.3.3: Effective Conductivity.....	59
Section 3.3.4: Surface Imaging and Crystalline Deposits	62
Section 3.3.5: Micromorphology.....	67
Section 3.3.6: Microcracking.....	80
Section 3.4: Summary	84
Chapter 4 – Summary and Future Work.....	86
Section 4.1: Summary and Discussion of Work Completed.....	86
Section 4.2: Research Contributions	88
Section 4.3: Limitations and Future Work	90
Chapter 5 – Appendices	92
A1: Reliability Results for Ink C and Ink D.....	92
A2: Investigating Scanning Electron Microscope as Potentially Damaging Printed Hybrid Electronics.....	97
A3: DTC180201 Hot and Cold Temperature Normalized Resistance Plots.....	100
A4: Atomic Force Microscopy (AFM) Results.....	102
A5: Laser Profilometry Results of Cross-Sectioned Samples.....	106
A6: Image Processing Methodology	108
A7: Additional Micromorphology Image Processing Results	113
A7.1: Number of Agglomerations as a Function of Flow Rate.....	113
A7.2: Percent Area of Agglomerations as a Function of Flow Rate	116
A7.3: Agglomerate Size and Spacing Histograms	119
A7.4: Variation in Agglomerate Size and Spacing.....	128
A7.5: Average Agglomerate Size and Spacing as a Function of Flow Rate	137
A7.6: Standard Deviation of Agglomerate Size and Spacing as a Function of Flow Rate	144
A7.7: Skewness of Agglomerate Size and Spacing as a Function of Flow Rate	149
A8: Finite Element Analysis on Shrinkage Stress	155
References.....	160

Table of Tables

Table 1.1: Effect of independently increasing each process variables on printed line geometry.	9
Table 2.1: Summary of thermal cycles exposure for each test coupon board printed with Ink A.	37
Table 3.1: Effect of independently increasing each process variables on printed line geometry.	44
Table 3.2: Test matrix for varying flow rate design of experiments.	47
Table 3.3: Associated deposition rate for each combination of carrier and sheath gas flow rate.	49
Table 3.4: Mean and standard deviation for four corner and middle flow rate single-pass traces' width, cross-sectional area, overspray, coverage, and max thickness.	56
Table 3.5: Parameters calculated for all 30 different traces.	57
Table 3.6: Resistance per unit length measurements for serpentine traces.	60
Table 3.7: Number of agglomerations in single-pass trace on the surface.	72
Table 3.8: Agglomeration percent area in single-pass trace on the surface.	73
Table 3.9: Average agglomeration size in single-pass trace on the surface.	75
Table 3.10: Presence of cracks observed or not observed in serpentine traces for a) single-pass and b) double-pass traces.	84
Table 5.1: Summary of number of SEM exposures each test coupon board with Ink A has been subjected to.	99
Table 5.2: Number of agglomerations in single-pass trace on the surface.	113
Table 5.3: Number of agglomerations in double-pass trace on the surface.	114
Table 5.4: Number of agglomerations in single-pass trace in the bulk.	115
Table 5.5: Number of agglomerations in double-pass trace in the bulk.	115
Table 5.6: Agglomeration percent area in single-pass trace on the surface.	116
Table 5.7: Agglomeration percent area in double-pass trace on the surface.	117
Table 5.8: Agglomeration percent area in single-pass trace in the bulk.	118
Table 5.9: Agglomeration percent area in double-pass trace in the bulk.	118
Table 5.10: Average agglomeration size in single-pass trace on the surface.	137
Table 5.11: Average agglomeration size in double-pass trace on the surface.	138
Table 5.12: Average agglomeration size in single-pass trace in the bulk.	138
Table 5.13: Average agglomeration size in double-pass trace in the bulk.	139
Table 5.14: Average agglomeration spacing in single-pass trace on the surface.	140
Table 5.15: Average agglomeration spacing in double-pass trace on the surface.	141
Table 5.16: Average agglomeration spacing in single-pass trace in the bulk.	142
Table 5.17: Average agglomeration spacing in double-pass trace in the bulk.	143
Table 5.18: Skewness values for agglomeration size and spacing histograms for different flow rates, number of passes (SP – single pass or DP – double pass), and type of image (surface of cross-section).	150

Table of Figures

Figure 1.1: Schematic of the carrier and sheath gas flow geometry as well as a-c) different locations of interest in the AJP process (Chen et al., 2018).....	4
Figure 1.2: Sintering temperature profile utilized for all silver nanoparticle inks throughout this research.....	6
Figure 2.1: a) schematic of fillet (red) technology with trace (black) traversing die (gray) and substrate (white), b) optical microscope image of fine pitch AJP traces printed over substrate, fillet, and die, and c) SEM image of AJP traces printed over substrate, fillet, and die.....	15
Figure 2.2: Interconnect over fillet specimen for Ink A (IoF171101).	16
Figure 2.3: Improved wire interconnection method for IoF171101 on FR4 substrate, with additive silver pad printed on a copper pad fabricated with a conventional subtractive process.....	17
Figure 2.4: a) Baseline test coupon board design and b) individual baseline test structures with and without additional Polymer N barrier layer.	19
Figure 2.5: Coarser agglomerates can be seen on IoF171101’s Fillet 8 line segment 1 after 250 cycles compared to DTC180201’s traces after 0 and 250 cycles.....	21
Figure 2.6: Bulk porosity (micron-scale pores) is identified to be greater in the cross-section of the IoF171101 traces relative to that in the DTC180201 traces.....	21
Figure 2.7: Bulk porosity in IoF171101 highlighted through image processing thresholds.	22
Figure 2.8: Normalized effective conductivity histogram plots for a) IoF171101 and b) DTC180201.....	24
Figure 2.9: Temperature profile for IoF171101 compared to DTC180201.....	25
Figure 2.10: Temperature and resistance profiles for the first six thermal cycles that IoF171701 underwent.	26
Figure 2.11: Temperature and resistance profiles for the first six thermal cycles that DTC180201 underwent.....	27
Figure 2.12: Normalized resistance of IoF171101 at the hot and cold temperature dwells as a function of cycle number.	28
Figure 2.13: Normalized resistance of DTC180201 failed structures at the a) hot and b) cold temperature dwells as a function of cycle number.....	30
Figure 2.14: Normalized resistance of DTC180201 ‘survivor’ structures at the a) hot and b) cold temperature dwells as a function of cycle number.	31
Figure 2.15: Normalized resistance of DTC180201 structures with intermittent resistance anomalies at the a) hot and b) cold temperature dwells as a function of cycle number. ..	32
Figure 2.16: Normalized resistance of DTC180201 structures exhibiting continuous wearout (steadily increasing resistance) at the a) hot and b) cold temperature dwells as a function of cycle number.	33
Figure 2.17: Trace delamination failure at the top of the specimen.	34
Figure 2.18: a) SEM image of transverse and longitudinal microcracks observed in some of IoF171101’s traces after 250 thermal cycles, b) SEM image of trace delamination, and c) optical image of trace delamination and disintegration.	35
Figure 2.19: SEM image of interfacial crack in one of IoF171101’s trace cross-section.	36
Figure 2.20: Three examples of whiskers found in Board 3 for the Ink A test coupons. .	38

Figure 2.21: Optical images of pad lifting for DTC180201 B2C3.	38
Figure 3.1: Schematic of the carrier and sheath gas flow geometry as well as a-c) different locations of interest in the AJP process (Chen et al., 2018).....	42
Figure 3.2: Test structure and coupon design for varying flow rate design of experiments.	46
Figure 3.3: Deposition rate as a function of carrier and sheath gas flow rate.....	50
Figure 3.4: Representative example of a) height contour plot from VK Analyzer and b) post-processing plots from MATLAB for Board 4 Serpentine 3 Segment C left edge.	52
Figure 3.5: Distribution plots for trace a) width, b) cross-sectional area, c) overspray, d) coverage, and e) max thickness.	56
Figure 3.6: Trace a) width, b) cross-sectional area, c) coverage, d) overspray, and e) thickness for the double-pass prints as a function of gas flow rates.	59
Figure 3.7: Trace resistance per unit length as a function of gas flow rate plotted on a a) full y-axis and b) abridged y-axis.	61
Figure 3.8: Normalized effective conductivity as a function of carrier and sheath gas flow rate.....	62
Figure 3.9: Surface images for a) single and b) double pass traces at 500x magnification.	63
Figure 3.10: Comparison of trace surface between single and double pass traces.	64
Figure 3.11: Example of traces with a) no crystalline deposits, b) deposits at the edges, c) deposits along the centerline, and d) deposits randomly dispersed.	65
Figure 3.12: Energy dispersive X-ray spectroscopy plots when sampling the printed trace and the crystalline deposits.	66
Figure 3.13: Representative optical image with overhead view of Board 4 Serpentine 3 single (Segment B) and double pass (Segment C) trace.	66
Figure 3.14: Surface images for a) single and b) double pass traces at 50,000x magnification.	68
Figure 3.15: Cross-section images for a) single and b) double-pass traces at 100,000x magnification.	69
Figure 3.16: Number of agglomerations in single-pass trace on the surface as a function of carrier and sheath gas flow rate.	72
Figure 3.17: Agglomeration percent area in single-pass trace on the surface as a function of carrier and sheath gas flow rate.	73
Figure 3.18: Agglomeration size in single-pass trace on the surface for major diagonal cases.	74
Figure 3.19: Variation in agglomeration size in single-pass trace on the surface for major diagonal cases.	74
Figure 3.20: Average agglomeration size in single-pass trace on the surface as a function of carrier and sheath gas flow rate.	75
Figure 3.21: Standard deviation of agglomeration size in single-pass trace on the surface as a function of carrier and sheath gas flow rate.....	76
Figure 3.22: Skewness of agglomeration size in single-pass trace on the surface as a function of carrier and sheath gas flow rate.....	76
Figure 3.23: Agglomeration size distribution for single-pass trace in the bulk vs. on the surface for the a) C = 30, S = 30 and b) C = 100, S = 50 serpentines.	78

Figure 3.24: Agglomeration size in single-pass trace on the surface for minor diagonal cases.	79
Figure 3.25: Agglomerate spacing in double-pass trace in the bulk for major diagonal cases.	80
Figure 3.26: Examples of microcracking in serpentine traces with a) 80 and b) 100 sccm carrier gas flow rate.	81
Figure 3.27: Cross-section SEM images of traces with a) crack at the top of C = 65, S = 30 single-pass, b) crack in the middle of C = 80, S = 50 single-pass, c) crack at the bottom of C = 100, S = 50 double-pass, and d) crack at the left in the middle of C = 100, S = 40 double-pass.	83
Figure 3.28: Cross-section SEM images of traces with poor adhesion between printed silver line and polymer substrate in a) C = 30, S = 50 double-pass and b) C = 100, S = 50 single-pass.	84
Figure 5.1: a) Interconnect over fillet specimen for Ink C (IoF170601) and b) zoomed in digital image of the serpentine traces on one of the four silicon dies populated on the FR4 circuit card.	92
Figure 5.2: Initial morphology comparison between Inks A and C from an overhead view.	93
Figure 5.3: a) Example of silver pad lifting off of substrate as result of sintered silver glob, b) spike in resistance profile indicating open circuit, c) improved wire interconnection method.	94
Figure 5.4: a) little observable damage on the surface of the traces corresponding to Fillet 5 and b) signs of longitudinal microcracking at traces at the top of Fillet 8 after 200 thermal cycles.	95
Figure 5.5: Example of pad lifting failure for RTC180508.	96
Figure 5.6: Initial test matrix for Ink A baseline test coupons to investigate if SEM environment damages printed electronic samples.	98
Figure 5.7: Optical and scanning electron microscope images for a Board 2 structure. ..	98
Figure 5.8: a) Optical microscope image after 100 thermal cycles and before SEM exposure, b) SEM image after 100 thermal cycles and first optical microscope documentation, and c) optical microscope image after 100 thermal cycles and after SEM exposure.	99
Figure 5.9: Normalized resistance of all DTC180201 structures at the a) hot and b) cold temperature dwells as a function of cycle number.	101
Figure 5.10: a) surface topology and b) phase plot of IoF171101 as well as c) surface topology and d) phase plot of DTC180201.	104
Figure 5.11: Fast Fourier transform comparison between IoF171101 and DTC180201 line roughness profiles generated by AFM.	105
Figure 5.12: Example of line roughness plots generated for a) IoF171101 and b) DTC180201.	106
Figure 5.13: Fast Fourier transform comparison between IoF171101 and DTC180201 line roughness profiles generated by laser profilometry.	107
Figure 5.14: Example of original SEM image uploaded to software.	109
Figure 5.15: Example of agglomerations counted by software a) without and b) with shading over the counted objects.	110
Figure 5.16: Example of all agglomerations counted and highlighted.	111

Figure 5.17: Example of Voronoi diagram to quantify agglomerations spacing distribution.	112
Figure 5.18: Number of agglomerations in single-pass trace on the surface as a function of carrier and sheath gas flow rate.	114
Figure 5.19: Number of agglomerations in double-pass trace on the surface as a function of carrier and sheath gas flow rate.	114
Figure 5.20: Number of agglomerations in single-pass trace in the bulk as a function of carrier and sheath gas flow rate.	115
Figure 5.21: Number of agglomerations in double-pass trace in the bulk as a function of carrier and sheath gas flow rate.	116
Figure 5.22: Agglomeration percent area in single-pass trace on the surface as a function of carrier and sheath gas flow rate.	117
Figure 5.23: Agglomeration percent area in double-pass trace on the surface as a function of carrier and sheath gas flow rate.	117
Figure 5.24: Agglomeration percent area in single-pass trace in the bulk as a function of carrier and sheath gas flow rate.	118
Figure 5.25: Agglomeration percent area in double-pass trace in the bulk as a function of carrier and sheath gas flow rate.	119
Figure 5.26: Agglomeration size in single-pass trace on the surface for major diagonal cases.	120
Figure 5.27: Agglomeration size in single-pass trace on the surface for minor diagonal cases.	120
Figure 5.28: Agglomeration size in double-pass trace on the surface for major diagonal cases.	121
Figure 5.29: Agglomeration size in double-pass trace on the surface for minor diagonal cases.	121
Figure 5.30: Agglomeration size in single-pass trace in the bulk for major diagonal cases.	122
Figure 5.31: Agglomeration size in single-pass trace in the bulk for minor diagonal cases.	122
Figure 5.32: Agglomeration size in double-pass trace in the bulk for major diagonal cases.	123
Figure 5.33: Agglomeration size in double-pass trace in the bulk for minor diagonal cases.	123
Figure 5.34: Agglomerate spacing in single-pass trace on the surface for major diagonal cases.	124
Figure 5.35: Agglomerate spacing in single-pass trace on the surface for minor diagonal cases.	124
Figure 5.36: Agglomerate spacing in double-pass trace on the surface for major diagonal cases.	125
Figure 5.37: Agglomerate spacing in double-pass trace on the surface for minor diagonal cases.	125
Figure 5.38: Agglomerate spacing in single-pass trace in the bulk for major diagonal cases.	126
Figure 5.39: Agglomerate spacing in single-pass trace in the bulk for minor diagonal cases.	126

Figure 5.40: Agglomerate spacing in double-pass trace in the bulk for major diagonal cases.	127
Figure 5.41: Agglomerate spacing in double-pass trace in the bulk for minor diagonal cases.	127
Figure 5.42: Variation in agglomeration size in single-pass trace on the surface for major diagonal cases.	129
Figure 5.43: Variation in agglomeration size in single-pass trace on the surface for minor diagonal cases.	129
Figure 5.44: Variation in agglomeration size in double-pass trace on the surface for major diagonal cases.	130
Figure 5.45: Variation in agglomeration size in double-pass trace on the surface for minor diagonal cases.	130
Figure 5.46: Variation in agglomeration size in single-pass trace in the bulk for major diagonal cases.	131
Figure 5.47: Variation in agglomeration size in single-pass trace in the bulk for minor diagonal cases.	131
Figure 5.48: Variation in agglomeration size in double-pass trace in the bulk for major diagonal cases.	132
Figure 5.49: Variation in agglomeration size in double-pass trace in the bulk for minor diagonal cases.	132
Figure 5.50: Variation in agglomeration spacing in single-pass trace on the surface for major diagonal cases.	133
Figure 5.51: Variation in agglomeration spacing in single-pass trace on the surface for minor diagonal cases.	133
Figure 5.52: Variation in agglomeration spacing in double-pass trace on the surface for major diagonal cases.	134
Figure 5.53: Variation in agglomeration spacing in double-pass trace on the surface for minor diagonal cases.	134
Figure 5.54: Variation in agglomeration spacing in single-pass trace in the bulk for major diagonal cases.	135
Figure 5.55: Variation in agglomeration spacing in single-pass trace in the bulk for minor diagonal cases.	135
Figure 5.56: Variation in agglomeration spacing in double-pass trace in the bulk for major diagonal cases.	136
Figure 5.57: Variation in agglomeration spacing in double-pass trace in the bulk for minor diagonal cases.	136
Figure 5.58: Average agglomeration size in single-pass trace on the surface as a function of carrier and sheath gas flow rate.	137
Figure 5.59: Average agglomeration size in double-pass trace on the surface as a function of carrier and sheath gas flow rate.	138
Figure 5.60: Average agglomeration size in single-pass trace in the bulk as a function of carrier and sheath gas flow rate.	139
Figure 5.61: Average agglomeration size in double-pass trace in the bulk as a function of carrier and sheath gas flow rate.	140
Figure 5.62: Average agglomeration spacing in single-pass trace on the surface as a function of carrier and sheath gas flow rate.	141

Figure 5.63: Average agglomeration spacing in double-pass trace on the surface as a function of carrier and sheath gas flow rate.....	142
Figure 5.64: Average agglomeration spacing in single-pass trace in the bulk as a function of carrier and sheath gas flow rate.	143
Figure 5.65: Average agglomeration spacing in double-pass trace in the bulk as a function of carrier and sheath gas flow rate.	144
Figure 5.66: Standard deviation of agglomeration size in single-pass trace on the surface as a function of carrier and sheath gas flow rate.....	145
Figure 5.67: Standard deviation of agglomeration size in double-pass trace on the surface as a function of carrier and sheath gas flow rate.....	145
Figure 5.68: Standard deviation of agglomeration size in single-pass trace in the bulk as a function of carrier and sheath gas flow rate.....	146
Figure 5.69: Standard deviation of agglomeration size in double-pass trace in the bulk as a function of carrier and sheath gas flow rate.....	146
Figure 5.70: Standard deviation of agglomeration spacing in single-pass trace on the surface as a function of carrier and sheath gas flow rate.	147
Figure 5.71: Standard deviation of agglomeration spacing in double-pass trace on the surface as a function of carrier and sheath gas flow rate.	147
Figure 5.72: Standard deviation of agglomeration spacing in single-pass trace in the bulk as a function of carrier and sheath gas flow rate.....	148
Figure 5.73: Standard deviation of agglomeration spacing in double-pass trace in the bulk as a function of carrier and sheath gas flow rate.....	148
Figure 5.74: Skewness of agglomeration size in single-pass trace on the surface as a function of carrier and sheath gas flow rate.....	151
Figure 5.75: Skewness of agglomeration size in double-pass trace on the surface as a function of carrier and sheath gas flow rate.....	151
Figure 5.76: Skewness of agglomeration size in single-pass trace in the bulk as a function of carrier and sheath gas flow rate.	152
Figure 5.77: Skewness of agglomeration size in double-pass trace in the bulk as a function of carrier and sheath gas flow rate.....	152
Figure 5.78: Skewness of agglomeration spacing in single-pass trace on the surface as a function of carrier and sheath gas flow rate.....	153
Figure 5.79: Skewness of agglomeration spacing in double-pass trace on the surface as a function of carrier and sheath gas flow rate.....	153
Figure 5.80: Skewness of agglomeration spacing in single-pass trace in the bulk as a function of carrier and sheath gas flow rate.....	154
Figure 5.81: Skewness of agglomeration spacing in double-pass trace in the bulk as a function of carrier and sheath gas flow rate.....	154
Figure 5.82: Zoomed-in model geometry for a) thin and b) thick trace.	156
Figure 5.83: Maximum in-plane principal stress contours for the a) thin and b) thick trace.	159
Figure 5.84: Maximum in-plane principal stress direction for the a) thin and b) thick trace.....	159

List of Abbreviations

LPS –	Laboratory for Physical Sciences
AJP –	Aerosol jet printer or aerosol jet printing
CALCE –	Center for Advanced Life Cycle Engineering
AFM –	Atomic force microscopy
IoF –	Interconnect over fillet
sccm –	Standard cubic centimeters per minute
HTOL –	High temperature operation life
LTOL –	Low temperature operation life
SEM –	Scanning electron microscopy
DAQ –	Data acquisition
DLS –	Different leveled surface
IoF171101 –	Ink A interconnect over fillet specimen
DTC180201 –	Ink A baseline test coupons
IoF170601 –	Ink C interconnect over fillet specimen
CTC180508 –	Ink C baseline test coupons
RTC180508 –	Ink D baseline test coupons

Chapter 1 – Introduction

In this chapter, the problem statement for this thesis is defined followed by background information on the subject and a literature review. The rest of this thesis is structured as follows: Chapter 2 discusses the preliminary quality and reliability findings between printed hybrid electronics that were fabricated in a mostly similar fashion, Chapter 3 is motivated by the results of Chapter 2 and investigates the impact of varying carrier and sheath gas flow rate on print quality, and Chapter 4 summarizes all of the major findings and technical contributions provided. Some background information in this chapter will be repeated in Chapters 2 and 3 to make submitting journal publications easier.

Section 1.1: Problem Statement

The quality of printed conductors, specifically of silver nanoparticle inks, in printed hybrid electronics will be assessed as a function of print parameters, specifically carrier and sheath gas flow rates. Quality will be evaluated by the printed line's macroscale and micromorphological features.

Section 1.2: Background and Motivation

With the advent of additive manufacturing in every field of engineering, printed hybrid electronics are no exception and on the rise because they help address the emergence of multifunctional structures with easier processing. Many companies are exploring printed electronic technologies because of some of its advantages and

functionalities (e.g., three-dimensional printed conformal form factors on curvilinear surfaces) that are not achievable through conventional technologies.

The manufacturing quality, manufacturing defects, and manufacturing yield for printed hybrid electronics are of different scale as compared to that witnessed for conventional electronics. This stems from a large variety of different process parameters and process challenges. Currently there is little understanding of the field, specifically for aerosol jet printing (AJP). The employment of numerical simulations helps avoid long-iterative trial and error. As a result, the present research team took a fundamental approach to the problem by computationally modeling the print process involving all the necessary parameters that dictate the process yield and quality (Chen et al., 2018). These simulations have been conducted down to the particle level and provides understanding that will help make these technologies successful. This project is all about exploring various aspects of this technology with a focus on the fabrication and reliability of these products.

As additive manufacturing becomes more prevalent in the fabrication of electronics addressing the growing complexity of devices, there is a need to create well-formed, robust circuitization, and interconnects between components mounted onto different leveled surfaces. To connect dies and different components on curvilinear substrates, the components will need to be bonded to the substrate. Conventionally, this has been achieved with wirebonds or soldering, but printed hybrid electronics offer a remarkable alternative via printed fillets with printed interconnects over them. The printed interconnect over fillet technology is discussed more in-depth in Chapter 2. Through printed hybrid electronics, new form factors can be obtained such as

conformable or embedded electronics with the hope that electronics can be fabricated directly into parts themselves without the need for printed circuit boards or surface-mounted components.

AJP is a direct-write printing technology built on the fundamentals of additive manufacturing. The process involves the liquid material of interest in atomized form creating a dense aerosol of micron-scale droplets with diameters typically ranging from one to five microns (Hon et al., 2008). The majority of inks, with a wide range of viscosities between 0.7 and 2,500 cPs, capable of being aerosolized can be used for the AJP. The aerosolized liquid drops are carried by nitrogen gas, denoted as carrier gas, to the deposition head through a mist tube and then focused within the head through the sheath gas before being sprayed onto the substrate. In addition to focusing and collimating the particles within the carrier gas flow, the sheath gas forms an outer layer around the aerosolized stream to prevent the contact between the aerosol particles and the inner walls (which in turn will prevent the condensation of solvents and hence help prevent clogging). Figure 1.1 shows the schematic of an ink stream as it enters the nozzle chamber from the mist tube through the nozzle and continuing to the substrate (Chen et al., 2018).

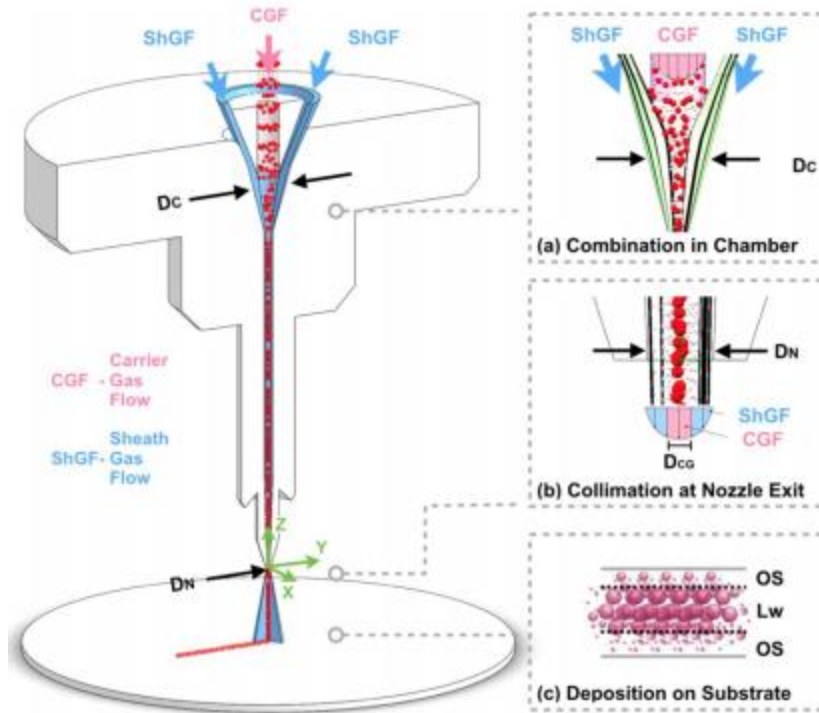


Figure 1.1: Schematic of the carrier and sheath gas flow geometry as well as a-c) different locations of interest in the AJP process (Chen et al., 2018).

Unlike syringe printing, AJP is a non-contact, droplet-based technique that can be executed with a working distance of one to five millimeters away from the substrate leading to less dependence on the surface topology (Salary et al., 2017). Relative to inkjet printing, AJP allows finer printed features, which directly leads to more flexibility, scalability, and conformal printability. The printed features typically have controllable ink stream widths from five microns to five millimeters (Hon et al., 2008). Direct-write technologies and specifically AJP are a powerful tool in the world of microelectronics as it allows for rapid prototyping of various components such as interconnects, sensors, and thin film transistors to name a few (Hoey et al., 2012). Conventional electronics manufacturing techniques such as photolithography or electroplating are limited due to geometry, harsh operating conditions, and/or material properties that AJP helps overcome (Salary et al., 2017).

Adjustable parameters possible through the AJP process include but are not limited to carrier and sheath gas flow rate, nozzle diameter, working distance between the nozzle tip and substrate, stage speed, stage temperature, substrate type, and atomizer energy among others. The properties of the ink such as its surface tension, solids loading, viscosity, wettability, and other environmental conditions can also impact the final quality of the trace. Because of the several parameters that can be changed, defining a set printing parameter space is not trivial because some of a line's morphological properties, such as trace width, can be achieved through different combination of parameters, but can then lead to a difference in another subtle features such as agglomerations.

Silver inks that are used in a wide variety of printed hybrid electronics are a suspension of silver nanoparticles in an organic binder that is then evaporated and sintered. There are numerous different silver inks that are all different, but as a part of this study one ink was the primary focus, referred to as Ink A, with two other inks discussed in Appendix A1. The nanoparticle silver inks used for AJP are compatible with a pneumatic atomizer. Ink A has a viscosity of 1.1 Pa·s or 1,100 cP and contains 75.1 mass percent of silver nanoparticles in a solvent according to the manufacturer. The silver lines were printed in a single or double pass using the Optomec Inc. AJ 200 series printer.

Two initial specimens were printed at flow rates of 80 and 50 standard cubic centimeters per minute (sccm) for carrier gas and 50 and 30 sccm for sheath gas. A subsequent varying flow rate design of experiment was conducted with carrier gas flow rates of 30, 50, 65, 80, and 100 sccm and sheath gas flow rates of 30, 40, and 50 sccm. A nozzle with a 300-micron diameter and 7.5 mm length was used. The printer stage temperature was constant at 50 °C and the print speed was constant at 1 mm/s. The

printing was conducted on FR4 or silicon substrate with a dielectric layer of Polymer N either printed or spin coated onto the surface before depositing the silver ink.

The printed lines were sintered in an oven at 150 °C for three hours after spending a half-hour at 80 °C as an intermediate dwell (Figure 1.2). The ramp rate was a half-hour from room temperature to 80 °C and then another half-hour to get from 80 °C to 150 °C. The sintering is done in two steps because reduced adhesion was observed without the intermediate dwell. Moreover, it minimizes the damage to the polymer substrate and to the interface between the printed silver trace and polymer substrate (Park et al., 2013). The preheating step removes the organic binder from the silver nanoparticle ink without abrupt vaporization, while the main sintering step completes the necking connectives among the silver nanoparticles for high electrical conductivity.

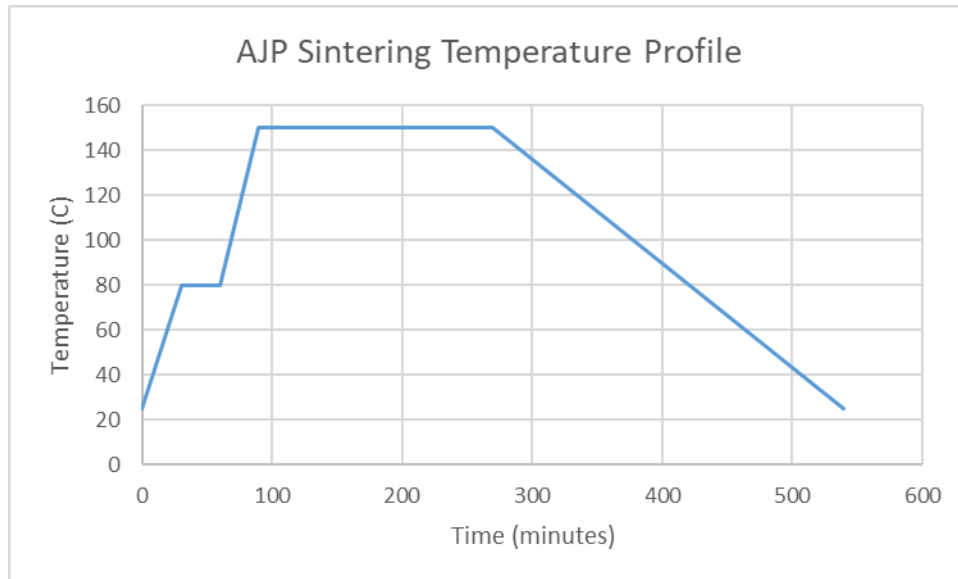


Figure 1.2: Sintering temperature profile utilized for all silver nanoparticle inks throughout this research.

Moving away from conventional technologies can also lead to a worry that the technologies that will replace something that has worked for so long will not be as reliable. Chapter 2 addresses thermal cycling durability testing conducted to investigate

the reliability of printed hybrid electronics. Chapter 2 also begins to investigate trace morphology attributes that qualify a printed trace and can impact a device's functional integrity. A good quality printed line is homogenous and continuous across its length, width, and thickness as well as adheres well to its intended target. Conductive lines require narrow width for high-density circuitry and sufficient thickness for large cross-sectional area and high current carrying capacity.

Section 1.3: Literature Review

The current literature available on printed hybrid electronics has been thoroughly discussed, but print process variation and the trace's corresponding quality and reliability has not been exhaustively researched and is an important next step for the field to move forward.

Section 1.3.1: Printed Hybrid Electronics

An algorithm to aerosol jet print fillet structures, a surface transition ramp, that enables an electrical transition between different leveled surfaces has been completed (Gu et al., 2017). Fine-pitch printed conductors over microstructure fillets allows the following advantages over wirebonding: (a) smaller space requirements, (b) decreased risk of short-circuits in high density interconnect regions, and (c) reduced electrical length of the interconnect leading to a small and controlled electrical impedance discontinuity. In a separate publication, Gu et al. (2017) devised a method for measuring the deposition rate of an AJP ink stream by printing material into an array of inkwells with known volumes that were fabricated using photolithography.

Chen et al. (2018) developed a three-dimensional computational fluid dynamics model of the aerosol carrier gas flow that is confined by an annular sheath gas flow to pinpoint the fundamental fluid mechanics principles that control the overspray as a function of droplet size distribution and sheath gas flow rate. Put simply, overspray is the ink particles that are deposited outside of the intended trace width. Their results explain that there is an abundance of smaller sized drops in the overspray region at low sheath gas flow rates, the overspray first reduces and then increases as the sheath gas flow rate increases, and there is no longer a prevalence of smaller particles in the overspray region at larger sheath gas flow rates. There is a point of diminishing return for sheath gas flow rate because at high enough levels, the particle droplets start to cross the nozzle axis and then travel back toward the axis resulting in over collimation and increased overspray.

Roberson et al. (2011) characterized the morphology of inkjet printed traces made from a microparticle and nanoparticle silver ink. Scanning electron microscope (SEM) images for traces printed with the two different particle size silver ink as well as varying sintering profiles are provided. The nanoparticle ink can attain a more conductive microstructure since the nanoparticles can sinter at lower temperatures, but lines printed with the microparticle ink had similar resistivity. Microstructures with larger grains and less porosity are more conductive.

Mahajan et al. (2013) found that a trace's line width decreases with increasing focusing ratio, defined as sheath gas flow rate divided by carrier gas flow rate, as well as stage speed. The thickness or height of the traces also increases with an increasing focusing ratio, but decreases with increasing stage speed. The decrease in line width with

increasing focusing ratio is more dramatic in smaller nozzles. The complete general trends investigated by Mahajan are presented in Table 1.1 below.

Process Variable	Line Width	Line Thickness
Focusing Ratio	Decreases	Increases
Nozzle Diameter	Increases	Decreases
Carrier Gas Flow Rate	Remains the Same	Increases
Stage Speed	Decreases	Decreases

Table 1.1: Effect of independently increasing each process variables on printed line geometry.

Smith et al. (2017) demonstrated that there is a general trend of decreasing line width with increasing substrate temperature and that overspray is more significant at higher temperatures. A higher substrate temperature also resulted in a more resistive line leading to a material resistivity four to five times larger than that of bulk silver at 100 °C for silicon, glass, and polyimide substrates. Ultrasonic atomization generates droplets of the ink and Agarwala et al. (2017) showed that the thickness of a printed line increases with increasing ultrasonic current. Salary et al. (2017) developed a computational fluid dynamics model that verified the overall line morphology trends observed through an in-situ online monitoring camera when varying flow rate parameters. For a fixed carrier gas flow rate and print speed of 30 sccm and 1 mm/s, respectively, they recommended a process window between 40 and 100 sccm for the sheath gas flow rate to optimize the printed line density, edge quality, overspray, and line discontinuity.

A limited amount of work has focused on the reliability of printed hybrid electronics. Salam et al. (2008) studied the reliability of printed interconnects by analyzing their microstructure, particularly surface roughness and heterogeneity. Cook (2013) reported the presence of crack formation in AJP fabricated copper traces subjected to mechanical and electrical fatigue, but no images were presented. Happonen (2016) studied the cyclic bending reliability of printed conductors fabricated by screen and roll-

to-roll methods. Some of the key findings from this paper indicate (i) decreasing line width increased lifetime; (ii) multi-pass printing of a given line decreased lifetime; (iii) polymer film thick silver paste with the smallest volume fraction of conductive silver particles increased lifetime; and (iv) decreasing substrate thickness also increased lifetime. Hackler et al. (2017) printed on polyethylene terephthalate substrates using a roll-to-roll screen printing process and exposed these test coupons to high temperature operation life (HTOL) and low temperature operation life (LTOL) tests. The HTOL and LTOL tests were defined to run for 168 hours or one week at 125 °C (HTOL) and -25 °C (LTOL) in ambient air. At the time of their publication, the testing was not completed.

Section 1.3.2: Gaps in the Literature

There has been some work done to begin understanding the effects of different AJP printing parameters on the final quality of a printed trace, but there is still plenty more to be done. Operating process windows that others have suggested are specific to the AJP printer used for the study, the type of ink being utilized, and less quantifiable features such as the printer maintenance. Moreover, the definition of print quality as a function of print parameters has been mostly qualitative aside from quantifying a line's overall macroscale geometry such as width and thickness and average bulk electrical properties such as conductivity. Few studies have investigated the micromorphology of the printed trace, such as its average agglomeration length scales in the bulk as well as on the surface. Moreover, limited work has been done on the long-term reliability and durability of printed hybrid electronics, specifically AJP, to estimate a life time for the traces when exposed to accelerated thermal cycling.

Section 1.4: Research Objectives

This research study began with assessing the thermal cycling durability of two types of specimens: an interconnect over fillet (IoF) specimen and simple baseline test structures. These two specimens lasted vastly different lifetimes. The revelation of fundamentally different micromorphology between the two printed samples suggested a possible correlation between print quality and thermal cycling reliability. Observing these different correlations can lead to insights into the reliability of the trace without going through expensive and time consuming durability testing. Potential reasons for the difference in quality observed includes printing at different carrier and sheath gas flow rates as well as the ink condition. Attempts were made to increase the solids fraction of the ink by bubbling nitrogen to displace the solvent from the ink, but such trials led to minimal changes in the ink's dryness. As a result, for this study, a systematic design of experiment into flow rate variation was conducted and an investigation into ink dryness's role on trace quality was tabled for future work. Carrier and sheath gas flow rates were varied with the hopes of replicating varying quality traces to establish a correlation between the print parameters and the print quality. Although this correlation may be qualitatively generic, it is quantitatively specific to the printer, ink, and test specimen used in this design of experiments. The impact of this study can provide insights into the optimal range of print parameters for printing high quality traces.

Chapter 2 – Ink A Reliability Studies

In this chapter, the thermal cycling durability of two different aerosol jet print batches using silver nanoparticle Ink A is compared and investigated for differences.

Section 2.1: Introduction

Additively manufactured printed hybrid electronics, especially those printed with aerosol jet printing (AJP), provide a unique opportunity for specialty products such as electronics printed on curved surfaces. However, the print and sintering processes produce intrinsically different microstructures and defects compared to conventional processes like wirebonds and soldering. Therefore, an in-depth understanding of their robustness and reliability is imperative before printed hybrid electronics can replace conventional surface mounted assemblies in commercial products. AJP allows for many advantages over conventional technologies but can also be problematic given the innumerable permutations of issues related to the material being printed, the printer machine itself, and other process factors that can arise. These include but are not limited to the stage platen temperature (i.e. 25 °C or 50 °C), substrate type (i.e. FR4, silicon, glass slide), flow behavior (laminar or turbulent), atomizer energy (pneumatic or ultrasonic), stand-off distance (1 to 5 mm), nozzle length and tip diameter, print speed (0.1 to 10 mm/s), aerosol viscosity, carrier and sheath gas flow rate, ink chemistry and condition, integrity of translation stage, environmental conditions, and many more (Salary et al., 2017).

A limited amount of work has focused on the reliability of printed hybrid electronics. Salam et al. (2008) studied the reliability of printed interconnects by

analyzing their microstructure, particularly surface roughness and heterogeneity. Cook (2013) reported the presence of crack formation in AJP fabricated copper traces subjected to mechanical and electrical fatigue, but no images were presented. Happonen (2016) studied the cyclic bending reliability of printed conductors fabricated by screen and roll-to-roll methods. Some of the key findings from this paper indicate (i) decreasing line width increased lifetime; (ii) multi-pass printing of a given line decreased lifetime; (iii) polymer film thick silver paste with the smallest volume fraction of conductive silver particles increased lifetime; and (iv) decreasing substrate thickness also increased lifetime. Hackler et al. (2017) printed on polyethylene terephthalate substrates using a roll-to-roll screen printing process and exposed these test coupons to high temperature operation life (HTOL) and low temperature operation life (LTOL) tests. The HTOL and LTOL tests were defined to run for 168 hours or one week at 125 °C (HTOL) and -25 °C (LTOL) in ambient air. At the time of their publication, the testing was not completed. Limited work has been done on the long-term reliability and durability of printed hybrid electronics, specifically AJP, to estimate a life time for the traces when exposed to accelerated thermal cycling.

In this study, the reliability of two different types of samples fabricated with AJP is investigated. Accelerated thermal cycling durability results are presented and an investigation to correlate the quality of the trace to its associated lifetime is suggested.

Section 2.2: Test Specimens

Silver inks that are used to print conductive features are used in a wide variety of printed hybrid electronics and they are typically a suspension of silver nanoparticles in an

organic binder or solvent. The solvent is then evaporated during sintering, after the ink is deposited on a substrate. There are numerous different silver inks, but for this study, a commercial ink (termed Ink A here) is utilized. Ink A has a viscosity of 1.1 Pa·s or 1,100 cP and contains 75.1 weight percent of silver nanoparticles in a solvent, according to the manufacturer's specification. In other studies detailed in Appendix A1, different conductor and non-conductor inks will be studied to determine which is best in various situations.

Section 2.2.1: Interconnect over Fillet (IoF) Specimen

To connect dies and different components on a substrate, pads on the components need to be bonded to corresponding pads on the substrate. Conventionally, in face-up dies this has been achieved with wirebond technology or soldering. However, the strain relief loop in wirebonds adds to the space requirements, increases parasitic losses, and increases the vulnerability of wire-sweep problems during transfer molding processes. Additive manufacturing methods offer alternate methods to perform this interconnection by using fillets with interconnects printed over them, as shown in Figure 2.1 (Gu et al., 2017). The fillets serve as a ramp between the substrate and top of the die for the printed traces instead of printing down the die at a right angle, which would have an undesirable stress concentration and could be difficult to print. In Figure 2.1a, the IoF geometry is depicted with the substrate, fillet, and die components. These fillets are built-up layer by layer, using a commercial polymer dielectric material (designated as Polymer N in this study). Polymer N is also used as a layer of adhesion-promoting dielectric film over the substrate and dies, to facilitate the adhesion of printed conductor traces that are printed

over the dies, fillets, and substrate. For this study, AJP and direct write methods were utilized to print the Polymer N fillets as well as the silver traces and Polymer N adhesion undercoating dielectric layer.

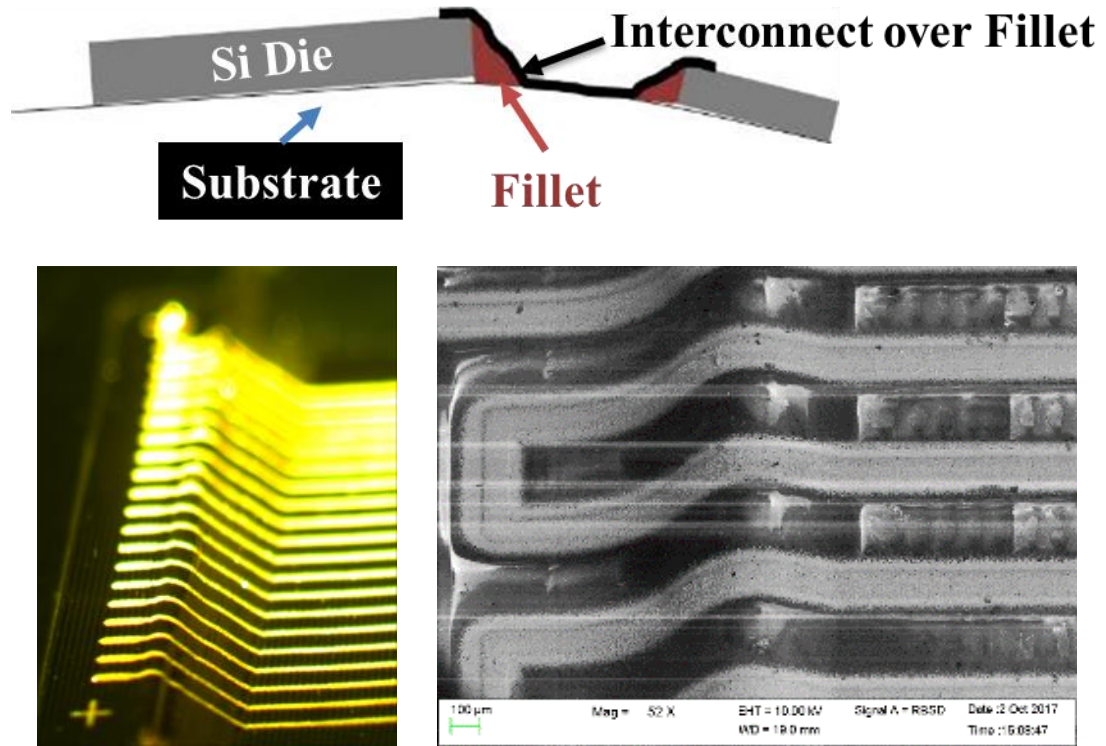


Figure 2.1: a) schematic of fillet (red) technology with trace (black) traversing die (gray) and substrate (white), b) optical microscope image of fine pitch AJP traces printed over substrate, fillet, and die, and c) SEM image of AJP traces printed over substrate, fillet, and die.

This IoF test specimen is populated with four 10-millimeter square silicon die of 375-micron thickness on a FR4 substrate (Figure 2.2). For convenience of discussion, we have defined four directions of the substrate: North, South, East and West. A fillet is printed along the northern and southern edges of each die, resulting in a total of eight triangular prismatic fillets. The fillets and adhesion layer are printed with Polymer material N and cured with in-situ UV curing. The fillet geometry and print process are described elsewhere in the literature (Gu et al., 2017). A 10-micron thick layer of

Polymer N is also printed over these three regions (FR4 substrate, Polymer N fillet, and silicon die), as an adhesion and dielectric layer before the Ink A trace is printed on top.

The IoF traces are printed at a carrier gas flow rate of 80 sccm and sheath gas flow rate of 50 sccm. Other print parameters include print speed (1 mm/s), deposition rate (0.00075 mm³/s), liquid thickness per pass (5 microns), ink stream width (150 microns), number of passes (2), and stage temperature (50 °C). The serpentine pattern of the trace allows for different geometry of traces, straight segments and right angles, as well as numerous trace segments for repeatability. This Ink A IoF specimen is denoted IoF171101.

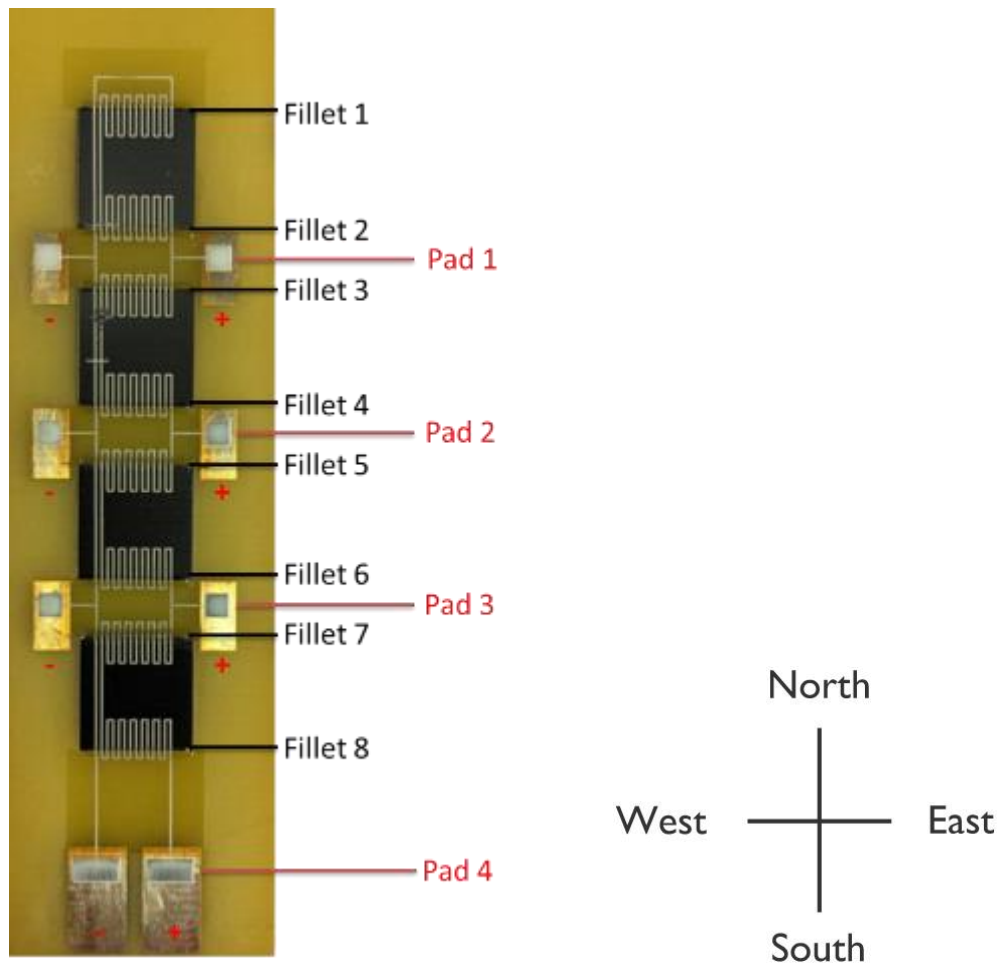


Figure 2.2: Interconnect over fillet specimen for Ink A (IoF171101).

These traces are connected to bond pads that are printed for in-situ DC resistance monitoring. Previous printed pad designs (outlined in Appendix A1) were unsuccessful due to sintered silver paste's (which was used to connect a wire to a silver pad directly on FR4 substrate) poor durability during thermal cycling tests. As shown in Figure 2.3, this problem was remediated by using a conventional copper-clad FR4 substrate and forming copper bond pads by a conventional subtractive etching process. The printed silver pad contact terminals were printed on the copper pads, such that a wire could be soldered directly to that copper pad. This hybrid method provided a more reliable connection to the data acquisition equipment.

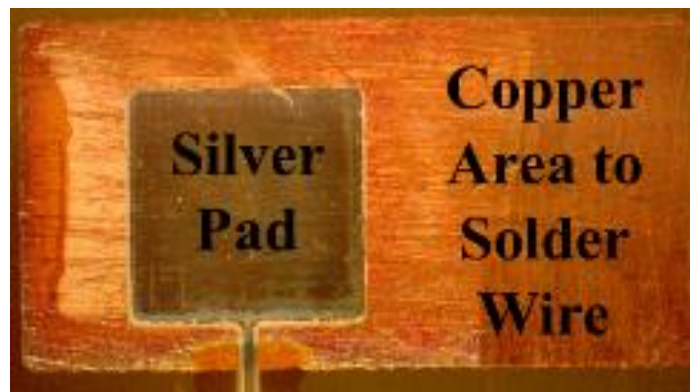
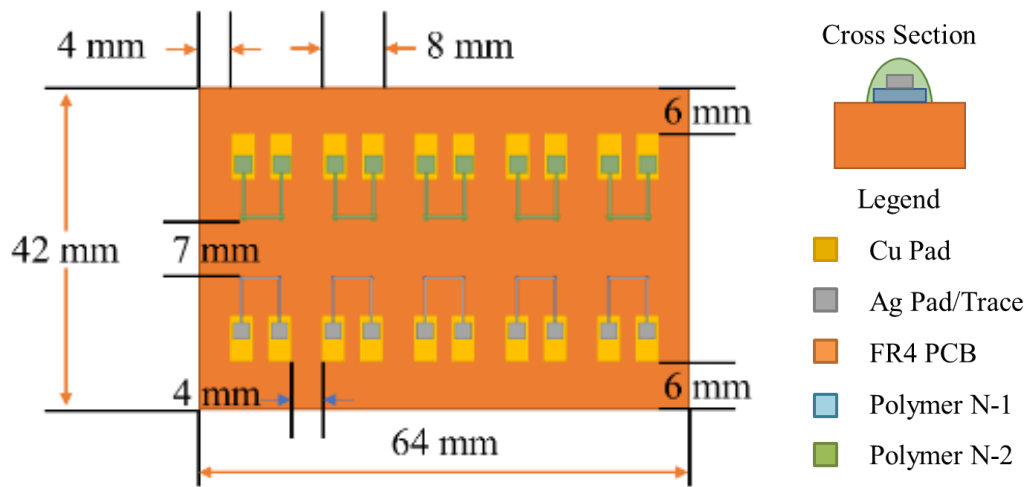


Figure 2.3: Improved wire interconnection method for IoF171101 on FR4 substrate, with additive silver pad printed on a copper pad fabricated with a conventional subtractive process.

Section 2.2.2: Baseline Test Coupons

As a comparative benchmark, simple baseline test structures were fabricated in addition to the IoF171101 specimen, using the same Ink A. Each baseline test coupon board, with the batch denoted as DTC180201, is populated with 10 silver test traces that are three sides of a five-millimeter square (Figure 2.4a). Each test trace is connected to pads for in-situ DC resistance monitoring. Of the 10 structures, the lower row of five

structures had the same stack up as IoF171101, consisting of Ink A silver trace printed on top of a 10-micron thick adhesion and dielectric layer of Polymer N on top of FR4 substrate. The upper row of five structures had an additional layer of Polymer N as a barrier layer on top of the silver trace, as seen in the cross-section depicted in Figure 2.4b. The purpose of this buried test structure was to evaluate the effect of the barrier layer on the reliability of the printed electronic design. Five test coupon boards were fabricated for a total of 50 test structures to allow for sufficient statistical replicates.



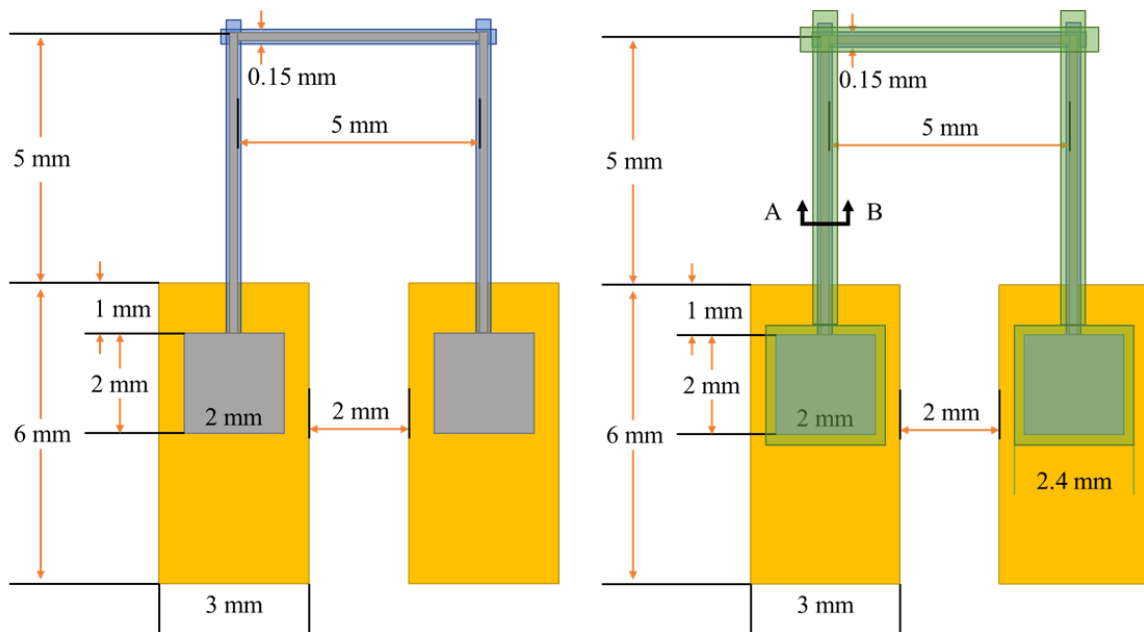


Figure 2.4: a) Baseline test coupon board design and b) individual baseline test structures with and without additional Polymer N barrier layer.

Before Ink A was hooked up to the printer's atomizer for printing the DTC specimens, the solids fraction of the ink was measured and it was determined that solvent needed to be added in order to keep the ink within recommended specifications. This is needed because the act of printing and aerosolizing tends to remove solvent from the ink. As such, 0.8 mL of a specified co-solvent was added to the ink. To achieve the desired deposition rate ($R_{\text{ink}} = 0.00075 \text{ mm}^3/\text{s}$), the DTC180201 traces were printed at a carrier gas flow rate of 50 sccm and sheath gas flow rate of 30 sccm. This flow rate is significantly lower than that used in the IoF171101 specimen potentially because the solvent content was different for the ink in the two cases. Other print parameters including print speed (1 mm/s), deposition rate ($0.00075 \text{ mm}^3/\text{s}$), liquid thickness per pass (5 microns), ink stream width (150 microns), number of passes (2), and stage temperature ($50 \text{ }^\circ\text{C}$) were kept the same as the IoF171101 fabrication.

Section 2.2.3: Macroscale Geometry

From imaging the IoF171101 and DTC180201 trace's surface and cross-section, the thickness and width was determined by extrapolating the microscope's scale bar. The IoF171101 thickness was 7.2 ± 1.2 microns with a sample size of six and the DTC180201 thickness was 9.3 ± 1.9 microns with a sample size of eight, while the widths were 149 ± 2.5 and 125 ± 11.6 microns, respectively, with a sample size of 30.

Section 2.2.4: Microscale Morphology

Surface SEM images reveal coarser surface granularity (agglomerates of larger size and spacing) and porosity on the surface of the silver traces of IoF171101, compared to those of DTC180201 (Figure 2.5). The finer granularity in the baseline test coupons compared to the coarser surface granularity of the IoF171101 specimen, allows higher surface-to-volume ratios in the agglomerates, thus permitting greater degree of sintering and lower percentage of porosity. This can potentially result in higher bulk as well as interfacial strength and will be verified in subsequent thermal cycling durability tests, as reported in Section 2.4. Cross-section images confirmed higher bulk porosity in the traces of the IoF171101 specimen relative to the baseline test coupon (Figure 2.6). Extensive microscale porosity distributions can be observed in IoF171101, whereas the DTC180201 cross-section nearly resembles homogeneous silver with only some extent of nanoscale porosity visible only under much higher magnification on SEM or atomic force microscopy (Appendix A4).

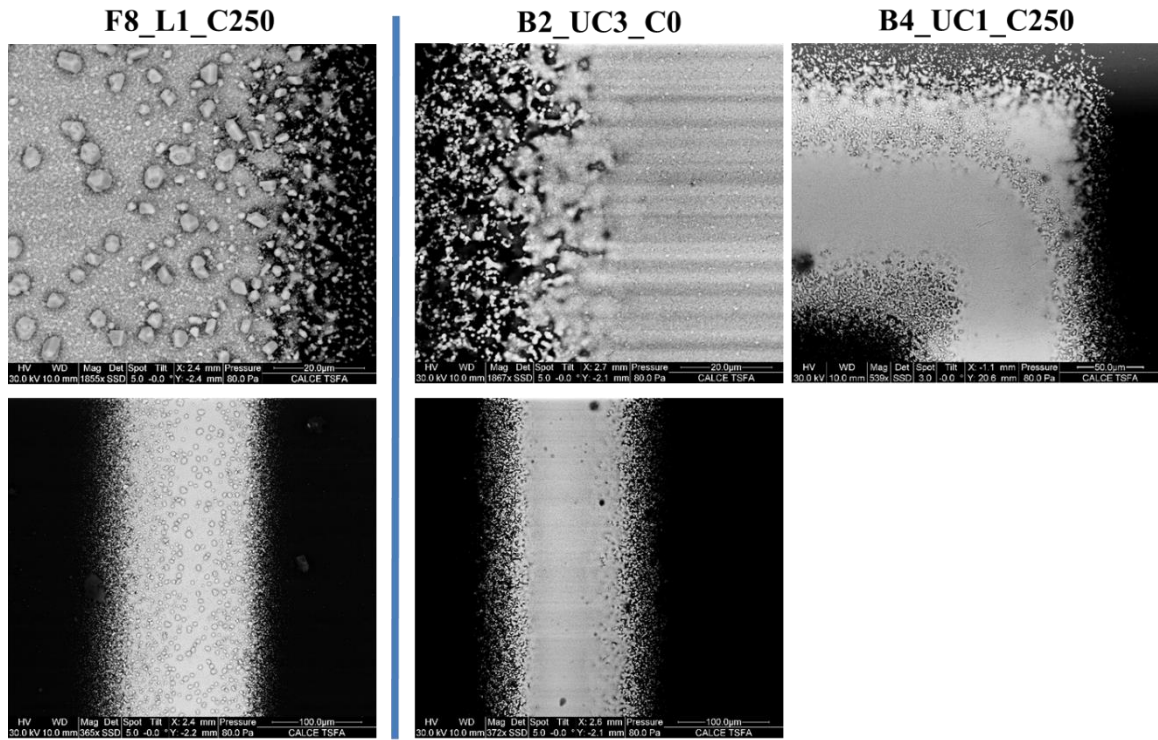


Figure 2.5: Coarser agglomerates can be seen on IoF171101's Fillet 8 line segment 1 after 250 cycles compared to DTC180201's traces after 0 and 250 cycles.

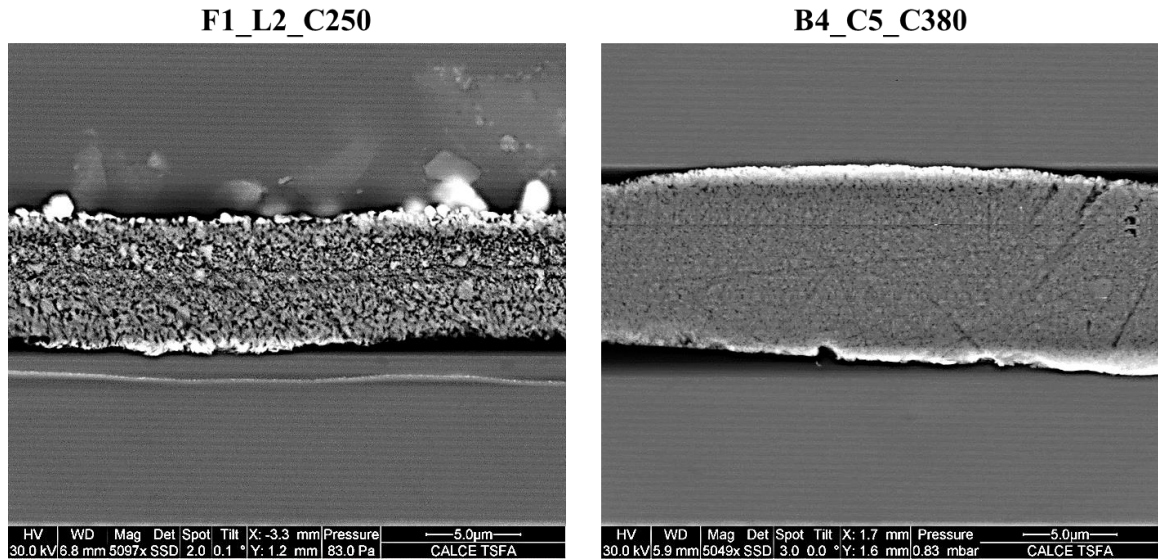


Figure 2.6: Bulk porosity (micron-scale pores) is identified to be greater in the cross-section of the IoF171101 traces relative to that in the DTC180201 traces.

Through image processing with a commercial software and smart segmentation methodology described in Appendix A6, the percent bulk porosity in IoF171101 is 8.2 percent, while in DTC180201 it is just 0.36 percent, which supports the visual observation that the former is more porous (Figure 2.7). The average pore diameter and area for the IoF171101 is 0.027 μm and 0.0019 μm^2 across 2,617 features captured.

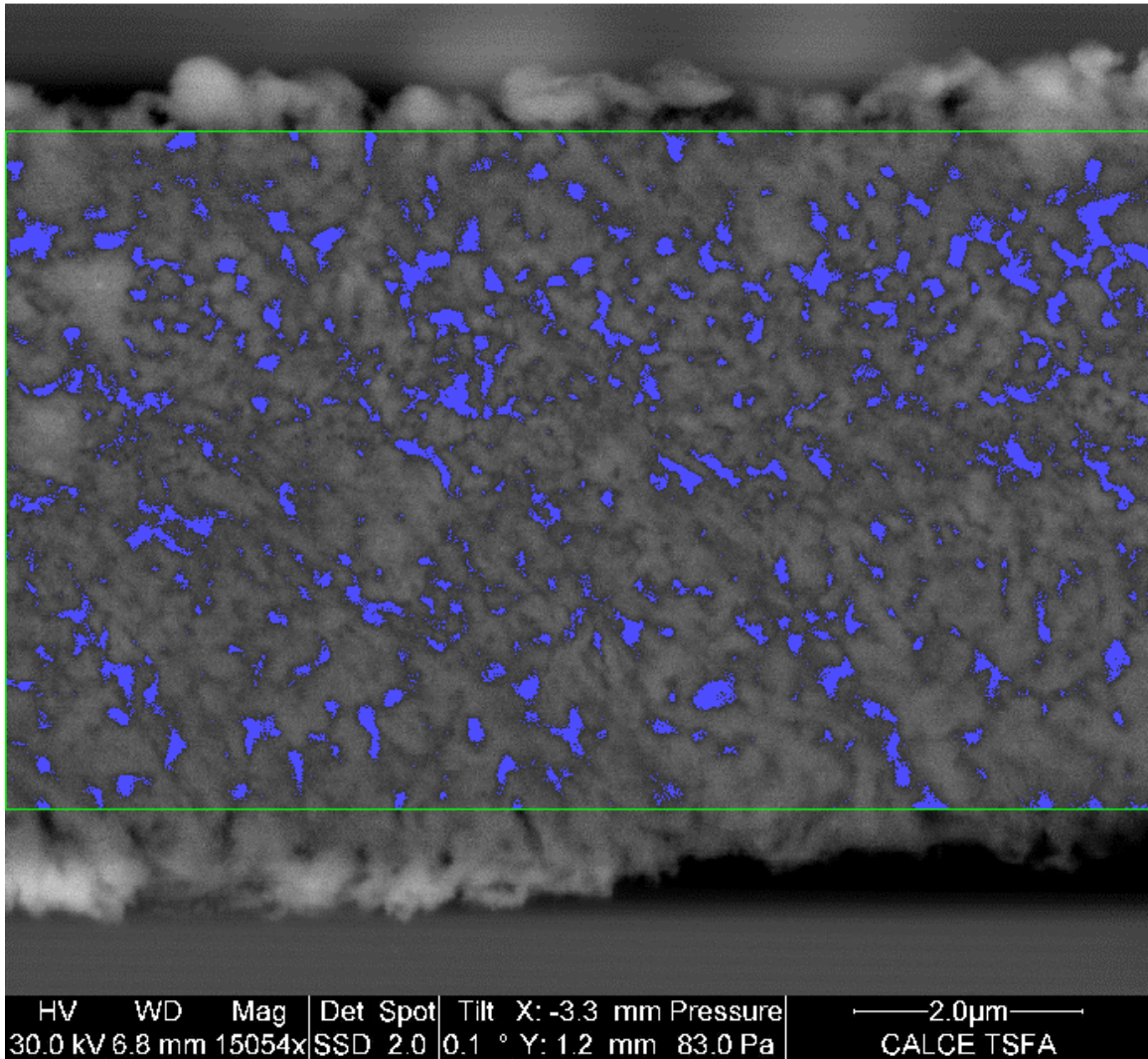


Figure 2.7: Bulk porosity in IoF171101 highlighted through image processing thresholds.

Section 2.2.5: Effective Conductivity

The printed traces are micro and nanoporous silver structures so at best it is possible to estimate a volume averaged, homogenized and effective resistivity and conductivity as is the case with other composite materials. As a result, these measurements will be higher than the typical resistivity of bulk silver of 1.59×10^{-8} ohm-meters (Serway, 1994). The effective resistivity of the IoF171101 and DTC180201 traces before thermal cycling were estimated by dividing the measured two-wire DC resistance of the structure by the length of the trace and multiplying it by the cross-sectional area of the trace: $\rho=R*A/L$. In the future, four-wire resistance measurements need to be made in order to remove additional resistance the setup is adding leading to a higher calculated effective resistivity than in actuality. For the IoF171101, the cross-sectional area was estimated by a nominal trace width of 149 microns and a nominal thickness of 7.2 microns. For the DTC180201, the cross-sectional area was estimated by a nominal trace width of 125 microns and a nominal thickness of 9.3 microns. Effective conductivity of the traces was then calculated by inverting the calculated effective resistivity. The statistics of the normalized, to the largest value, effective conductivity measurements are shown in Figure 2.8. The statistics of the IoF171101 specimen appears to follow a bimodal distribution, while that of the DTC180201 batch follows a unimodal distribution. This may suggest that the quality of the IoF171101 print was inferior to that of the DTC180201 prints.

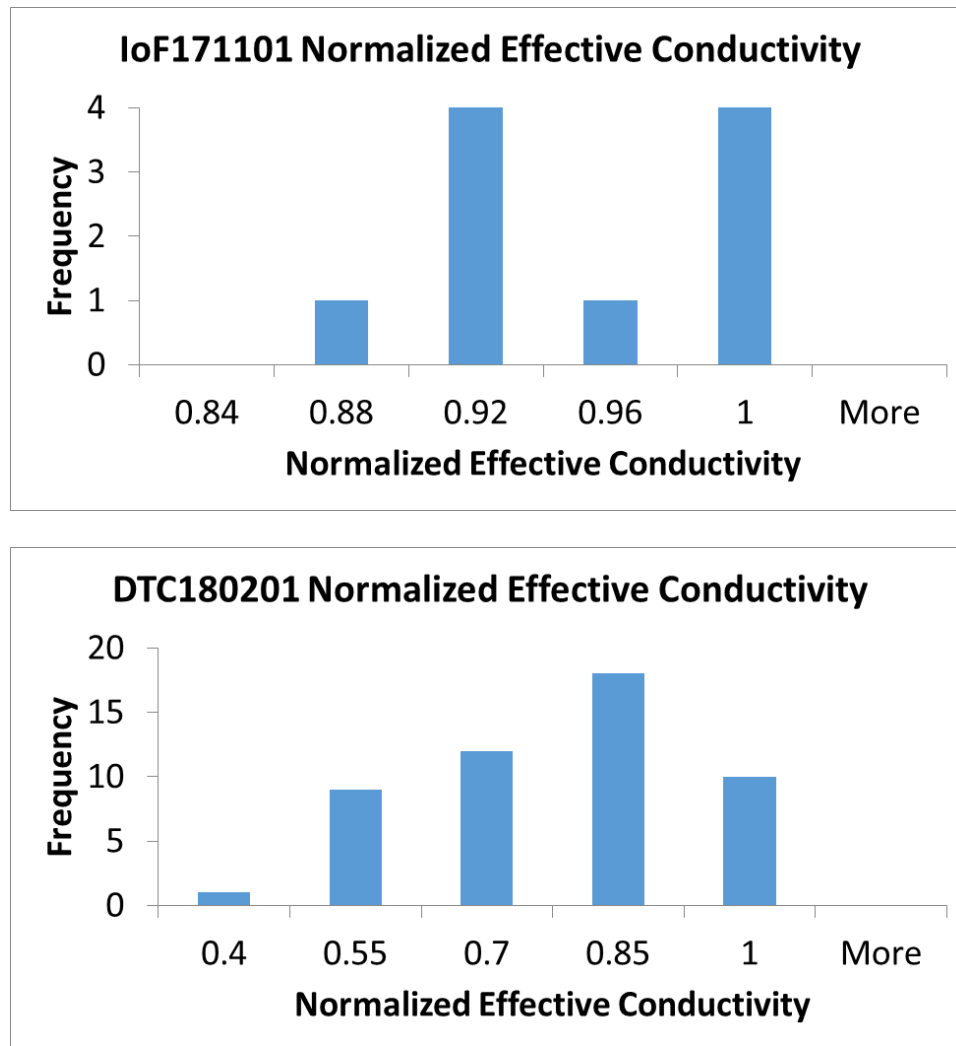


Figure 2.8: Normalized effective conductivity histogram plots for a) IoF171101 and b) DTC180201.

Section 2.3: Test Plan

The temperature profile used for accelerated thermal cycling of IoF171101 and DTC180201 was between -40 and 125 °C. IoF171101 had a half-hour dwell at the hot temperature and 10 °C per minute ramps in between the two extreme temperatures, while the DTC180201 had 10-minute dwells at the hot and cold temperature and 8 °C per minute ramps in between the two extreme temperatures (Figure 2.9). Both profiles

completed one cycle in just over an hour. The slight changes in profile were made out of convenience based on the availability of thermal chambers in the lab and is not believed to have greatly affected obtained reliability results.

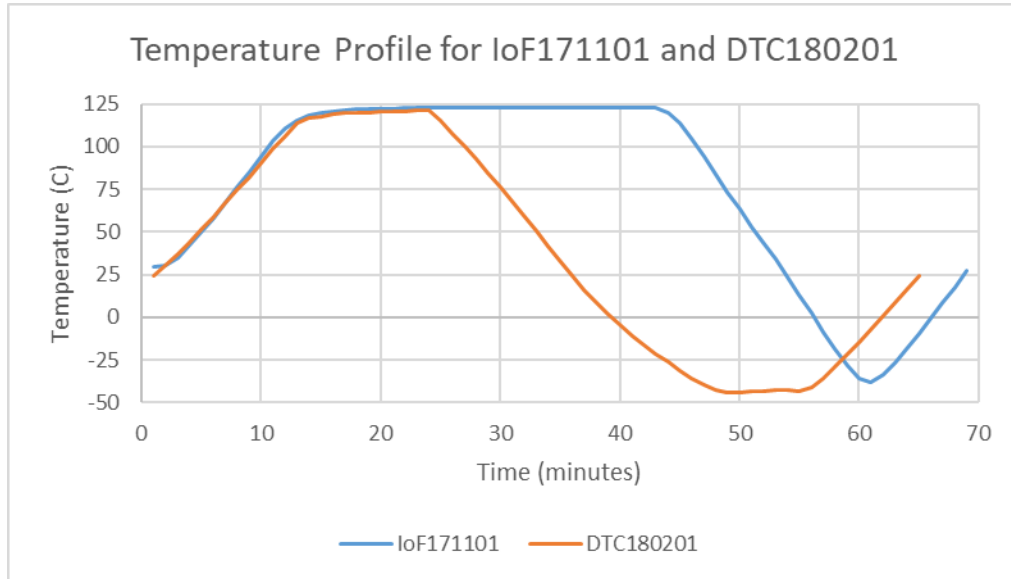


Figure 2.9: Temperature profile for IoF171101 compared to DTC180201.

The two or four-wire resistance of each sample during thermal cycling was monitored by connecting each structure's pads to an Agilent 34980A data acquisition instrument (DAQ) that recorded data with a sampling frequency of one data-point per minute. The temperature inside of the chamber was also recorded by the DAQ with a Type K thermocouple. Two-wire resistance measurements were made at Pads 1, 2, and 3 since they were secondary pads, while four-wire resistance measurement was made at Pad 4 of the IoF171101. Pad 4 monitors all the traces printed along the specimen, while Pad 1 only monitors the traces up to Fillet 2, Pad 2 only monitors the traces up to Fillet 4, and Pad 3 only monitors the traces up to Fillet 6. These secondary pads would help in locating a potential failure site. For example, a resistance spike in Pad 4 and not in any of the other pads, could indicate that the failure occurred beyond Fillet 6.

As expected early in the thermal cycling durability testing, the resistance of the IoF171101 traces varied smoothly as a function of temperature and no anomalous spikes were observed (Figure 2.10). The measured resistance values increase from Pads 1 to 2 to 3 because those pads are monitoring increasingly longer trace length. Pads 3 and 4 happen to measure similar magnitude resistances even though Pad 4 monitors a longer length of trace than Pad 3 because a four-wire connection measurement was made at Pad 4, which eliminated the additional resistance added from the wires that were used to connect IoF171101 to a data acquisition instrument. Any resistance spikes in the secondary pads were also detectable in the pads after it.

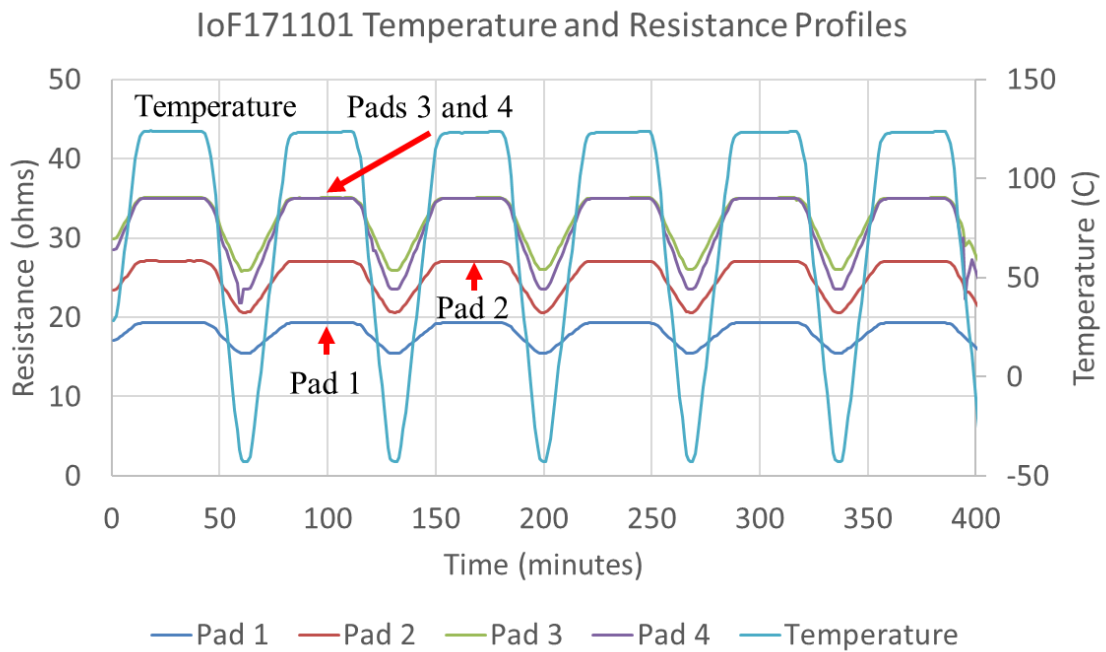


Figure 2.10: Temperature and resistance profiles for the first six thermal cycles that IoF171701 underwent.

Also, as expected, early in the thermal cycling durability testing for DTC180201, the resistance of the printed traces varied smoothly as a function of temperature and no anomalous spikes were observed. All 50 test structures are not displayed in Figure 2.11

for simplicity, but four test structures are provided as representative examples. In accordance with industry standards, increases in DC resistance of at least 20 percent from nominal temperature dependent values were used as a failure indicator for both the IoF171101 and DTC180201.

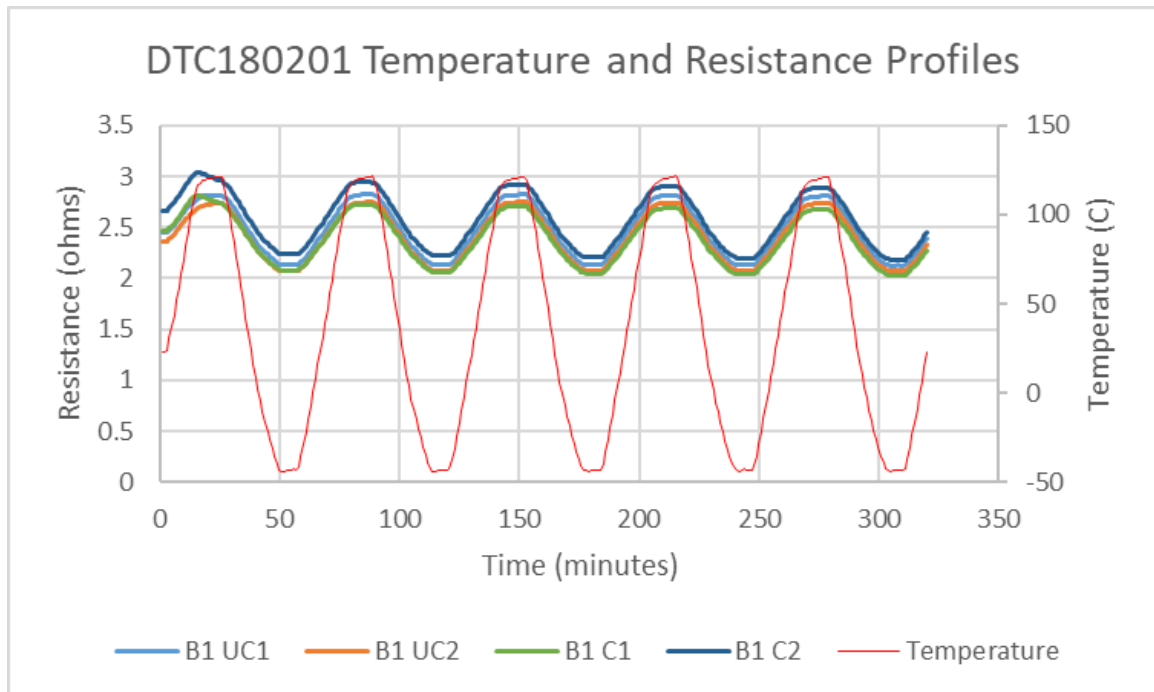


Figure 2.11: Temperature and resistance profiles for the first six thermal cycles that DTC180201 underwent.

Section 2.4: Results

The findings from the thermal cycling tests on the IoF171101 and DTC180201 specimens are: (i) the changes in the electrical resistance of the traces as a function of thermal cycling; and (ii) destructive failure analysis of the specimens whose DC resistance exceeded a pre-defined failure threshold.

Section 2.4.1: Resistance Profiles

The Pad 4 resistance values for IoF171101 at the end of the hot (125 °C) and cold (-40 °C) temperature dwell portions of the cycle was extracted following extensive MATLAB post-processing of the resistance data that was recorded at a sampling rate of one data point per minute. These resistance values were normalized based on the hot and cold temperature resistance recorded from the first cycle (Figure 2.12). The first spike in the cold temperature resistance was observed after the 65th cycle, but no spike in the hot temperature resistance was observed until after 250 cycles were completed. The hot temperature resistance of the IoF171101 specimen decreases with cycle number, which is expected because the printed traces could be undergoing further sintering during the temperature cycling process.

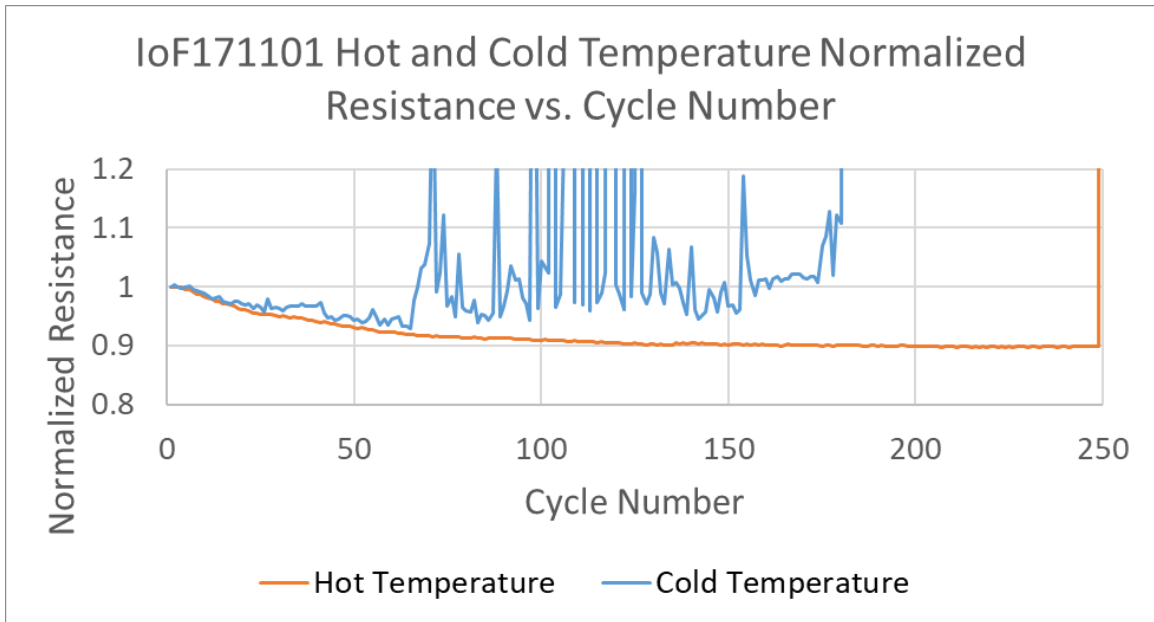
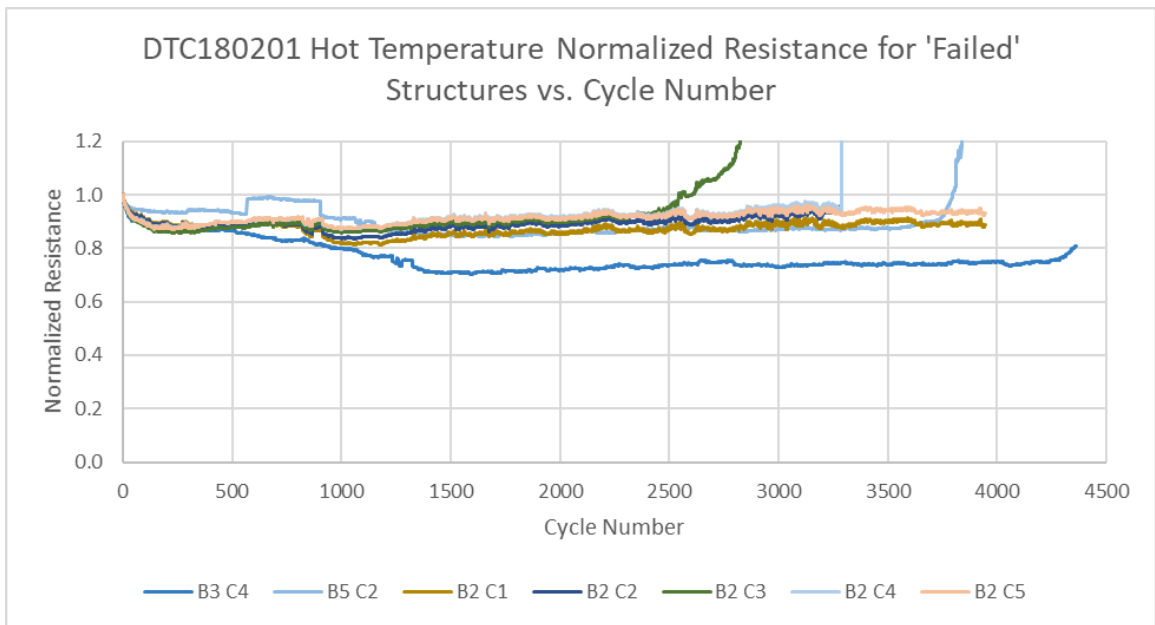


Figure 2.12: Normalized resistance of IoF171101 at the hot and cold temperature dwells as a function of cycle number.

For the DTC180201 print batch, 50 structures were monitored with in-situ DC resistance measurements. To avoid a plot that is too cluttered and difficult to interpret, the

hot and cold temperature resistance profiles for all 50 structures are provided in Appendix A3. Selected resistance profiles are provided here, including: 1) seven test structures that saw resistance spikes at the cold temperature dwell denoted as ‘failed’ structures (Figure 2.13); 2) a handful of representative structures that did not see any irregular resistance variations, denoted as ‘survivor’ structures (Figure 2.14); 3) four structures that showed an unusual intermittent drops in resistance before stabilizing to expected values, denoted as structures with ‘intermittent resistance anomalies’ (Figure 2.15); and 4) two structures that had steadily rising resistances, denoted as structures exhibiting ‘continuous wearout’ (Figure 2.16). The seven failed structures were all covered traces with the additional burying layer of Polymer N and were grouped as failed because they had a resistance spike at the cold temperature dwell. Three of those seven also had resistance spikes later on at the hot temperature dwell, but for completeness all seven failed structure’s hot temperature resistances are plotted despite four structures not having a hot temperature dwell resistance spike.



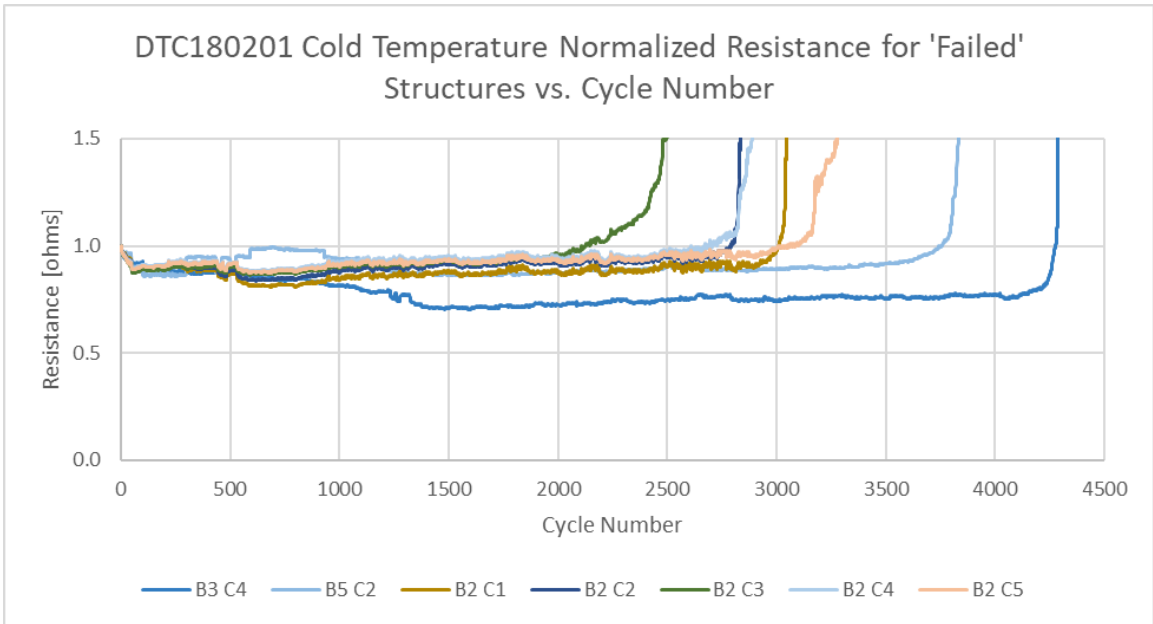
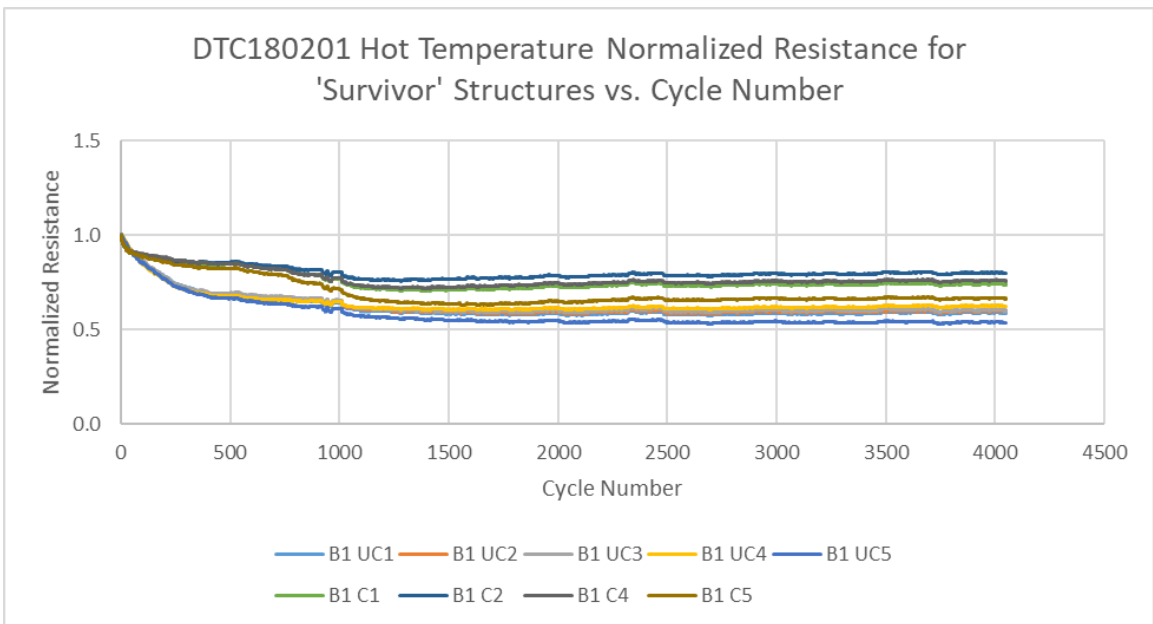


Figure 2.13: Normalized resistance of DTC180201 failed structures at the a) hot and b) cold temperature dwells as a function of cycle number.



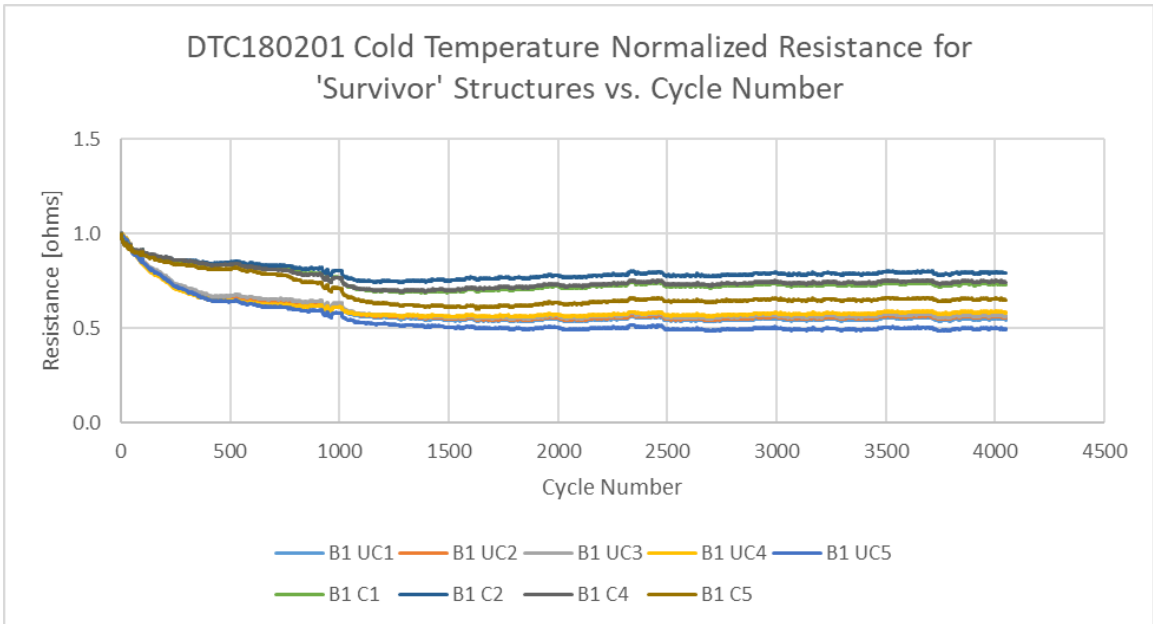
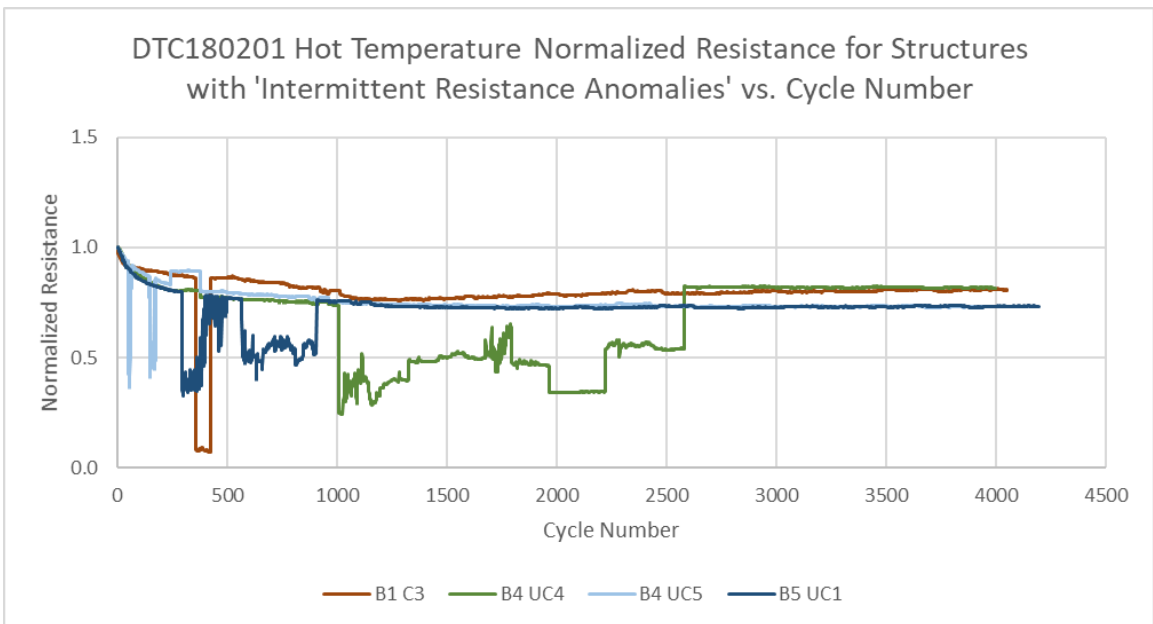


Figure 2.14: Normalized resistance of DTC180201 'survivor' structures at the a) hot and b) cold temperature dwells as a function of cycle number.



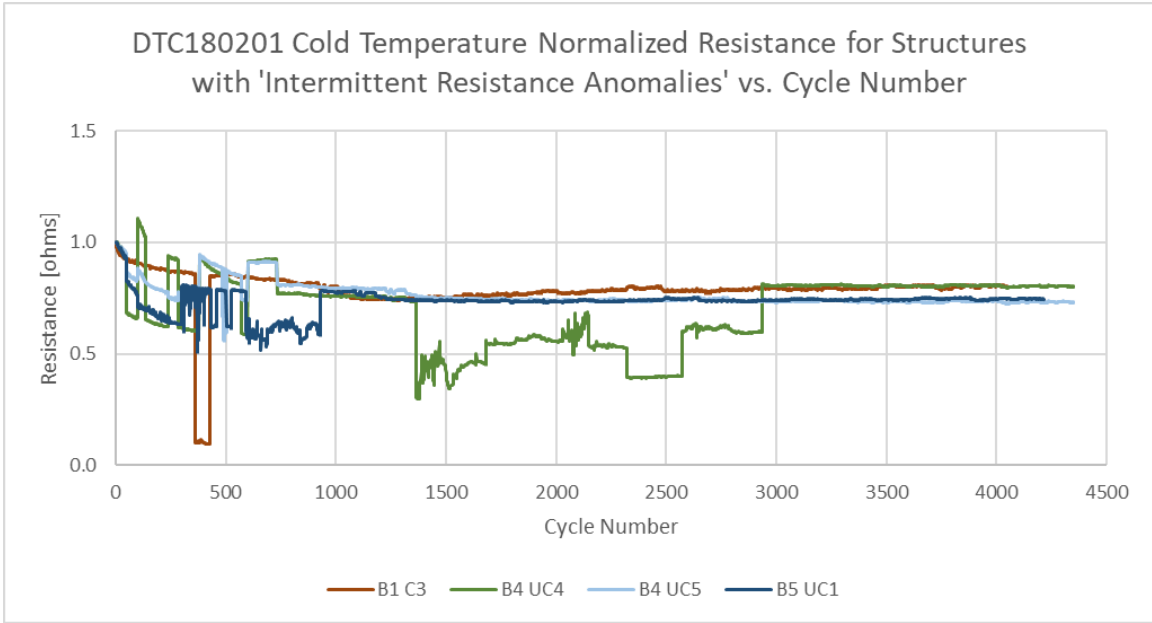
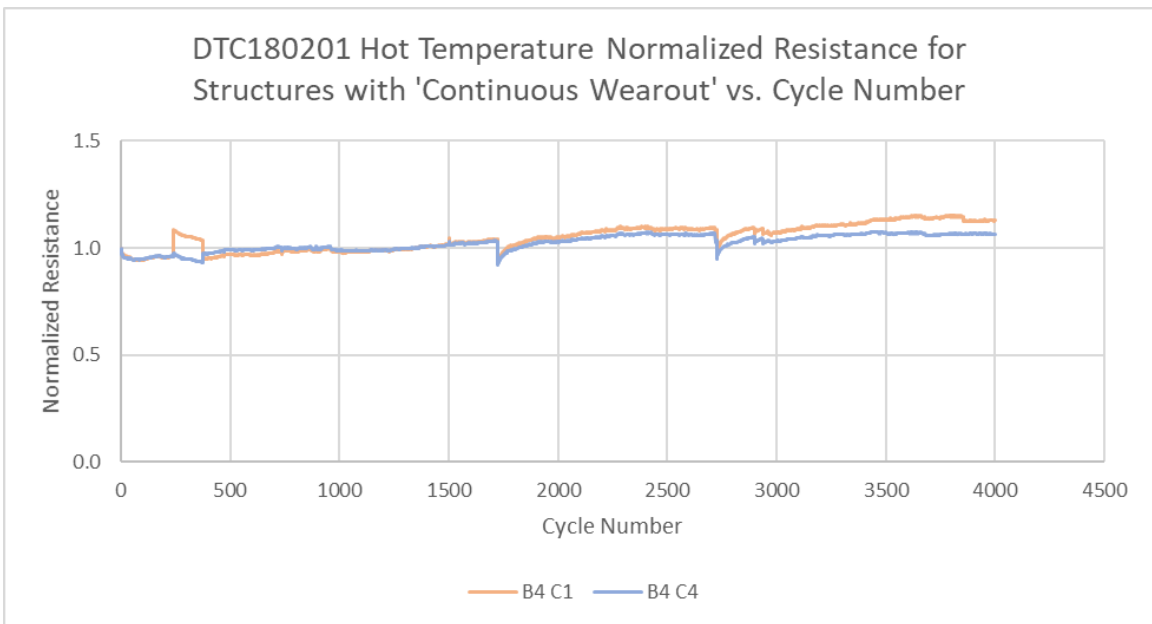


Figure 2.15: Normalized resistance of DTC180201 structures with intermittent resistance anomalies at the a) hot and b) cold temperature dwells as a function of cycle number.



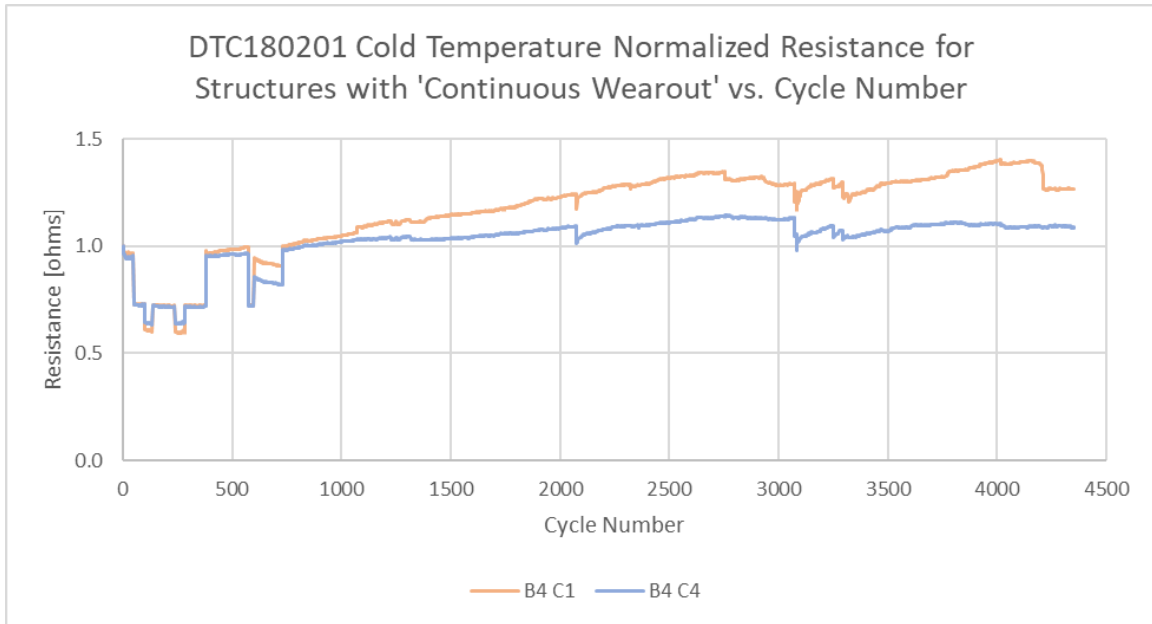


Figure 2.16: Normalized resistance of DTC180201 structures exhibiting continuous wearout (steadily increasing resistance) at the a) hot and b) cold temperature dwells as a function of cycle number.

Section 2.4.2: Failure Analysis

The IoF171101 specimen lasted 250 thermal cycles before a failure was observed in the hot temperature resistance values. Subsequent post-mortem investigations revealed that the failure site was in the top-most trace. The visible failure signature was manifested as localized longitudinal cracking and delamination and was unrelated to the fillet technologies (Figure 2.17). These results helped gain confidence in the durability of the IoF technology which includes the printed fillet as well as the traces printed on top of the fillet.¹ Resistance values of this failed IoF specimen did indicate failures at cold temperatures prior to 250 cycles, but these resistance anomalies could not be observed

¹ An identical IoF specimen was printed with another commercial ink as well and have been subjected to this same thermal cycling test. That specimen has survived 200 cycles, corroborating the durability of the IoF technology. The test results for these additional specimens are reported in Appendix A1.

when documenting the specimen at room temperature. This is not uncommon in thermal cycling fatigue tests where small microcracks sometimes open up initially under local tensile stress states at one of the temperature extremes, hot or cold depending on the specimen architecture, but close-up under local compressive stress states at other temperatures, thus making it difficult to duplicate these resistance anomalies at room-temperature post-mortem. Eventually such microcracks are observed to propagate and grow in severity, creating resistance increases at all temperatures.

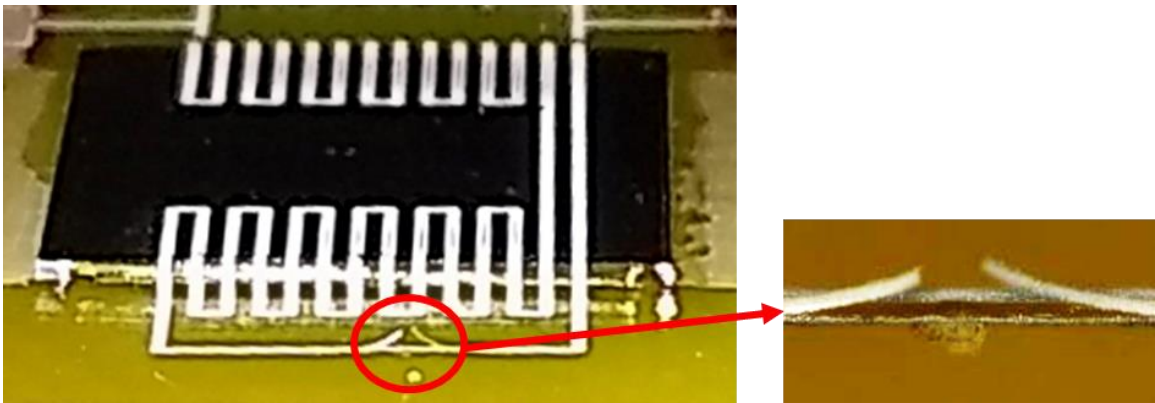


Figure 2.17: Trace delamination failure at the top of the specimen.

The initial test plan was to repair the small crack and delamination and return the repaired specimen to thermal cycling. However, severe damage was observed upon more extensive failure analysis. During SEM documentation, transverse and longitudinal microcracks, which could be expected from such thermal cycling, were visible in several locations (Figure 2.18a). A day later, after the failed specimen was withdrawn from the test chamber, severe growth in delaminations and trace discontinuities were observed (Figure 2.18b). The in-situ DC resistance measurements during the thermal cycling had not picked up such circuit discontinuities, but was confirmed with multimeter resistor measurements after the delaminations and discontinuities were observed. This continuing post-test growth in the damage level may potentially be from the release of locked-in

residual stress that had evolved during the specimen fabrication and during the temperature cycling test (Figure 2.18c).

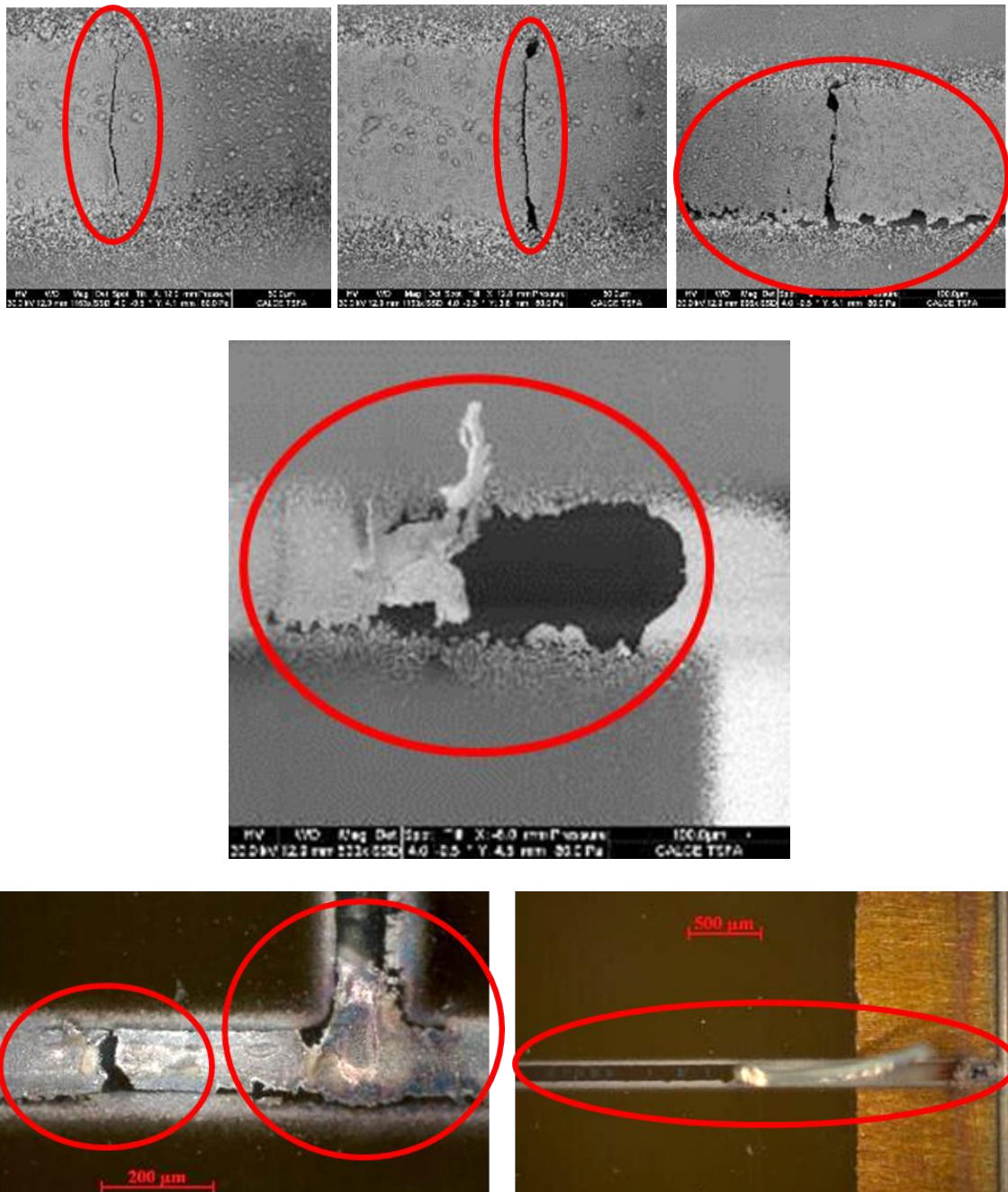


Figure 2.18: a) SEM image of transverse and longitudinal microcracks observed in some of IoF171101's traces after 250 thermal cycles, b) SEM image of trace delamination, and c) optical image of trace delamination and disintegration.

In addition to the already discussed surface view documentation, a portion of the IoF171101 was cross-sectioned and examined for internal features and damage signatures in the trace after undergoing 250 thermal cycles. Following grinding and polishing of the trace during sample preparation, SEM imaging revealed a crack in the printed line's cross-section, which is in the middle of the trace that is speculated to correspond to the interface between the first and second print pass during fabrication (Figure 2.19). The two passes were used to reach the desired trace thickness of 10 microns. It is unknown whether this crack is the result thermal cycling damage accumulation or was preexisting in the specimen before temperature cycling. Later work suggested the interface failure was unrelated to stresses experienced during cross-sectioning, grinding and polishing. This interface does appear to be a site of embedded weakness compared to the rest of the structure, potentially acting as a latent defect site.

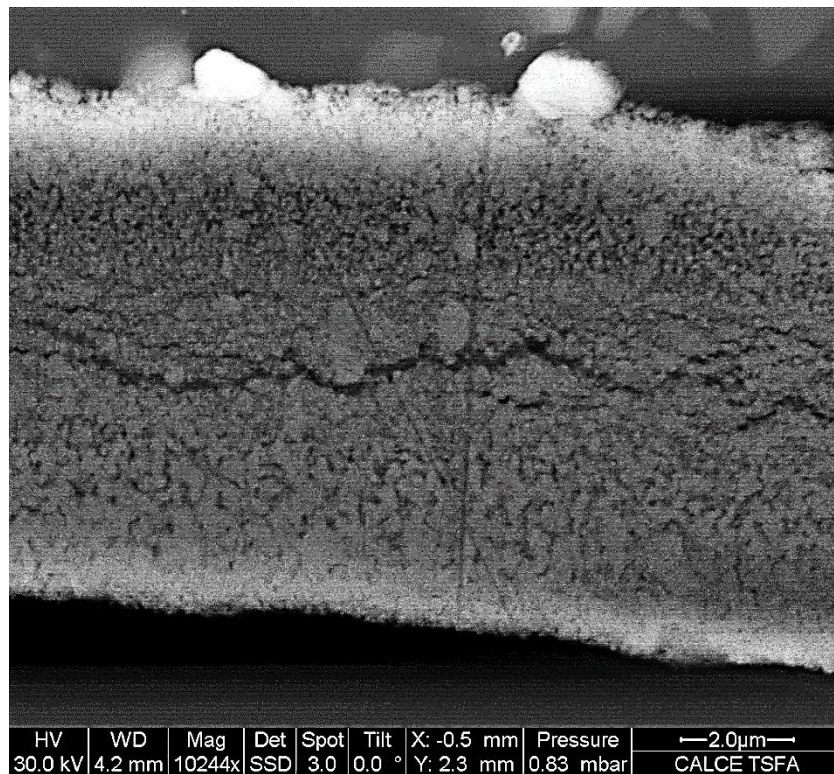


Figure 2.19: SEM image of interfacial crack in one of IoF171101's trace cross-section.

On the other hand, for DTC180201, despite thousands of thermal cycles, as summarized in Table 2.1, the Ink A baseline test coupons showed little damage to the traces. No serious anomalies in the electrical DC resistance values and no delamination or disintegration damage similar to that seen in the IoF171101 specimen were observed. This indicates that the DTC180201 print batch with Ink A is more robust than the corresponding IoF171101 print batch, since these DTC180201 structures have already survived thousands of thermal cycles. In contrast, the IoF171101 had exhibited microcracking after just 250 cycles.

Specimen Name	DTC180201_B1	DTC180201_B2	DTC180201_B3	DTC180201_B4	DTC180201_B5
Thermal Cycles	3,700	3,600	4,000	3,600	3,850

Table 2.1: Summary of thermal cycles exposure for each test coupon board printed with Ink A.

The minimal damage seen in the Ink A test coupons mainly consisted of whisker-like features extruding out of some traces, which is not uncommon for metallic materials (Figure 2.20). As an example, tin whiskers have been observed and documented in equipment that used tin-rich solder plating in the early 20th century (Lie et al., 2009). These whiskers can be problematic if they cause short circuits as is the case when they grow between metal solder pads or break-off and span across neighboring electrical elements. However, no resistance spikes or anomalies have been observed so far in this study as a result of whisker growth.

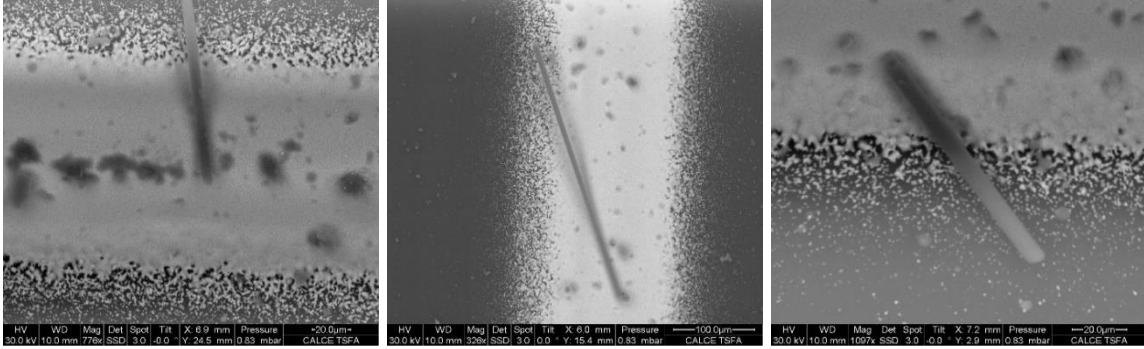


Figure 2.20: Three examples of whiskers found in Board 3 for the Ink A test coupons.

For the seven test structures that exhibited resistance spikes at the cold temperature dwell, the root-cause is believed to be the delamination of the printed pads on top of the copper island (Figure 2.21). Although no cause for failure in the printed lines were found during documentation of these structures, resistance spiked did occur because there was a break in the circuit from the soldered wire to the actual test structure. This could suggest that larger sized printed features are more susceptible to thermal cycling.

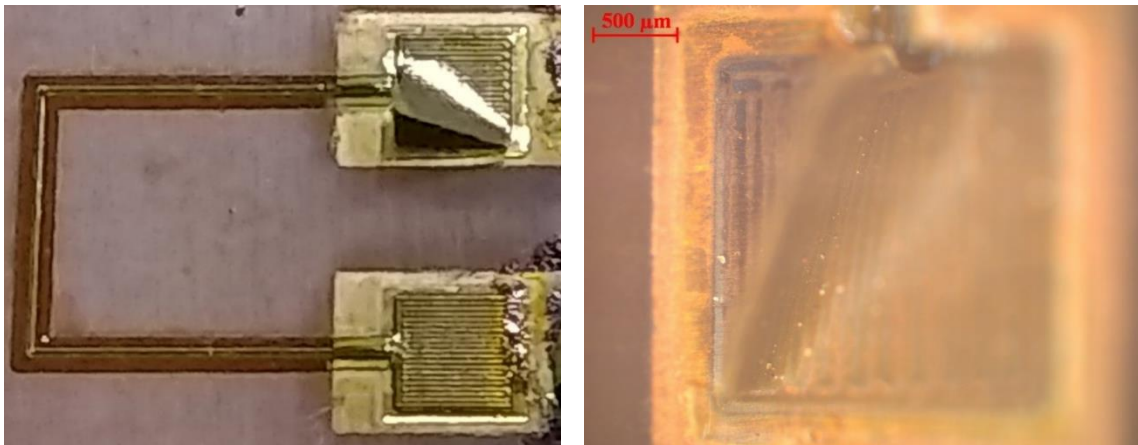


Figure 2.21: Optical images of pad lifting for DTC180201 B2C3.

Section 2.5: Summary

Two different printed electronic specimens were successfully fabricated with Ink A. The first was an IoF specimen (IoF171101) that had printed lines traversing surfaces at different level (FR4 substrate and an elevated silicon die) with the help of an intervening polymer fillet ramp. The second specimen type was a baseline test coupon design (designated as DTC180201 specimen) that is simpler in nature, containing three sides of a five mm square on a single surface at a single level (without any different leveled surfaces). The IoF171101 and the DTC180201 specimens were documented with SEM imaging prior to any testing. The IoF171101 specimen showed coarser micromorphology and larger agglomerate features on the surface of the traces as well as greater bulk porosity within the trace. This difference is theorized to be the reason for vastly different reliability results following accelerated thermal cycling durability testing. The IoF171101 failed after just 250 thermal cycles, showing extensive microcracking as well as delaminations, whereas the DTC180201 structures lasted over 3,500 thermal cycles with failures unrelated to the printed traces and minimal observed damaged. The differences in the reliability results in these two different print batches of AJP traces appear to be the result of variable trace quality, as defined by micromorphological properties such as agglomeration and porosity. The ink condition such as solvent composition and content as well as the process parameters such as the flow rates of carrier gas and sheath gas for the IoF171101 and DTC180201 print batches were not identical, although both were printed with Ink A. Further work is needed to investigate the effect of ink condition namely dryness as defined by solids loading and solvent composition as well as gas flow rate on the quality of an AJP line. The impact of carrier

and sheath gas flow rate on trace quality will be the subject of further investigation in a separate study in the next chapter.

Chapter 3 – Effect of Gas Flow Rate on Trace Quality

In this chapter, a design of experiment is conducted to understand the impact of carrier and sheath gas flow rate on aerosol jet printed trace quality.

Section 3.1: Introduction

Aerosol jet printing (AJP) is a direct-write printing technology built on the fundamentals of additive manufacturing. The process involves the liquid material of interest in atomized form creating a dense aerosol of micron-scale droplets with diameters typically ranging from one to five microns (Hon et al., 2008). The majority of inks, with a wide range of viscosities between 0.7 and 2,500 cPs, capable of being aerosolized can be used for the AJP. The aerosolized liquid drops are carried by nitrogen gas, denoted as carrier gas, to the deposition head through a mist tube and then focused within the head through the sheath gas before being sprayed onto the substrate. In addition to focusing and collimating the particles within the carrier gas flow, the sheath gas forms an outer layer around the aerosolized stream to prevent the contact between the aerosol particles and the inner walls (which in turn will prevent the condensation of solvents and hence help prevent clogging). Figure 1.1 shows the schematic of an ink stream as it enters the nozzle chamber from the mist tube through the nozzle and continuing to the substrate (Chen et al., 2018). The reliability of AJP electronics is related to the quality of the printed traces. To maintain consistent print quality, the effect of printing parameters and ink condition must be well understood. This study focuses on the influence of carrier and sheath gas flow rates on important macroscale and microscale

features of printed conductor traces, for a selected commercial ink printed with an aerosol jet printer.

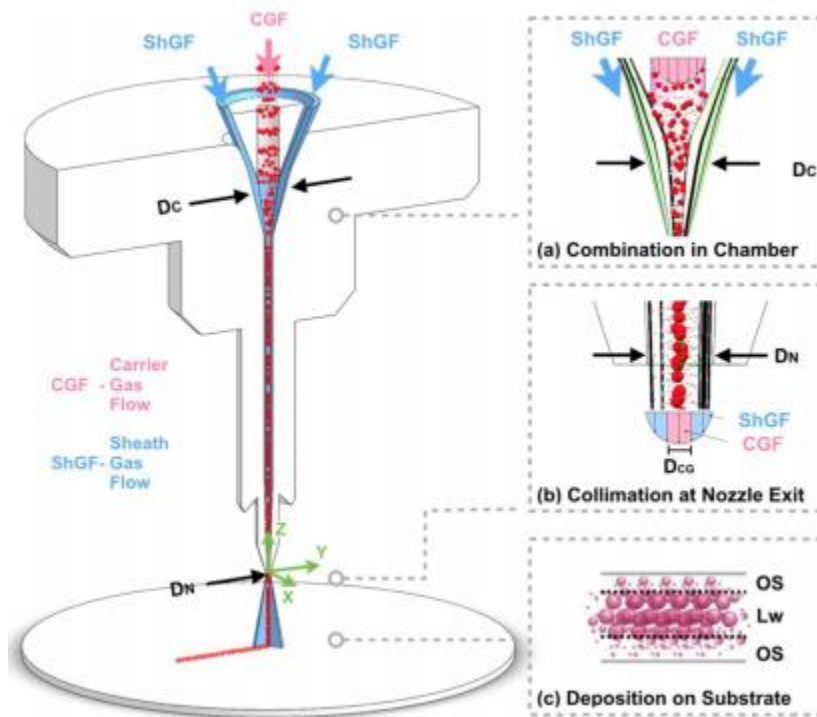


Figure 3.1: Schematic of the carrier and sheath gas flow geometry as well as a-c) different locations of interest in the AJP process (Chen et al., 2018).

A prior study revealed that the reliability of two AJP fabricated conducting traces, printed with a selected commercial Ink A, was vastly different, despite using identical values for the majority of the print parameters such as deposition rate, print speed, and stage temperature. An interconnect over fillet specimen (IoF171101) printed with Ink A lasted just 250 accelerated thermal cycles from -40 to 125 °C before exhibiting microcracking as well as severe delamination of the traces. On the other hand, simpler baseline test coupons (DTC180201), also printed with Ink A, lasted over 3,500 accelerated thermal cycles from -40 to 125 °C without exhibiting any significant damage to the printed lines. The suspected differences between the two print batches included the ink condition and flow rates of the carrier gas and sheath gas in the AJP process.

IoF171101 was printed at carrier and sheath gas flow rates of 80 standard cubic centimeters per minute (sccm) and 50 sccm, respectively, while DTC180201 was printed at corresponding flow rates of 50 sccm and 30 sccm, respectively. The reason for this difference in the flow rates is that the solvent content is suspected to be different in the two print batches, thus requiring different flow rates to achieve the same deposition rate ($0.00075 \text{ mm}^3/\text{s}$). The ink's solvent content and the flow rates used to print could both have potentially contributed to the differences in the quality and reliability of the IoF171101 and DTC180201 prints. This study focuses on the influence of the flow rates on the print features, while the influence of ink condition is deferred to a future study.

Chen et al. (2018) developed a three-dimensional computational fluid dynamics model of the aerosol carrier gas flow that is confined by an annular sheath gas flow to pinpoint the fundamental fluid mechanics principles that control the overspray as a function of droplet size distribution and sheath gas flow rate. Put simply, overspray is the ink particles that are deposited outside of the intended trace width. Their results explain that there is an abundance of smaller sized drops in the overspray region at low sheath gas flow rates, the overspray first reduces and then increases as the sheath gas flow rate increases, and there is no longer a prevalence of smaller particles in the overspray region at larger sheath gas flow rates. There is a point of diminishing return for sheath gas flow rate because at high enough levels, the particle droplets start to cross the nozzle axis and then travel back toward the axis resulting in over collimation and increased overspray.

Roberson et al. (2011) characterized the morphology of inkjet printed traces made from a microparticle and nanoparticle silver ink. Scanning electron microscope (SEM) images for traces printed with the two different particle size silver ink as well as varying

sintering profiles are provided. The nanoparticle ink can attain a more conductive microstructure since the nanoparticles can sinter at lower temperatures, but lines printed with the microparticle ink had similar resistivity. Microstructures with larger grains and less porosity are more conductive.

Mahajan et al. (2013) found that a trace's line width decreases with increasing focusing ratio, defined as sheath gas flow rate divided by carrier gas flow rate, as well as stage speed. The thickness or height of the traces also increases with an increasing focusing ratio, but decreases with increasing stage speed. The decrease in line width with increasing focusing ratio is more dramatic in smaller nozzles. The complete general trends investigated by Mahajan are presented in Table 3.1 below.

Process Variable	Line Width	Line Thickness
Focusing Ratio	Decreases	Increases
Nozzle Diameter	Increases	Decreases
Carrier Gas Flow Rate	Remains the Same	Increases
Stage Speed	Decreases	Decreases

Table 3.1: Effect of independently increasing each process variables on printed line geometry.

Salary et al. (2017) developed a computational fluid dynamics model that verified the overall line morphology trends observed through an in-situ online monitoring camera when varying flow rate parameters. For a fixed carrier gas flow rate and print speed of 30 sccm and 1 mm/s, respectively, they recommended a process window between 40 and 100 sccm for the sheath gas flow rate to optimize the printed line density, edge quality, overspray, and line discontinuity.

There has been some work done to begin understanding the effects of different AJP printing parameters on the final quality of a printed trace, but there is still plenty more to be done. Operating process windows that others have suggested are specific to the AJP printer used for the study, the type of ink being utilized, and less quantifiable

features such as the printer maintenance. Moreover, the definition of print quality as a function of print parameters has been mostly qualitative aside from quantifying a line's overall macroscale geometry such as width and thickness and average bulk electrical properties such as conductivity. Few studies have investigated the micromorphology of the printed trace, such as its average agglomeration length scales in the bulk as well as on the surface. The quality of the printed serpentine test structures is characterized in this study by a set of selected macroscale and micromorphological features described later.

Section 3.2: Approach

The study uses a design of experiment, where the two flow parameters (carrier gas flow rate and sheath gas flow rate) are parametrically varied and their influence on selected response variables (print features) are quantified.

Section 3.2.1: Test Coupon

Test structures were designed to have silver nanoparticle Ink A conductor traces of a serpentine design with five segments, for repeatability, printed on a Polymer N adhesion and dielectric layer that is spincoated on a FR4 substrate. The trace segments are 20 mm in length and are printed with one mm pitch (Figure 3.2). The FR4 substrate was designed to be 24 mm wide and 24 mm long to accommodate the 20 mm long serpentine design. A square substrate was utilized as it is easier to spincoat the Polymer N layer onto such a geometry. The additional space along the width of the substrate was used to print three serpentine structures on each substrate board. Typically, two print passes are always conducted to produce a thick enough trace for functionality purposes,

but it was presumed that differences in print features would be more obvious in a single pass trace because the second pass may be filling in potential defects and smooth over potential differences left from the first pass. To understand the effects of a second pass, a double pass segment was printed on the top three of the five segments (C-E) of each serpentine, highlighted in black, while a single pass segment was printed on the bottom two segments (A-B) of each serpentine, highlighted in white. Each substrate board is labeled with a board number on the rear and the bottom of each board is shaded with a Sharpie such that a structure number can be assigned, with the bottom serpentine being labeled as serpentine one and the top serpentine being labeled as serpentine three.

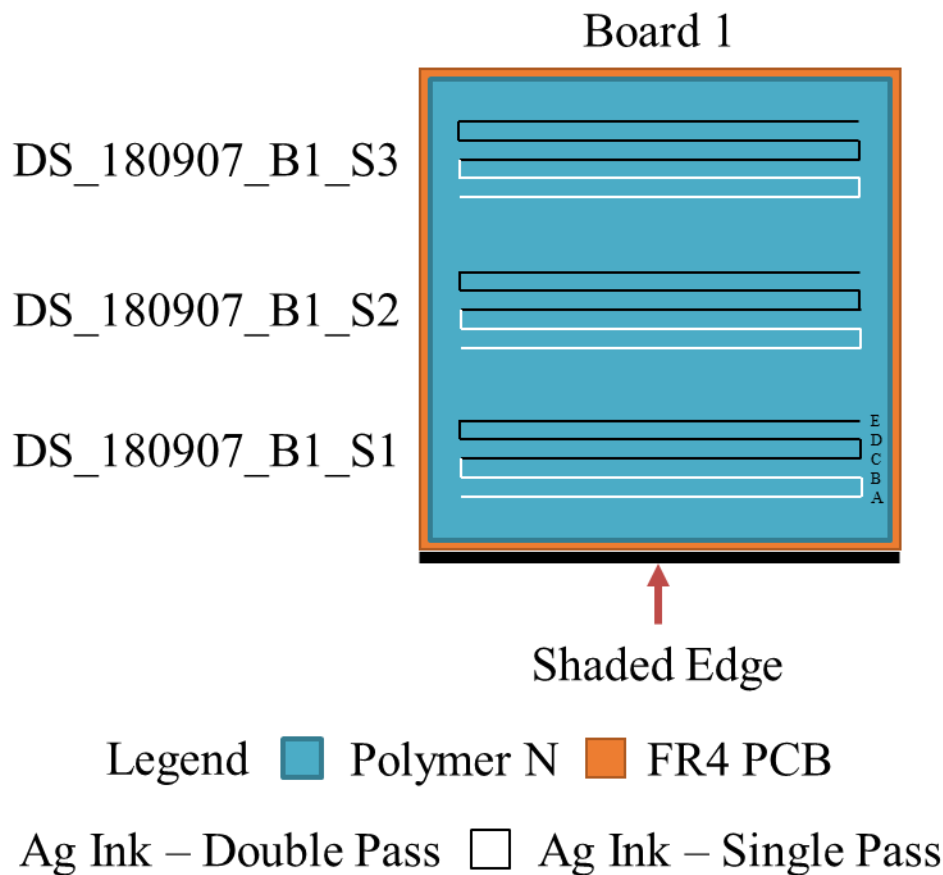


Figure 3.2: Test structure and coupon design for varying flow rate design of experiments.

Section 3.2.2: Test Plan

Ink A at a solids fraction of 73.4 mass percent silver nanoparticles in a commercial solvent was used to print the aforementioned serpentine test structures. 15 test structures were printed across five test coupon boards, where each board was printed at a specified carrier gas flow rate. The carrier gas flow rate was parametrically varied, with values of 30, 50, 65, 80, or 100 sccm. On each test coupon, the three serpentine were printed at different sheath gas flow rates of 30, 40, or 50 sccm (Table 3.2). These upper and lower limits for both types of flow rates were guided by recommendations from the manufacturer of the aerosol jet printer used and by prior experience of the team members. Other important print parameters include print speed (1 mm/s) and stage temperature (50 °C).

Board #	Structure #	Carrier (sccm)	Sheath (sccm)
1	1	50	30
1	2	50	40
1	3	50	50
2	1	80	30
2	2	80	40
2	3	80	50
3	1	65	30
3	2	65	40
3	3	65	50
4	1	100	30
4	2	100	40
4	3	100	50
5	1	30	30
5	2	30	40
5	3	30	50

Table 3.2: Test matrix for varying flow rate design of experiments.

In an effort to quantify the quality of each of the serpentine printed at these various flow rate combinations, several print features were investigated:

1. The corresponding deposition rate was measured using an inkwell technique (Gu et al., 2017).
2. Laser profilometry was conducted and post-processed to determine multiple macroscale geometric features of the trace (i.e. width, thickness, overspray width).
3. The resistance values of the serpentines were also measured to assess their effective conductivity.
4. Scanning electron microscope (SEM) images were taken of the serpentines' surface to examine other macroscale features such as crystalline deposits and longitudinal cracks.
5. SEM images were taken of the serpentines' surface as well as cross-section to analyze the micromorphology of the traces such as agglomeration characteristics.

Section 3.3: Results

The quality of the serpentine traces with varying flow rate parameters was quantified by measuring the deposition rate, macroscale geometric properties of the trace, effective conductivity, as well as the agglomeration size and spacing distribution on the surface and in the bulk.

Section 3.3.1: Deposition Rate

As expected due to the varying gas flow rates at which material is being transported in the AJP process, the deposition rate of each serpentine was different. The deposition rate was estimated for each flow-rate combination by noting the time required

to fill a calibrated inkwell of known volume (0.0063 mm^3). This method was established and discussed in detail by Gu et al. (2017). The corresponding deposition rate for each gas flow rate combination is presented in Table 3.3 and plotted in Figure 3.3. As expected, the deposition rate increased with increasing carrier gas flow rate when more material is being drawn from the reservoir of ink and slightly decreased with increasing sheath gas flow rate, when the stream is being squeezed tighter.

Carrier (sccm)	Sheath (sccm)	Deposition Rate (mm^3/s)
30	30	0.00019
30	40	0.00016
30	50	0.00013
50	30	0.00126
50	40	0.00097
50	50	0.00090
65	30	0.00210
65	40	0.00158
65	50	0.00126
80	30	0.00315
80	40	0.00210
80	50	0.00180
100	30	0.00350
100	40	0.00315
100	50	0.00252

Table 3.3: Associated deposition rate for each combination of carrier and sheath gas flow rate.

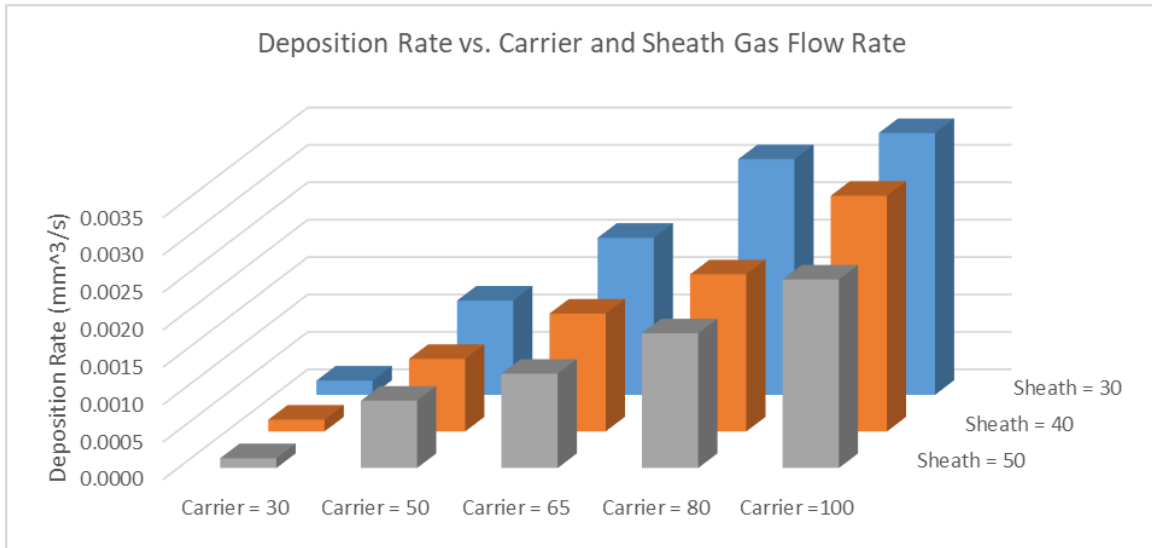
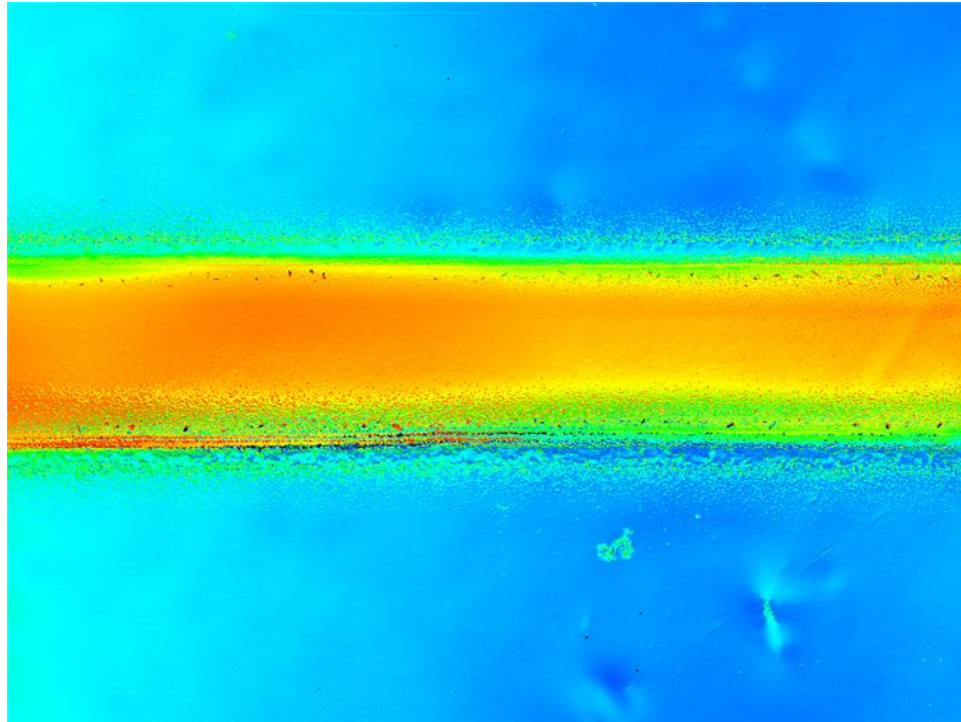


Figure 3.3: Deposition rate as a function of carrier and sheath gas flow rate.

Section 3.3.2: Profilometry

A commercial confocal microscope was used to conduct laser profilometry on the printed serpentine traces with varying flow rates. Using a MATLAB post-processing code developed by Chen et al. (2018), the trace width, cross-sectional area, overspray, percent coverage, and thickness were estimated, based on the height map contour generated by the profilometry software. Examples of the height map contour plots and output from Chen’s post-processing code are presented in Figure 3.4. In the height map contour, the substrate is the blue area representing the lowest elevation, while the yellow and orange area represents the higher elevation and is the printed trace. Threshold criteria are selected for print height, to define the longitudinal boundaries (width) of the trace and overspray. Chen’s MATLAB code is then used to post-process the results and output (i) a three-dimensional image of the trace, (ii) a two-dimensional cross-section that is averaged over the length of the trace imaged, and (iii) an overhead view of the trace with width (red) and overspray (blue) boundaries. Quantitative data such as the trace width,

cross-sectional area, overspray length on each side, percent coverage, and maximum thickness or height are also generated.



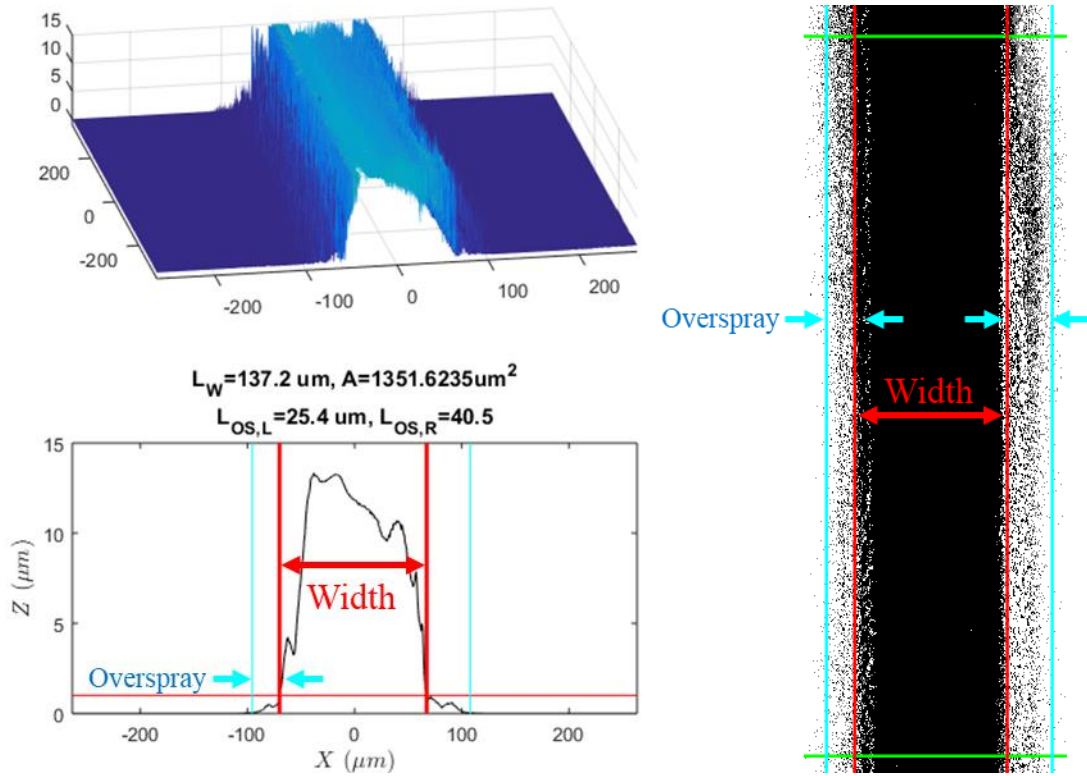
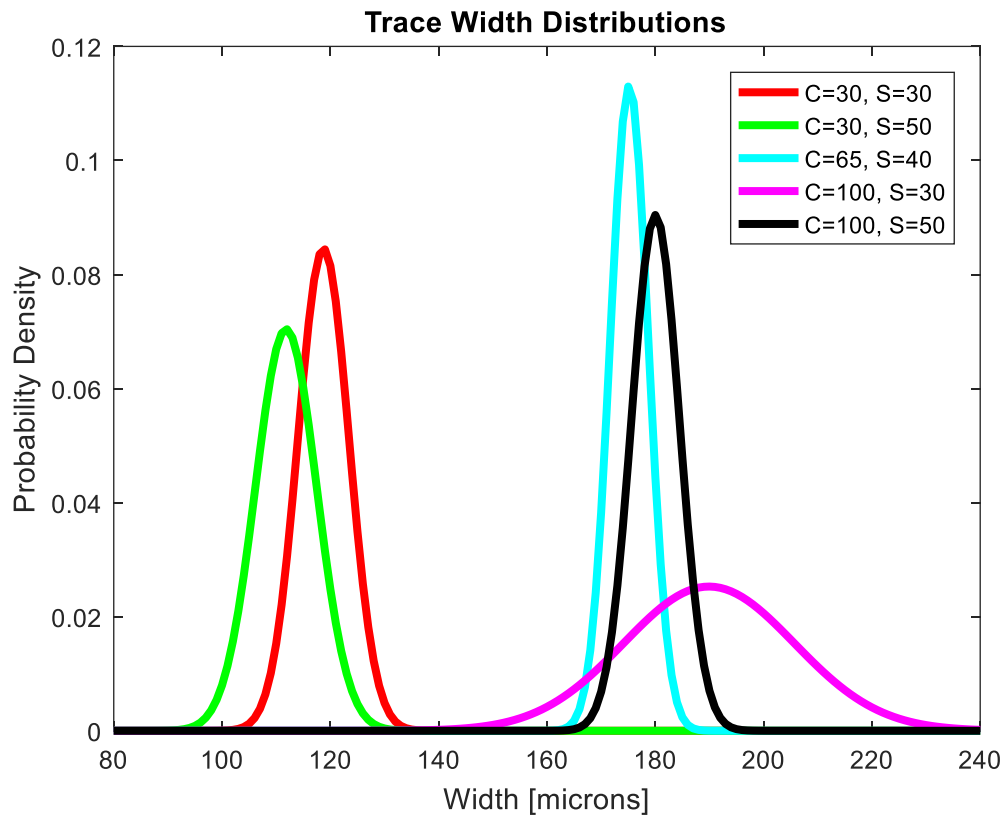


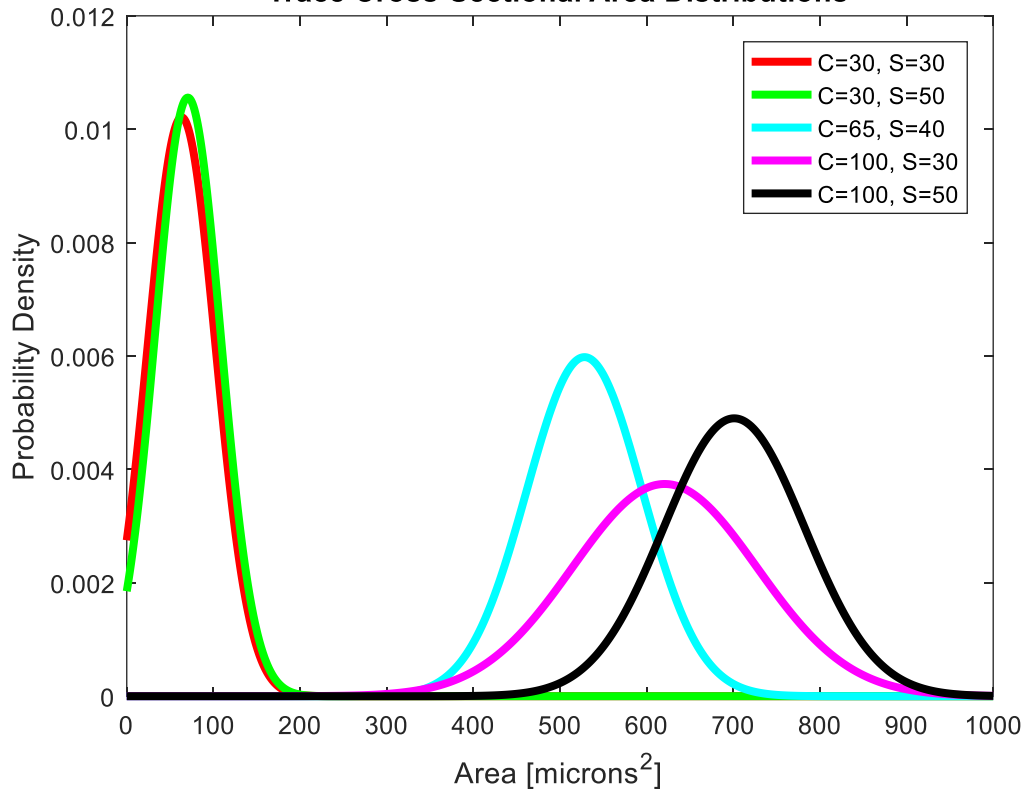
Figure 3.4: Representative example of a) height contour plot from VK Analyzer and b) post-processing plots from MATLAB for Board 4 Serpentine 3 Segment C left edge.

For the four corner cases of the design of experiment (carrier gas flow rate of 30 and 100 sccm and sheath gas flow rate of 30 and 50 sccm) as well as for the middle case (carrier gas flow rate of 65 sccm and sheath gas flow rate of 40 sccm), multiple laser profilometry scans were completed along the single-pass portion of the serpentine. A total of 14 scans were conducted evenly spaced across the 40 mm of single-pass traces, to estimate the statistics of the variability of these parameters (Figure 3.5). The mean and standard deviation values are summarized in Table 3.4. Trace width, cross-sectional area, and maximum thickness increased, as expected, with increase in the carrier gas flow rate, whereas the effect of sheath gas flow rate was much smaller. The printed line's coverage increased marginally with an increase in either carrier or sheath gas flow rates. Overspray was mostly similar across these five flow rate combinations. However, it was slightly

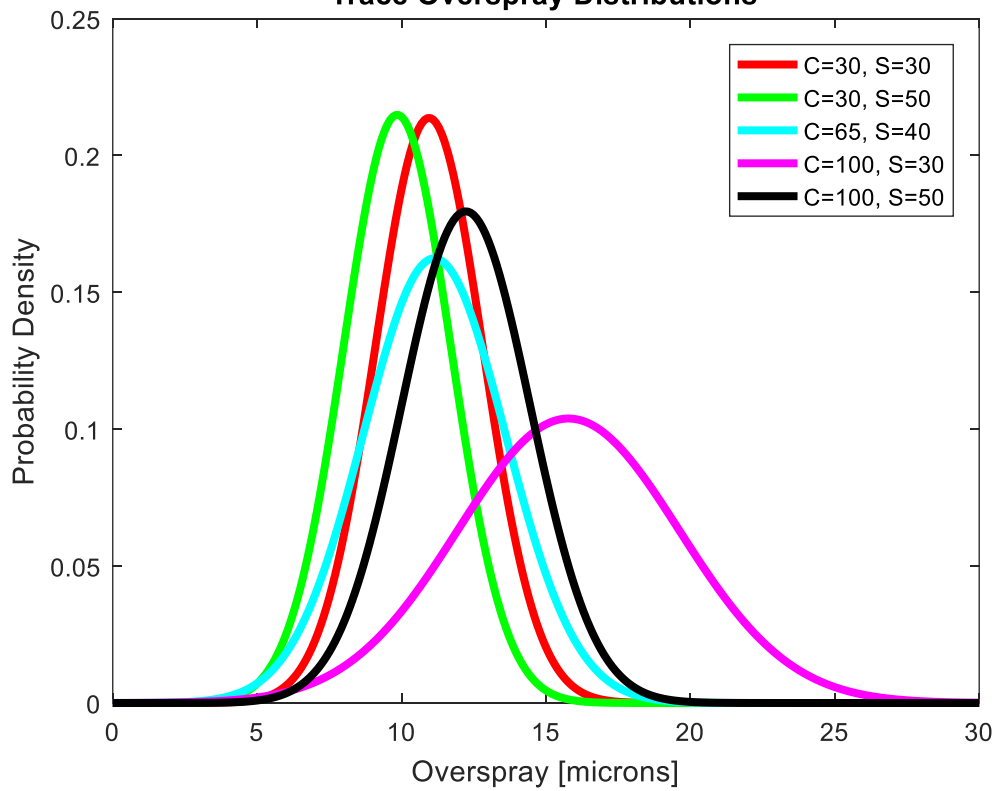
elevated in the trace with carrier gas flow rate of 100 sccm and sheath gas flow rate of 30 sccm, because there was not enough sheath gas to focus the high amount of carried material leading to the overspray. This is the same reason why there was a larger spread in the distribution in trace width for the trace with carrier gas flow rate of 100 sccm and sheath gas flow rate of 30 sccm, because the ink was not consistently collimated to the center.

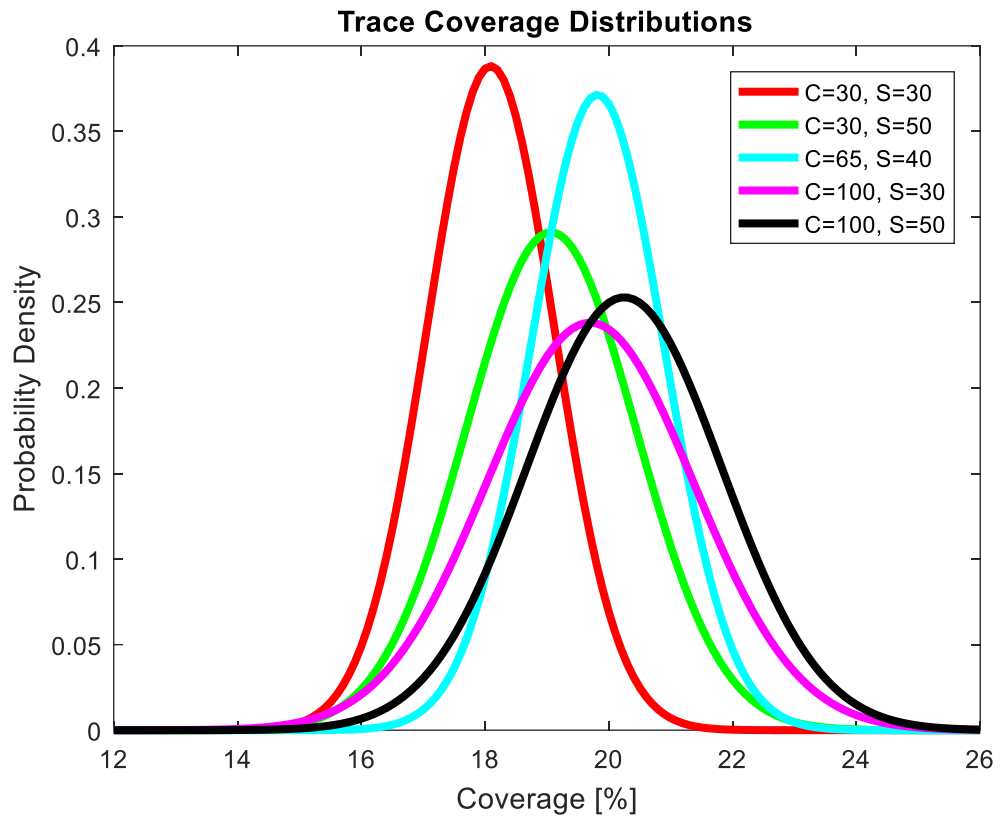


Trace Cross-Sectional Area Distributions



Trace Overspray Distributions





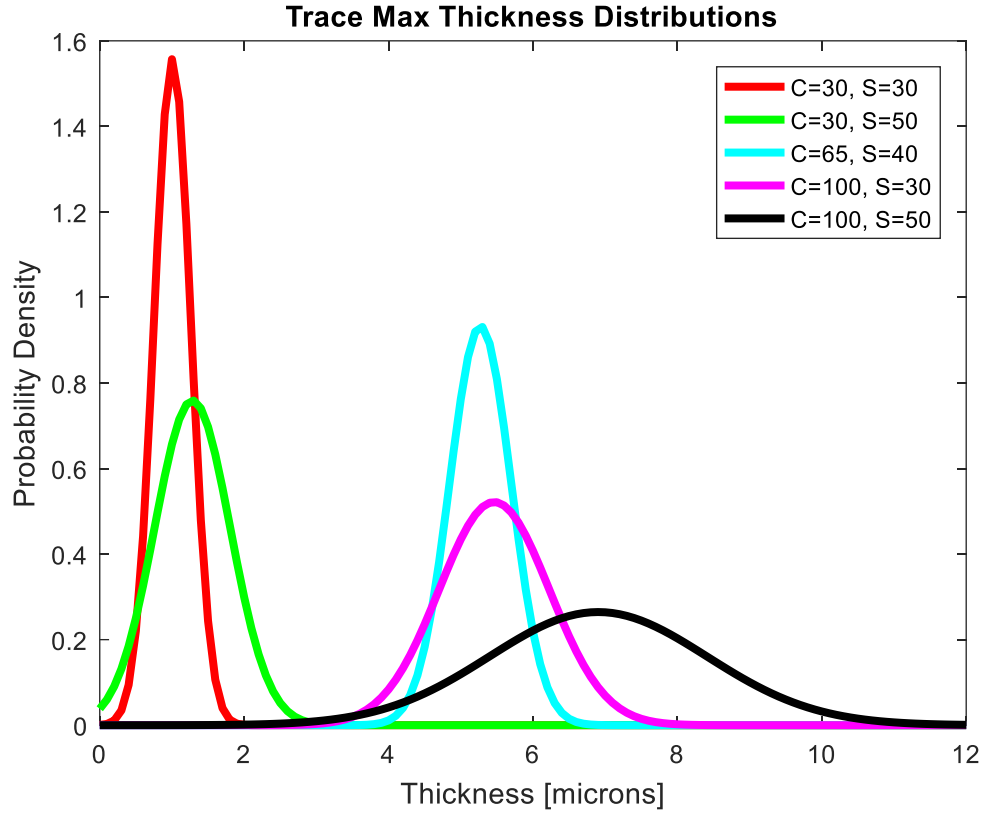


Figure 3.5: Distribution plots for trace a) width, b) cross-sectional area, c) overspray, d) coverage, and e) max thickness.

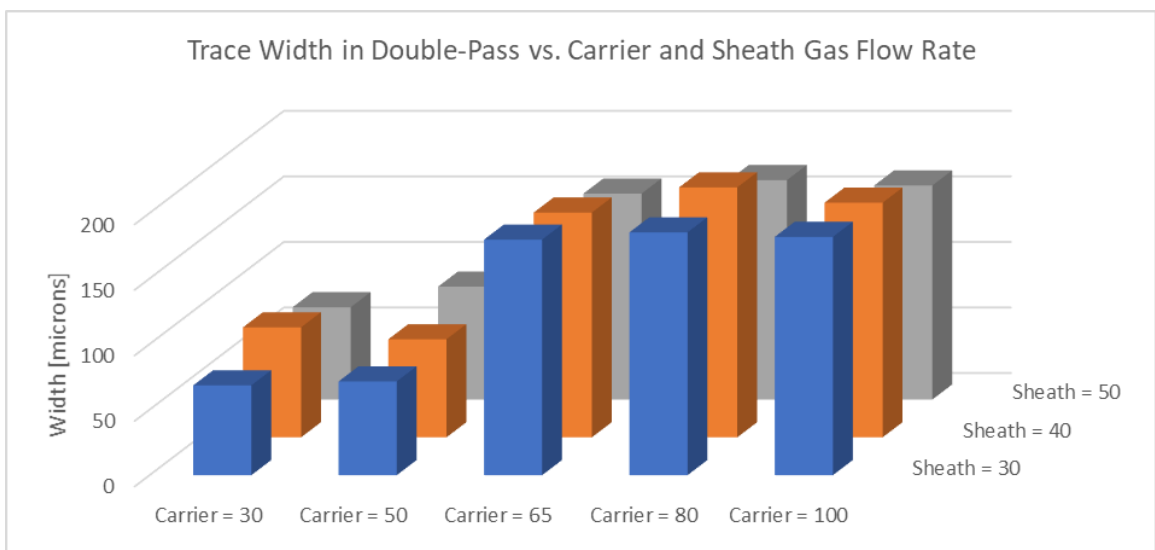
Flow Rates	Width (μm)	Area (μm^2)	Overspray (μm)	Coverage (%)	Thickness
C = 30, S = 30	119 \pm 4.7	63.3 \pm 39.1	11.0 \pm 1.9	18.1 \pm 1.0	1.0 \pm 0.3
C = 30, S = 50	112 \pm 5.7	70.5 \pm 37.8	9.8 \pm 1.9	19.1 \pm 1.4	1.3 \pm 0.5
C = 65, S = 40	175 \pm 3.5	528 \pm 66.7	11.1 \pm 2.5	19.8 \pm 1.1	5.3 \pm 0.4
C = 100, S = 30	190 \pm 15.8	621 \pm 107	15.8 \pm 3.8	19.7 \pm 1.7	5.5 \pm 0.8
C = 100, S = 50	180 \pm 4.4	701 \pm 81.4	12.2 \pm 2.2	20.2 \pm 1.6	6.9 \pm 1.5

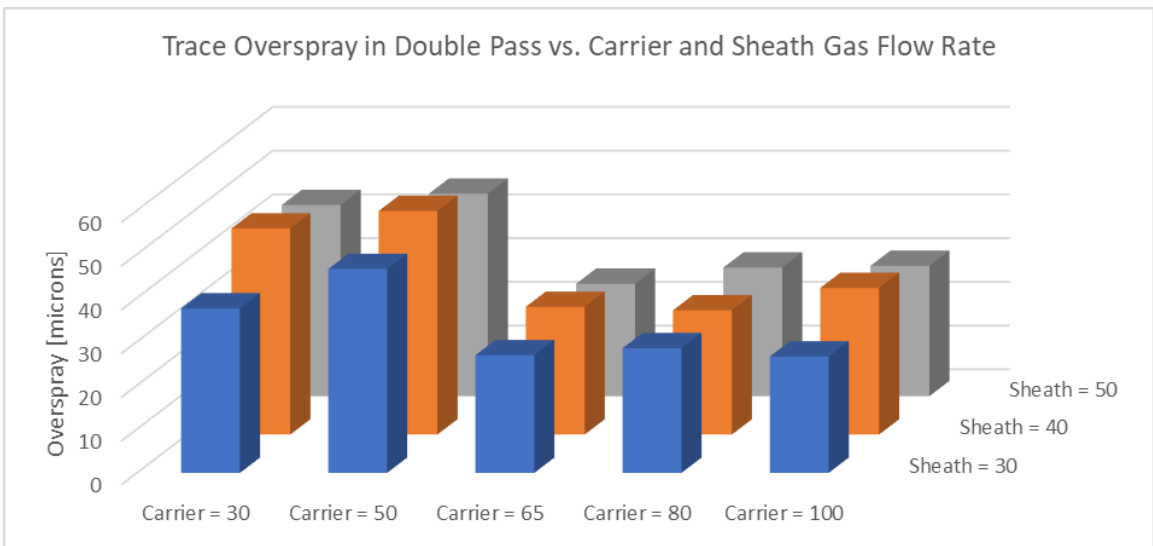
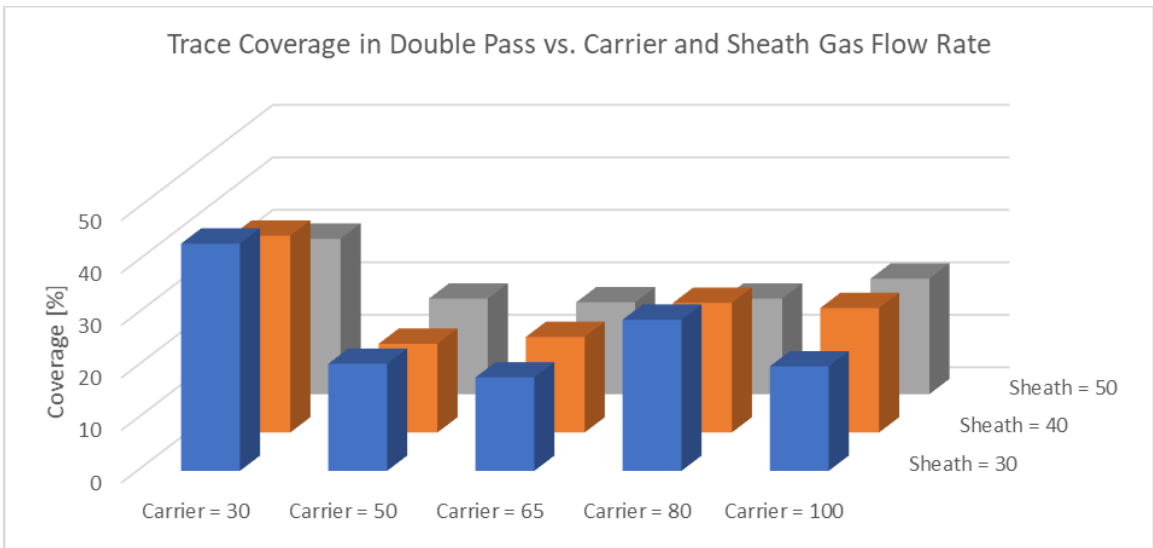
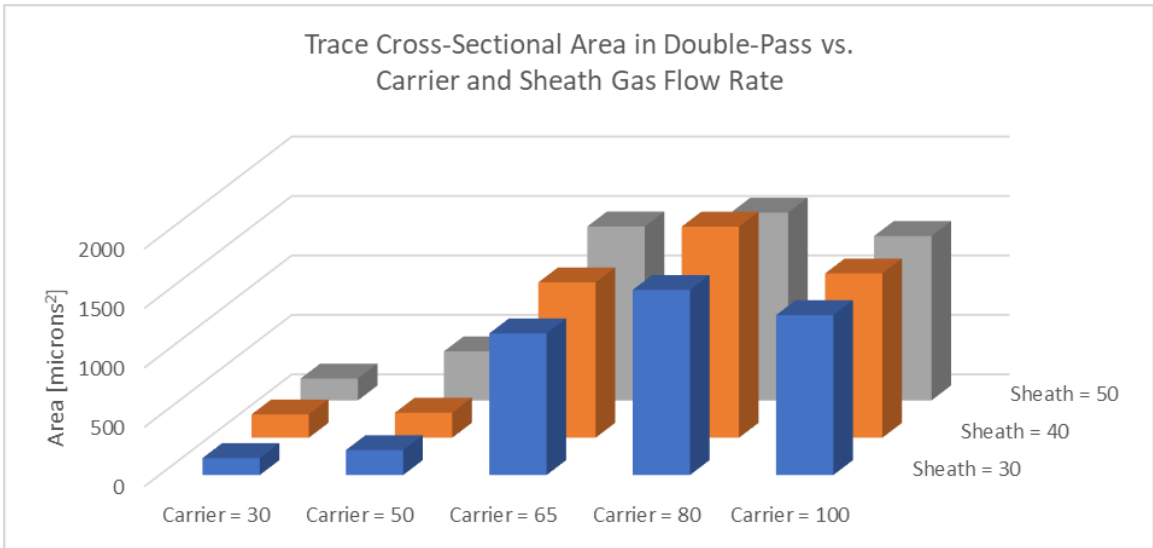
Table 3.4: Mean and standard deviation for four corner and middle flow rate single-pass traces' width, cross-sectional area, overspray, coverage, and max thickness.

In addition to the built-up statistics for five of the serpentine, two laser profilometry scans were conducted on each of the 15 serpentine traces, one over a single-pass trace and one over a double-pass trace. Those results are summarized in Table 3.5 and plotted as a 3D bar chart for the double-pass traces in Figure 3.6.

Carrier	Sheath	Pass	Width (μm)	Area (μm^2)	Overspray (μm)	Coverage	Thickness (μm)
30	30	1	42.9	67.3	37.4	53.8	1.6
30	30	2	68.5	142.4	43.3	37.6	2.9
30	40	1	47.0	77.3	34.8	64.1	1.8
30	40	2	83.9	195.7	37.5	47.1	3.5
30	50	1	41.8	65.6	28.1	54.9	1.7
30	50	2	70.4	183.6	29.6	43.7	4.0
50	30	1	51.4	99.2	23.1	56.9	2.2
50	30	2	71.5	209.6	20.4	46.6	4.2
50	40	1	38.2	54.6	25.9	54.8	1.4
50	40	2	74.8	210.2	16.9	51.1	4.0
50	50	1	60.8	132.4	20.4	53.5	2.8
50	50	2	86.1	412.6	18.2	46.3	7.1
65	30	1	131.0	455.1	27.8	26.4	4.6
65	30	2	179.7	1191.2	17.8	26.9	11.7
65	40	1	147.5	513.1	24.4	31.8	5.2
65	40	2	171.5	1306.6	18.2	29.2	13.2
65	50	1	137.9	566.9	22.6	29.1	5.5
65	50	2	157.1	1462.9	17.5	25.7	14.4
80	30	1	135.1	272.8	8.2	27.4	2.8
80	30	2	185.2	1557.0	28.8	28.5	13.5
80	40	1	168.1	661.9	22.6	31.0	6.0
80	40	2	190.7	1775.5	24.7	28.4	16.4
80	50	1	155.0	701.6	20.2	30.0	6.4
80	50	2	167.4	1579.4	18.2	29.4	16.5
100	30	1	150.2	600.3	31.9	21.5	5.4
100	30	2	181.8	1345.1	19.9	26.6	12.3
100	40	1	161.2	637.4	22.0	21.1	6.0
100	40	2	179.0	1382.0	23.7	33.5	12.2
100	50	1	153.7	645.9	24.0	31.1	6.2
100	50	2	163.3	1383.0	22.0	29.8	13.5

Table 3.5: Parameters calculated for all 30 different traces.





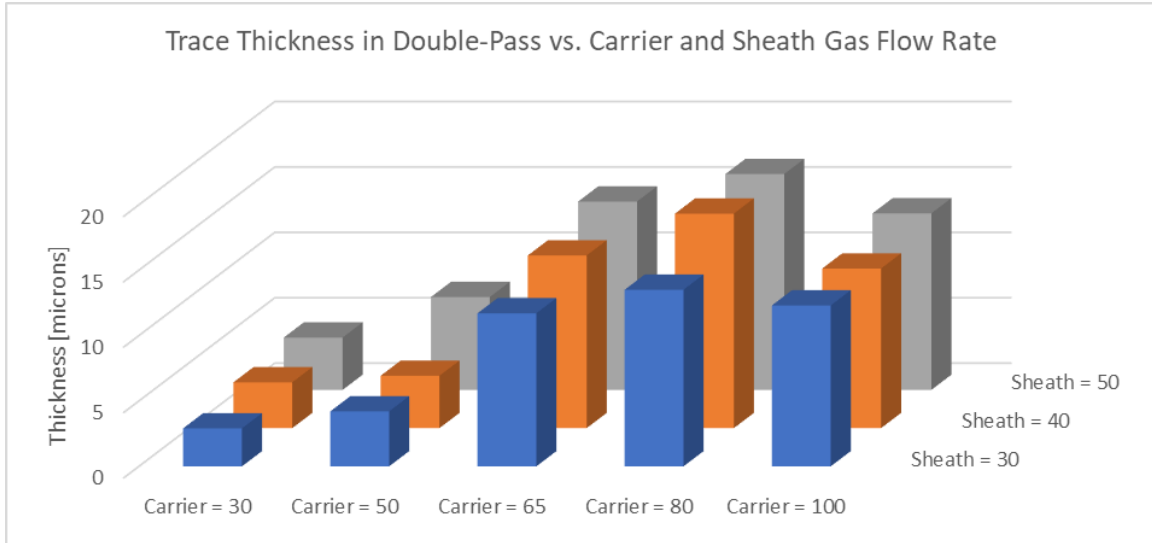


Figure 3.6: Trace a) width, b) cross-sectional area, c) coverage, d) overspray, and e) thickness for the double-pass prints as a function of gas flow rates.

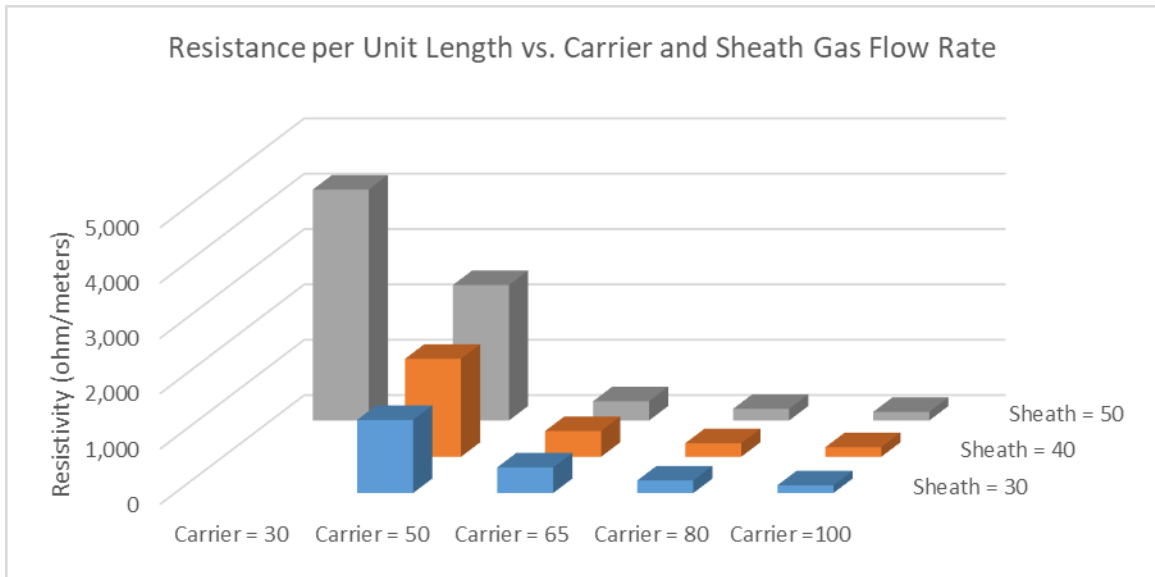
Section 3.3.3: Effective Conductivity

Using a commercial precision LCR meter and commercial precision positioner to make exact contact, the two-wire resistance of the serpentine traces were measured and normalized per unit length (Table 3.6). Four-wire resistance measurements should have been made to ensure the removal of the resistance added from the probing setup. These values are plotted in Figure 3.7 with a full and abridged y-axis, the latter to best show the continued decreasing nature of resistance with increased carrier gas at the higher flow rates, which is to be expected given those traces have higher cross-sectional area and $R/L = \rho/A$. The 104 mm serpentine trace resistance went down as the carrier gas flow rate increased and was nearly independent of sheath gas flow rate. The intermediate sheath gas value of 40 sccm led to slightly higher resistances than the 30 or 50 sccm levels. At a carrier gas flow rate of 30 or 50 sccm, the resistance values were large as the printed serpentine density was likely below the percolation threshold because of the low

deposition rate. A resistance value could be measured across the top most segment of the serpentine, segment E, for a carrier gas flow rate of 50 sccm, but not for 30 sccm.

Carrier	Sheath	Resistance per Length
30 sccm	30 sccm	OVL
30 sccm	40 sccm	OVL
30 sccm	50 sccm	4173 ohm/meters
50 sccm	30 sccm	1320 ohm/meters
50 sccm	40 sccm	1770 ohm/meters
50 sccm	50 sccm	2447 ohm/meters
65 sccm	30 sccm	464 ohm/meters
65 sccm	40 sccm	466 ohm/meters
65 sccm	50 sccm	347 ohm/meters
80 sccm	30 sccm	227 ohm/meters
80 sccm	40 sccm	244 ohm/meters
80 sccm	50 sccm	211 ohm/meters
100 sccm	30 sccm	140 ohm/meters
100 sccm	40 sccm	173 ohm/meters
100 sccm	50 sccm	156 ohm/meters

Table 3.6: Resistance per unit length measurements for serpentine traces.



Resistance per Unit Length vs. Carrier and Sheath Gas Flow Rate

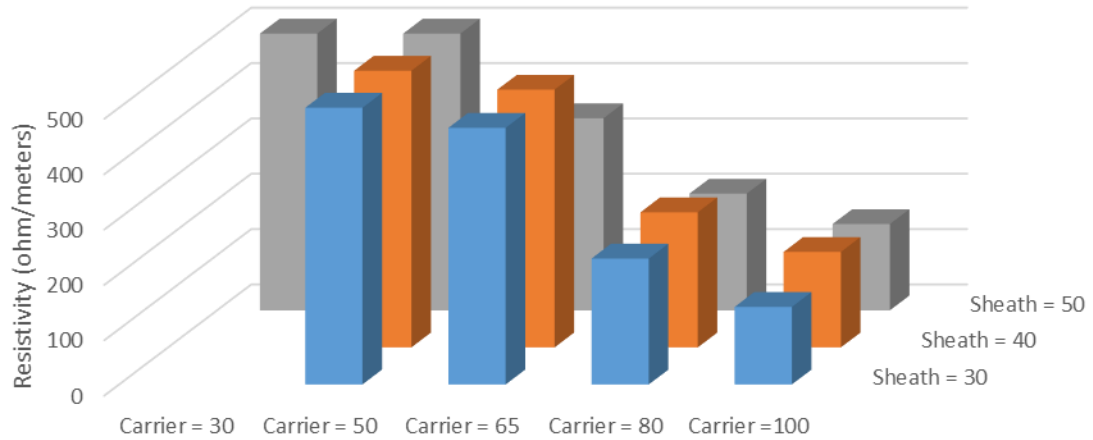


Figure 3.7: Trace resistance per unit length as a function of gas flow rate plotted on a a) full y-axis and b) abridged y-axis.

The printed traces are micro and nanoporous silver structures so at best it is possible to estimate a volume averaged, homogenized and effective resistivity and conductivity as is the case with other composite materials. As a result, these measurements will be higher than the typical resistivity of bulk silver of 1.59×10^{-8} ohm-meters (Serway, 1994). AJP electronics with Ink A have been reported to have resistivity 5.5 times larger than bulk silver, which has a typical value of 1.59×10^{-8} ohm-meters (Gu et al., 2017). The resistance values for the varying flow rate serpentine were normalized by geometry to determine the effective conductivity of each serpentine which is plotted in Figure 3.8 once normalizing to the largest value among flow rates. These values were calculated by taking the measured DC resistance of the structure dividing it by the length of the trace and multiplying it by the cross-sectional area of the trace to get the effective resistivity, $\rho = R \cdot A / L$, and then taking the inverse, $\sigma = 1/\rho$. The cross-sectional area was taken from the profilometry post-processing results. Interestingly, effective conductivity

increases with increasing carrier gas despite the increasing agglomeration sizes that will be discussed in Section 3.3.5.

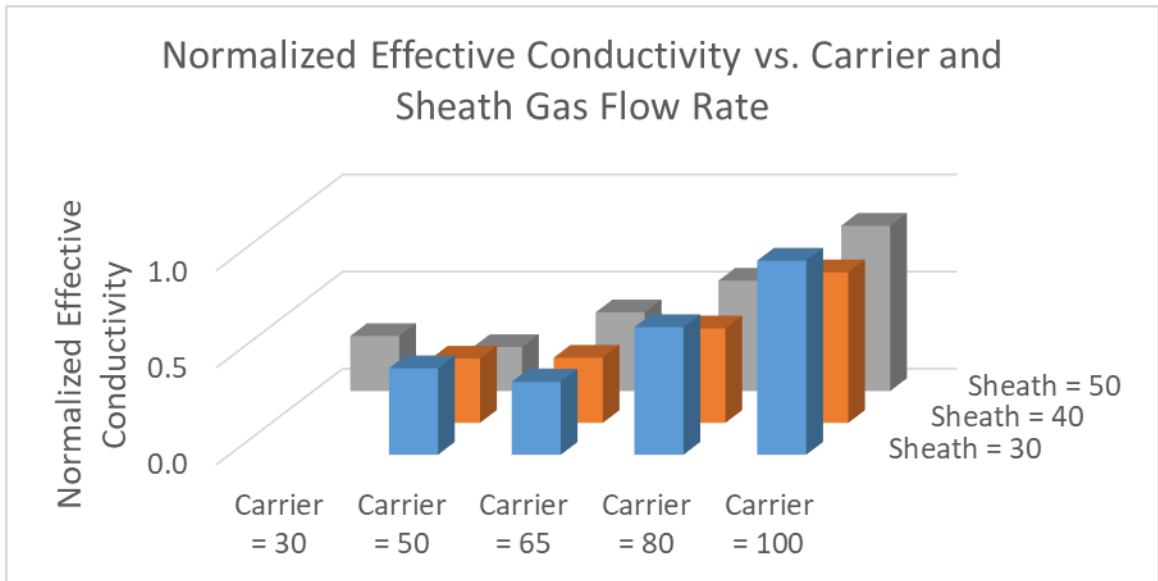


Figure 3.8: Normalized effective conductivity as a function of carrier and sheath gas flow rate.

Section 3.3.4: Surface Imaging and Crystalline Deposits

SEM was utilized to document the surface of the serpentine traces with varying flow rate parameters. All 15 serpentine traces were imaged at 500x magnification, both for single pass and for double pass (Figure 3.9). There was not a noticeable difference among features on the surface between single and double pass traces (Figure 3.10).

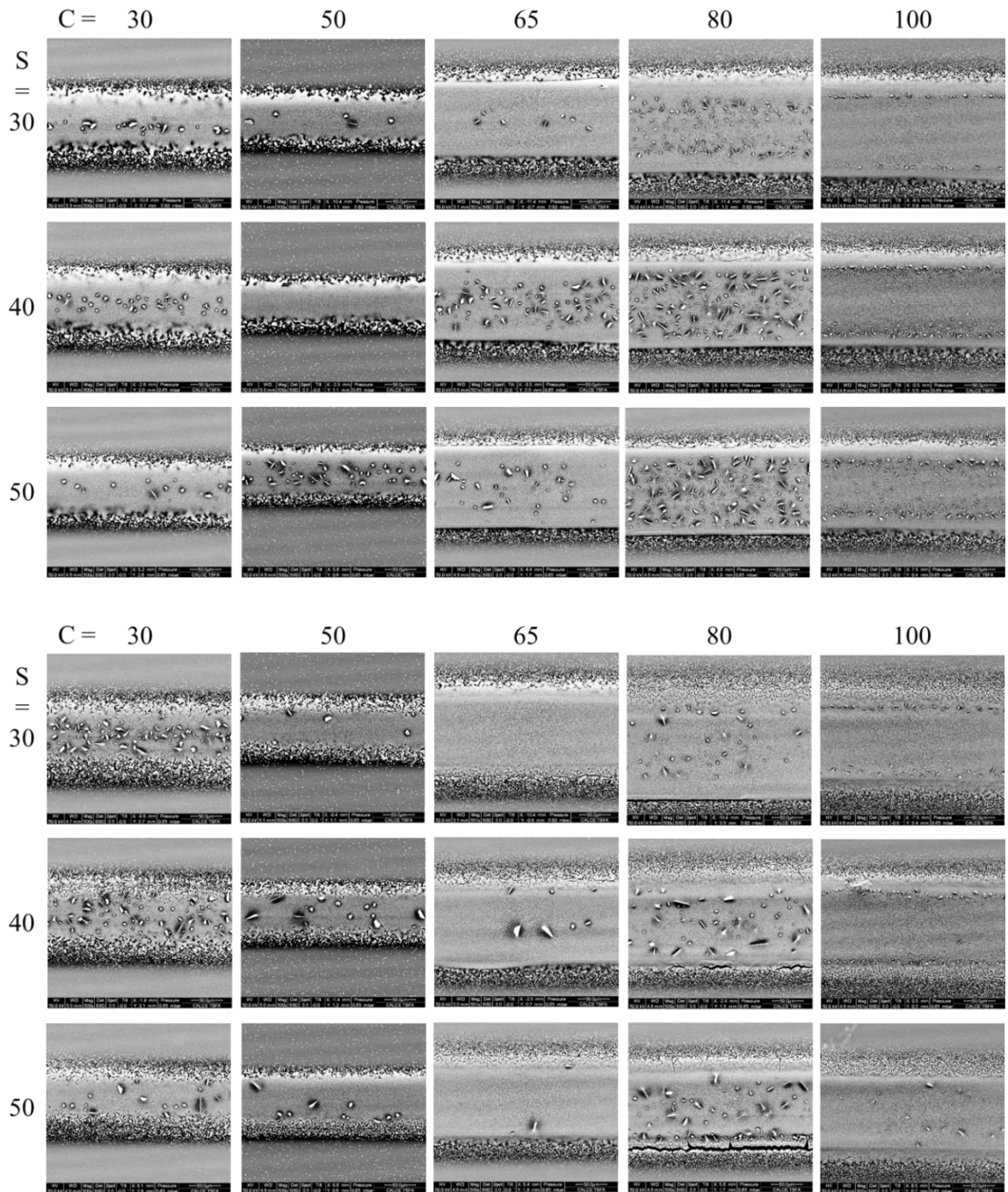


Figure 3.9: Surface images for a) single and b) double pass traces at 500x magnification.

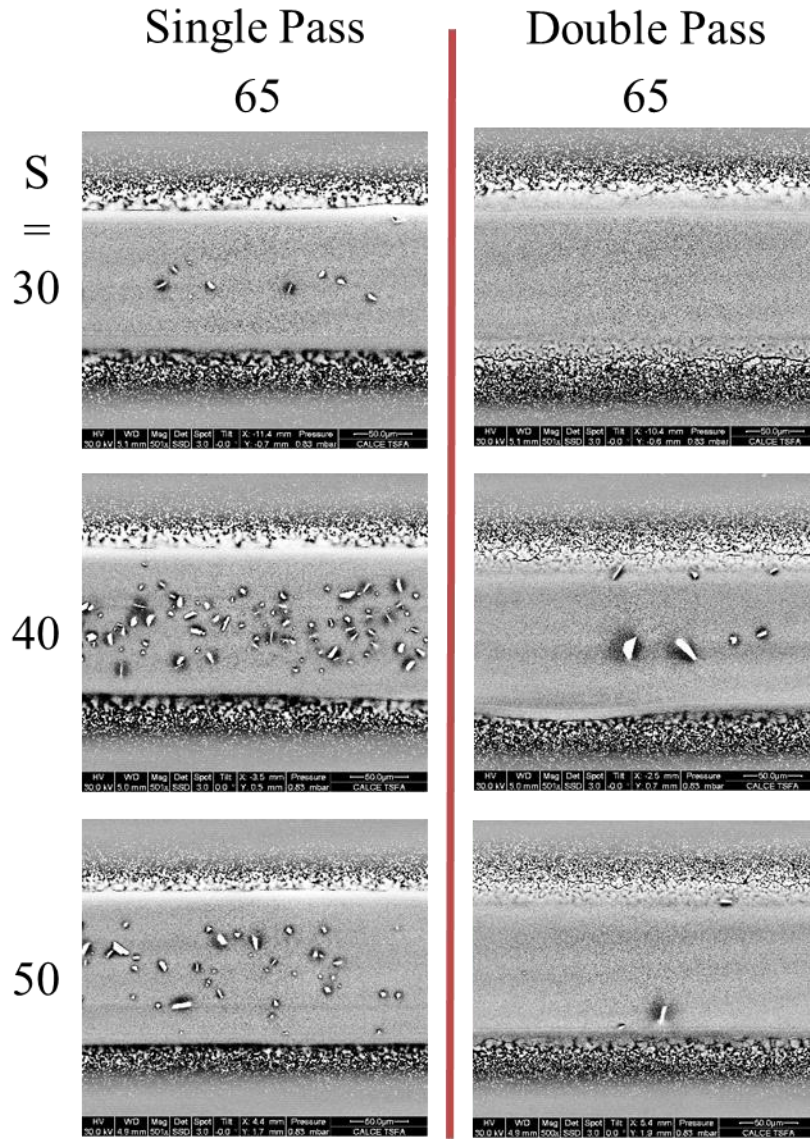


Figure 3.10: Comparison of trace surface between single and double pass traces.

From these low magnification surface images, the presence of crystalline deposits were observed on top of these traces and visible on 90 percent of the 75 trace segments printed. Of the traces that did have the deposits, they were 1) aggregated mostly along the edge, 2) along the centerline, or 3) randomly dispersed throughout the width of the trace. The third case was the most predominant, but a total of four cases (including the case of a trace without any deposits) are presented in Figure 3.11. Energy dispersive X-ray

spectroscopy reveals that these crystalline deposits are likely of silver composition as the elemental spectroscopy curves on the deposits are nearly identical to those on the silver particles in the traces (Figure 3.12). Similar crystalline deposits in printed metal features have been reported elsewhere in the literature (Cook, 2013). Three areas on the trace were sampled as well as three areas on the deposits for completeness. The quantitative composition of both areas sampled were over 97 percent silver in each case.

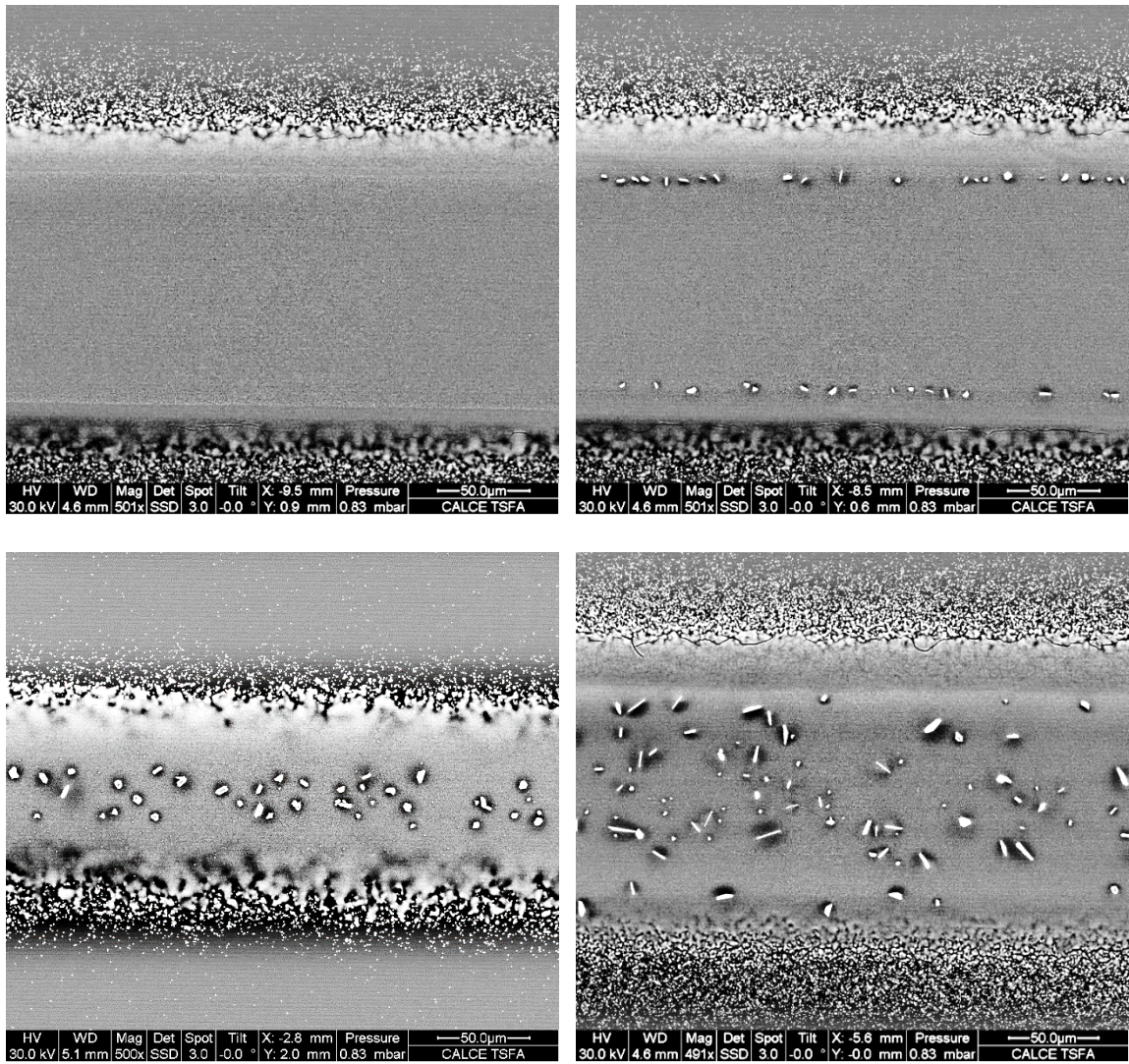


Figure 3.11: Example of traces with a) no crystalline deposits, b) deposits at the edges, c) deposits along the centerline, and d) deposits randomly dispersed.

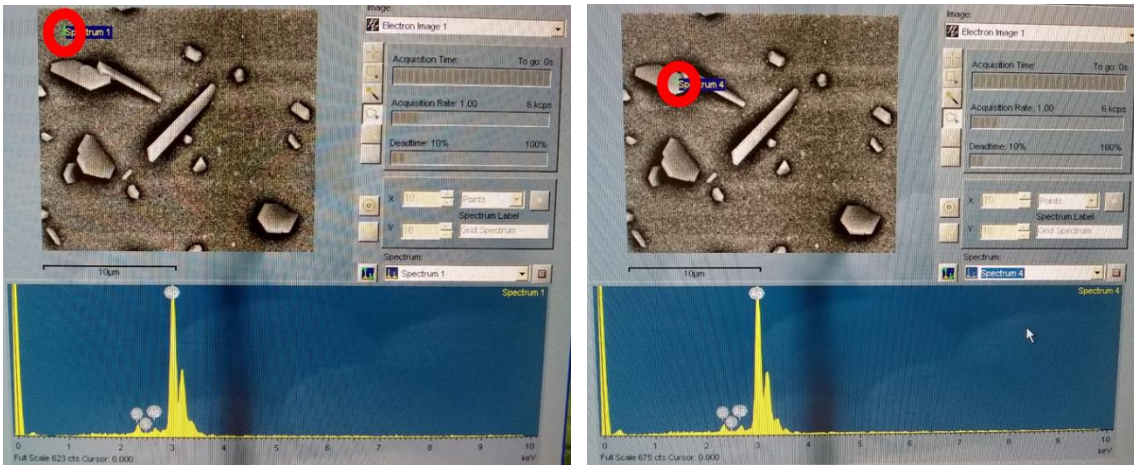


Figure 3.12: Energy dispersive X-ray spectroscopy plots when sampling the printed trace and the crystalline deposits.

Optical microscopy was also conducted to observe the surface features of the different serpentine traces. Not much new information was obtained from this avenue of imaging, compared to SEM, so just a few representative images are provided (Figure 3.13). The double pass trace on the right is wider and taller, thus creating a larger optical shadow along the edges.

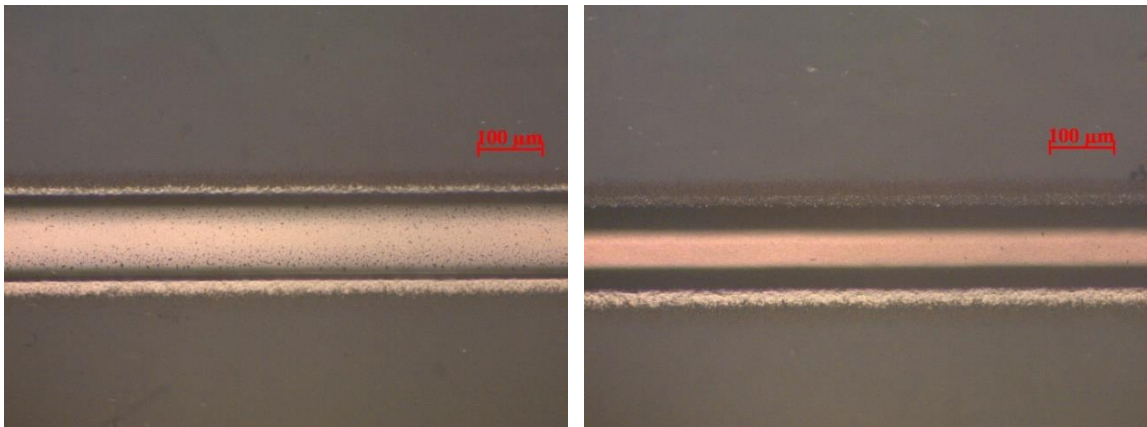
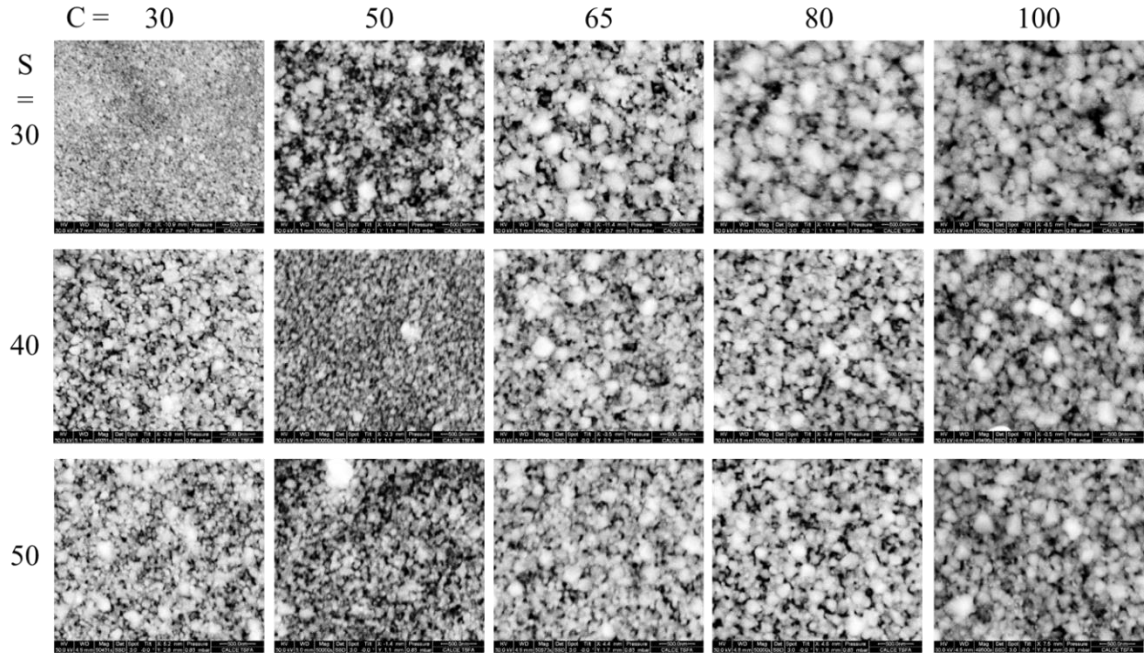


Figure 3.13: Representative optical image with overhead view of Board 4 Serpentine 3 single (Segment B) and double pass (Segment C) trace.

Section 3.3.5: Micromorphology

The surfaces of the 15 serpentine traces were also imaged at 50,000x magnification for both the single and double pass traces to investigate the micromorphological features (Figure 3.14). Qualitatively, coarser agglomerate sizes are observed at the higher flow rates, which follows the trend seen from the IoF171101 ($C = 80$, $S = 50$) and DTC180201 ($C = 50$, $S = 30$) specimens. The cross-sections of the 15 serpentine traces imaged at that same length scale do not show this trend (Figure 3.15).

a) Single-Pass Traces



b) Double-Pass Traces

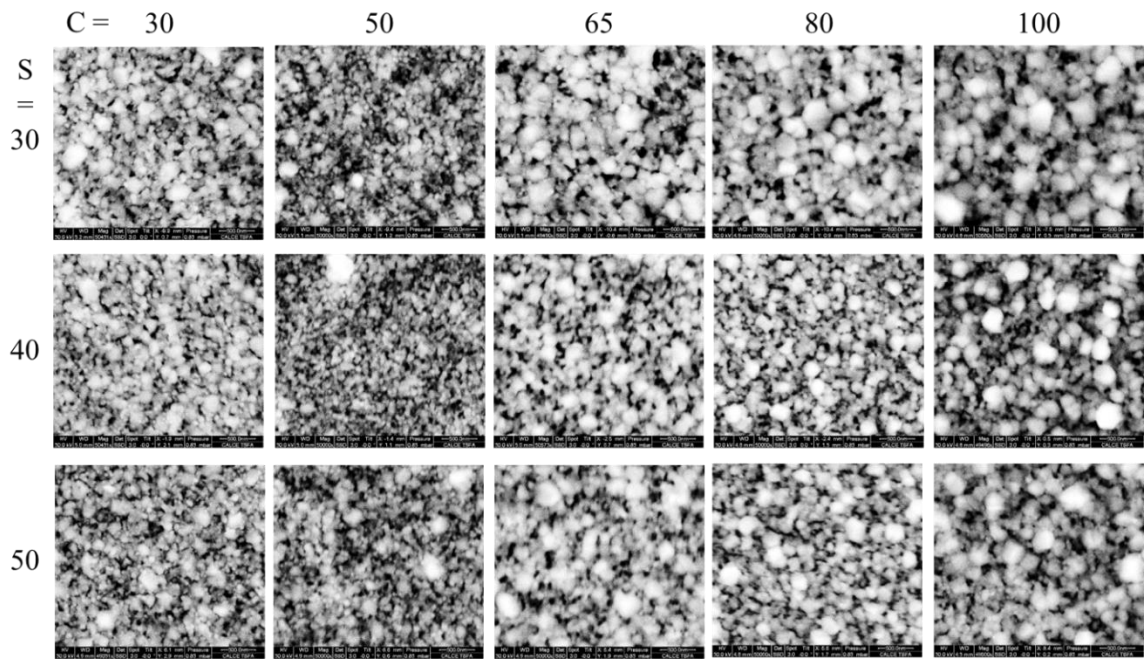
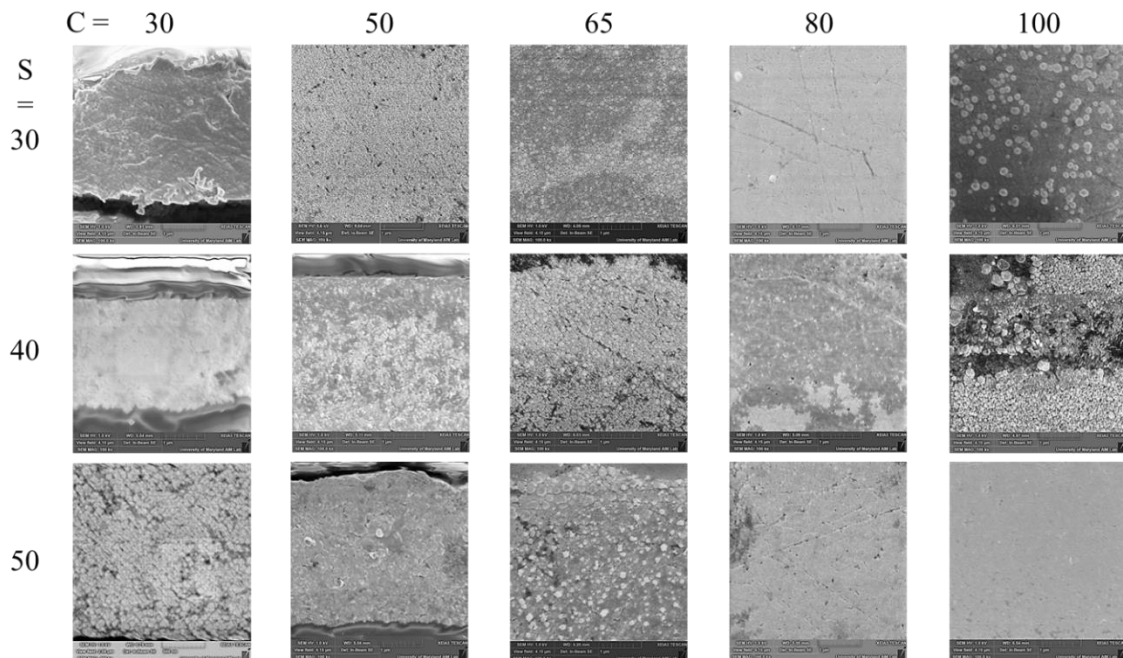


Figure 3.14: Surface images for a) single and b) double pass traces at 50,000x magnification.

a) Single-Pass Traces



b) Double-Pass Traces

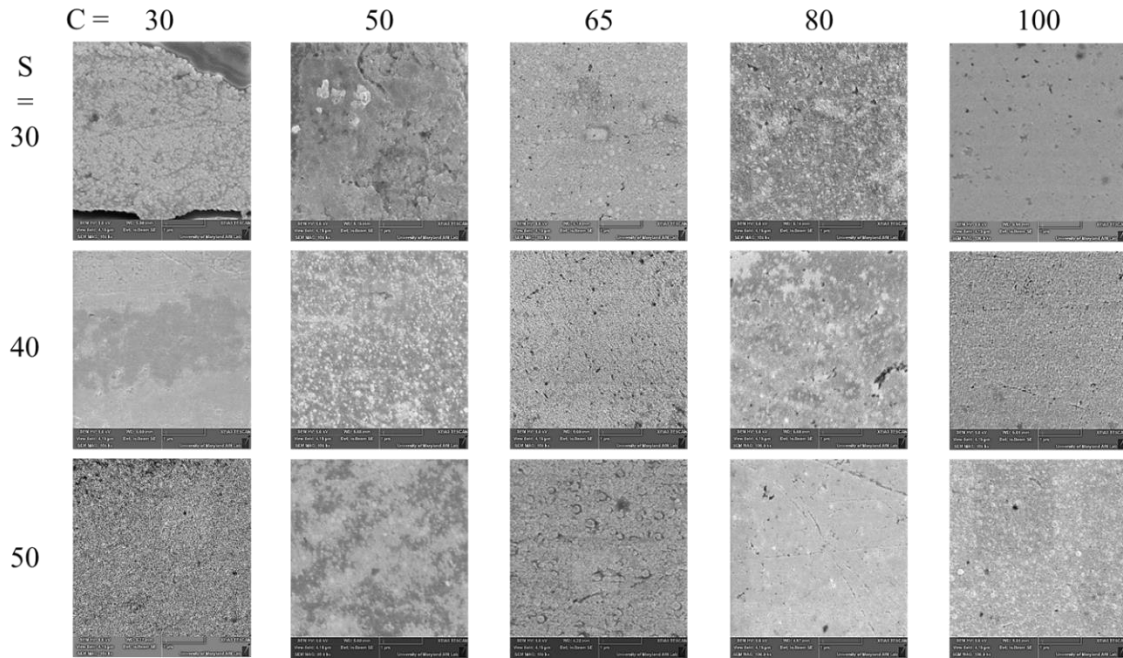


Figure 3.15: Cross-section images for a) single and b) double-pass traces at 100,000x magnification.

These high magnification images were digitally processed to quantify the size and spacing distribution of the agglomerates. This methodology is described in Appendix A6. The raw data extracted from the software included the agglomerate size for each feature counted as well as the shortest distance from one agglomerate to the nearest neighbors. This data was then post-processed to obtain various stochastic metrics (e.g. mean values, standard deviations, skewness, etc.).

Five images were post processed for each of the four corner cases and for the middle case in the matrix of flow rate combinations ($C = 30, S = 30$; $C = 30, S = 50$; $C = 65, S = 40$; $C = 100, S = 30$; $C = 100, S = 50$). This post-processing was repeated for both single-pass and double-pass trace segments as well as for both surface images and cross-section images. The size and spacing distributions for each image was normalized before averaging across the five images, to avoid one image from dominating if there was an

unusually high number of agglomerates counted by the image processing software. All of this data was presented in several different formats, which are included in full in Appendix A7, with just one example of each format provided here because not all of the data led to significant conclusions:

1. *Number of agglomerates (Table 3.7 and Figure 3.16)*. These plots include the number of features the image processing software counted as an agglomerate through its smart segmentation algorithm, based on sample information provided by the user. The 3D bar charts present the number of agglomerates on the z-axis. The x-y plane contains the 15 different flow rate combinations corresponding to the 15 different serpentine traces. Furthermore, there is a figure distinguishing between single and double-pass traces as well as surface or cross-section images in A7.1. The data from the 3D bar charts are also provided in tabular form. Standard deviations are also provided for selected flow rate combinations (corner cases and middle cases), where multiple images were processed.
2. *Percent area covered by the agglomerates (Table 3.8 and Figure 3.17)*. The 3D bar charts plot the percent area out of 100 on the z-axis and again lays out the 15 different flow rate combinations in the x-y plane. Again, there is a figure distinguishing between single and double-pass traces as well as surface or cross-section images in A7.2. The data from the 3D bar charts are provided in tabular form and for the flow rate combinations (corners and middle cases) that there are multiple images processed for, the standard deviation is also provided.
3. *Agglomerate size and spacing distributions (Figure 3.18)*. For the four corner and middle flow rate combinations that were averaged, the size and spacing

distributions were then fit to a histogram with log-scale bins, to deal with the highly right skewed nature of the data. The five flow rate combinations were grouped in threes for the histograms in terms of major ($C = 30, S = 30; C = 65, S = 40; C = 100, S = 50$) and minor ($C = 30, S = 50; C = 65, S = 40; C = 100, S = 30$) diagonals. Histograms are provided in A7.3 for major and minor diagonal cases, single and double-pass, surface and cross-section images, as well as agglomeration size and spacing.

4. *Variation in agglomerate size and spacing (Figure 3.19)*. The four corner flow rate combinations were grouped in twos for the plots in terms of major ($C = 30, S = 30; C = 100, S = 50$) and minor ($C = 30, S = 50; C = 100, S = 30$) diagonals. Plots are provided in A7.4 for major and minor diagonal cases, single and double-pass, surface and cross-section images, as well as agglomeration size and spacing.
5. *Average agglomerate size and spacing as a function of flow rate (Table 3.9 and Figure 3.20)*. The 3D bar charts plot the average agglomerate size and spacing on the z-axis and lays out the 15 different flow rate combinations in the x-y plane. Furthermore, there is a figure distinguishing between single and double-pass traces as well as surface or cross-section images in A7.5. The data from the 3D bar charts are provided in tabular form with the average and standard deviation for the agglomeration size and spacing.
6. *Standard deviation of agglomerate size and spacing (Figure 3.21)*. The 3D bar charts plot the standard deviation of the agglomerate size and spacing on the z-axis and lays out the 15 different flow rate combinations in the x-y plane.

Furthermore, there is a figure distinguishing between single and double-pass traces as well as surface or cross-section images in A7.6.

7. *Skewness of agglomerate size and spacing (Figure 3.22).* From the histograms presented in A7.3 and exemplified in Figure 3.18, a skewness factor can be calculated based on the log-scale based binning for the five serpentine traces with multiple image data averaged together. The more positive the skewness value, the more skewed right the histogram data is. The 3D bar charts plot the skewness of the agglomerate size and spacing on the z-axis and lays out the 5 different flow rate combinations in the x-y plane. Furthermore, there is a figure distinguishing between single and double-pass traces as well as surface or cross-section images in A7.7.

	Carrier = 30	Carrier = 50	Carrier = 65	Carrier = 80	Carrier = 100
Sheath = 30	225±161	145	101	158	64±14
Sheath = 40	345	337	98±27	152	123
Sheath = 50	230±90	210	181	140	83±36

Table 3.7: Number of agglomerations in single-pass trace on the surface.

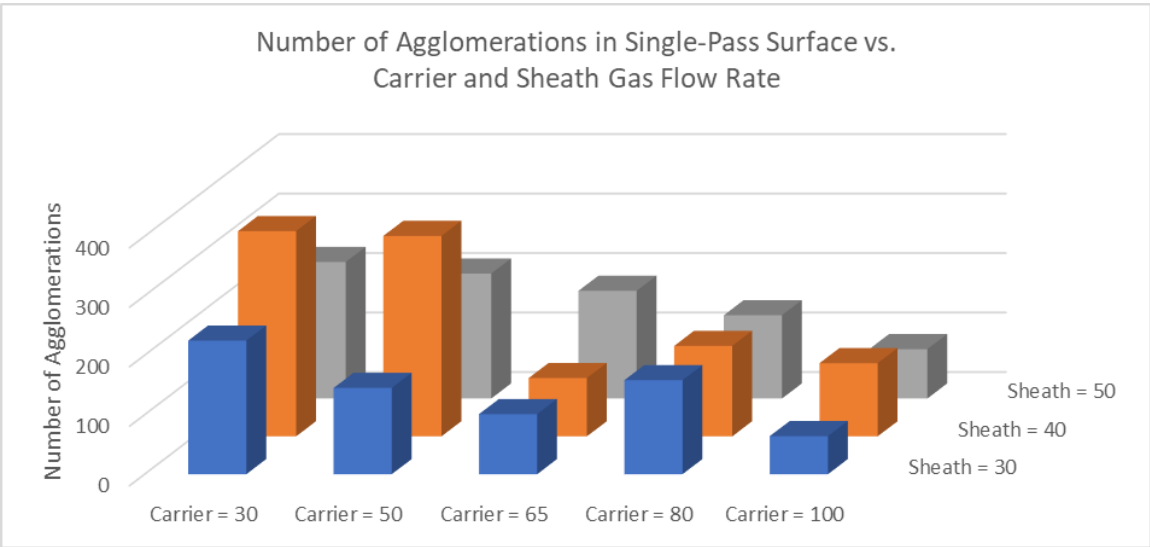


Figure 3.16: Number of agglomerations in single-pass trace on the surface as a function of carrier and sheath gas flow rate.

	Carrier = 30	Carrier = 50	Carrier = 65	Carrier = 80	Carrier = 100
Sheath = 30	13.54±4.05	15.83	25.64	27.29	21.64±3.12
Sheath = 40	9.89	15.62	20.96±1.33	17.03	25.85
Sheath = 50	15.69±2.16	24.70	19.97	29.92	21.02±7.27

Table 3.8: Agglomeration percent area in single-pass trace on the surface.

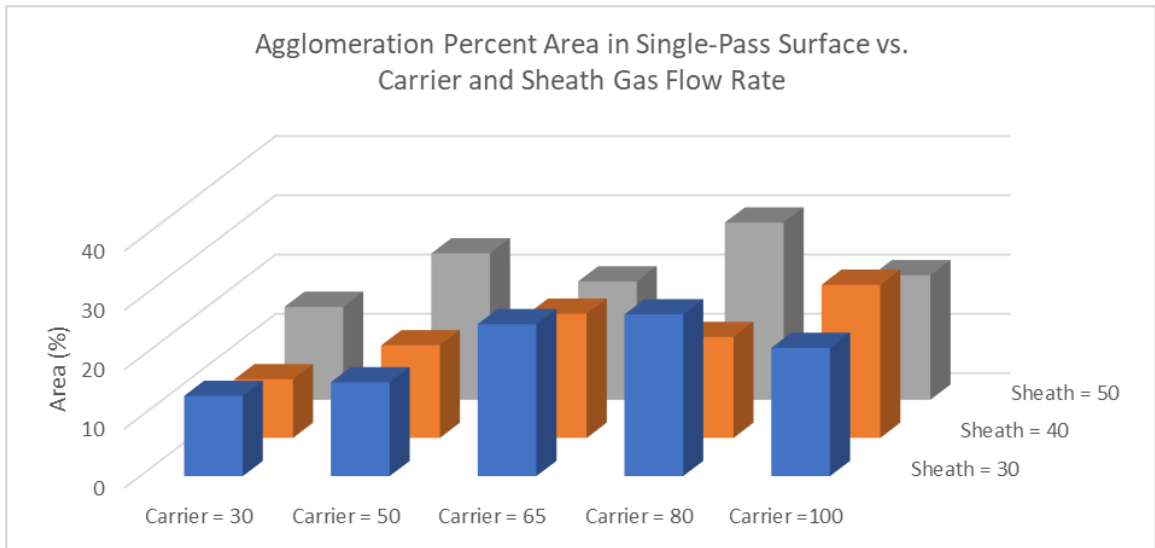


Figure 3.17: Agglomeration percent area in single-pass trace on the surface as a function of carrier and sheath gas flow rate.

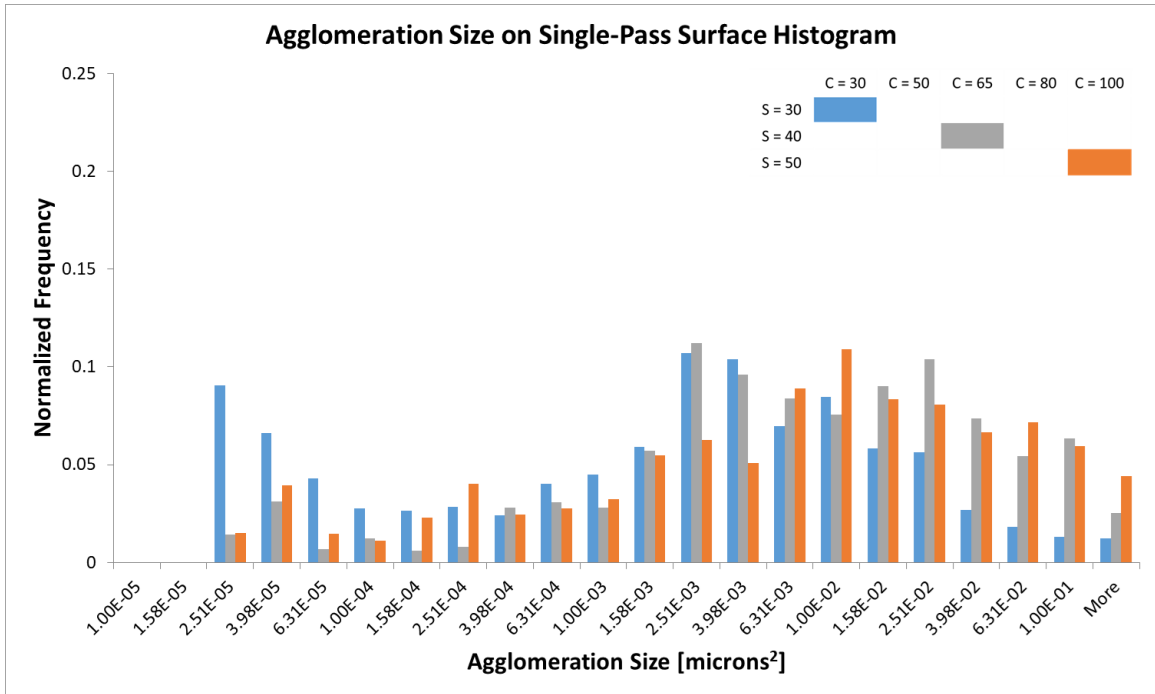


Figure 3.18: Agglomeration size in single-pass trace on the surface for major diagonal cases.

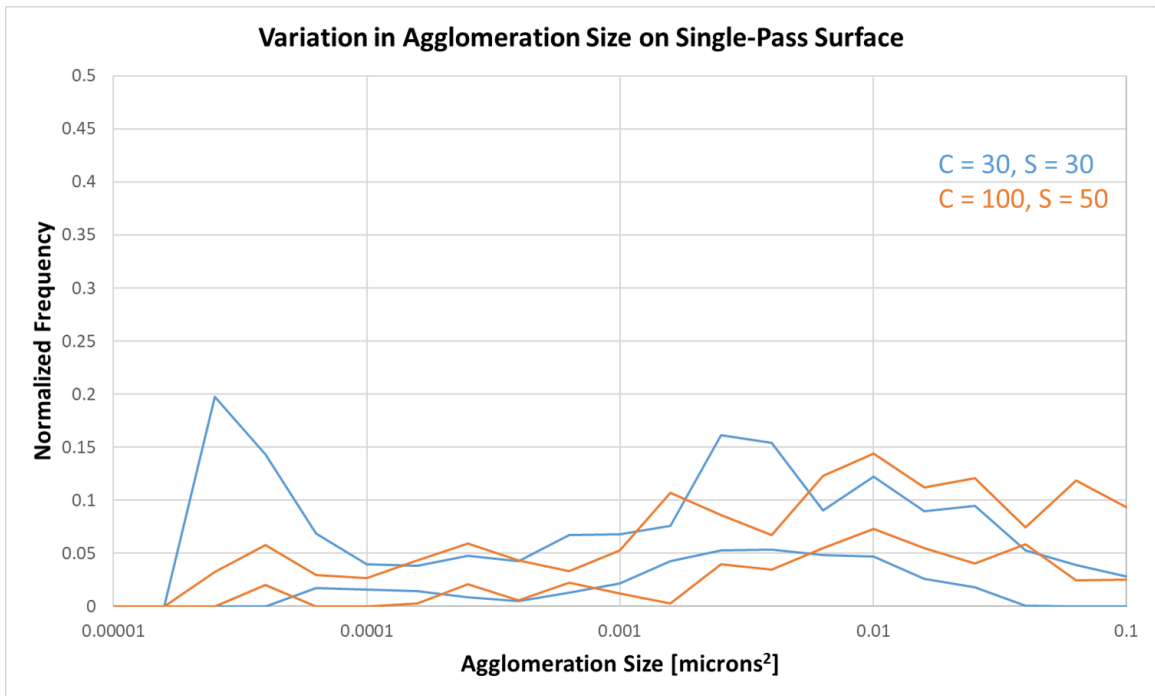


Figure 3.19: Variation in agglomeration size in single-pass trace on the surface for major diagonal cases.

	Carrier = 30	Carrier = 50	Carrier = 65	Carrier = 80	Carrier = 100
Sheath = 30	0.008±0.015	0.009±0.016	0.021±0.033	0.014±0.036	0.028±0.041
Sheath = 40	0.002±0.005	0.004±0.007	0.019±0.029	0.009±0.016	0.017±0.034
Sheath = 50	0.006±0.017	0.010±0.044	0.009±0.016	0.017±0.034	0.022±0.037

Table 3.9: Average agglomeration size in single-pass trace on the surface.

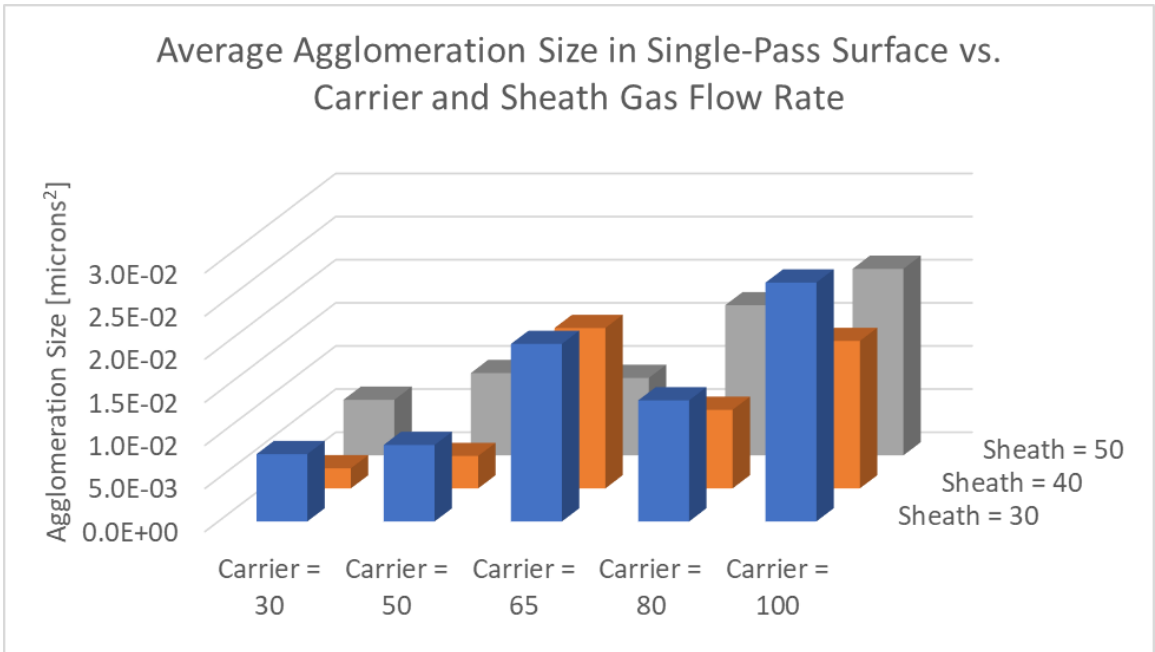


Figure 3.20: Average agglomeration size in single-pass trace on the surface as a function of carrier and sheath gas flow rate.

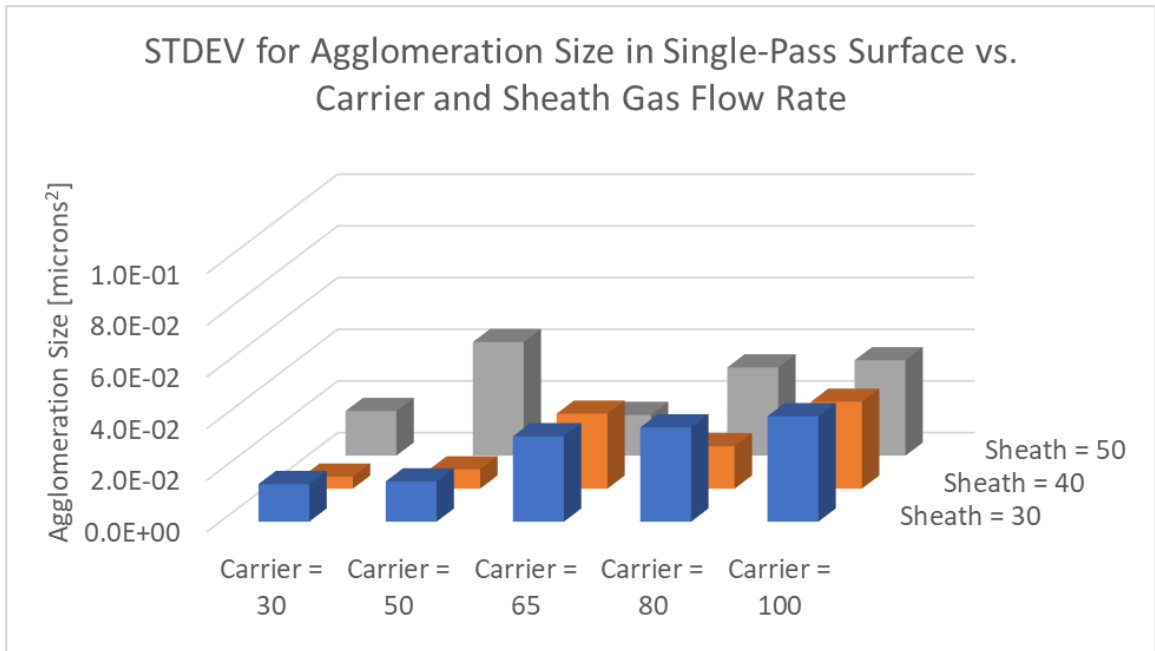


Figure 3.21: Standard deviation of agglomeration size in single-pass trace on the surface as a function of carrier and sheath gas flow rate.

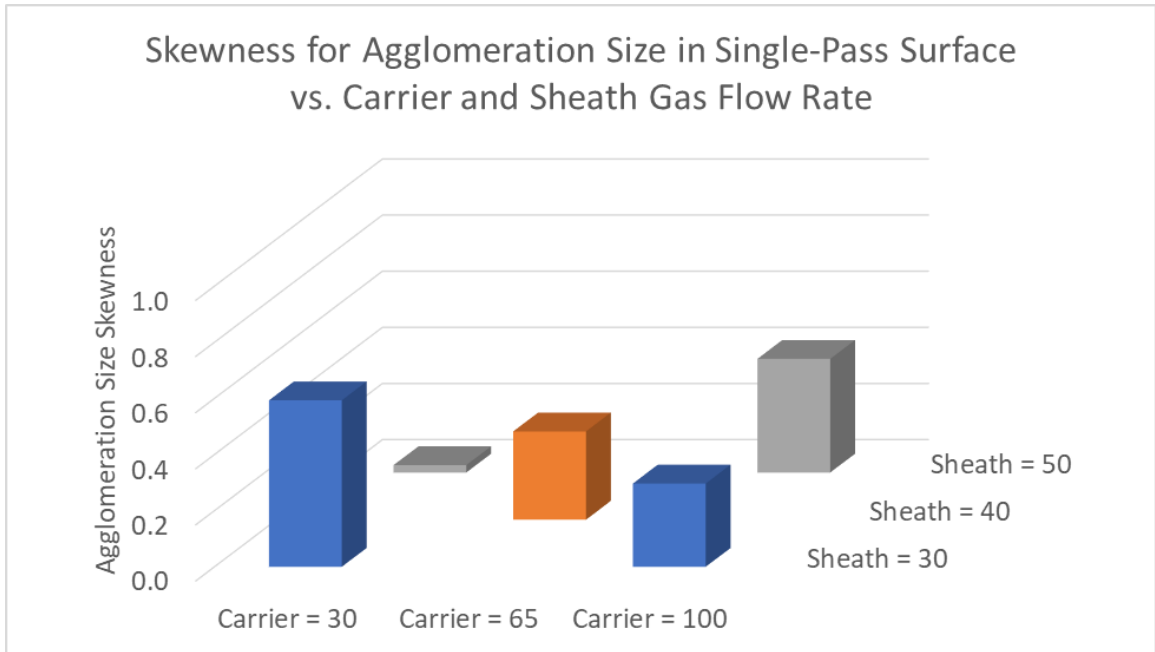
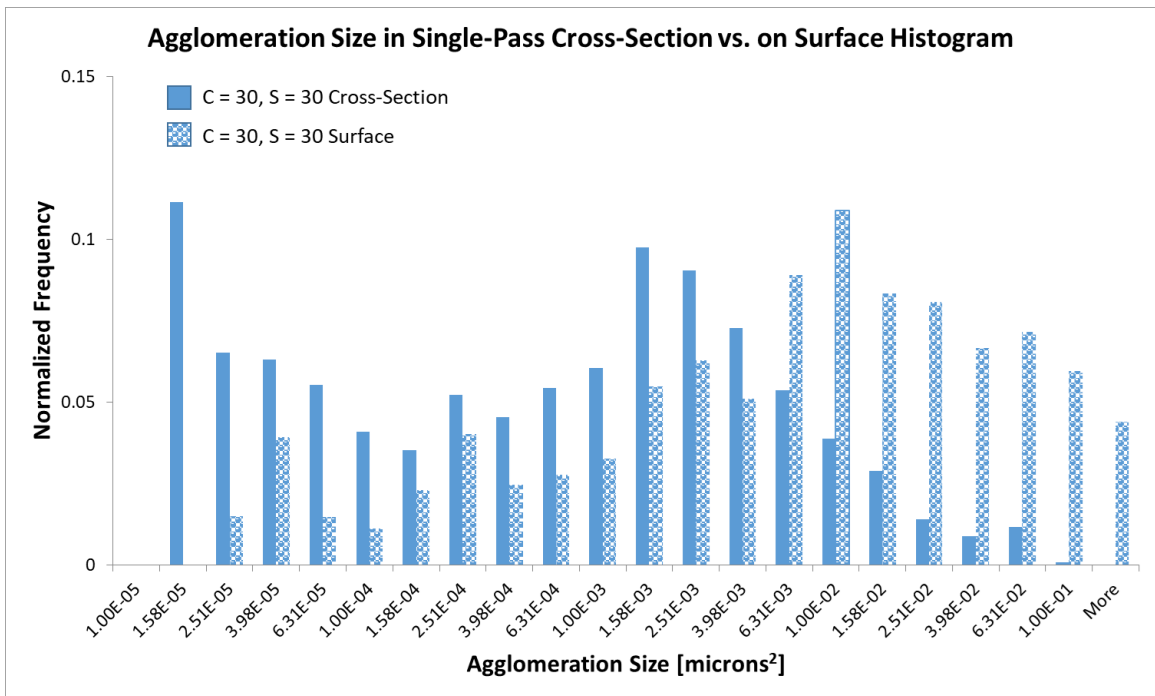


Figure 3.22: Skewness of agglomeration size in single-pass trace on the surface as a function of carrier and sheath gas flow rate.

A significant observation was that the agglomerates on the surface were bigger than those observed within the bulk of the trace, as evidenced by the histograms in Figure

3.23. This was the case for both the serpentine trace with the lowest flow rate combination, carrier gas of 30 sccm and sheath gas of 30 sccm, and the highest flow rate combination, carrier gas of 100 sccm and sheath gas of 50 sccm. The average agglomerate size on the surface for each of these two flow rate cases is 0.008 and 0.022 microns², respectively, while in the bulk it is 0.003 and 0.001, respectively. This might suggest that the clumping of the silver nanoparticles becomes progressively greater as the trace stacks up away from the substrate level.



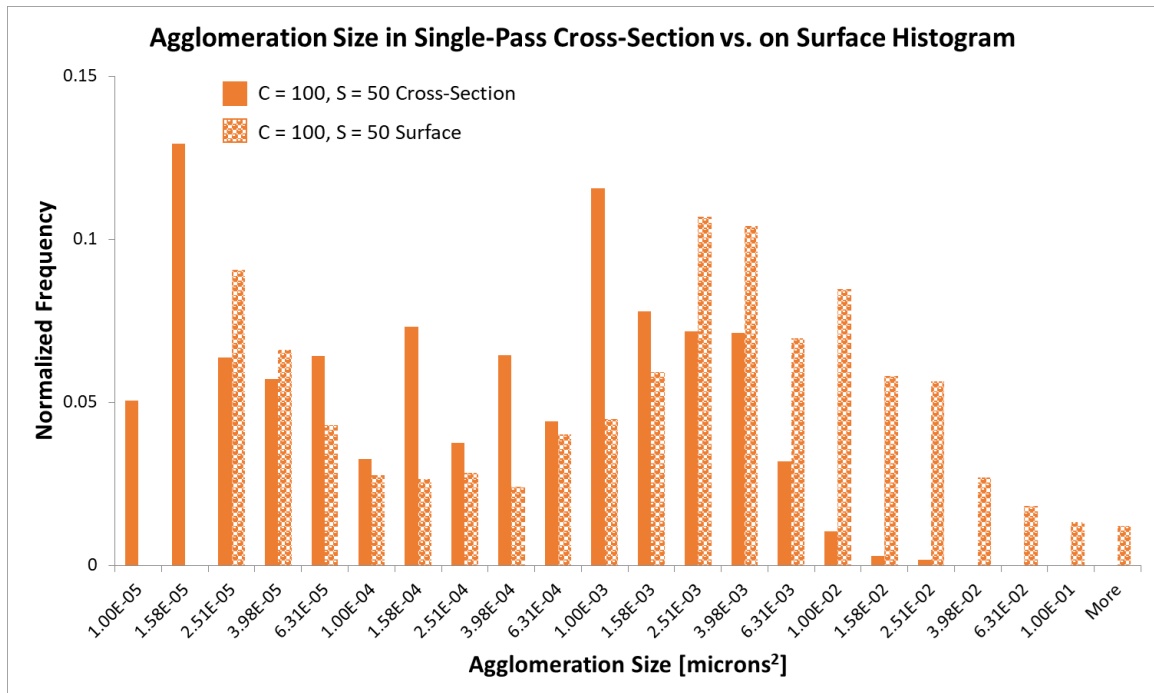


Figure 3.23: Agglomeration size distribution for single-pass trace in the bulk vs. on the surface for the a) $C = 30, S = 30$ and b) $C = 100, S = 50$ serpentines.

In Figure 3.24, the agglomerate size distribution on the surface for a single-pass trace is plotted for three different flow rate combinations: $C = 30, S = 50$; $C = 65, S = 40$; $C = 100, S = 30$. The trace with the lowest carrier gas of 30 sccm had predominantly the smallest agglomerates, while the trace with the highest carrier gas of 100 sccm had predominantly the largest agglomerates. This supports the previous qualitative observation made from looking at the raw high magnification surface images that the agglomerate sizes are coarser at higher carrier gas flow rates (Figure 3.14). Consistent with this trend, the intermediate carrier gas rate of 65 sccm predominantly has agglomerate sizes that are in between those for the end cases of 30 sccm and 100 sccm. The proportional relationship between agglomerate size and carrier gas flow rate is also supported by Figure 3.20 as the agglomerates get coarser from left to right as carrier gas flow rate increases.

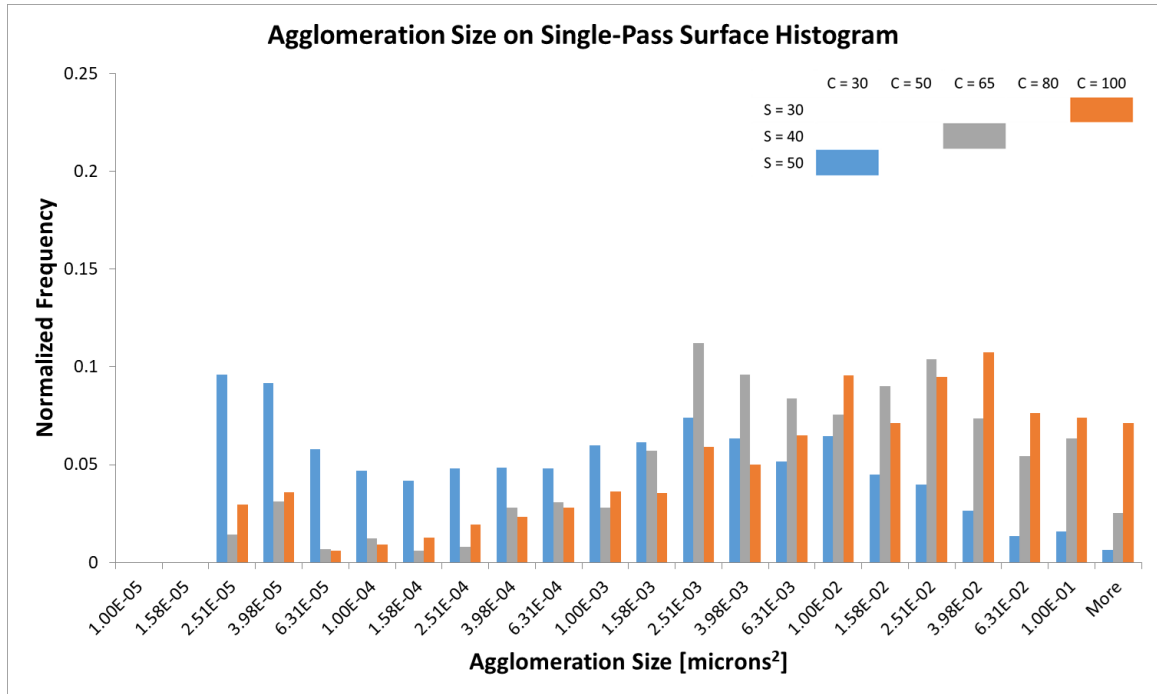


Figure 3.24: Agglomeration size in single-pass trace on the surface for minor diagonal cases.

In Figure 3.25, the agglomerate spacing distribution in the bulk for a double-pass trace is plotted for three different flow rate combinations: $C = 30, S = 30$; $C = 65, S = 40$; $C = 100, S = 50$. The trace with the lowest carrier gas flow rate of 30 sccm had predominantly the smallest spacing between agglomerates, while the trace with the highest carrier gas flow rate of 100 sccm had predominantly the largest spacing. Consistent with this trend, the intermediate carrier gas of 65 sccm predominantly has particle sizes that are in between the end cases of 30 sccm and 100 sccm. This also supports the idea that coarser agglomerates are occurring at higher carrier gas flow rates.

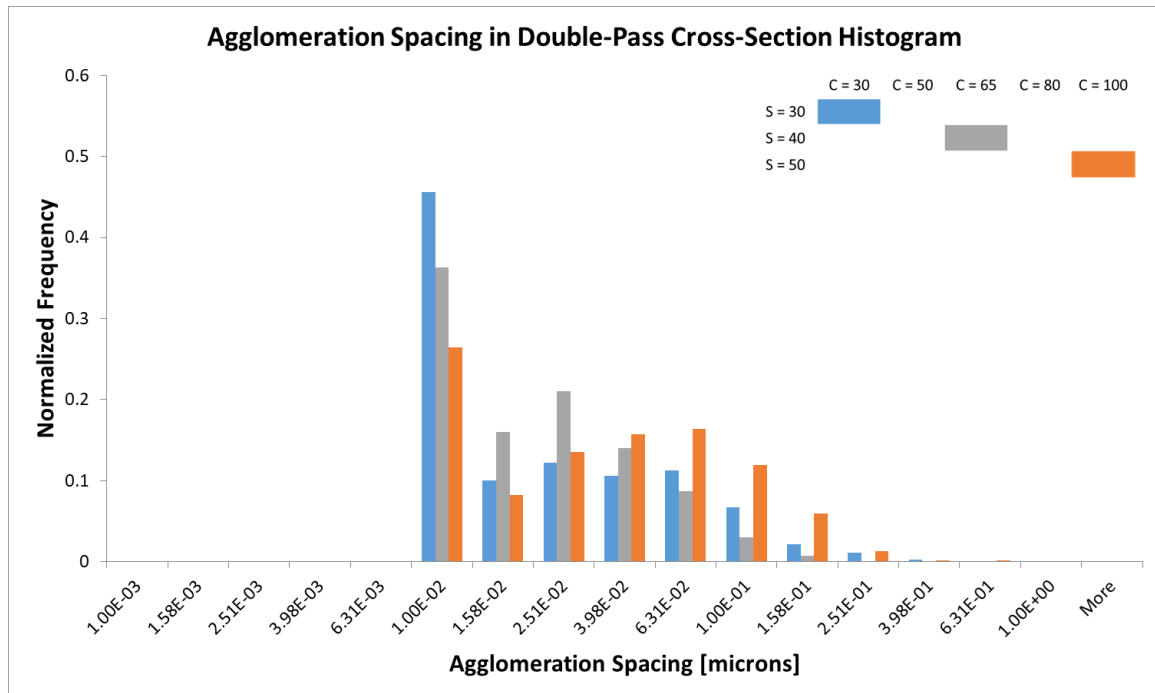


Figure 3.25: Agglomerate spacing in double-pass trace in the bulk for major diagonal cases.

Section 3.3.6: Microcracking

Another discovery from the low magnification surface imaging was the presence of microcracking at the higher carrier gas flow rates (Figure 3.26). At carrier gas flow rates greater than or equal to 65 sccm there was varying degrees of microcracking, predominantly aligned along the longitudinal direction, in all 45 traces examined, but at carrier gas flow rates less than or equal to 50 sccm there was not any visible microcracking in any of the 30 traces examined. There is not an apparent relationship between sheath gas flow rate and the prevalence of microcracking. The internal location of cracks, whether at the substrate interface, or at the interface between passes within the trace, or at both, was investigated during cross-sectioning. These longitudinal

microcracks are similar to those seen previously in IoF171101, which had a carrier gas flow rate of 80 sccm, after 250 thermal cycles.

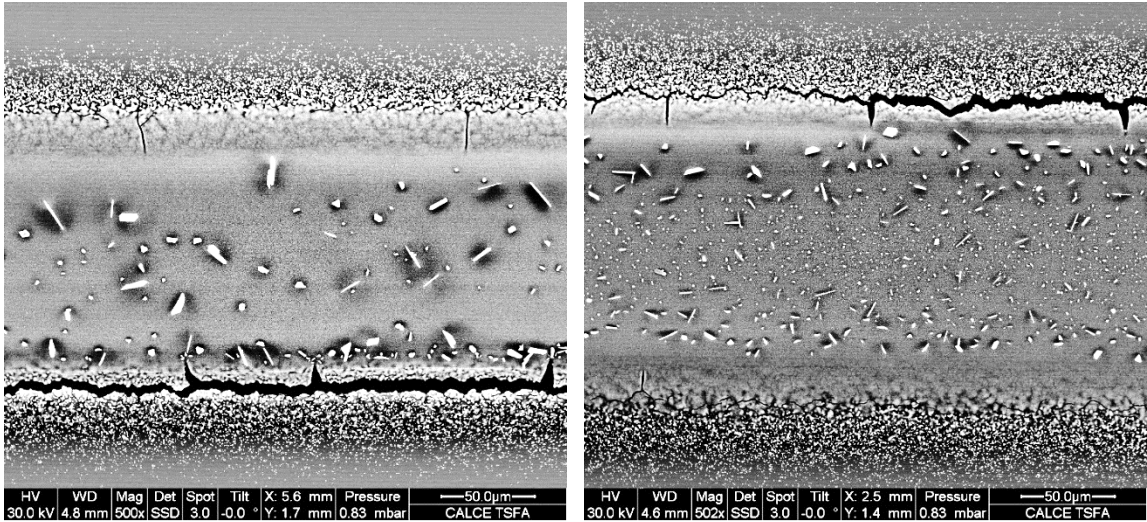
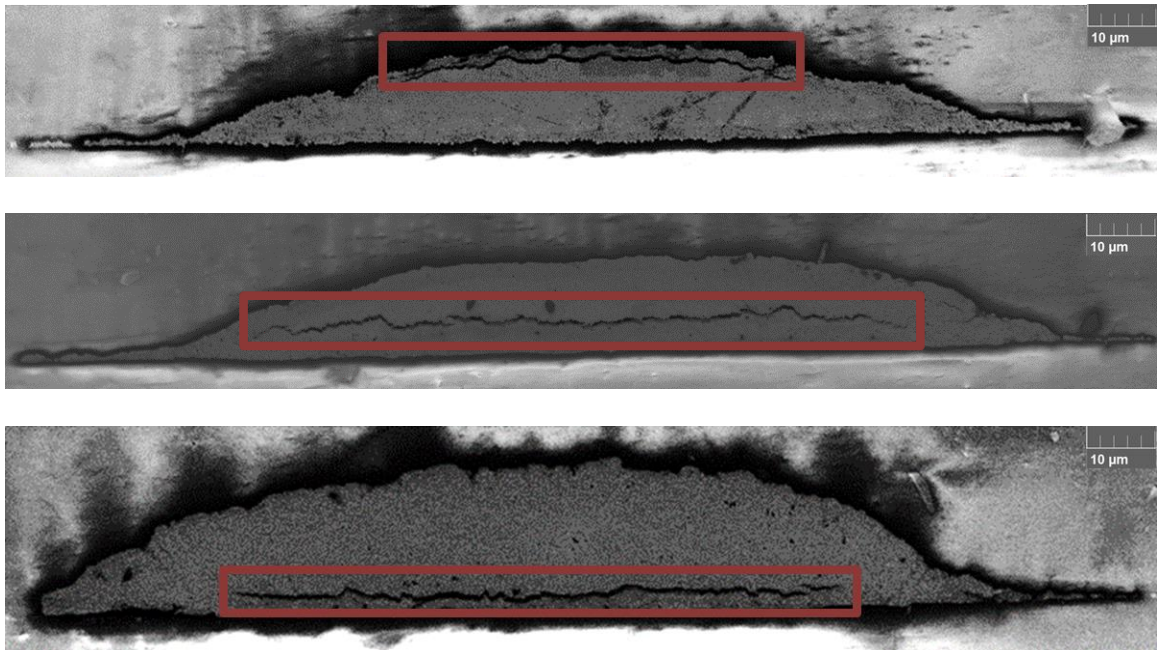


Figure 3.26: Examples of microcracking in serpentine traces with a) 80 and b) 100 sccm carrier gas flow rate.

To further investigate the location of microcracking within the serpentine traces, they were cross-sectioned with grinding and polishing specimen preparation techniques to allow for SEM imaging of the bulk trace. Upon inspection, cracks were observed in a variety of locations within the cross-section. In the single-pass traces, cracks were observed rarely at the top (Figure 3.27a) and frequently in the middle (Figure 3.27b). In the double-pass traces, cracks were observed occasionally on the sides in the middle (Figure 3.27c) and frequently towards the bottom (Figure 3.27d). Additionally, poor adhesion was sporadically observed in both the single-pass and double-pass traces as there was not always complete and consistent contact made with the Polymer N coating on the substrate (Figure 3.28). A summary of the occurrence of cracks in all 30 cross-sections documented, is provided in Table 3.10. The microcracking is most likely due to a combination of shrinkage stresses and capillary pressure, as the volatiles in the ink escape during the sintering process. Simple 1D models of capillary pressure in the

literature suggest that microcracking risks may be high for trace thickness beyond 10-100 nm and may further increase with increasing trace thickness (Singh et al., 2007). The principle of such crack formation is the evaporation-mediated agglomeration of the nanoparticles, which narrows the passage for the flows leading to a buildup of the capillary pressure, which eventually leads to the formation of periodic cracks. The relevance of these simple cracking models will be discussed in future publications, in the light of our experimental evidence of microcracking. These cracks are not believed to be the result of shrinkage stress post-sintering as explained in Appendix A8.



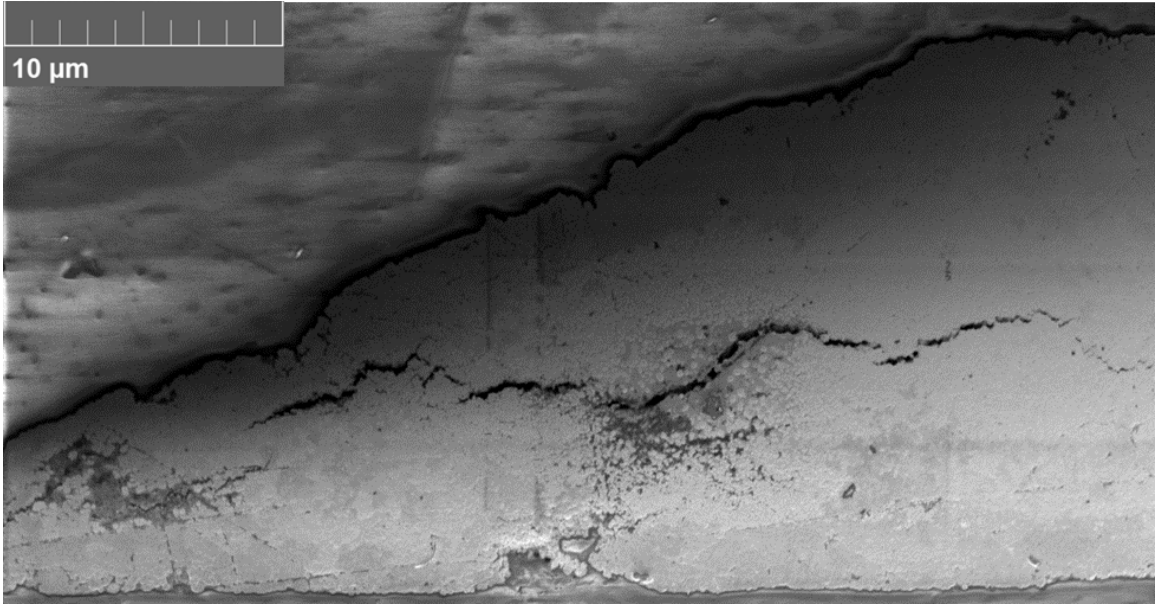
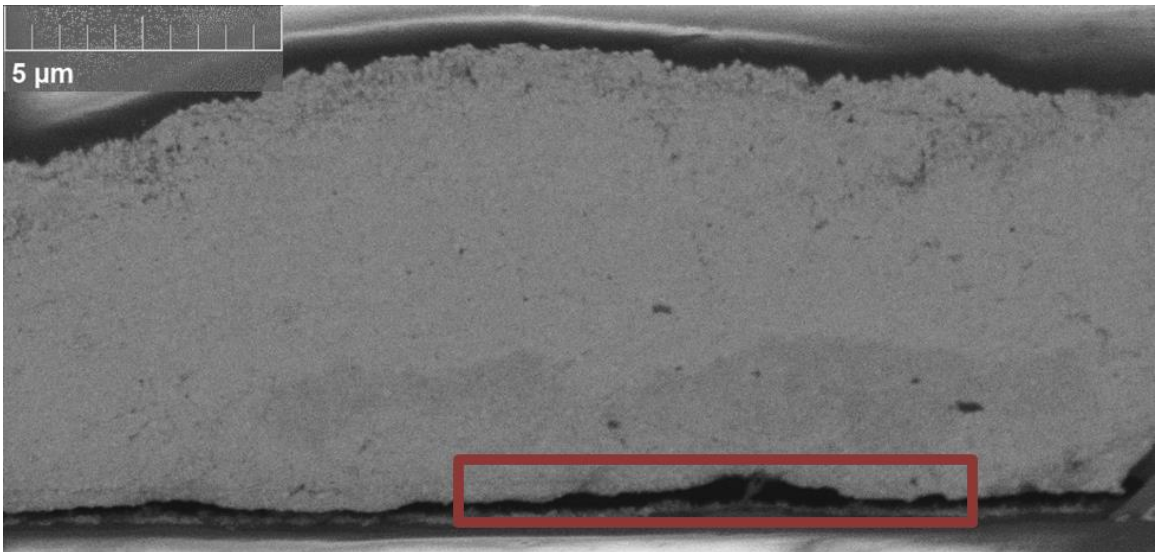


Figure 3.27: Cross-section SEM images of traces with a) crack at the top of $C = 65$, $S = 30$ single-pass, b) crack in the middle of $C = 80$, $S = 50$ single-pass, c) crack at the bottom of $C = 100$, $S = 50$ double-pass, and d) crack at the left in the middle of $C = 100$, $S = 40$ double-pass.



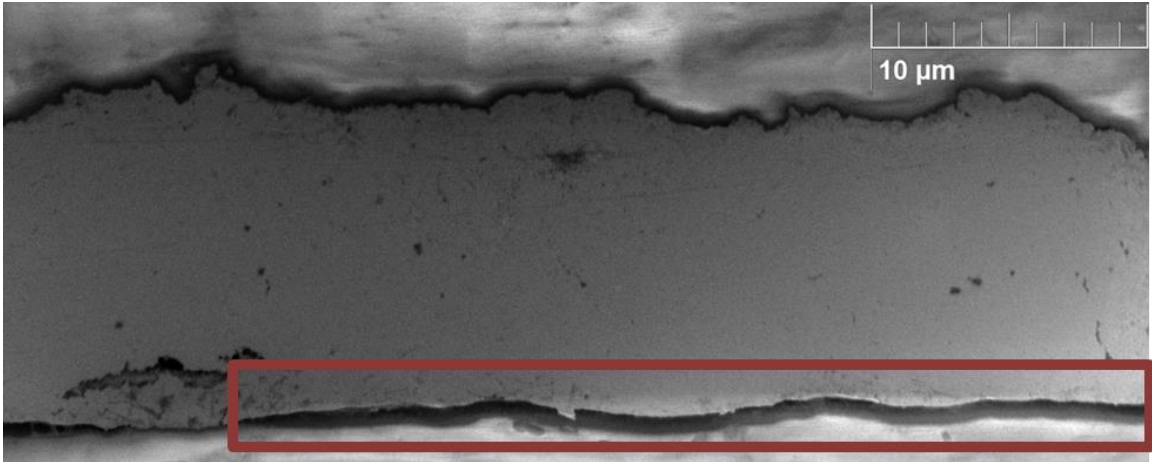


Figure 3.28: Cross-section SEM images of traces with poor adhesion between printed silver line and polymer substrate in a) $C = 30, S = 50$ double-pass and b) $C = 100, S = 50$ single-pass.

Single	Carrier				
Sheath	30	50	65	80	100
30	None	None	Crack at top	Crack in middle and top	Crack in middle
40	None	None	None	Crack in middle	Microcrack at bottom
50	None	None	Crack in middle	Crack in middle	Small microcracks

Double	Carrier				
Sheath	30	50	65	80	100
30	None	None	Microcrack on left, right	Microcrack across bottom	None
40	None	Small microcracks	Small microcrack	Crack at bottom	Microcrack on left, bottom
50	None	Small microcrack	Small microcrack	Crack at bottom	Crack at bottom

Table 3.10: Presence of cracks observed or not observed in serpentine traces for a) single-pass and b) double-pass traces.

Section 3.4: Summary

The desire to understand the effects of carrier and sheath gas flow rates on the quality of an aerosol jet printed trace motivated a design of experiment where 15 serpentine traces were printed at varying flow rates and then analyzed to judge the print quality. The carrier gas flow rates were 30, 50, 65, 80, and 100 sccm and the sheath gas flow rates were 30, 40, and 50 sccm. Part of the serpentine traces were single-pass, while the other part had a second-pass, which is typical in the printing of specimens intended

for functional application. For each flow rate combination, the deposition rate was estimated and the influence of increasing carrier gas and decreasing sheath gas on increase of deposition rate was quantified. Profilometry was conducted to quantify the macroscale geometric features such as trace width, cross-sectional area, overspray, and coverage. The flow rate of the carrier gas had a larger impact relative to that of the sheath gas for most of these macroscale geometric quantities. The effective conductivity of the printed silver traces interestingly increased with an increase in carrier gas. The presence of large silver crystalline deposits were mostly randomly present on the surface of the majority of traces with seemingly no relation to flow rate. High magnification imaging of the trace surfaces and digital image post-processing revealed that agglomerate coarseness (size and spacing) increased as the carrier gas flow rate increased. The agglomerate coarseness within the bulk (interior) of the trace cross-sections did not show a definitive trend with flow rates, but the largest agglomerates imaged in the trace's cross-section were noticeably smaller than those imaged on the surface of those same traces. Longitudinal microcracking was seen from an overhead view of the trace surface for the traces with higher carrier gas flow rates and these were also observed in cross-section images. The cracks appeared sometimes near the top, predominantly through the middle, and sometimes towards the bottom of the cross-section for various traces. These findings suggest that lower flow rates should be used to minimize microcracking and coarser agglomerations that cause the trace to be different from bulk and homogeneous silver. Given the lower deposition rates at lower carrier gas flow rates, additional passes or a lower print speed can be utilized to still reach the desired material deposition.

Chapter 4 – Summary and Future Work

This chapter will condense all of the information presented in the previous three chapters to allow for quicker and more efficient transfer of knowledge for the 3D printed hybrid electronics community.

Section 4.1: Summary and Discussion of Work Completed

Two different printed electronic specimens were successfully fabricated with Ink A. The first was an IoF specimen (IoF171101) that had printed lines traversing surfaces at different level (FR4 substrate and an elevated silicon die) with the help of an intervening polymer fillet ramp. The second specimen type was a baseline test coupon design (designated as DTC180201 specimen) that is simpler in nature, containing three sides of a five mm square on a single surface at a single level (without any different leveled surfaces). The IoF171101 and the DTC180201 specimens were documented with SEM imaging prior to any testing. The IoF171101 specimen showed coarser micromorphology and larger agglomerate features on the surface of the traces as well as greater bulk porosity within the trace. This difference is theorized to be the reason for vastly different reliability results following accelerated thermal cycling durability testing. The IoF171101 failed after just 250 thermal cycles, showing extensive microcracking as well as delaminations, whereas the DTC180201 structures lasted over 3,500 thermal cycles with failures unrelated to the printed traces and minimal observed damaged. The damage observed in the IoF specimens were found to be unrelated to the fillet regions. The differences in the reliability results in these two different print batches of AJP traces appear to be the result of variable trace quality, as defined by micromorphological

properties such as agglomeration and porosity. The ink condition such as solvent composition and content as well as the process parameters such as the flow rates of carrier gas and sheath gas for the IoF171101 and DTC180201 print batches were not identical, although both were printed with Ink A at the same deposition rates. Further work is needed to investigate the effect of ink condition namely dryness as defined by solids loading and solvent composition.

The desire to understand the effects of carrier and sheath gas flow rates on the quality of an aerosol jet printed trace motivated a design of experiment where 15 serpentine traces were printed at varying flow rates and then analyzed to judge the print quality. The carrier gas flow rates were 30, 50, 65, 80, and 100 sccm and the sheath gas flow rates were 30, 40, and 50 sccm. Part of the serpentine traces were single-pass, while the other part had a second-pass, which is typical in the printing of specimens intended for functional application. For each flow rate combination, the deposition rate was estimated and the influence of increasing carrier gas and decreasing sheath gas on increase of deposition rate was quantified. Profilometry was conducted to quantify the macroscale geometric features such as trace width, cross-sectional area, overspray, and coverage. The flow rate of the carrier gas had a larger impact relative to that of the sheath gas for most of these macroscale geometric quantities. The effective conductivity of the printed silver traces interestingly increased with an increase in carrier gas. The presence of large silver crystalline deposits were mostly randomly present on the surface of the majority of traces with seemingly no relation to flow rate. High magnification imaging of the trace surfaces and digital image post-processing revealed that agglomerate coarseness (size and spacing) increased as the carrier gas flow rate increased. The agglomerate

coarseness within the bulk (interior) of the trace cross-sections did not show a definitive trend with flow rates, but the largest agglomerates imaged in the trace's cross-section were noticeably smaller than those imaged on the surface of those same traces.

Longitudinal microcracking was seen from an overhead view of the trace surface for the traces with higher carrier gas flow rates and these were also observed in cross-section images. The cracks appeared sometimes near the top, predominantly through the middle, and sometimes towards the bottom of the cross-section for various traces. These findings suggest that lower flow rates should be used to minimize microcracking and coarser agglomerations that cause the trace to be different from bulk and homogeneous silver. Given the lower deposition rates at lower carrier gas flow rates, additional passes or a lower print speed can be utilized to still reach the desired material deposition.

Section 4.2: Research Contributions

Though questions remain, this research into printed hybrid electronics and additive manufacturing has proven very successful. Test structures with a silver nanoparticle conductive Ink A on Polymer N coated silicon and FR4 have been successfully fabricated. An IoF specimen lasted 250 accelerated thermal cycles before trace failures were observed unrelated to the fillet features. This study is the first to demonstrate that the AJP IoF technology may have sufficient robustness to be a viable alternative to wirebonds, under thermal cycling stresses. Additionally, this study is the first to report that the differences in thermal cycling durability observed in different AJP test specimens correlated with different levels of agglomeration coarseness and

porosity. This agglomeration coarseness is an important quality metric that is easy to check before conducting long and expensive thermal cycling durability testing.

Through this gathering of data, much was learned about different diagnostic techniques. A conventional methodology of grinding and polishing to cross-section the trace will not lead to satisfactory SEM cross-section images if the micron-scale printed electronic is embodied in a non-conductive epoxy material that will charge in the chamber. Coating of the polished surface of the trace with a non-amorphous material like carbon at particle sizes of less than 30 nm can effectively ground the surface to the SEM stage without distorting any of the agglomeration features. Other methods such as AFM and laser profilometry on the polished cross-section surface did not yield reliable information about agglomeration coarseness as it was more susceptible to the level of polishing as detailed in Appendix A4 and A5.

This study is also one of the first to systematically explore the relationship between AJP at different flow rates of carrier gas and sheath gas and the micromorphology of printed nanoparticle-based conductor inks (for thermal sintering). This study has been able to establish that higher flow rates are likely the cause of larger (coarser) agglomerations on the surface of traces, which was confirmed through SEM imaging and digital image processing. This methodology, detailed in Appendix A6, for quantifying the correlation is also a useful contribution of this study that can be helpful to others trying to quantify micromorphological features of printed hybrid electronics. Moreover, the presence of crystalline deposits observed informs other users of its occurrence. This study also establishes that higher carrier gas flow rates also leads to a higher probability of microcracking. This is an important guide for the AJP community.

Section 4.3: Limitations and Future Work

This work was limited as the 15 serpentine traces printed at varying flow rate combinations were not subjected to thermal cycling durability testing. Such an endeavor would have allowed us to see if the higher carrier gas flow rate traces failed sooner as a result of the microcracking and coarser agglomerations that were already present after fabrication. Moreover, a direct comparison could have been made to the failure analysis study on the IoF171101 specimen. Moreover, because there is a clear effect on AJP trace quality when the print parameters are altered, this can be investigated through physics of failure modeling. This is recommended for a future study.

Besides the change in gas flow rates, the other major difference between the printing of the IoF171101 and DTC180201 specimens was the addition of solvent to Ink A prior to the printing of DTC180201. This ensured that the ink was within solids fraction specifications. The solids fraction history of the ink before the two print batches is not known, but there is a chance that adding solvent to the ink immediately before printing may have been a reason for improved trace quality and reliability in the DTC180201. As a result, ink dryness which can be partially quantified by the ink's solids loading is another important parameter to be investigated for its impact on trace quality. This conclusion is also supported by the literature. Solvent evaporation, especially as a result of continuous nitrogen gas flow over the ink surface in the atomization cup, weakens the ink and can affect the print quality (Wadhwa et al., 2015). Secor et al. (2018) integrated a solvent bubbler on the sheath gas flow line to dry the ink in a controlled manner before printing. By increasing the vapor concentration in the sheath gas to suppress drying, more material was deposited on the substrate as opposed to ink that is

too dry that will not impact or remain on the substrate. Preliminary work was completed to increase the solids fraction of Ink A by bubbling nitrogen to displace the solvent and plans were made to pull a partial vacuum. In addition to the effect of ink condition, the sintering temperature profile should also be investigated to see if slower ramp rates and more uniform solvent evaporation improves trace quality. This is recommended to be continued in a future study.

In a future study, SEM imaging of the cross-section of traces can be divided into documenting the top and bottom of a double pass trace, the second and first print pass, respectively. This will shed light on if there is a difference in agglomeration size between multiple print passes and potentially understand how the sintering process interacts with each pass differently depending on its proximity to the surface or substrate. Image processing results from those sets of data can be compared as well as comparing the first print pass of a double pass trace to an ordinary single pass trace. Additional tasks that remain include 1) ranking the thermal cycling performance of different conductive inks, 2) exploring ways to improve durability of under-performing inks, and 3) performing physics of failure modeling of print parameters and observed failures to quantify the agglomeration physics.

Chapter 5 – Appendices

In this chapter, additional information and research conducted as a part of this thesis is discussed.

A1: Reliability Results for Ink C and Ink D

An interconnect over fillet (IoF) specimen, similar to the one previously discussed in Chapter 2, fabricated with Ink C underwent thermal cycling reliability testing (Figure 5.1). This sample will be denoted IoF170601.

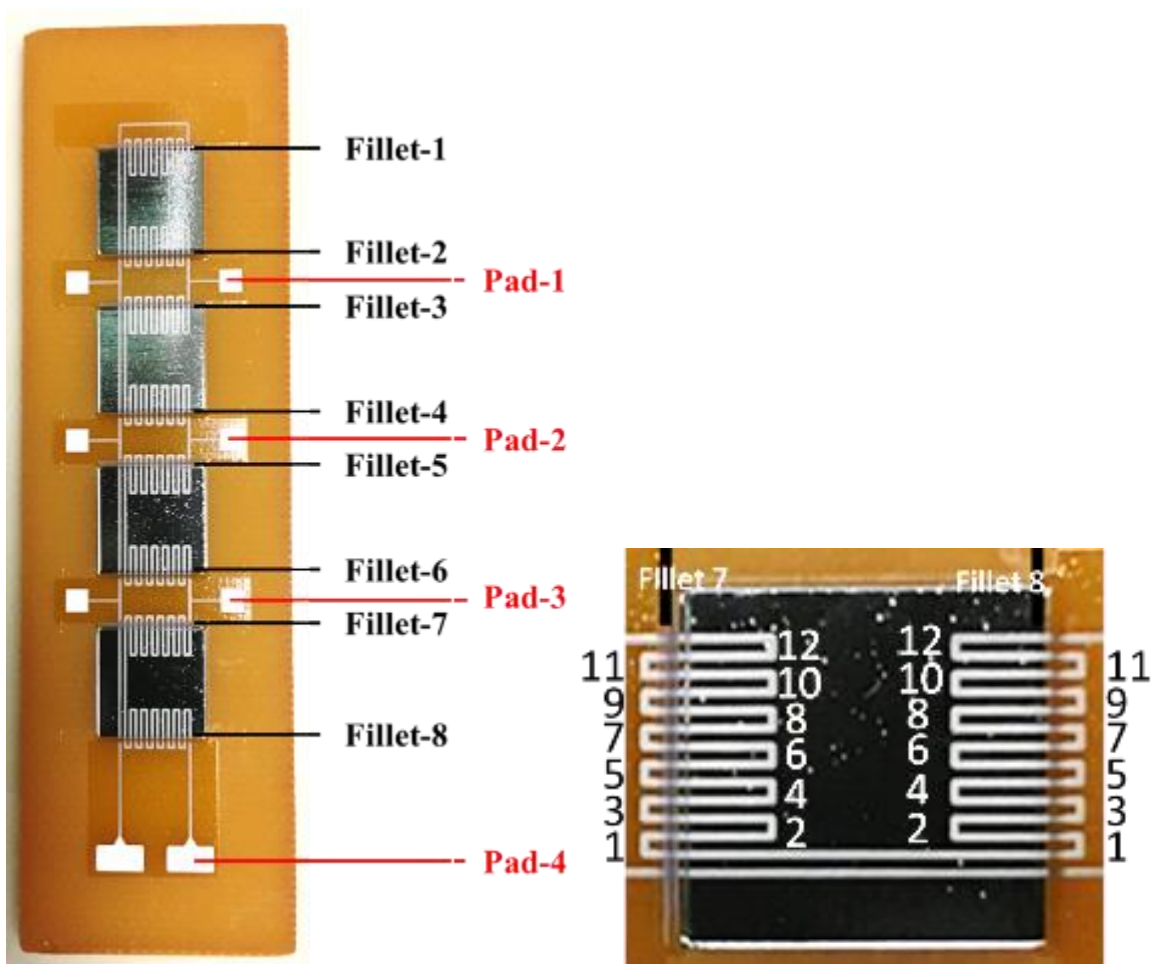


Figure 5.1: a) Interconnect over fillet specimen for Ink C (IoF170601) and b) zoomed in digital image of the serpentine traces on one of the four silicon dies populated on the FR4 circuit card.

An initial comparison between Inks A and C was a qualitative SEM image comparison of the traces before undergoing any thermal cycling (Figure 5.2). Ink A has more coarse particles that have agglomerated together whereas Ink C has a finer and more uniform spray of particles. Ink A also has a tighter distribution of particles meaning less overspray, which is something hard to control in the AJP process.

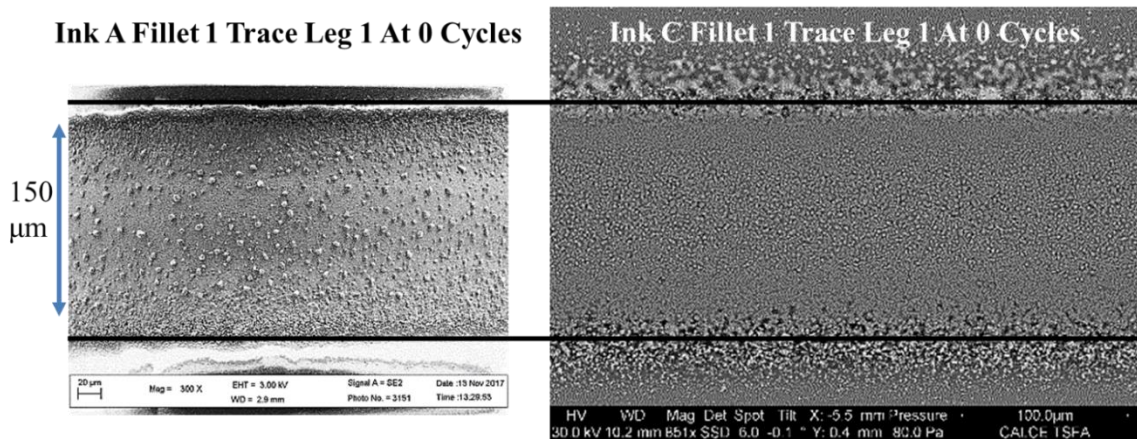


Figure 5.2: Initial morphology comparison between Inks A and C from an overhead view.

The temperature profile followed for accelerated thermal cycling of IoF170601 was also between -40 and 125 °C with a half-hour dwell at the hot temperature and 10 °C per minute ramps in between the two extreme temperatures. As expected early on in the thermal cycling durability testing, the resistance of the traces varied smoothly as a function of temperature and no anomalous spikes were observed. The earliest failures were in the connection pads, not in the AJP traces or Polymer N fillets, but with the connection to the outside world to allow for in-situ DC resistance monitoring. The sintered silver paste that connected a wire to the silver pad accumulated too much strain in the glob and as a result lifted the entire silver pad off of the substrate creating an open (Figure 5.3a). This was indicated in the resistance profiles as unusual spikes occurred (Figure 5.3b). The solution was to etch away from the substrate to allow for a copper

island under the silver pad such that a wire could be soldered directly to that copper island and create a more reliable connection to the outside world (Figure 5.3c).

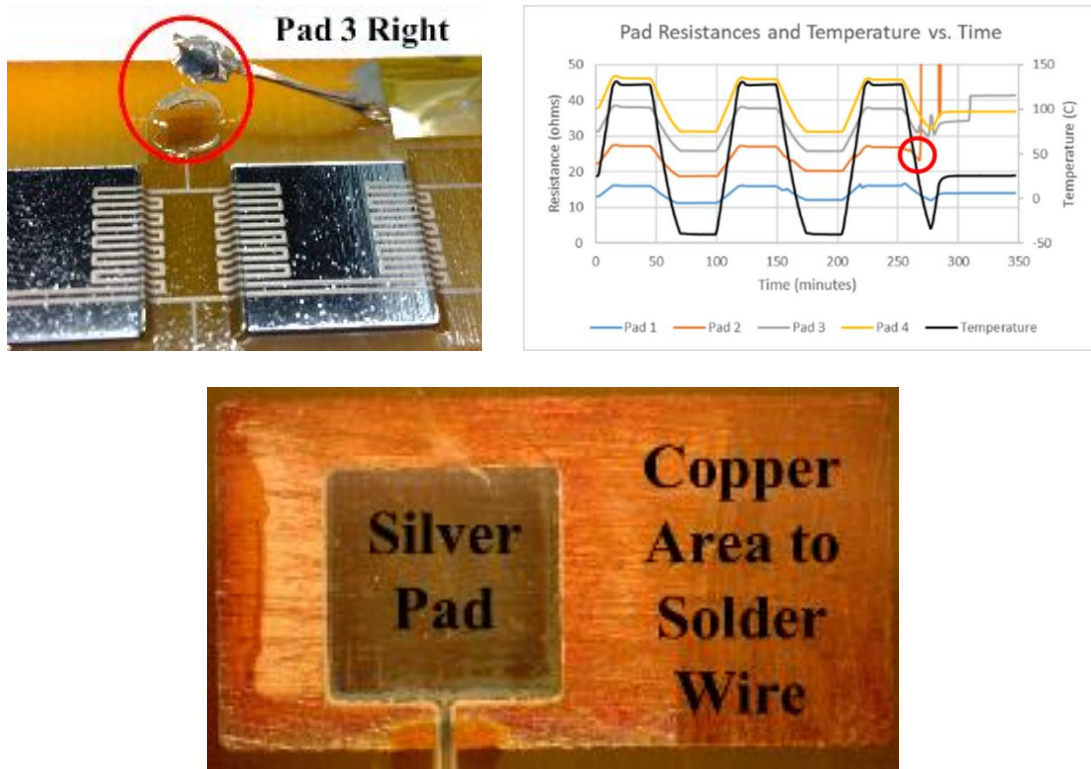


Figure 5.3: a) Example of silver pad lifting off of substrate as result of sintered silver glob, b) spike in resistance profile indicating open circuit, c) improved wire interconnection method.

After 200 thermal cycles from -40 to 125 °C, the Ink C IoF specimen (IoF170601) underwent failure analysis including SEM image documentation. Most of the traces showed little to no damage as exemplified by Fillet 5 in Figure 5.4a, which looked nearly the same as the pre-cycling images. Some damage was seen in Fillet 8 in Figure 5.4b with the presence of microcracking at the concave down bend in the fillet near the top of the die. It is possible that with further thermal cycling, a noticeable resistance change would have been observed in the in-situ monitoring as the crack grew to a full break in the trace.

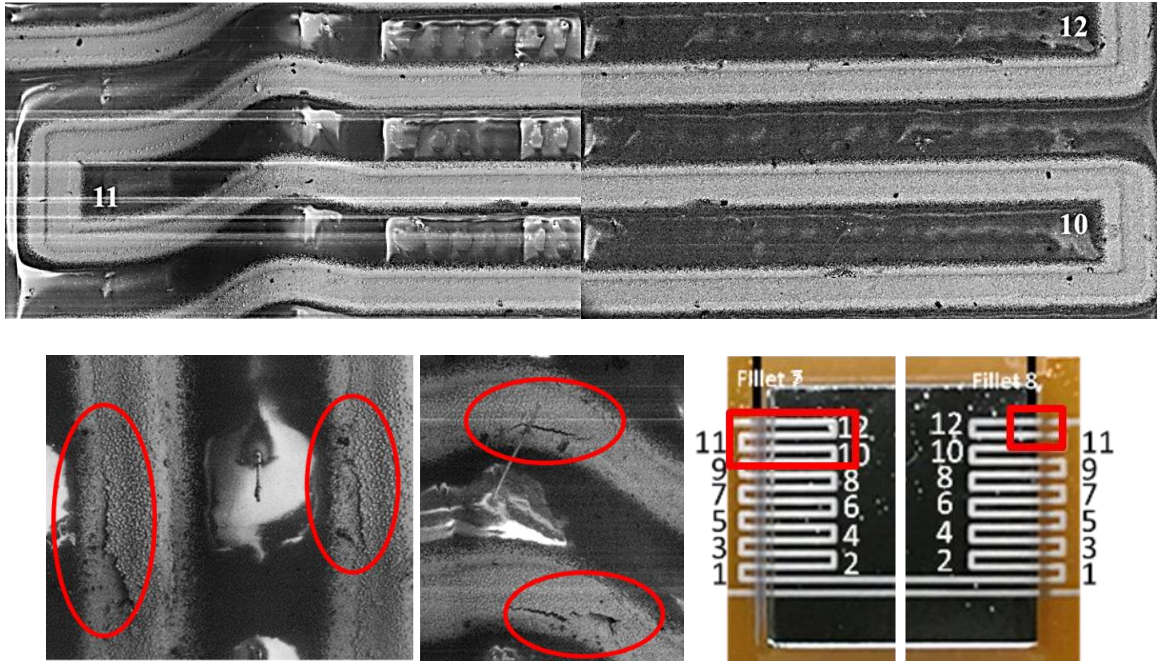


Figure 5.4: a) little observable damage on the surface of the traces corresponding to Fillet 5 and b) signs of longitudinal microcracking at traces at the top of Fillet 8 after 200 thermal cycles.

In addition to the Ink A baseline test coupon boards (DTC180201) fabricated and discussed in Section 2.1.2, the same baseline test coupon boards were produced for Ink C (CTC180508) and a new ink, Ink D, (RTC180508). Ink C was the same silver nanoparticle ink used to fabricate IoF170601 and Ink D was a new non-conductive ink that has applications as a printed resistor. Similar to DTC180201, CTC180508 had little visible damage to the traces after over two thousand thermal cycles. The RTC180508 structures had failures, beginning as the printed pads lifting off of the substrate, at the cold temperature portion of the thermal cycling profile (Figure 5.5). This was the result of unevaporated solvent meshing poorly with the Polymer N coating. This taught the group that a higher sintering temperature would be needed for Ink D to fully evaporate the solvent.



Figure 5.5: Example of pad lifting failure for RTC180508

A2: Investigating Scanning Electron Microscope as Potentially Damaging Printed Hybrid Electronics

The baseline test coupons discussed in Chapter 2 were also used to ensure that the electron beam and vacuum environment of the scanning electron microscope used for failure analysis was not causing any unintended damage to the sample. This was done as due diligence because it has been documented in the literature that the SEM environment can cause damage to polymer materials and the printed hybrid electronic samples do utilize Polymer N (Kitching et al., 1998). The DTC180201 boards underwent different loading conditions including: (i) thermal cycling; (ii) SEM exposure; and (iii) combination of both to see if any unexpected damage was afflicted.

The specimen selected for thermal cycling is designated Board 3, specimen selected for SEM exposure is designated Board 2, and the remaining specimens were selected for a combination of both are designated Board 1, 4, and 5. Board 2 was picked for SEM exposure because it had a slightly higher average resistance for its ten structures potentially meaning it was most likely to fail. The combination of both thermal cycling and SEM exposure occurred in two manners: 1) undergoing a certain number of thermal cycles (i.e. 50 or 150) initially and then five blocks of SEM exposure and storage or 2) alternating between 100 thermal cycles followed by one block of SEM exposure before returning to the thermal chamber and repeating the sequence. The first method was used for Boards 4 and 1, which underwent 50 and 150 thermal cycles, respectively, before five blocks of SEM exposure. Through this method, it can be seen if there is any delayed initiation or growth of damage due to locked-in residual stresses. The second method was used for Board 5, which underwent 100 thermal cycles followed by one block of SEM

exposure a total of four times. Each block of SEM exposure lasted approximately 30 minutes in which the e-beam high voltage was 30 kilovolts and the pressure was 83 Pascals. The test matrix discussed above is summarized in Figure 5.6. All structures subjected to accelerated thermal cycling were monitored in-situ with two-wire DC resistance measurement.

Dates	3/7/2018	3/8/2018	3/9/2018	3/10/2018	3/11/2018	3/12/2018	3/13/2018	3/14/2018	3/15/2018	3/16/2018	3/17/2018	3/18/2018	3/19/2018
Board 2		SEM 1	Storage		SEM 2	Storage	SEM 3	Storage	SEM 4	Storage	SEM 5		
Board 4	TC	SEM 1	Storage		SEM 2	Storage	SEM 3	Storage	SEM 4	Storage	SEM 5		
Board 5	Thermal Cycling				SEM 1	Thermal Cycling						SEM 2	
Board 1	Thermal Cycling						SEM 1	Storage	SEM 2	Storage	SEM 3		
Board 3	Thermal Cycling (Until Failure)												

Figure 5.6: Initial test matrix for Ink A baseline test coupons to investigate if SEM environment damages printed electronic samples.

All 50 test structures were initially optically documented to allow for a baseline for later comparison to know if damage or failure was the result of thermal cycling, SEM exposure, or simply a pre-existing defect (Figure 5.7).

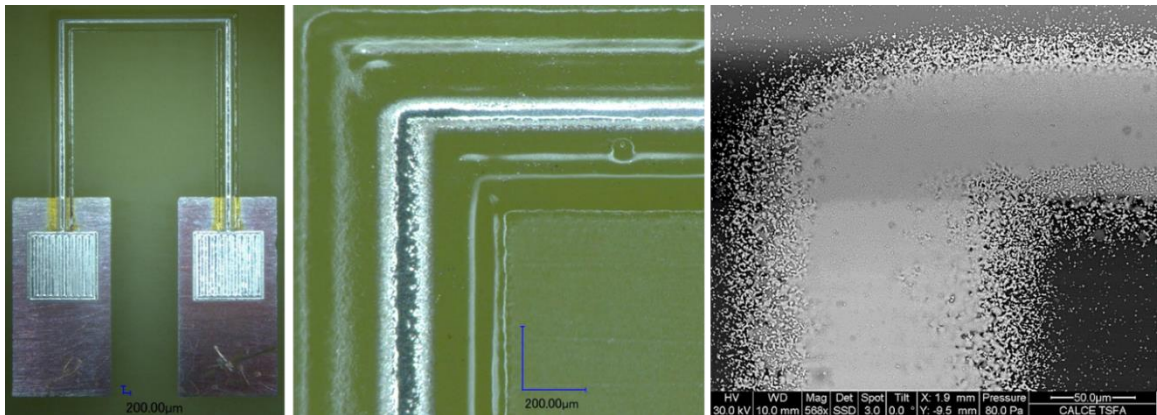


Figure 5.7: Optical and scanning electron microscope images for a Board 2 structure.

At aforementioned intervals, the appropriate test coupon board is removed from the test chamber for optical inspection to document thermal cycling damage. Then, the board is imaged with SEM as another means of documentation as well as loading the specimen with the e-beam and vacuum environment. Finally, the board is optically imaged again to re-document for any possible e-beam or vacuum damage. For example,

after 100 thermal cycles, Board 5 was pulled from the chamber to undergo SEM exposure. The test coupon board was optically documented before and after SEM exposure and showed no visible damage resulting from the thermal cycling nor the SEM environment (Figure 5.8).

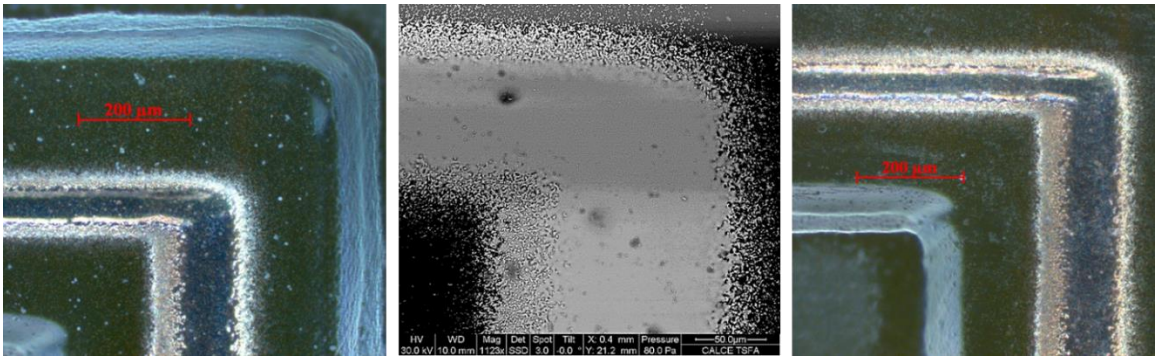


Figure 5.8: a) Optical microscope image after 100 thermal cycles and before SEM exposure, b) SEM image after 100 thermal cycles and first optical microscope documentation, and c) optical microscope image after 100 thermal cycles and after SEM exposure.

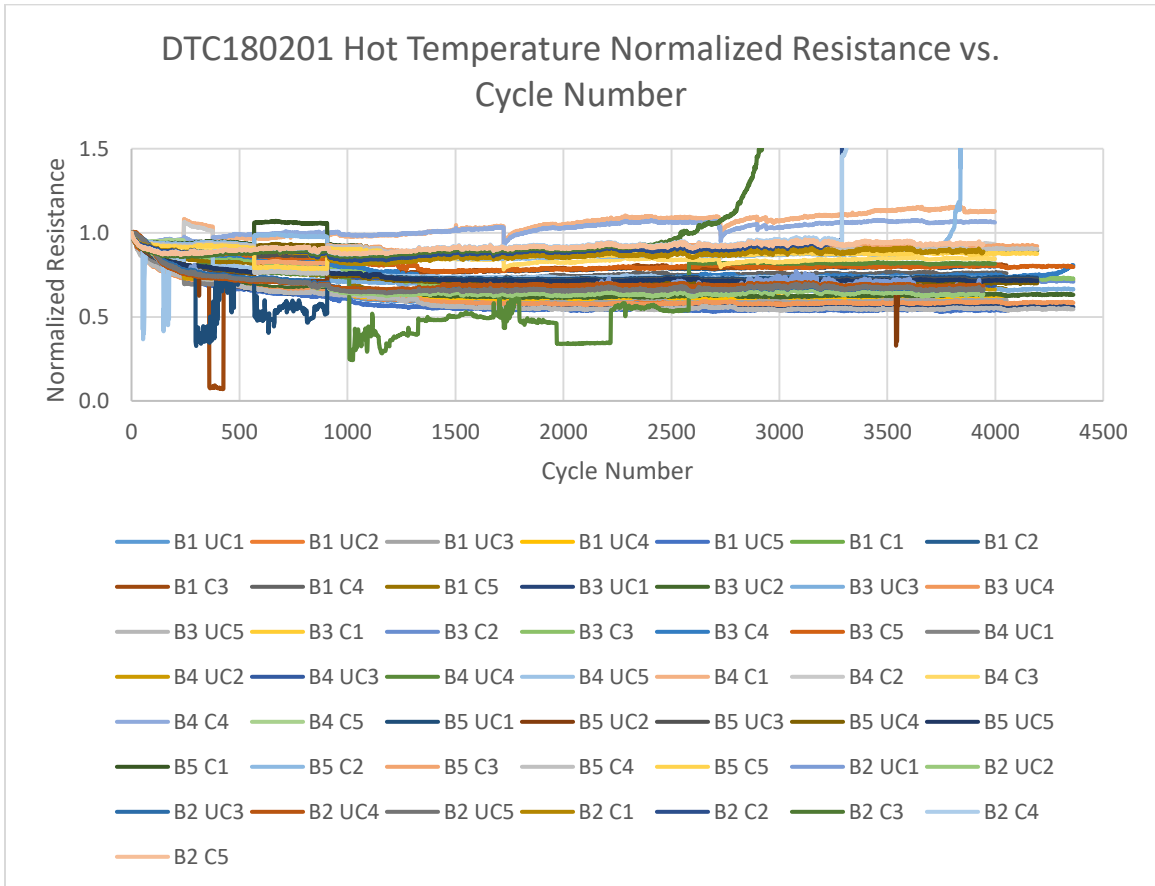
Despite several rounds of SEM exposure as summarized in Table 5.1, the Ink A test coupons showed little damage to the traces. These results indicate that SEM exposure is not resulting in damage to the AJP Ink A traces with Polymer N adhesion and dielectric layer.

Board No.	1	2	3	4	5
SEM Exposures	7	8	1	8	4

Table 5.1: Summary of number of SEM exposures each test coupon board with Ink A has been subjected to.

A3: DTC180201 Hot and Cold Temperature Normalized Resistance Plots

In Figure 5.9, the hot and cold temperature normalized resistance plots as a function of cycle number are provided for all 50 baseline test structures fabricated with Ink A. These plots compliment the results presented in Section 2.3.1.



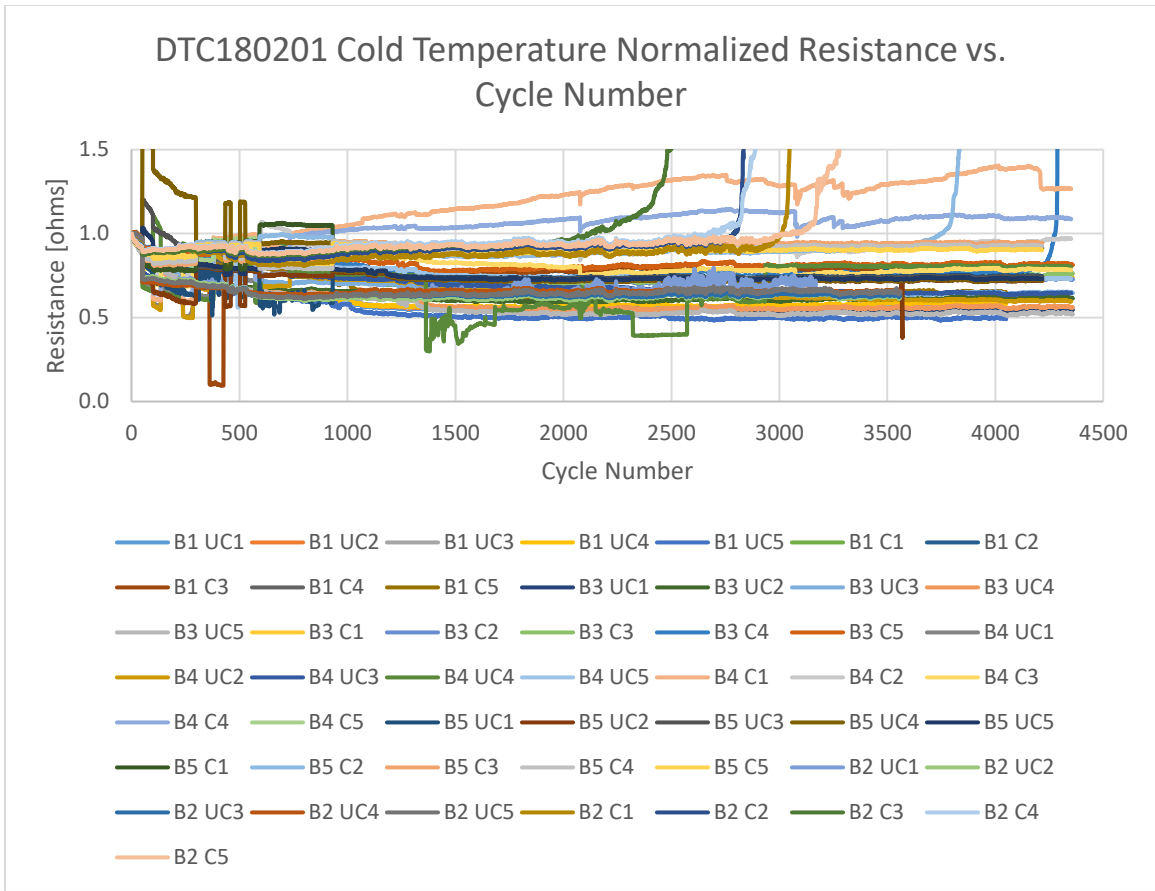
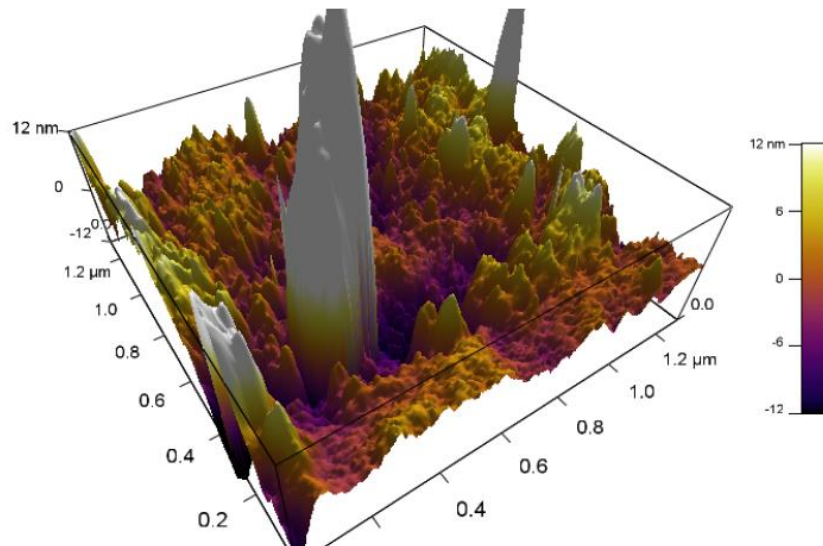
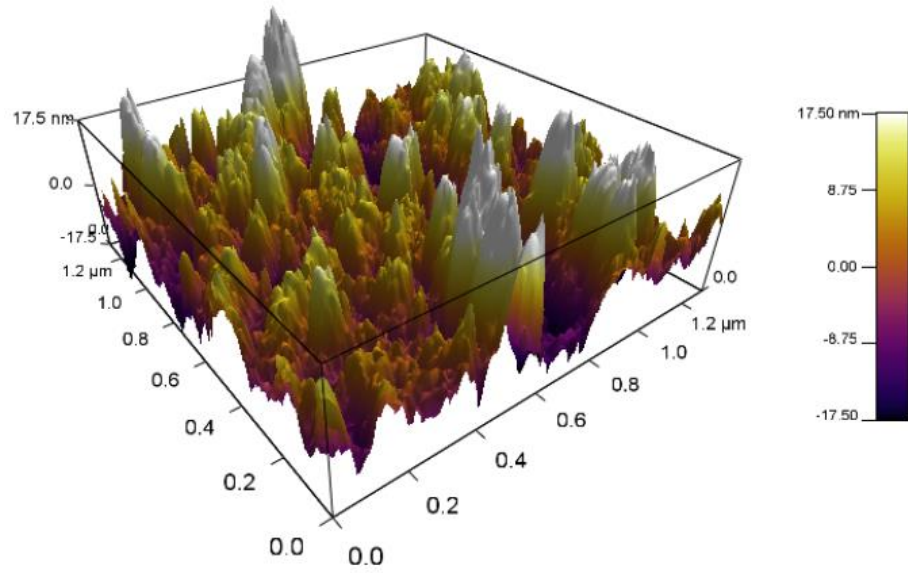
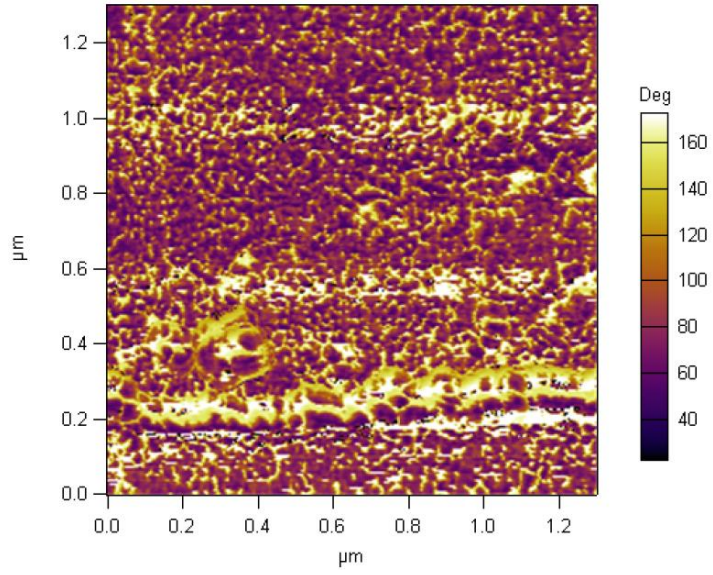


Figure 5.9: Normalized resistance of all DTC180201 structures at the a) hot and b) cold temperature dwells as a function of cycle number.

A4: Atomic Force Microscopy (AFM) Results

As a method to potentially quantify the visible bulk porosity discussed in Section 2.1.3, the team utilized AFM to characterize the cross-section topology of the IoF171101 and DTC180201. The AFM consists of a small cantilever beam with a sharp tip, also known as a probe, on the end that scans the surface of the specimen. The tip radius of curvature is on the order of nanometers and when it is brought into proximity of a sample, either through static (contact) or dynamic (non-contact or tapping) mode, the forces generated deflects the cantilever based on Hooke's law. In addition to using both static and dynamic mode to map the cross-section topology, a phase plot, only possible through dynamic mode, was generated to differentiate the various materials (Figure 5.10). In the phase plots presented, the purple area represents the silver trace, while the yellow area represents the epoxy resin that the sample was potted in for grinding and polishing purposes. This is known because a lower phase represents a stiffer material.





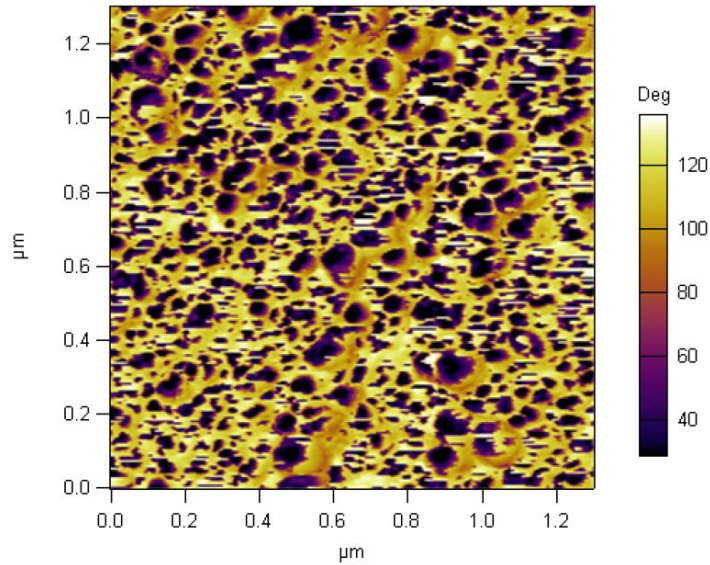


Figure 5.10: a) surface topology and b) phase plot of IoF171101 as well as c) surface topology and d) phase plot of DTC180201.

A modified fast Fourier transform was conducted on portions of the surface topology plot to see if there were any peaks in the IoF171101 history relative to the DTC180201 history that could be indicative of porosity. Such attempts were not fruitful as there was no high frequency corresponding to porosity size where the IoF171101 had a statistically significant higher magnitude than the DTC180201 (Figure 5.11). It is believed that the cross-section topology being captured by the AFM is telling the story of the level of grinding and polishing of the epoxy potted sample instead of any surface roughness as a result of varying levels of porosity.

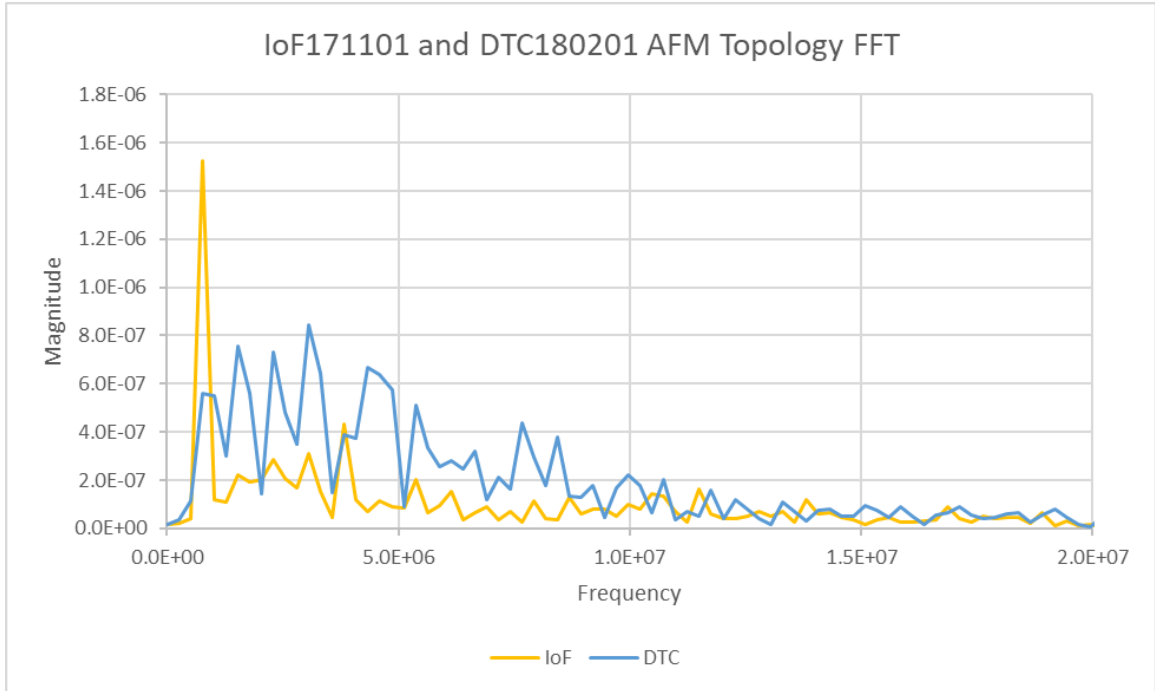


Figure 5.11: Fast Fourier transform comparison between IoF171101 and DTC180201 line roughness profiles generated by AFM.

A5: Laser Profilometry Results of Cross-Sectioned Samples

A commercial confocal microscope was used to conduct laser profilometry on the cross-sectioned IoF171101 and DTC180201 potted samples. Surface and line topology plots were generated similarly to the AFM results presented in Appendix A4 (Figure 5.12).

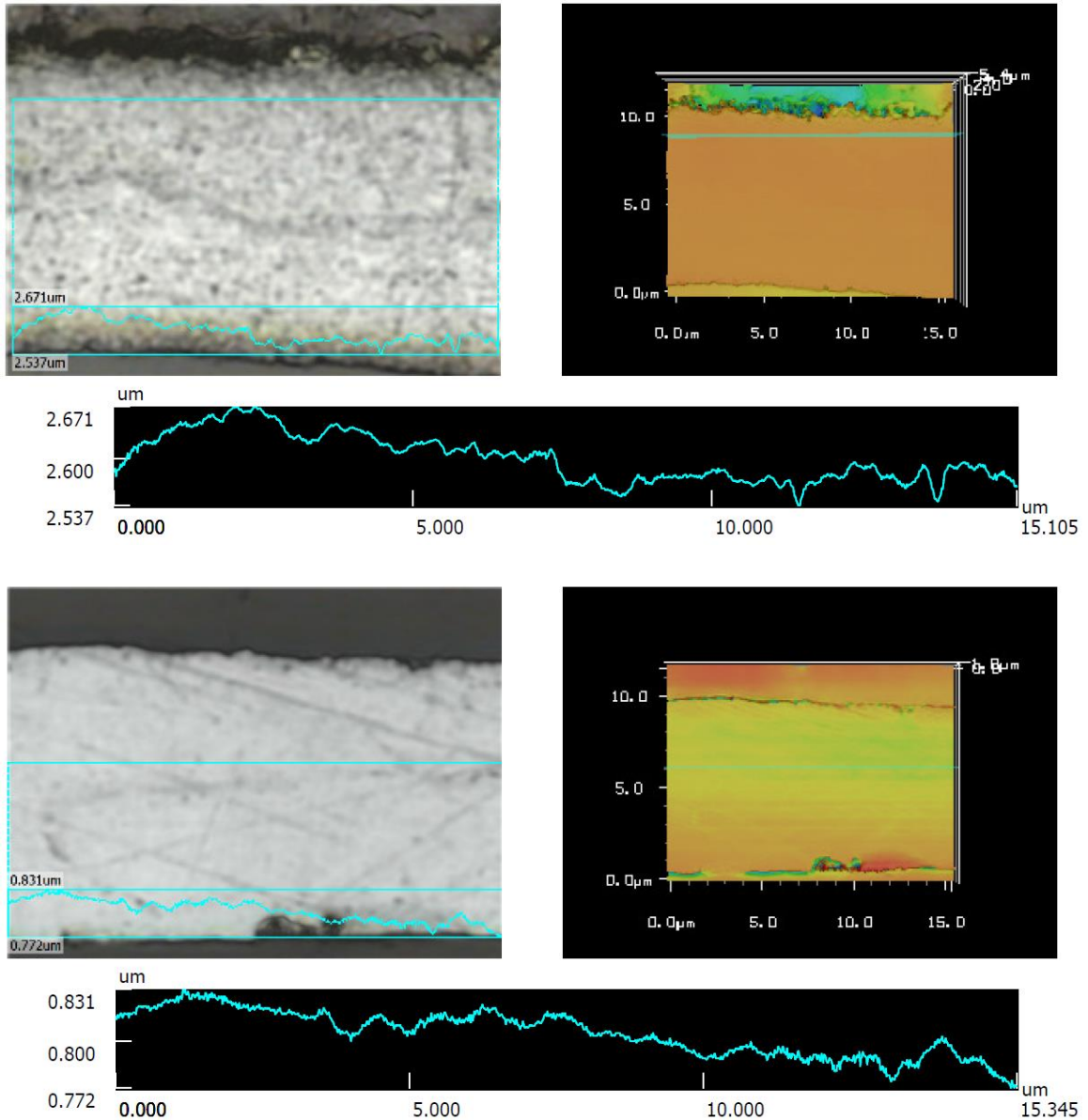


Figure 5.12: Example of line roughness plots generated for a) IoF171101 and b) DTC180201.

Again, similarly to AFM, the results generated from the modified fast Fourier transform did not correlate to identifying porosity features (Figure 5.13). Based on these results as well as those gathered from AFM, topology type analyses were not continued as a method to quantify porosity in the Ink A serpentine traces printed at varying gas flow rates.

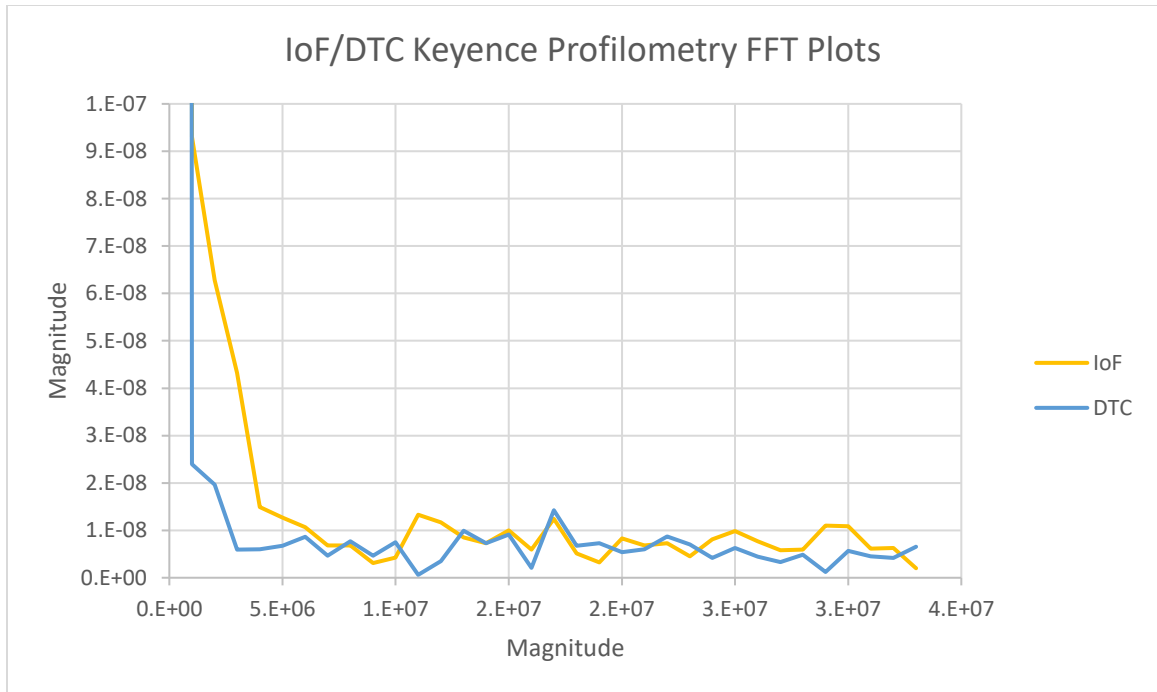


Figure 5.13: Fast Fourier transform comparison between IoF171101 and DTC180201 line roughness profiles generated by laser profilometry.

A6: Image Processing Methodology

A commercial image processing software was used to quantify the particle agglomeration size and spacing distribution of printed traces on the surface and in the bulk. A SEM image of the region of interest at 50,000x magnification with file extension of .tiff was uploaded to the software (Figure 5.14). Using the smart segmentation feature available in the software, a region where an agglomerate is seen is selected as an object of interest in blue and what is not of interest is selected as background in yellow (Figure 5.15). All of the agglomerations counted by the software in Figure 5.14 are highlighted in blue and green in Figure 5.16. The distinction between the two colors of agglomerations is an example of the threshold capability of the software to distinguish agglomerations with areas larger or smaller than any amount. From these features that are counted, the area, diameter, and many other characteristics can be quantified by the software. To quantify the spacing of one agglomeration to the next closest agglomeration, a Voronoi diagram can be generated and the center-to-center minimum distance can be extracted (Figure 5.17). In the examples provided in this section, the objects of interest are agglomerations, but a similar methodology can be followed if the object of interest is porosity in which case voids would be circled in blue and the background would be the in-plane silver ink trace.

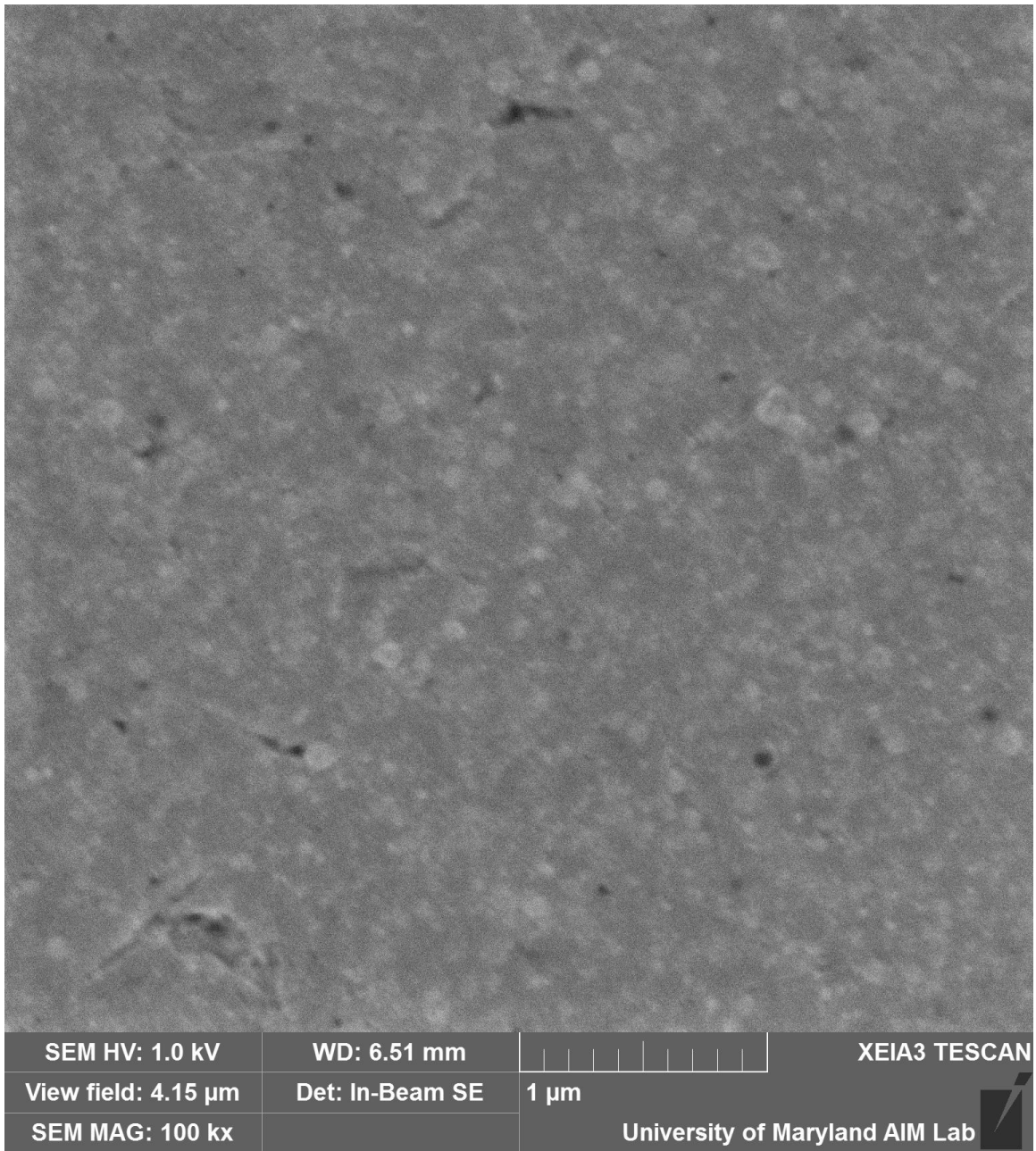


Figure 5.14: Example of original SEM image uploaded to software.

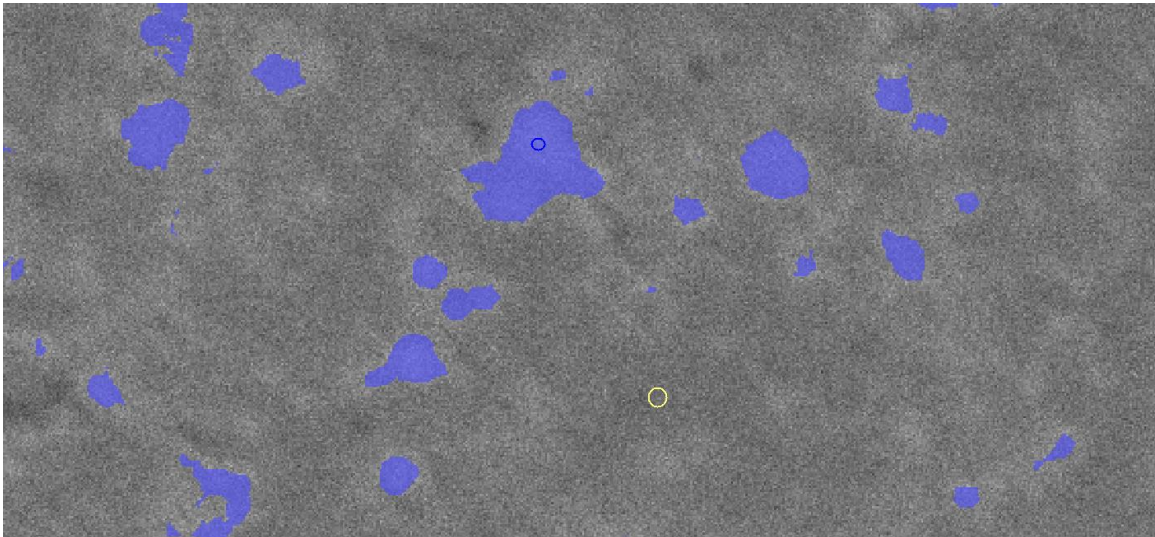
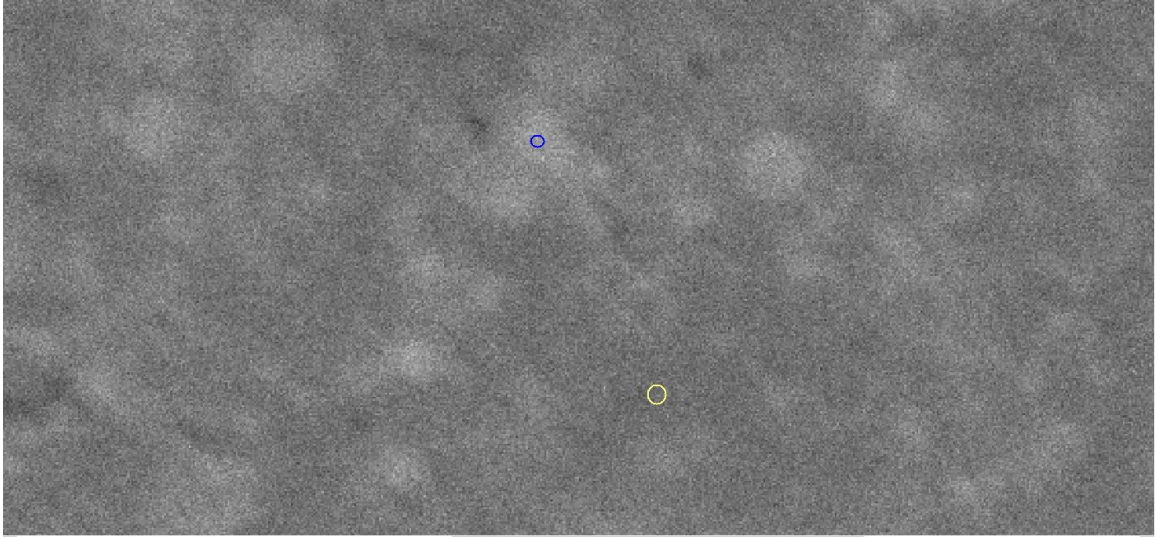


Figure 5.15: Example of agglomerations counted by software a) without and b) with shading over the counted objects.

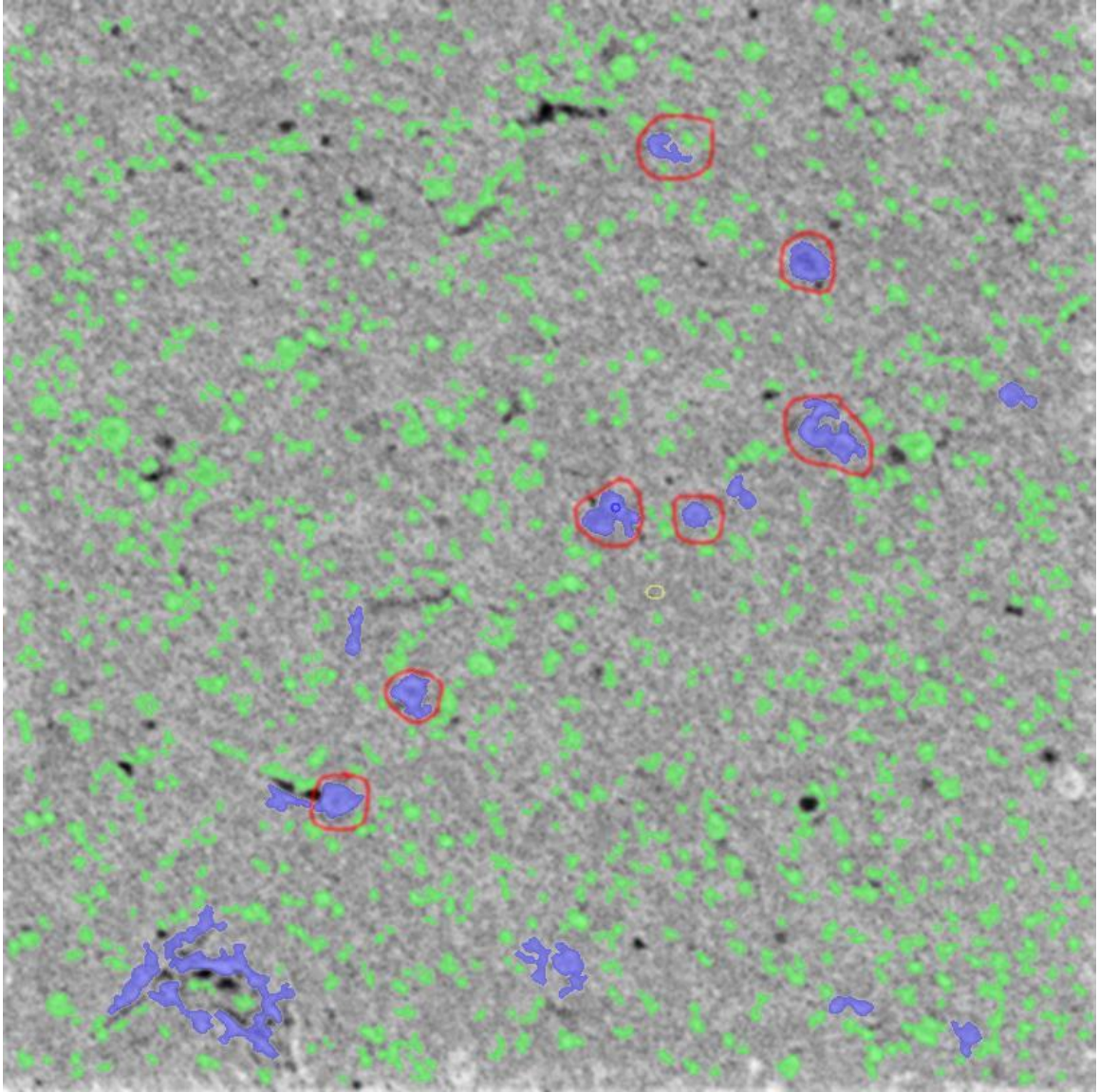


Figure 5.16: Example of all agglomerations counted and highlighted.

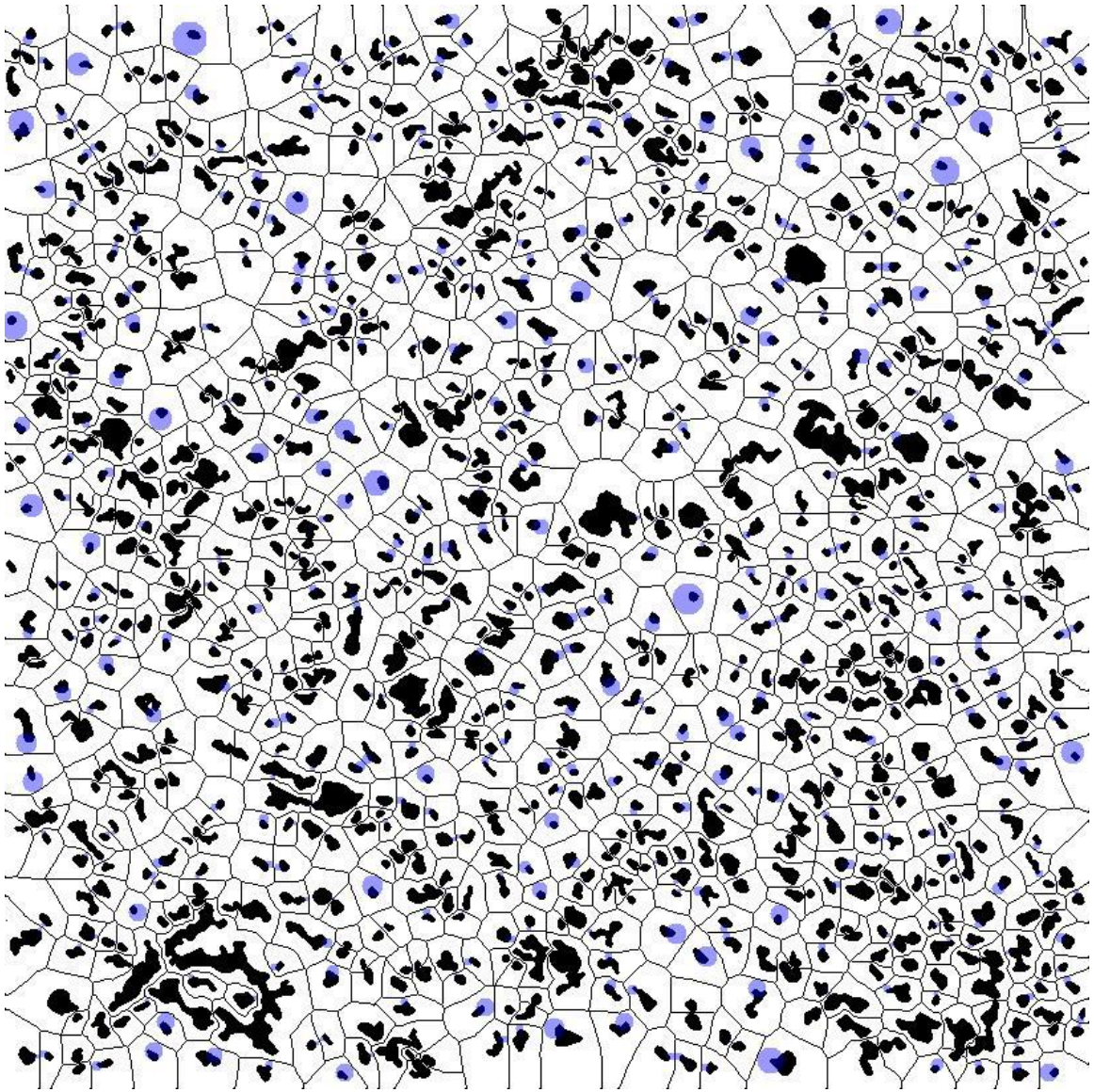


Figure 5.17: Example of Voronoi diagram to quantify agglomerations spacing distribution.

A7: Additional Micromorphology Image Processing Results

Several different manners to see if agglomeration size and spacing is correlated to gas flow rates are presented in full below after being discussed in brief in Section 3.3.5.

A7.1: Number of Agglomerations as a Function of Flow Rate

This section includes the number of features that the image processing software counted as an agglomerate through its smart segmentation algorithm. The 3D bar charts below plot the number of agglomerates on the z-axis and lays out the 15 different flow rate combinations corresponding to the 15 different serpentine traces printed in the x-y plane. Furthermore, there is a figure distinguishing between single and double-pass traces as well as surface or cross-section images. The data from the 3D bar charts are provided in tabular form and for the flow rate combinations, corners and middle, that there are multiple images processed for, the standard deviation is also provided.

	Carrier = 30	Carrier = 50	Carrier = 65	Carrier = 80	Carrier = 100
Sheath = 30	225±161	145	101	158	64±14
Sheath = 40	345	337	98±27	152	123
Sheath = 50	230±90	210	181	140	83±36

Table 5.2: Number of agglomerations in single-pass trace on the surface.

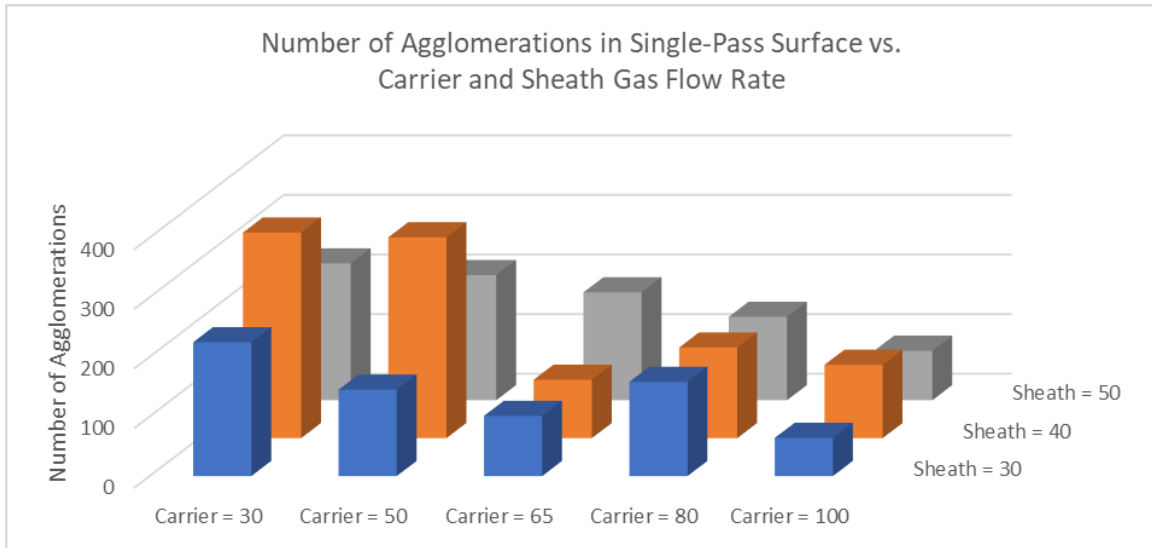


Figure 5.18: Number of agglomerations in single-pass trace on the surface as a function of carrier and sheath gas flow rate.

	Carrier = 30	Carrier = 50	Carrier = 65	Carrier = 80	Carrier = 100
Sheath = 30	100±29	211	125	81	116±89
Sheath = 40	260	185	90±49	126	62
Sheath = 50	105±41	103	74	85	190±78

Table 5.3: Number of agglomerations in double-pass trace on the surface.

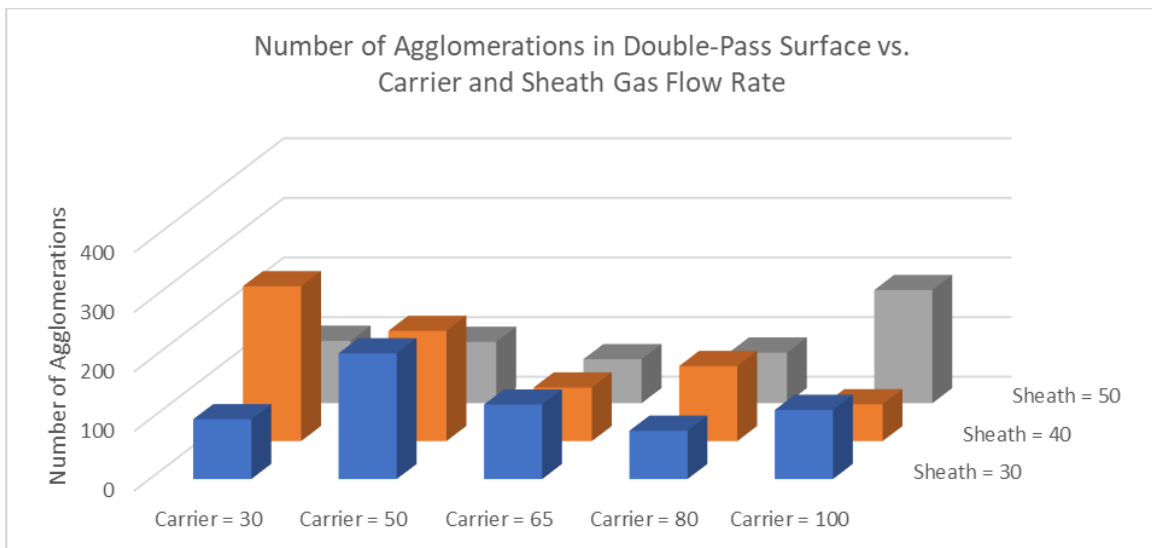


Figure 5.19: Number of agglomerations in double-pass trace on the surface as a function of carrier and sheath gas flow rate.

	Carrier = 30	Carrier = 50	Carrier = 65	Carrier = 80	Carrier = 100
Sheath = 30	348±197	313	425	272	277±243
Sheath = 40	426	370	1875±795	243	1106
Sheath = 50	386±174	560	1284	554	141±101

Table 5.4: Number of agglomerations in single-pass trace in the bulk.

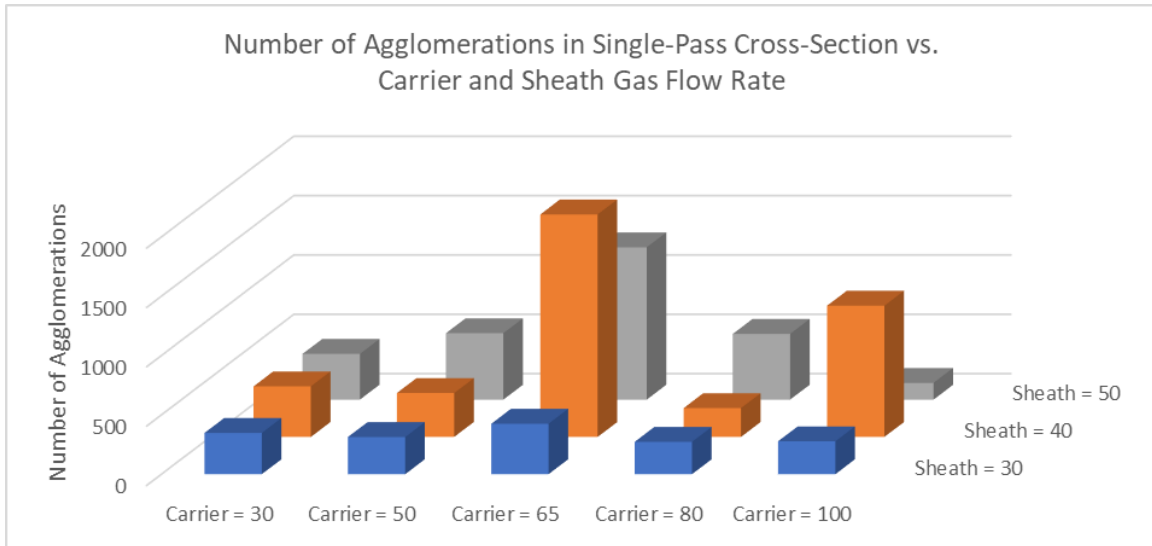


Figure 5.20: Number of agglomerations in single-pass trace in the bulk as a function of carrier and sheath gas flow rate.

	Carrier = 30	Carrier = 50	Carrier = 65	Carrier = 80	Carrier = 100
Sheath = 30	754±260	332	651	541	225±323
Sheath = 40	644	332	1625±1026	485	1241
Sheath = 50	306±183	368	485	631	603±134

Table 5.5: Number of agglomerations in double-pass trace in the bulk.

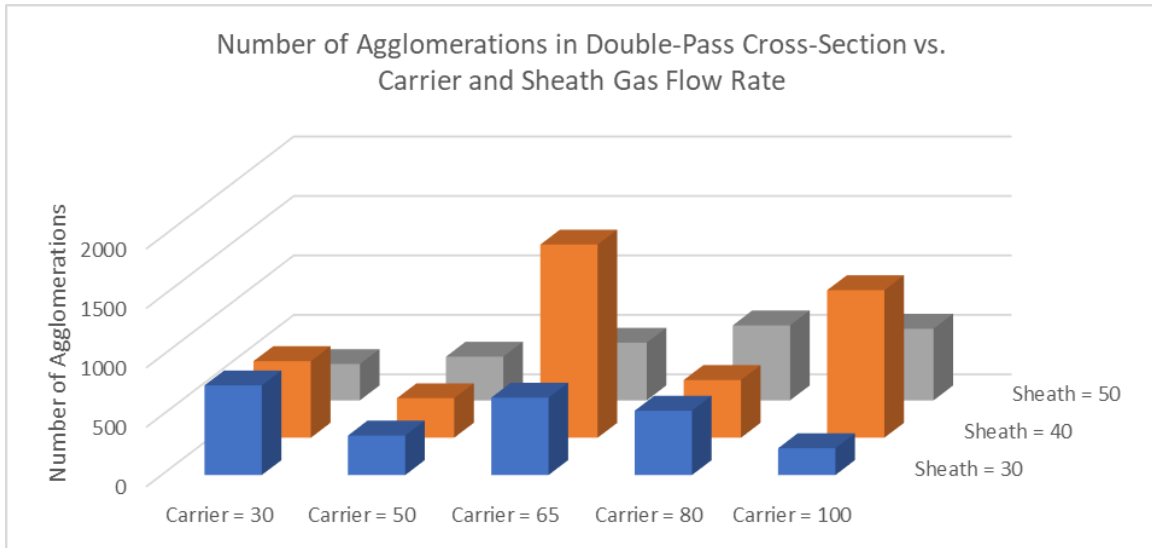


Figure 5.21: Number of agglomerations in double-pass trace in the bulk as a function of carrier and sheath gas flow rate.

A7.2: Percent Area of Agglomerations as a Function of Flow Rate

This section includes the percent area the agglomerations counted take up on the raw image that is fed into the image processing software. The 3D bar charts below plot the percent area out of 100 on the z-axis and lays out the 15 different flow rate combinations corresponding to the 15 different serpentine traces printed in the x-y plane. Furthermore, there is a figure distinguishing between single and double-pass traces as well as surface or cross-section images. The data from the 3D bar charts are provided in tabular form and for the flow rate combinations, corners and middle, that there are multiple images processed for, the standard deviation is also provided.

	Carrier = 30	Carrier = 50	Carrier = 65	Carrier = 80	Carrier = 100
Sheath = 30	13.54±4.05	15.83	25.64	27.29	21.64±3.12
Sheath = 40	9.89	15.62	20.96±1.33	17.03	25.85
Sheath = 50	15.69±2.16	24.70	19.97	29.92	21.02±7.27

Table 5.6: Agglomeration percent area in single-pass trace on the surface.

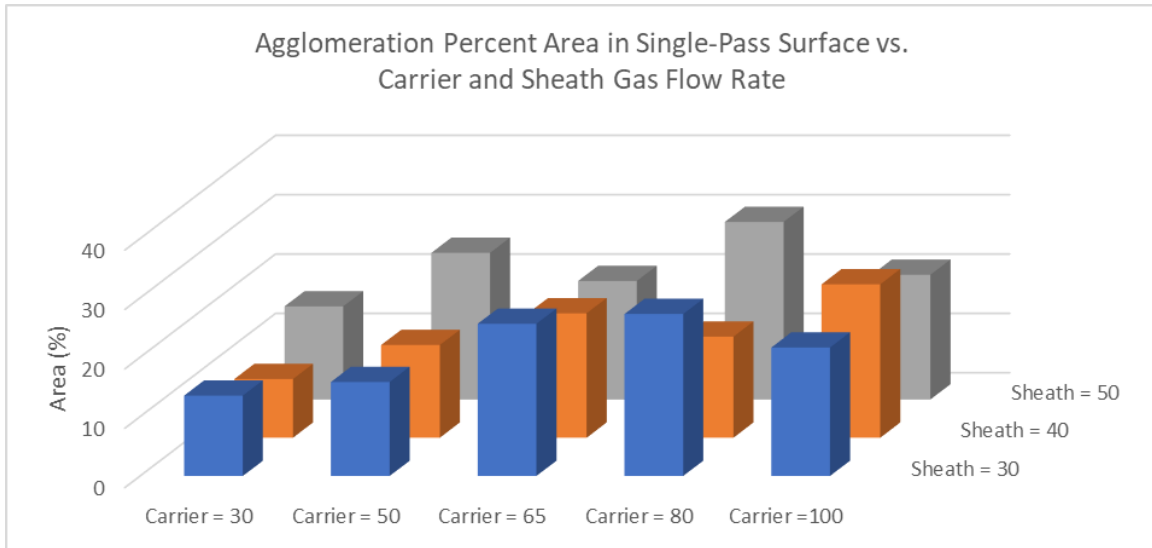


Figure 5.22: Agglomeration percent area in single-pass trace on the surface as a function of carrier and sheath gas flow rate.

	Carrier = 30	Carrier = 50	Carrier = 65	Carrier = 80	Carrier = 100
Sheath = 30	13.67±3.69	24.99	22.05	16.04	14.70±9.39
Sheath = 40	19.92	33.25	24.02±5.78	17.12	22.78
Sheath = 50	14.45±4.33	11.08	19.54	16.09	16.40±8.01

Table 5.7: Agglomeration percent area in double-pass trace on the surface.

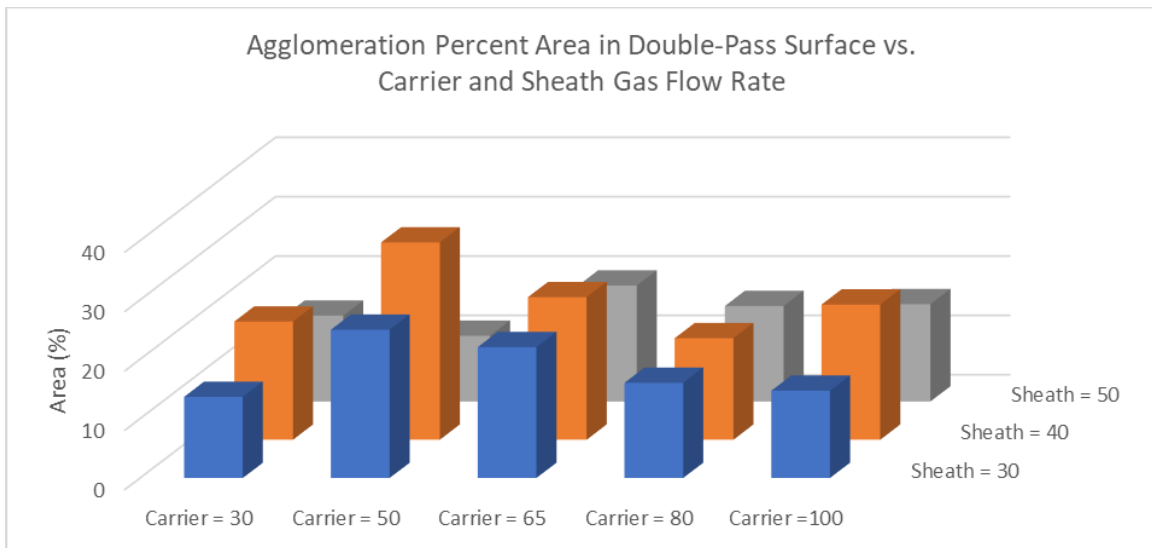


Figure 5.23: Agglomeration percent area in double-pass trace on the surface as a function of carrier and sheath gas flow rate.

	Carrier = 30	Carrier = 50	Carrier = 65	Carrier = 80	Carrier = 100
Sheath = 30	8.87±4.13	9.01	9.42	0.84	20.69±13.58
Sheath = 40	6.50	16.55	24.61±7.48	12.33	32.14
Sheath = 50	5.02±3.34	9.61	30.17	4.50	0.62±0.53

Table 5.8: Agglomeration percent area in single-pass trace in the bulk.

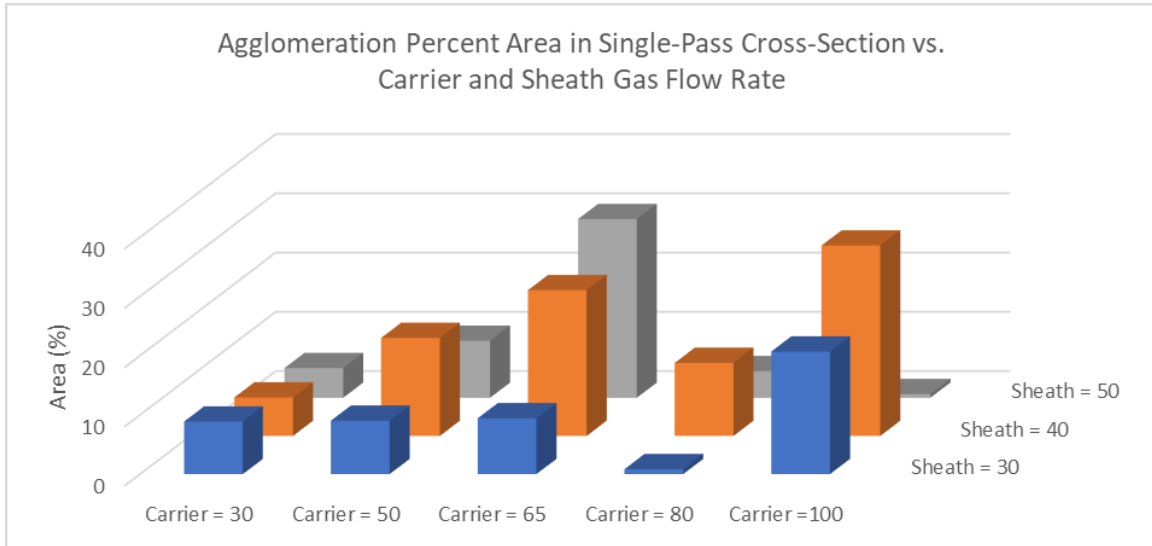


Figure 5.24: Agglomeration percent area in single-pass trace in the bulk as a function of carrier and sheath gas flow rate.

	Carrier = 30	Carrier = 50	Carrier = 65	Carrier = 80	Carrier = 100
Sheath = 30	9.70±4.06	14.18	39.86	14.13	1.97±3.53
Sheath = 40	3.50	5.05	17.66±8.46	23.70	3.10
Sheath = 50	1.46±1.13	23.79	33.31	10.70	14.03±5.98

Table 5.9: Agglomeration percent area in double-pass trace in the bulk.

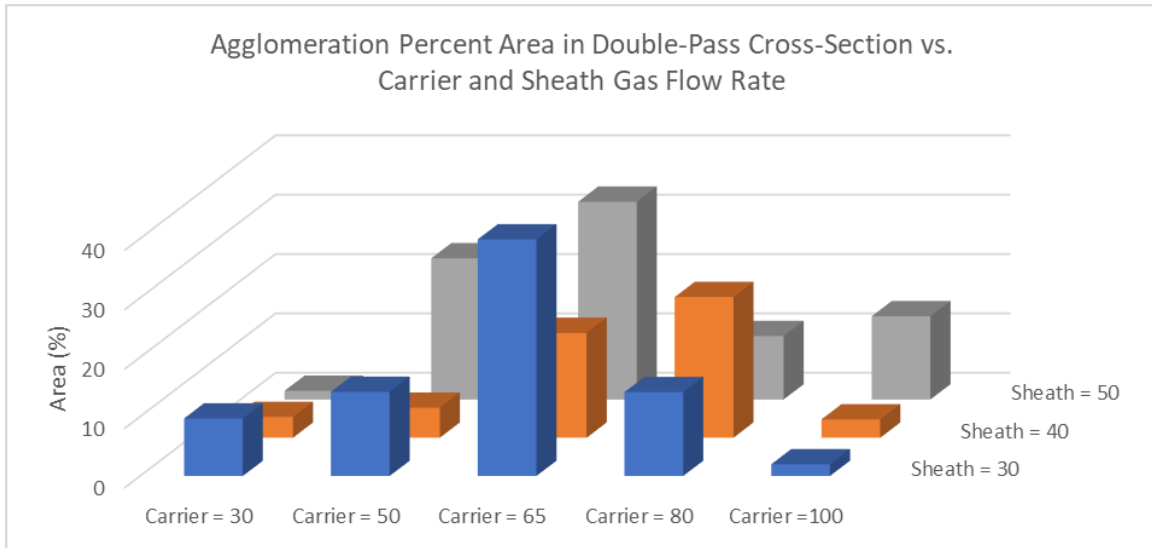


Figure 5.25: Agglomeration percent area in double-pass trace in the bulk as a function of carrier and sheath gas flow rate.

A7.3: Agglomerate Size and Spacing Histograms

For the four corner and middle flow rate combinations ($C = 30, S = 30$; $C = 30, S = 50$; $C = 65, S = 40$; $C = 100, S = 30$; $C = 100, S = 50$), five images were post-processed for single and double-pass as well as surface and cross-section cases. The size and spacing distributions for each image was normalized before averaging across the five images to avoid one image from dominating if there was an unusually high number of agglomerates counted by the image processing software. The size and spacing distributions were then fit to a histogram with log-scale bins, to deal with the highly right skewed nature of the data. The five flow rate combinations were grouped in threes for the histograms in terms of major ($C = 30, S = 30$; $C = 65, S = 40$; $C = 100, S = 50$) and minor ($C = 30, S = 50$; $C = 65, S = 40$; $C = 100, S = 30$) diagonals. Histograms are provided in this section for major and minor diagonal cases, single and double-pass, surface and cross-section images, as well as agglomeration size and spacing.

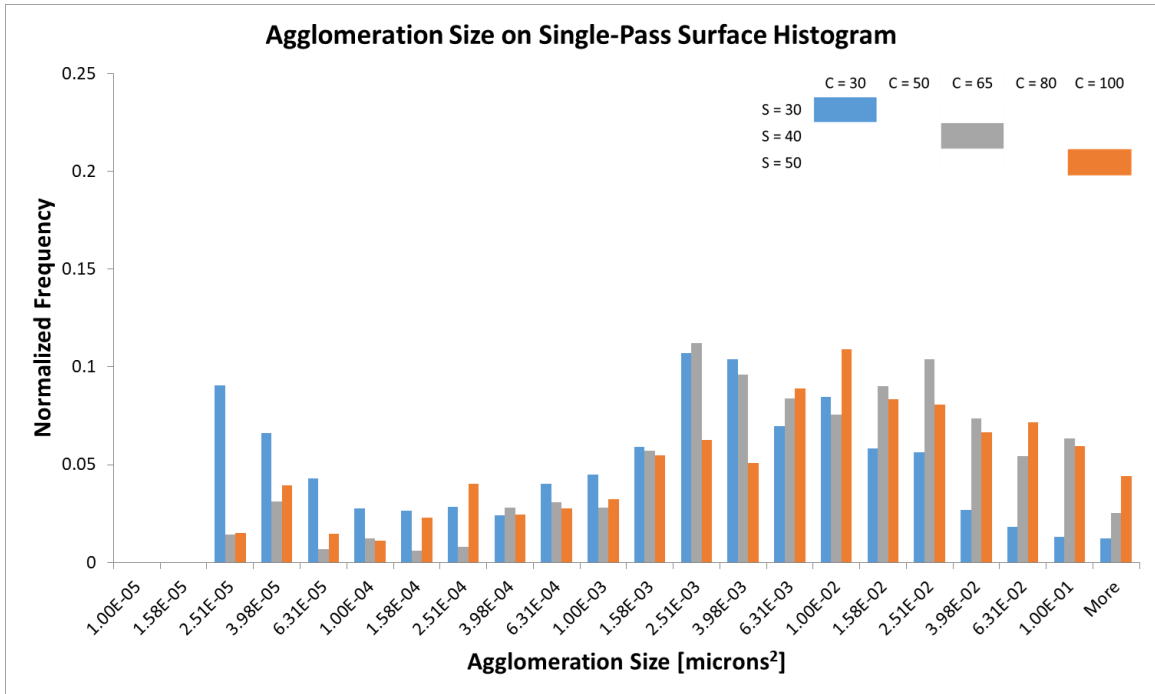


Figure 5.26: Agglomeration size in single-pass trace on the surface for major diagonal cases.

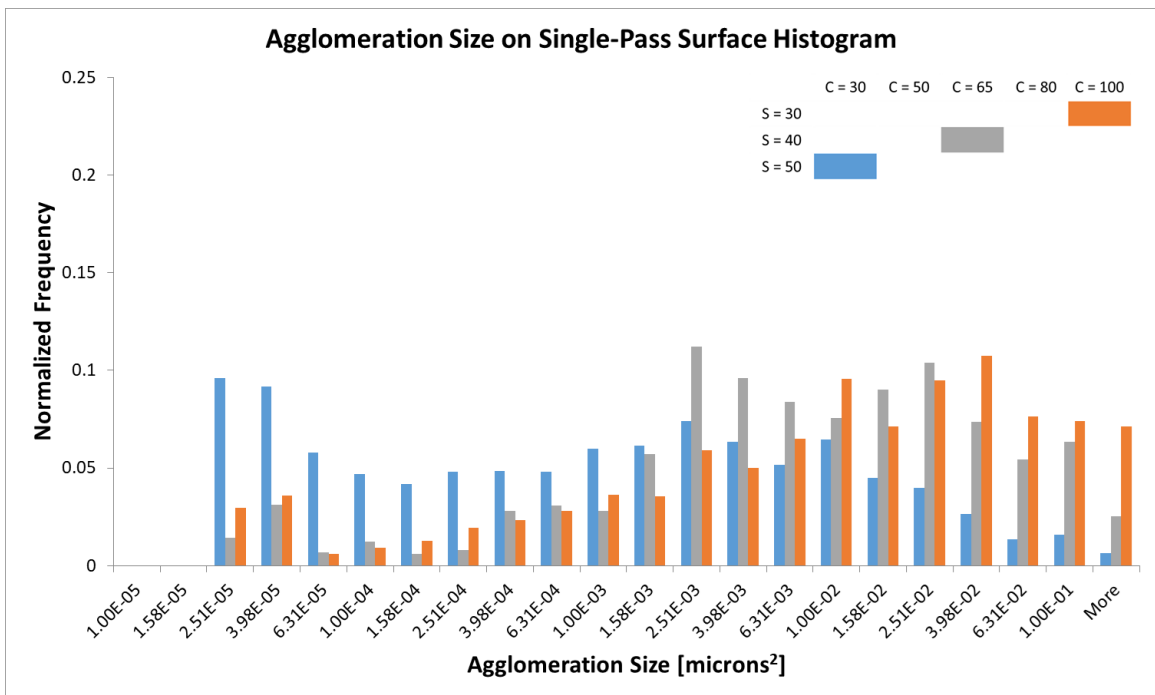


Figure 5.27: Agglomeration size in single-pass trace on the surface for minor diagonal cases.

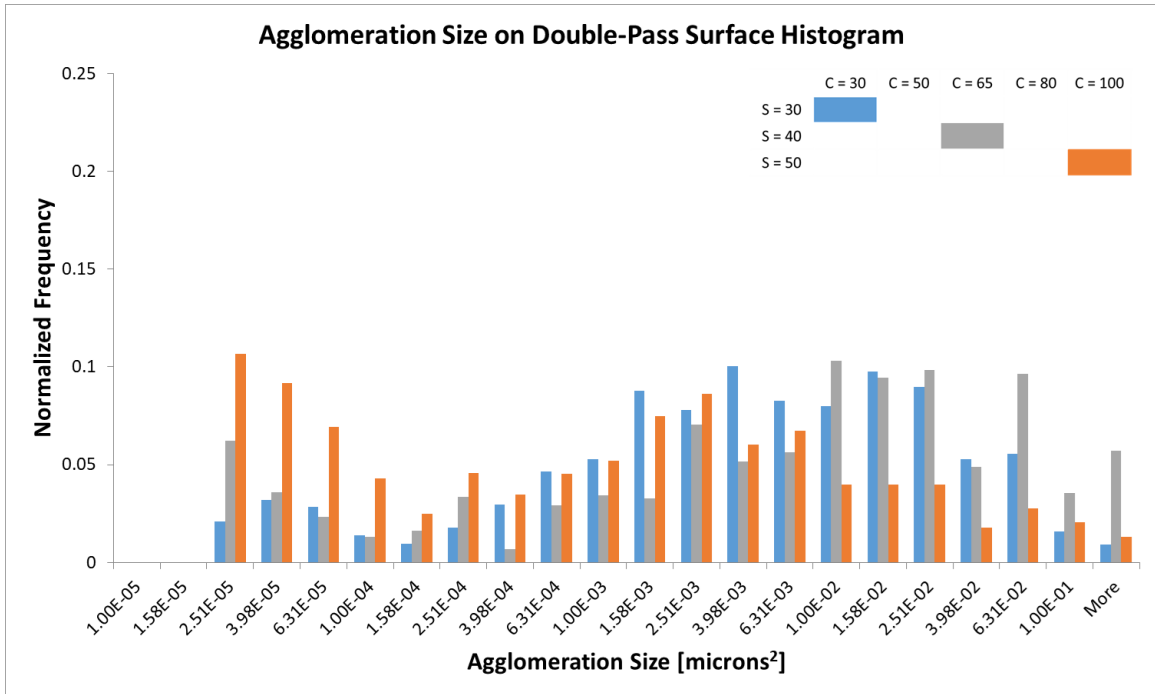


Figure 5.28: Agglomeration size in double-pass trace on the surface for major diagonal cases.

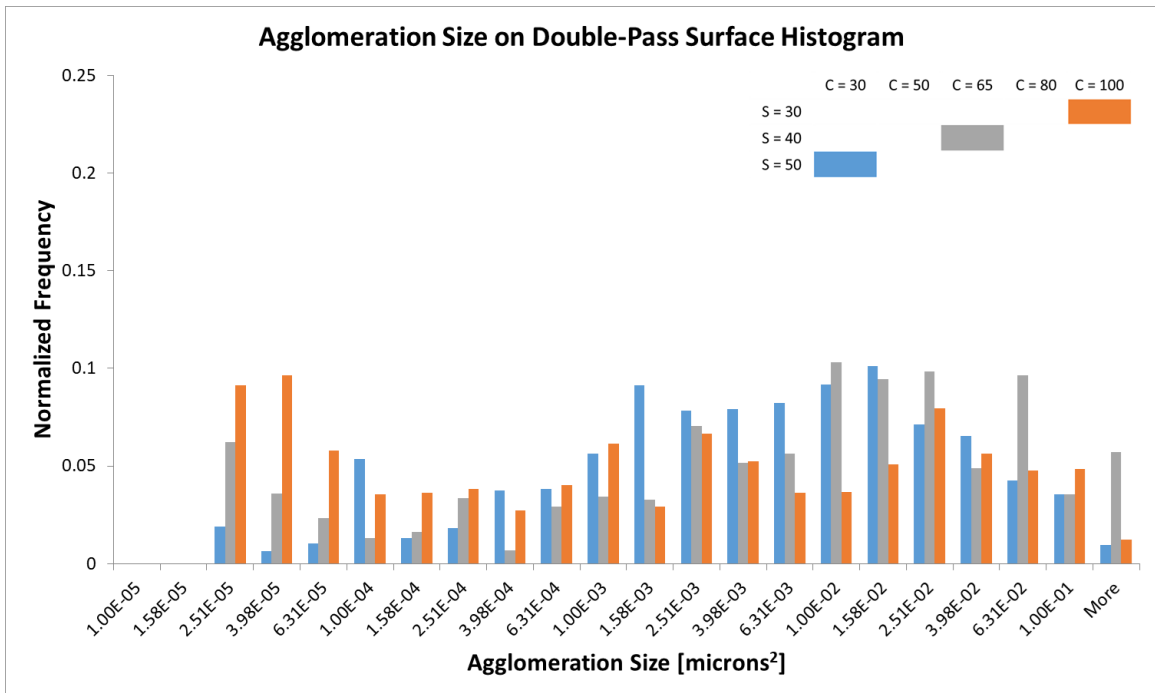


Figure 5.29: Agglomeration size in double-pass trace on the surface for minor diagonal cases.

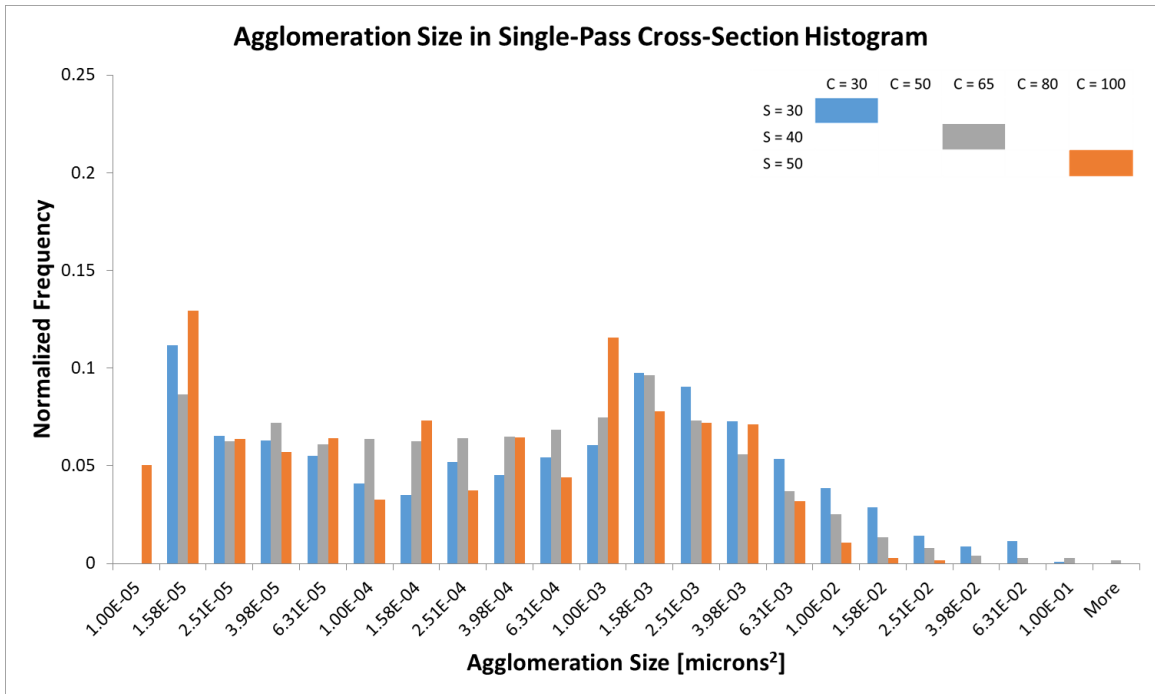


Figure 5.30: Agglomeration size in single-pass trace in the bulk for major diagonal cases.

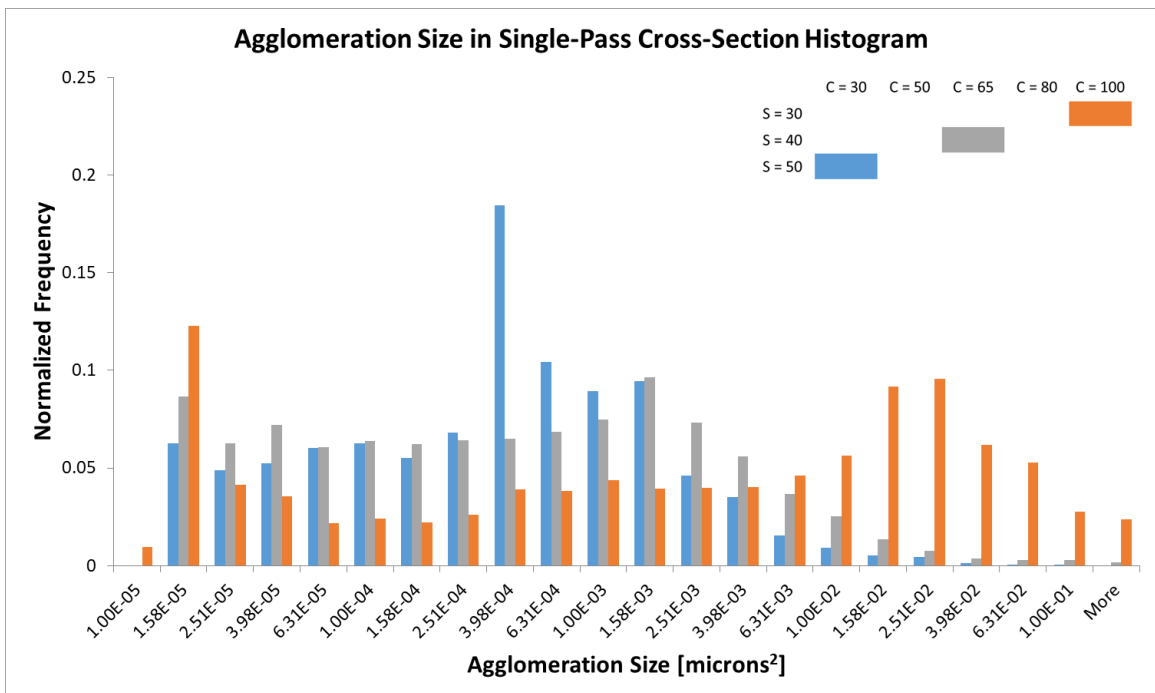


Figure 5.31: Agglomeration size in single-pass trace in the bulk for minor diagonal cases.

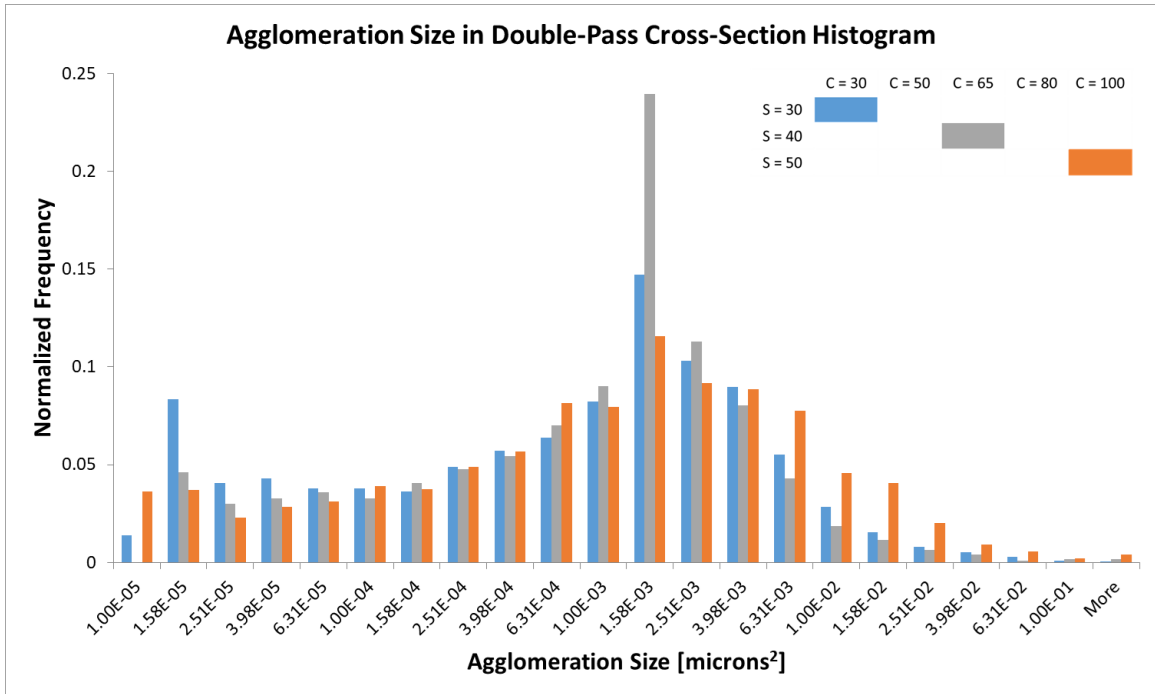


Figure 5.32: Agglomeration size in double-pass trace in the bulk for major diagonal cases.

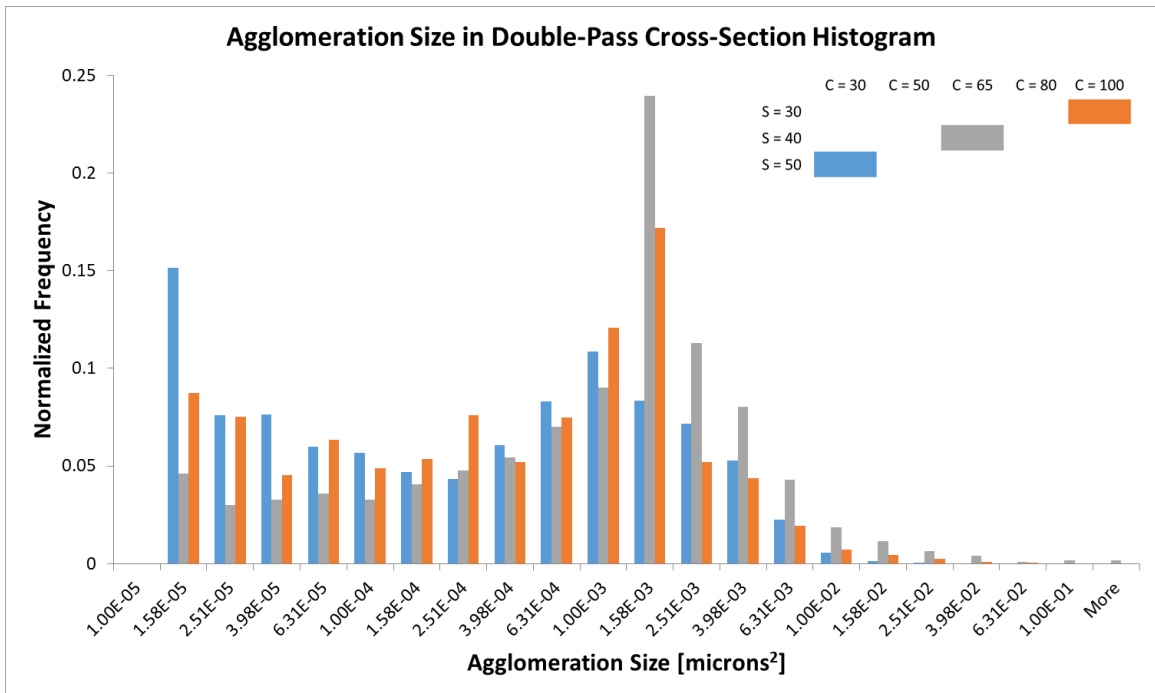


Figure 5.33: Agglomeration size in double-pass trace in the bulk for minor diagonal cases.

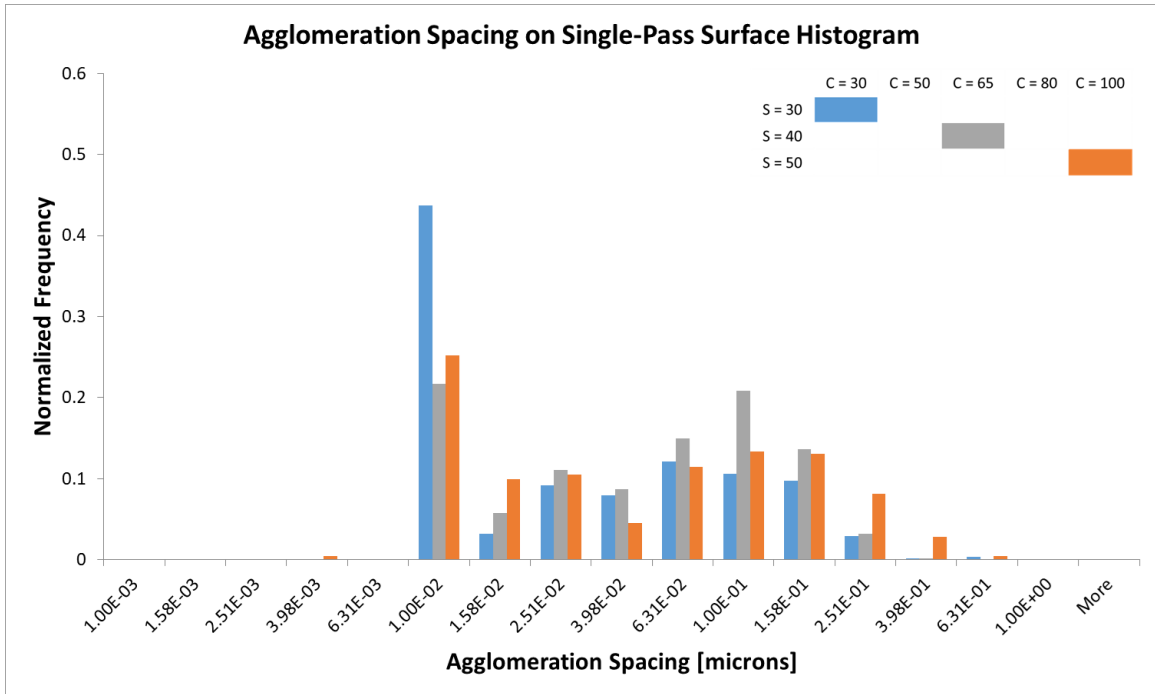


Figure 5.34: Agglomerate spacing in single-pass trace on the surface for major diagonal cases.

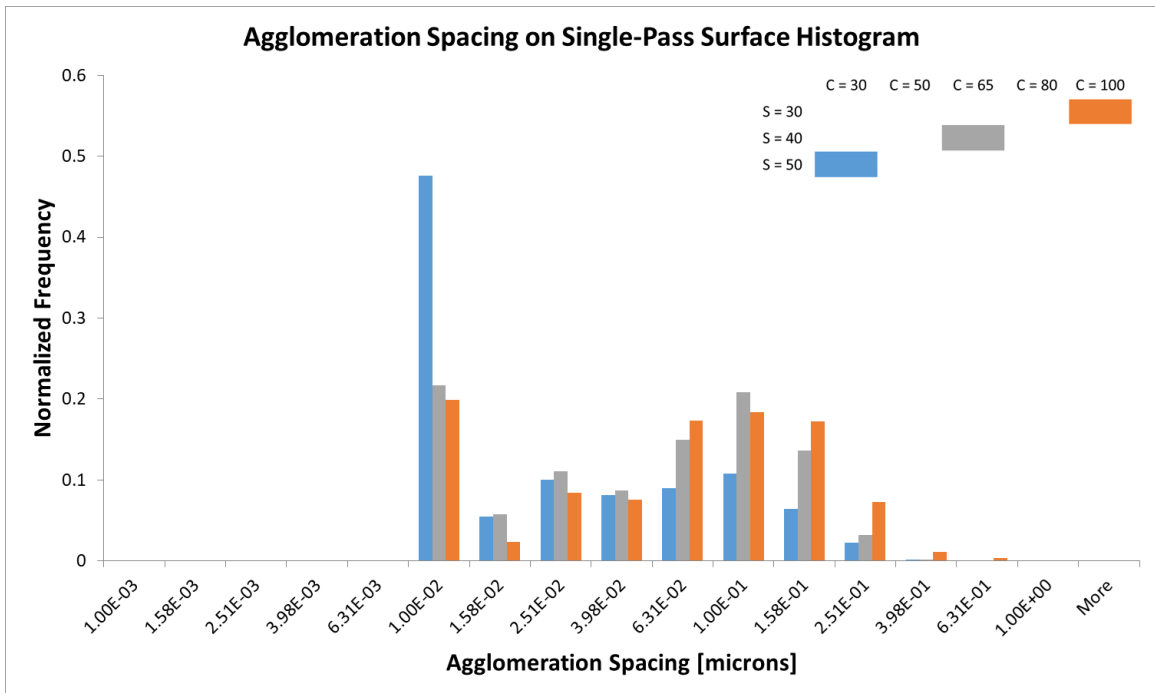


Figure 5.35: Agglomerate spacing in single-pass trace on the surface for minor diagonal cases.

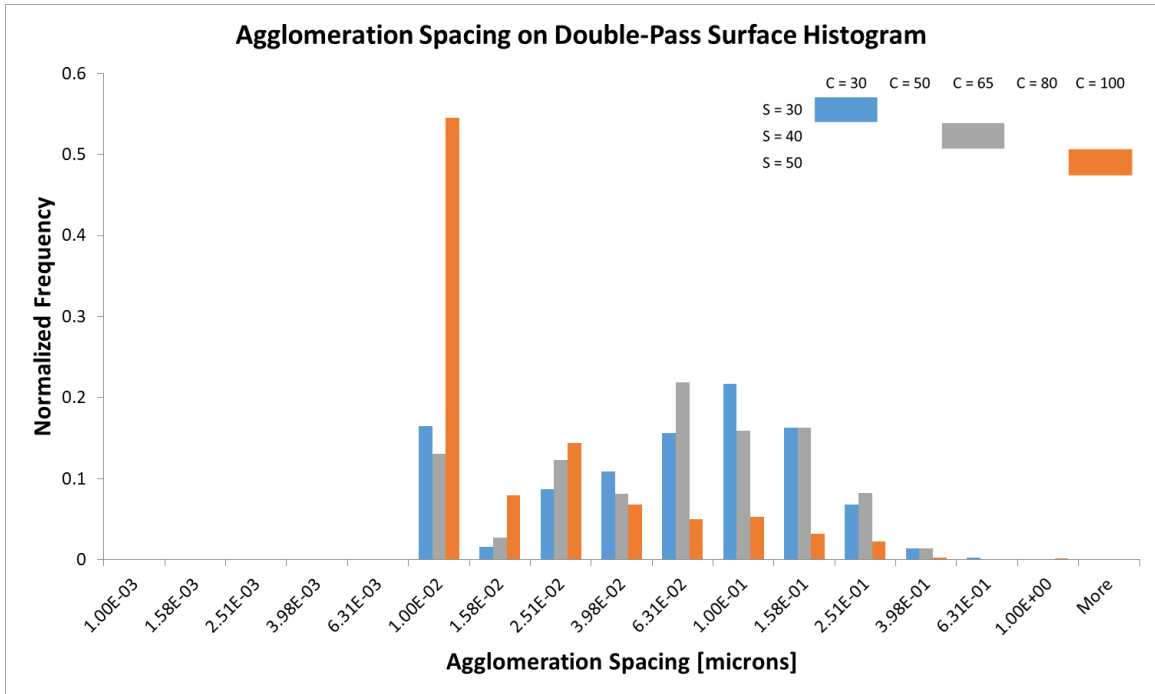


Figure 5.36: Agglomerate spacing in double-pass trace on the surface for major diagonal cases.

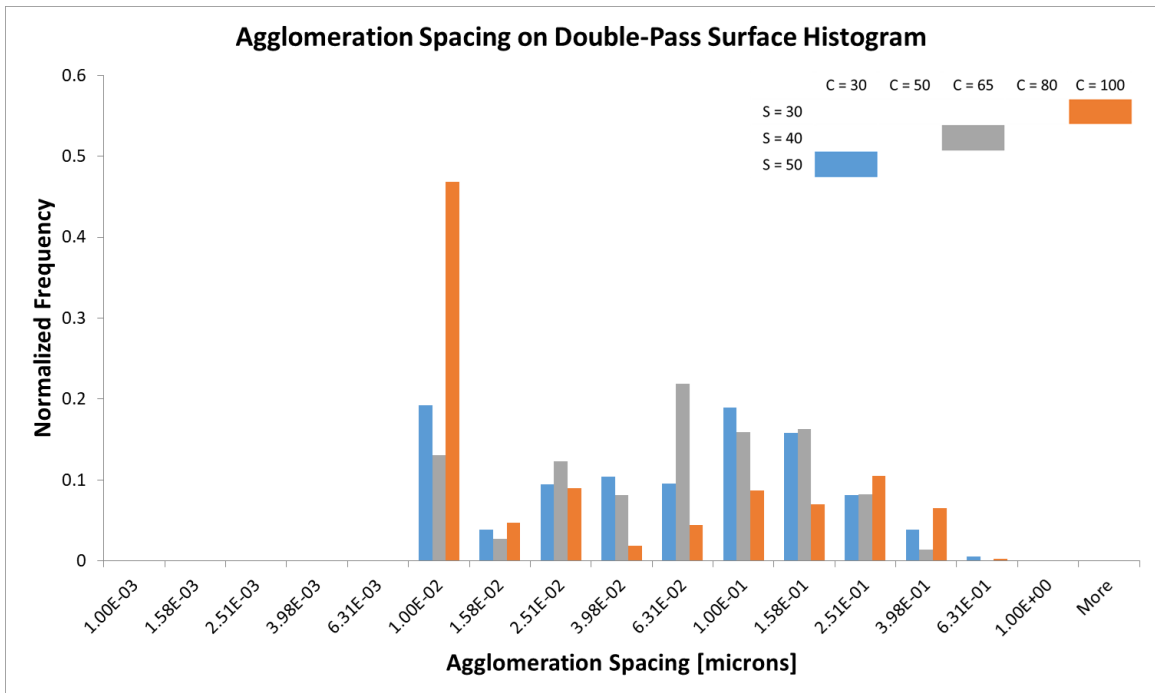


Figure 5.37: Agglomerate spacing in double-pass trace on the surface for minor diagonal cases.

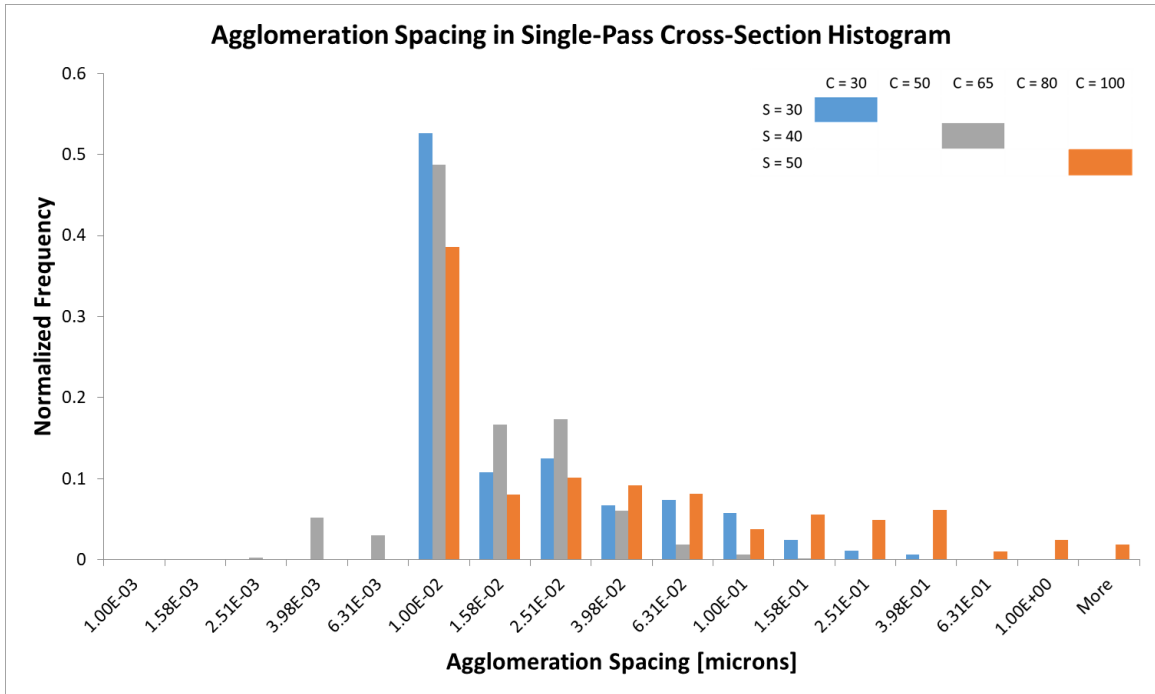


Figure 5.38: Agglomerate spacing in single-pass trace in the bulk for major diagonal cases.

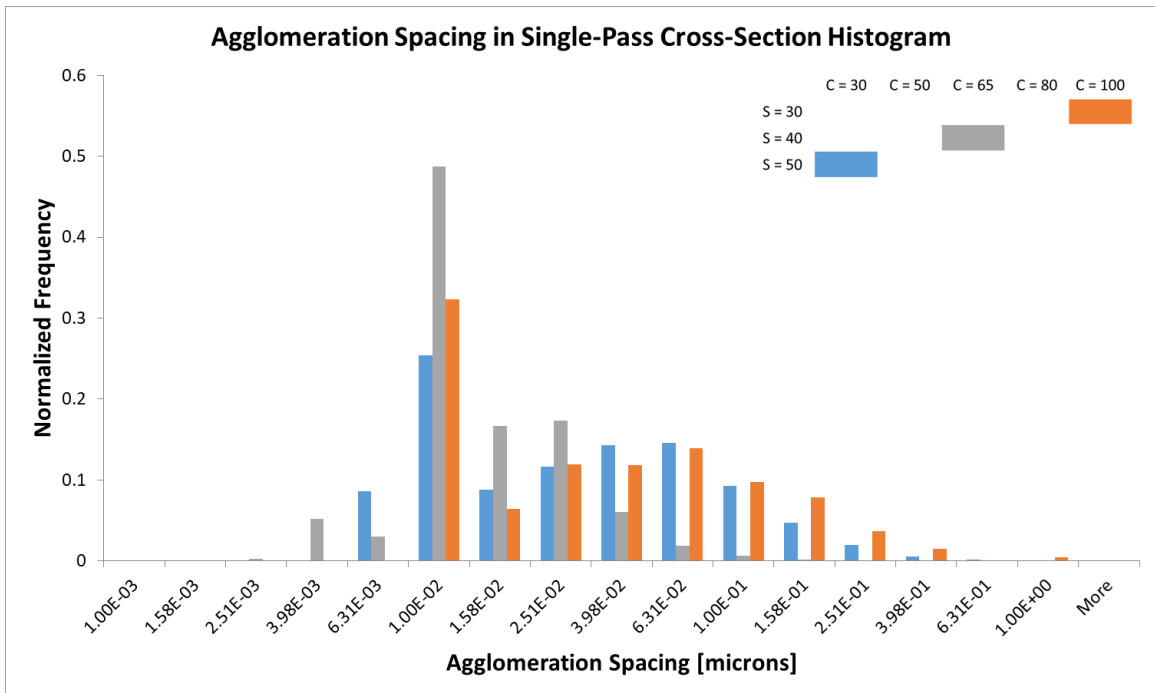


Figure 5.39: Agglomerate spacing in single-pass trace in the bulk for minor diagonal cases.

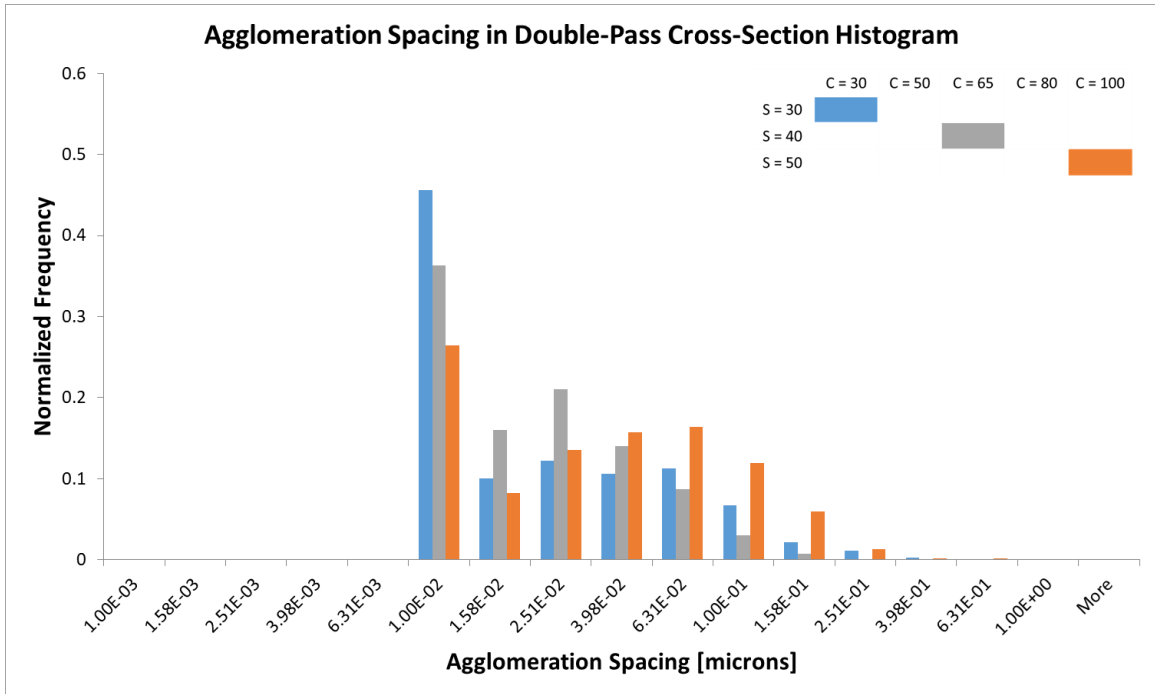


Figure 5.40: Agglomerate spacing in double-pass trace in the bulk for major diagonal cases.

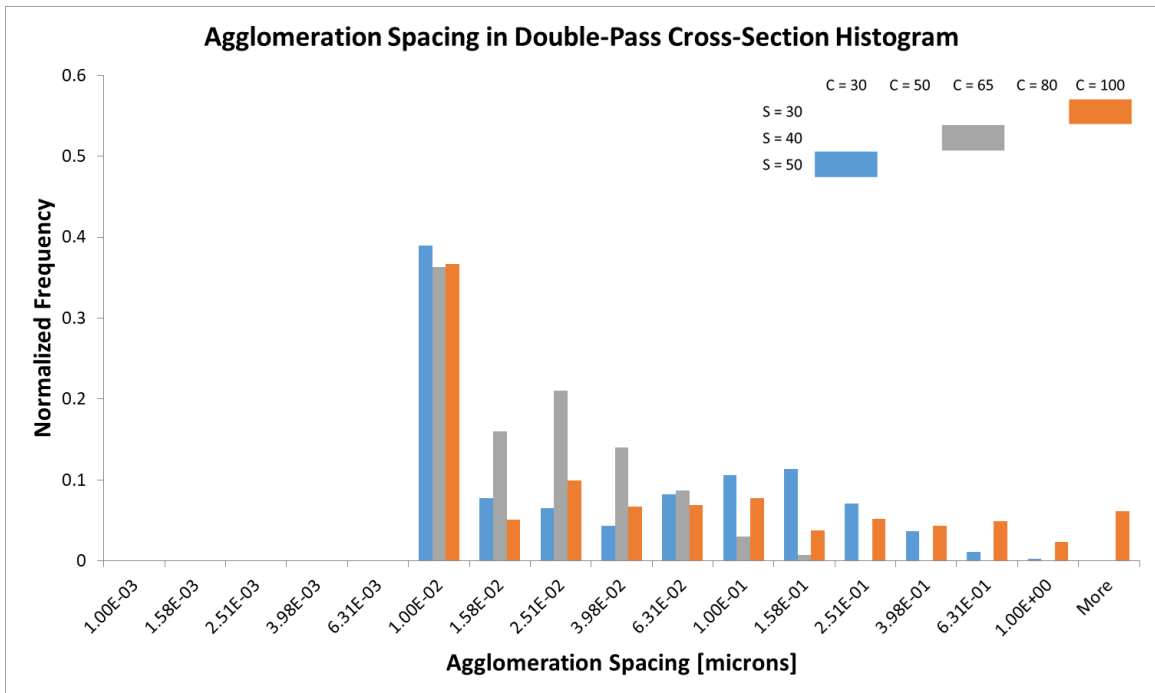


Figure 5.41: Agglomerate spacing in double-pass trace in the bulk for minor diagonal cases.

A7.4: Variation in Agglomerate Size and Spacing

For the four corner flow rate combinations ($C = 30, S = 30$; $C = 30, S = 50$; $C = 100, S = 30$; $C = 100, S = 50$), five images were post-processed for single and double-pass as well as surface and cross-section cases. The size and spacing distributions for each image was normalized before averaging across the five images to avoid one image from dominating if there was an unusually high number of agglomerates counted by the image processing software. The mean and standard deviation for the size and spacing distributions were then calculated. To understand the variation in the data, the mean plus-or-minus the standard deviation of the agglomeration size or spacing was plotted. The four corner flow rate combinations were grouped in twos for the plots in terms of major ($C = 30, S = 30$; $C = 100, S = 50$) and minor ($C = 30, S = 50$; $C = 100, S = 30$) diagonals. Plots are provided in this section for major and minor diagonal cases, single and double-pass, surface and cross-section images, as well as agglomeration size and spacing.

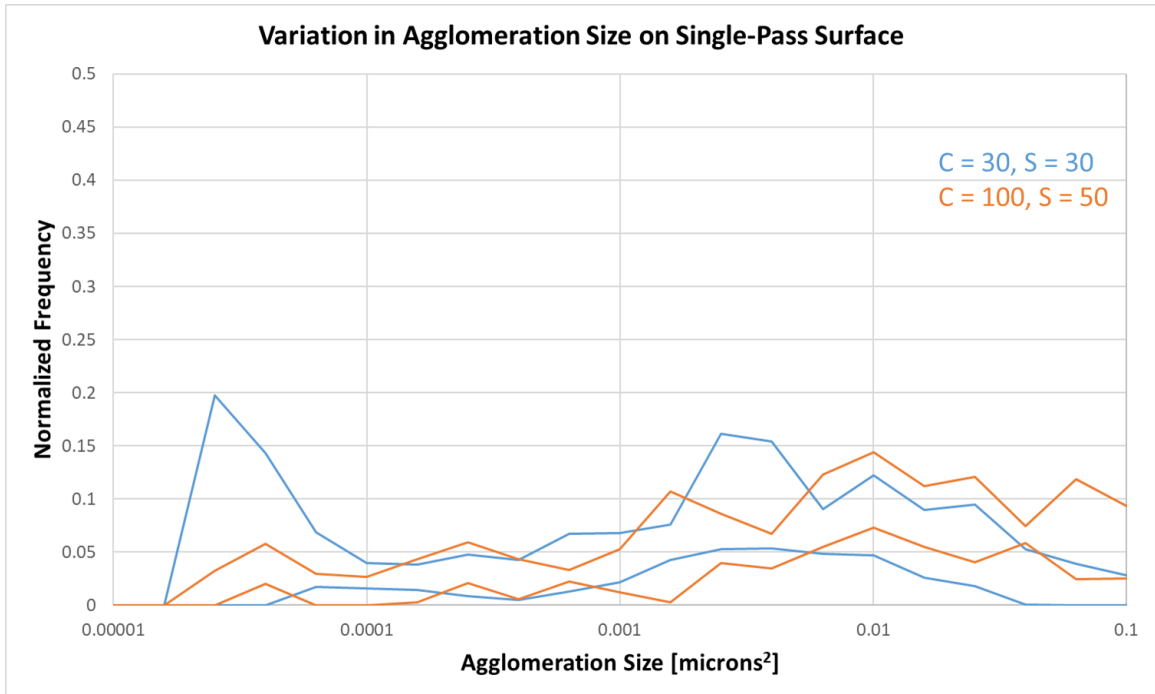


Figure 5.42: Variation in agglomeration size in single-pass trace on the surface for major diagonal cases.

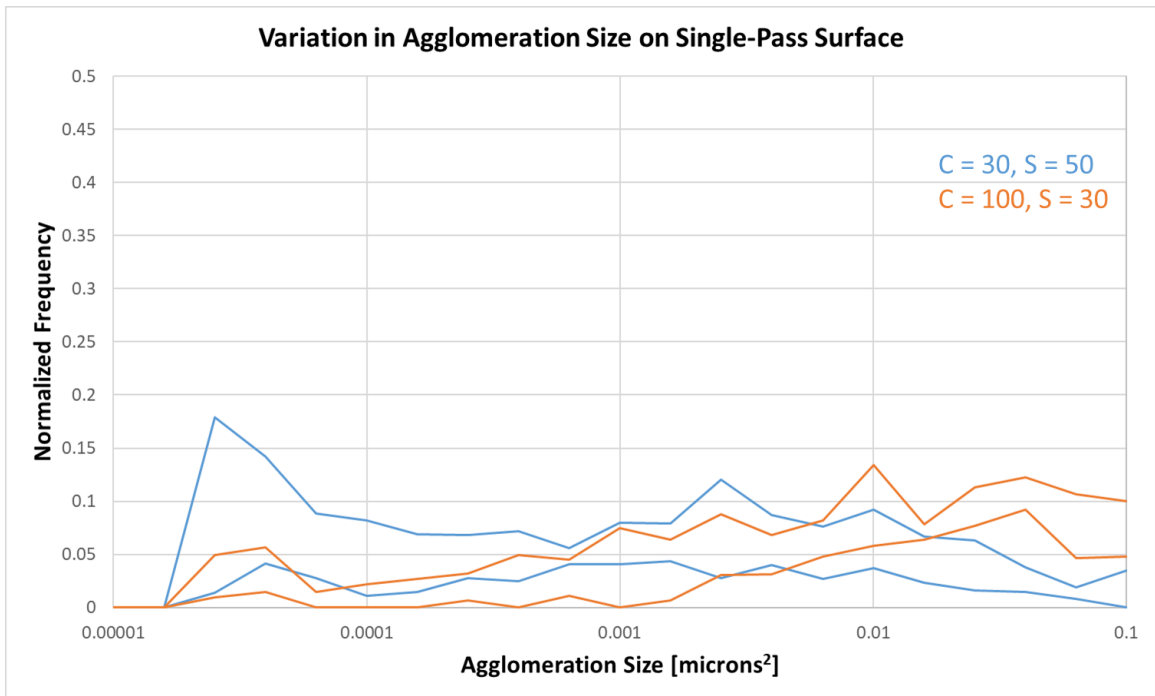


Figure 5.43: Variation in agglomeration size in single-pass trace on the surface for minor diagonal cases.

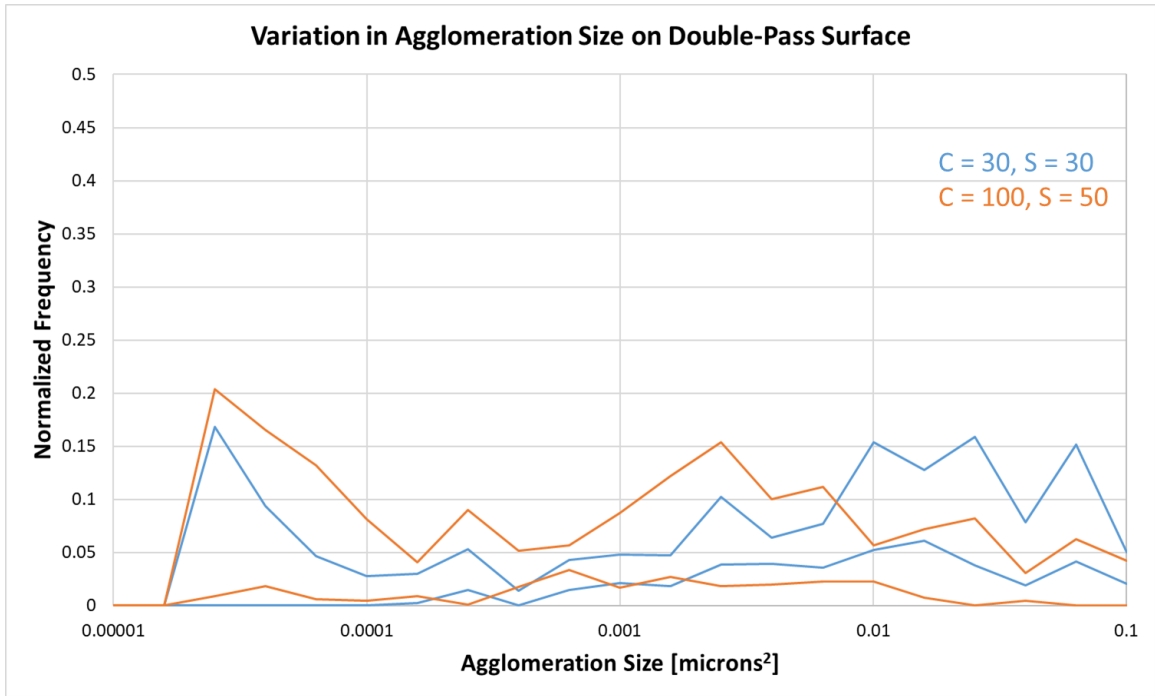


Figure 5.44: Variation in agglomeration size in double-pass trace on the surface for major diagonal cases.

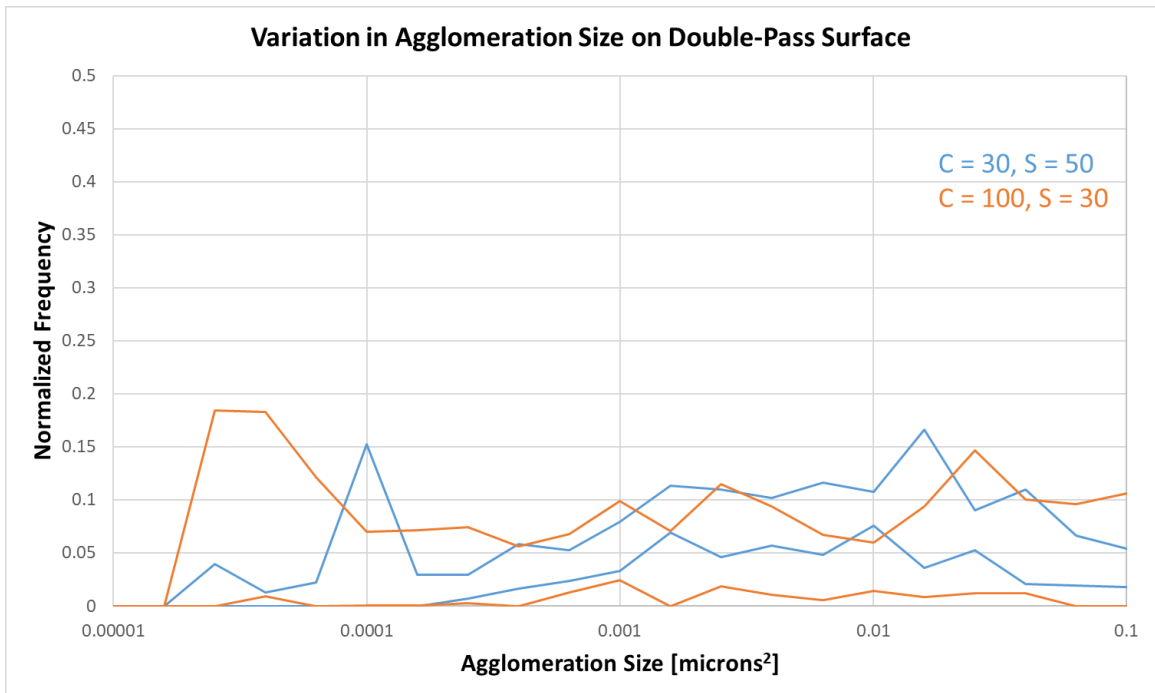


Figure 5.45: Variation in agglomeration size in double-pass trace on the surface for minor diagonal cases.

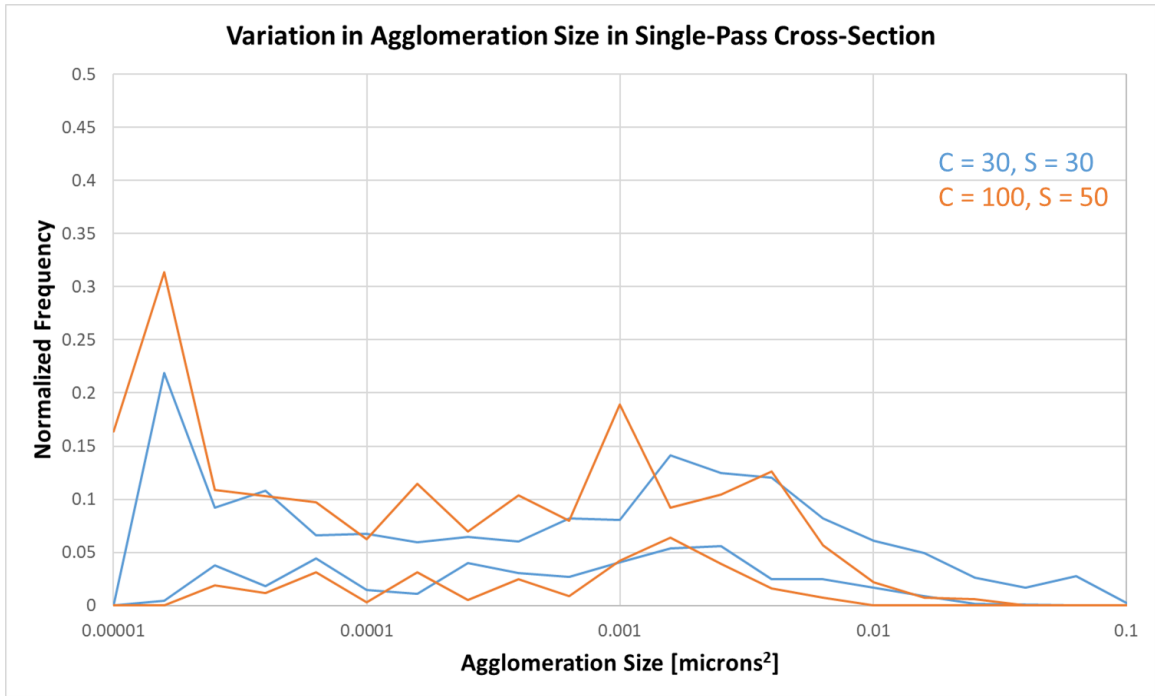


Figure 5.46: Variation in agglomeration size in single-pass trace in the bulk for major diagonal cases.

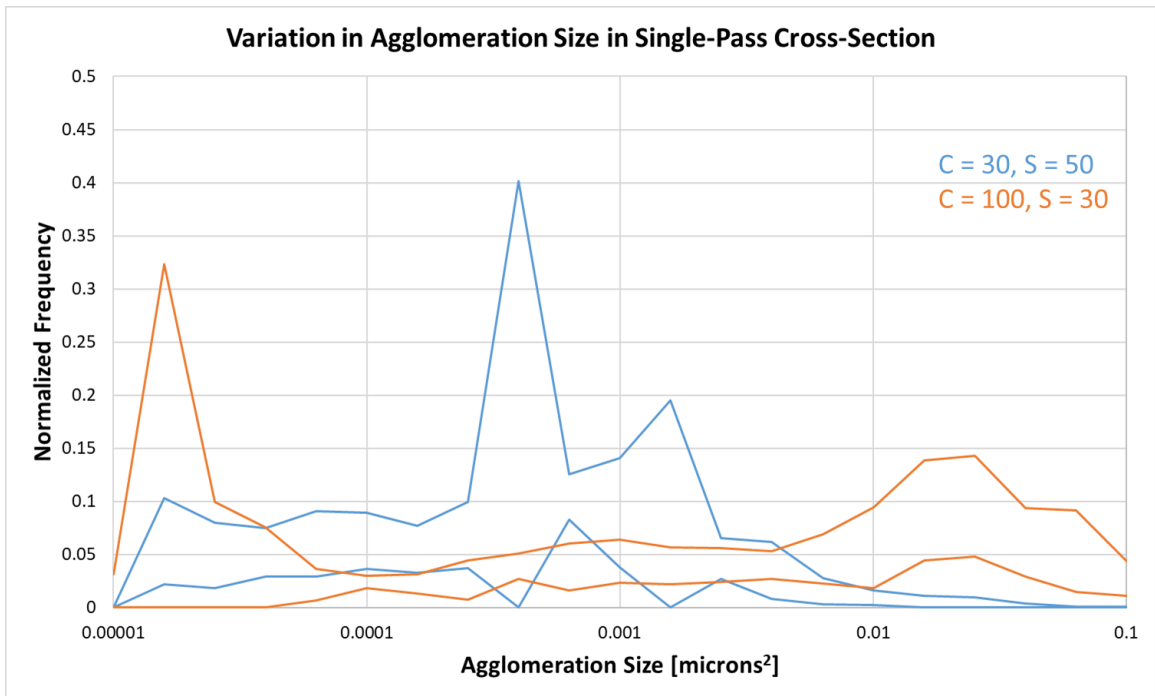


Figure 5.47: Variation in agglomeration size in single-pass trace in the bulk for minor diagonal cases.

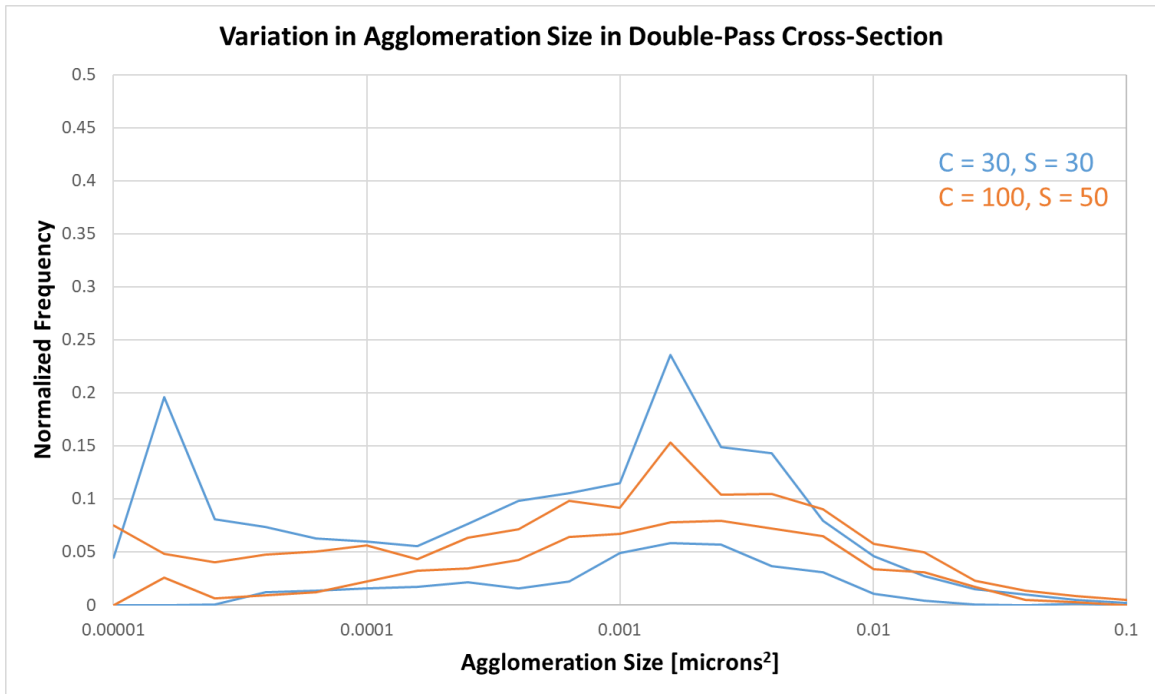


Figure 5.48: Variation in agglomeration size in double-pass trace in the bulk for major diagonal cases.

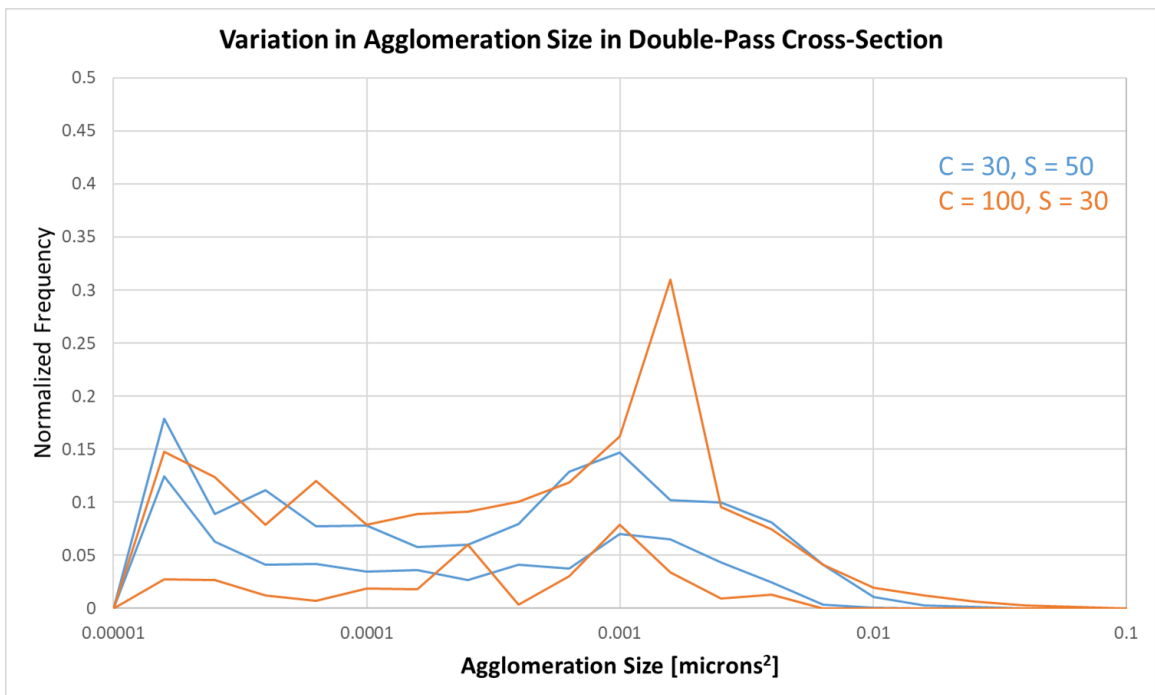


Figure 5.49: Variation in agglomeration size in double-pass trace in the bulk for minor diagonal cases.

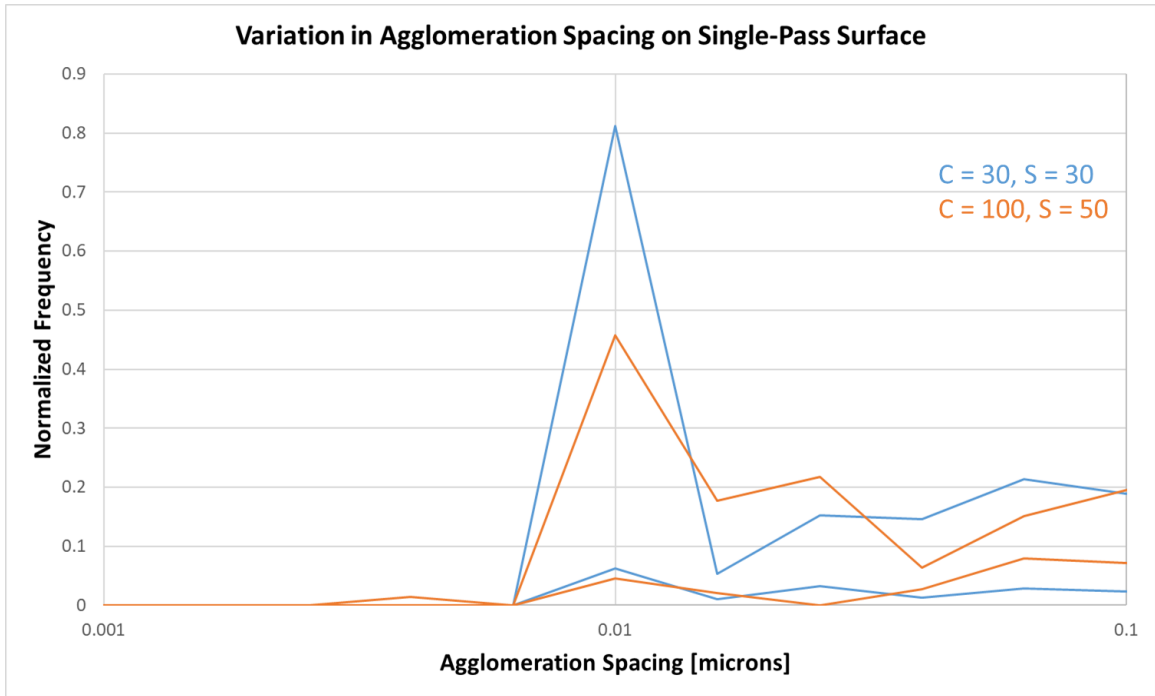


Figure 5.50: Variation in agglomeration spacing in single-pass trace on the surface for major diagonal cases.

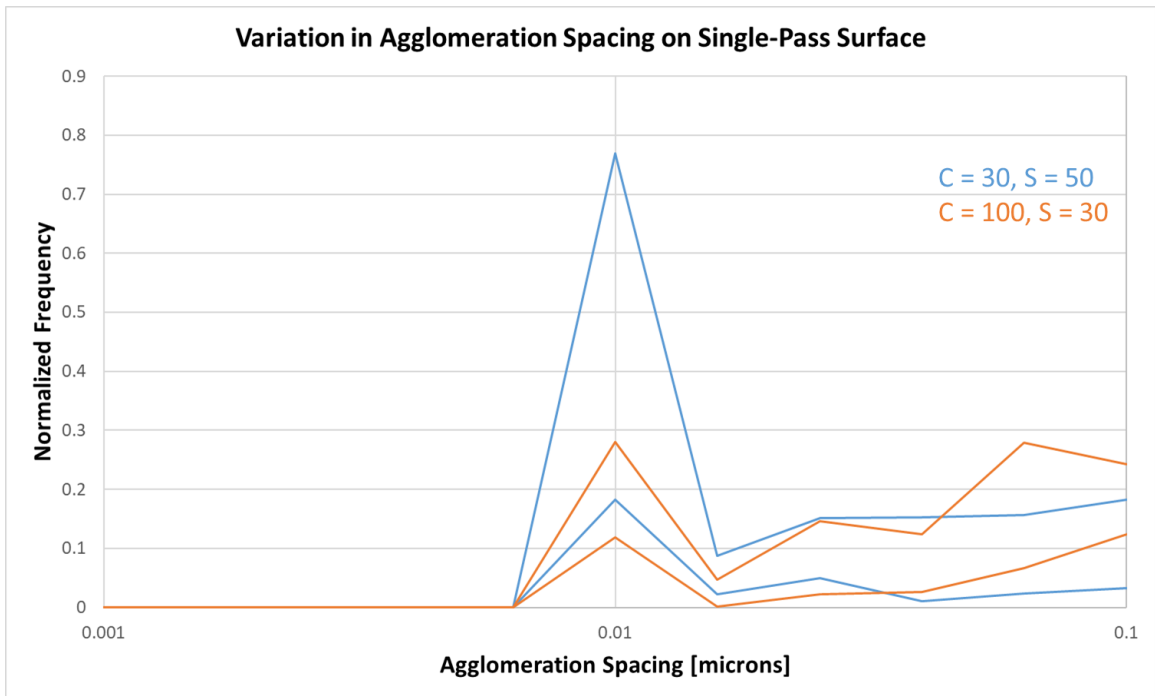


Figure 5.51: Variation in agglomeration spacing in single-pass trace on the surface for minor diagonal cases.

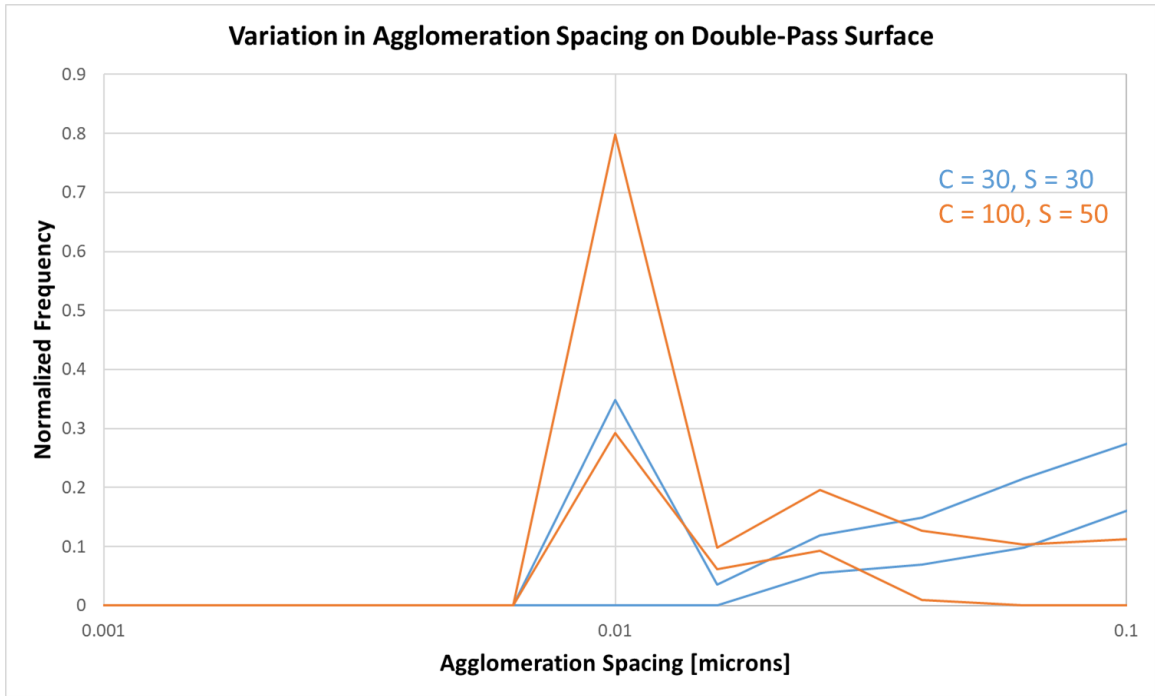


Figure 5.52: Variation in agglomeration spacing in double-pass trace on the surface for major diagonal cases.

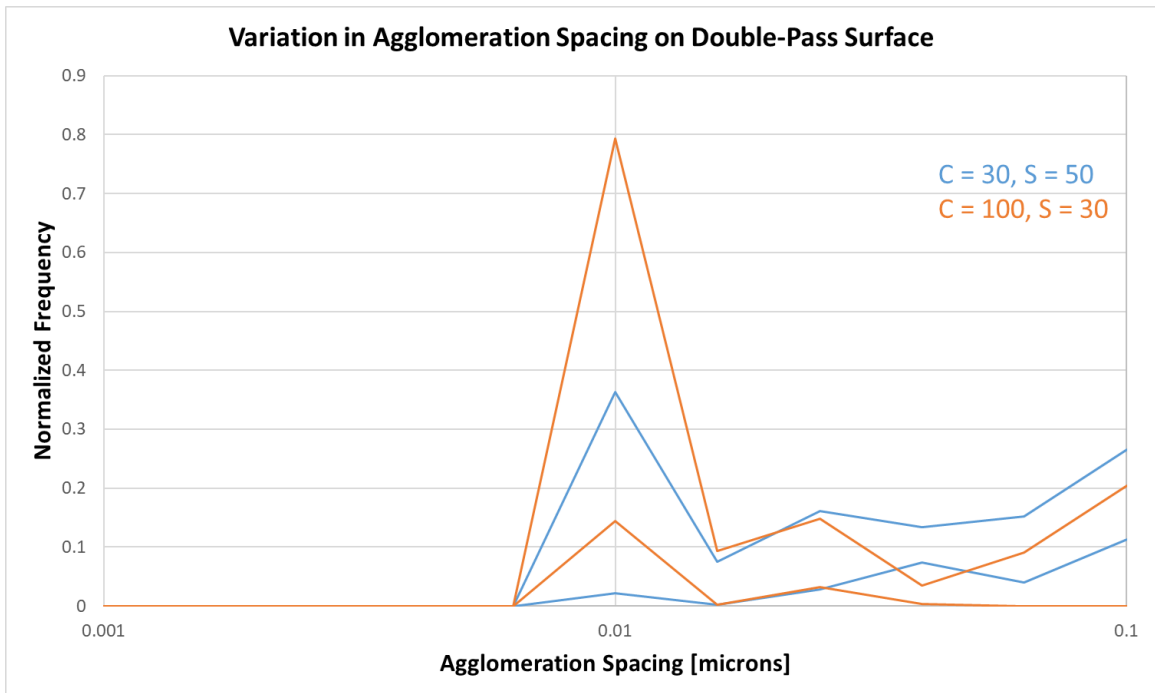


Figure 5.53: Variation in agglomeration spacing in double-pass trace on the surface for minor diagonal cases.

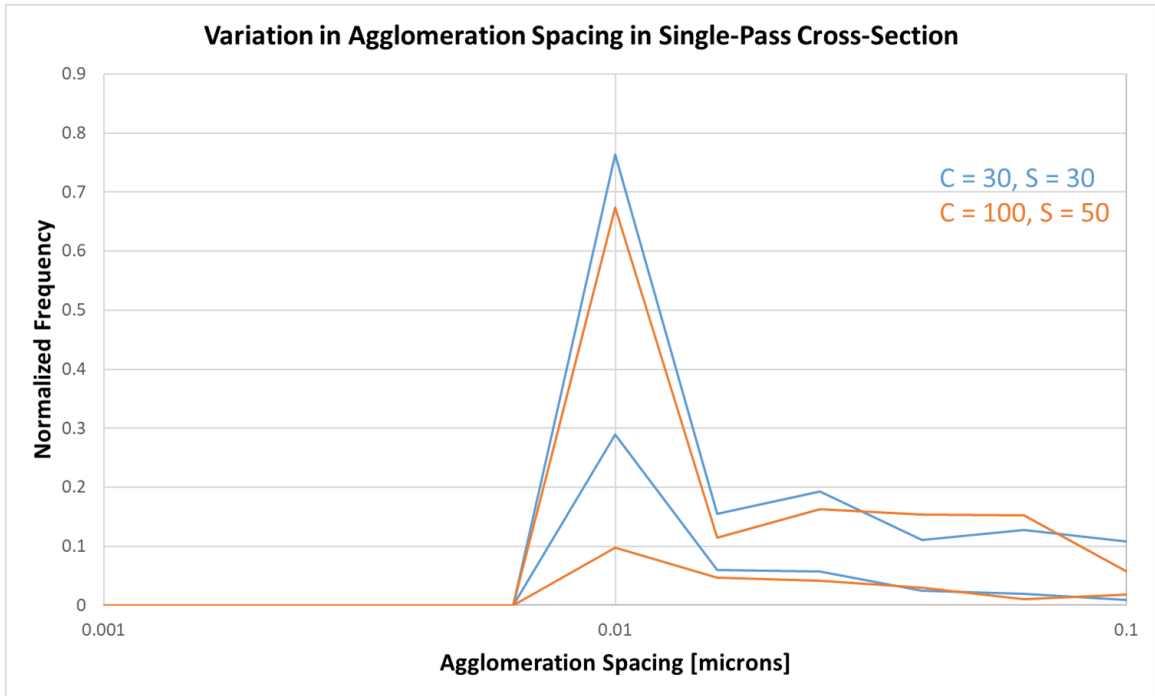


Figure 5.54: Variation in agglomeration spacing in single-pass trace in the bulk for major diagonal cases.

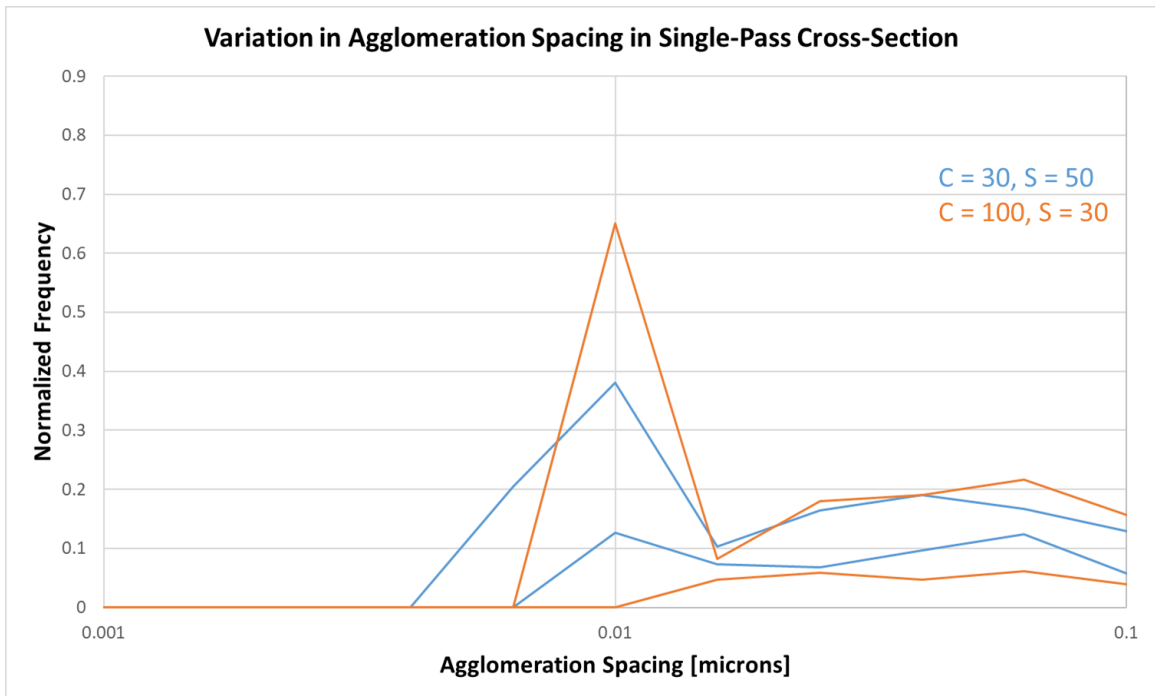


Figure 5.55: Variation in agglomeration spacing in single-pass trace in the bulk for minor diagonal cases.

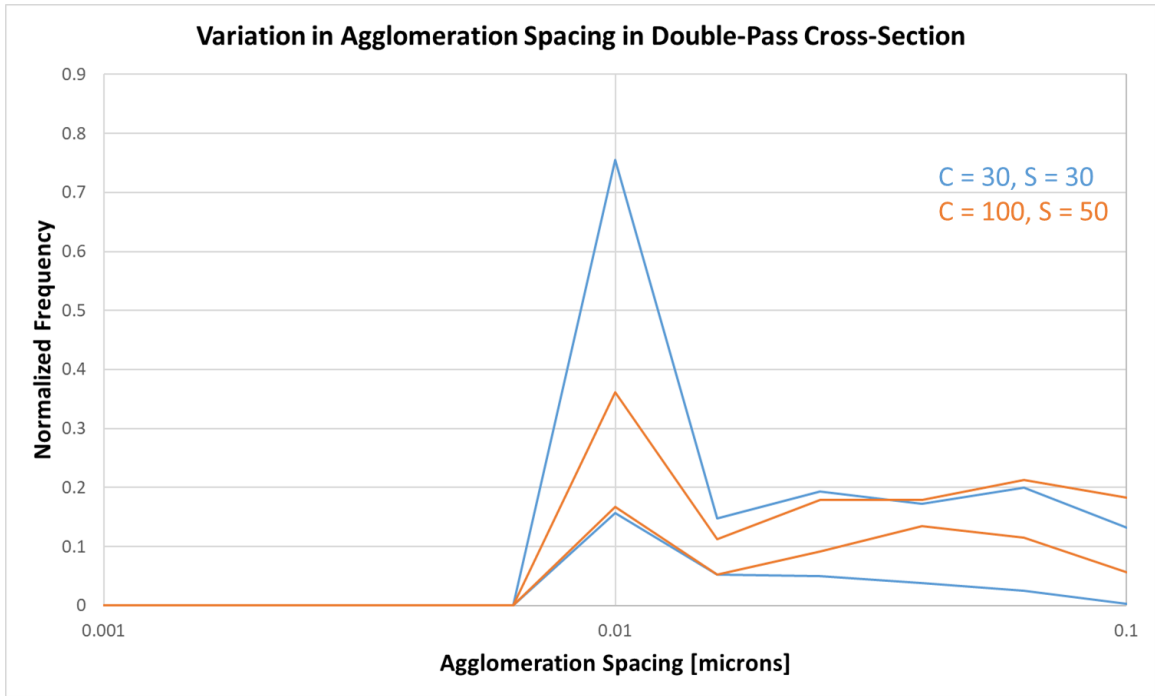


Figure 5.56: Variation in agglomeration spacing in double-pass trace in the bulk for major diagonal cases.

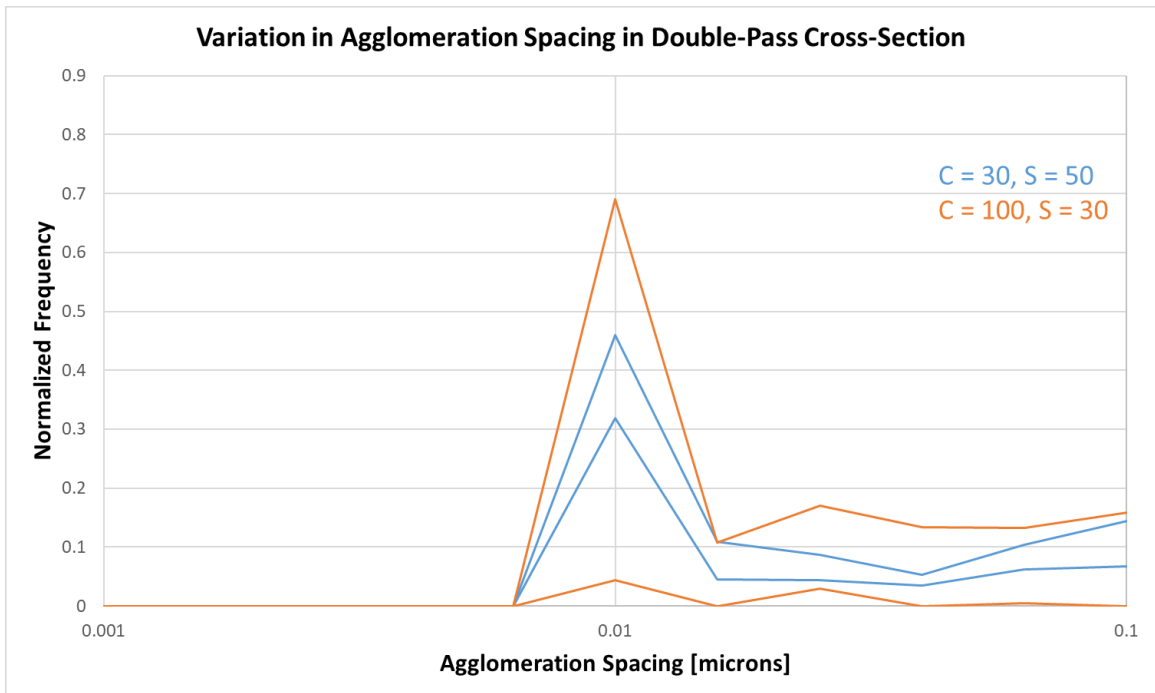


Figure 5.57: Variation in agglomeration spacing in double-pass trace in the bulk for minor diagonal cases.

A7.5: Average Agglomerate Size and Spacing as a Function of Flow Rate

From the image processing of high magnification images for 15 serpentine traces with varying flow rate combinations, an agglomeration size and spacing distribution was produced. The 3D bar charts below plot the average agglomerate size and spacing on the z-axis and lays out the 15 different flow rate combinations corresponding to the 15 different serpentine traces printed in the x-y plane. Furthermore, there is a figure distinguishing between single and double-pass traces as well as surface or cross-section images. The data from the 3D bar charts are provided in tabular form with the average and standard deviation for the agglomeration size and spacing.

	Carrier = 30	Carrier = 50	Carrier = 65	Carrier = 80	Carrier = 100
Sheath = 30	0.008±0.015	0.009±0.016	0.021±0.033	0.014±0.036	0.028±0.041
Sheath = 40	0.002±0.005	0.004±0.007	0.019±0.029	0.009±0.016	0.017±0.034
Sheath = 50	0.006±0.017	0.010±0.044	0.009±0.016	0.017±0.034	0.022±0.037

Table 5.10: Average agglomeration size in single-pass trace on the surface.

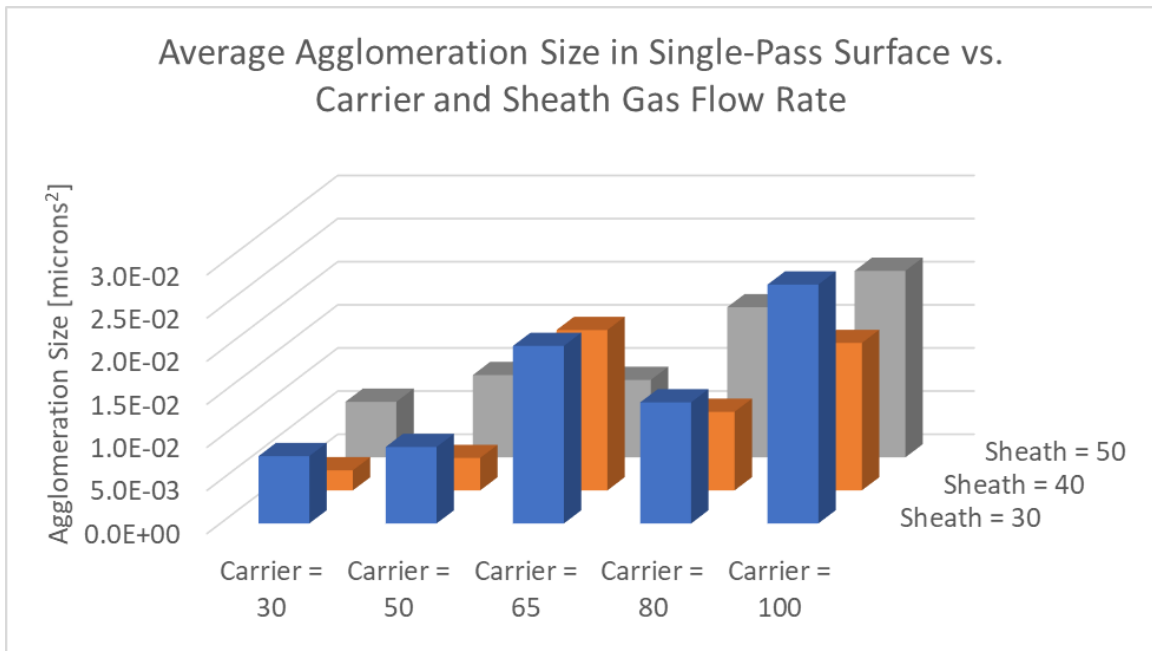


Figure 5.58: Average agglomeration size in single-pass trace on the surface as a function of carrier and sheath gas flow rate.

	Carrier = 30	Carrier = 50	Carrier = 65	Carrier = 80	Carrier = 100
Sheath = 30	0.012±0.019	0.010±0.018	0.014±0.027	0.016±0.024	0.014±0.029
Sheath = 40	0.006±0.013	0.015±0.041	0.024±0.045	0.011±0.015	0.030±0.043
Sheath = 50	0.013±0.020	0.009±0.016	0.021±0.034	0.015±0.020	0.009±0.023

Table 5.11: Average agglomeration size in double-pass trace on the surface.

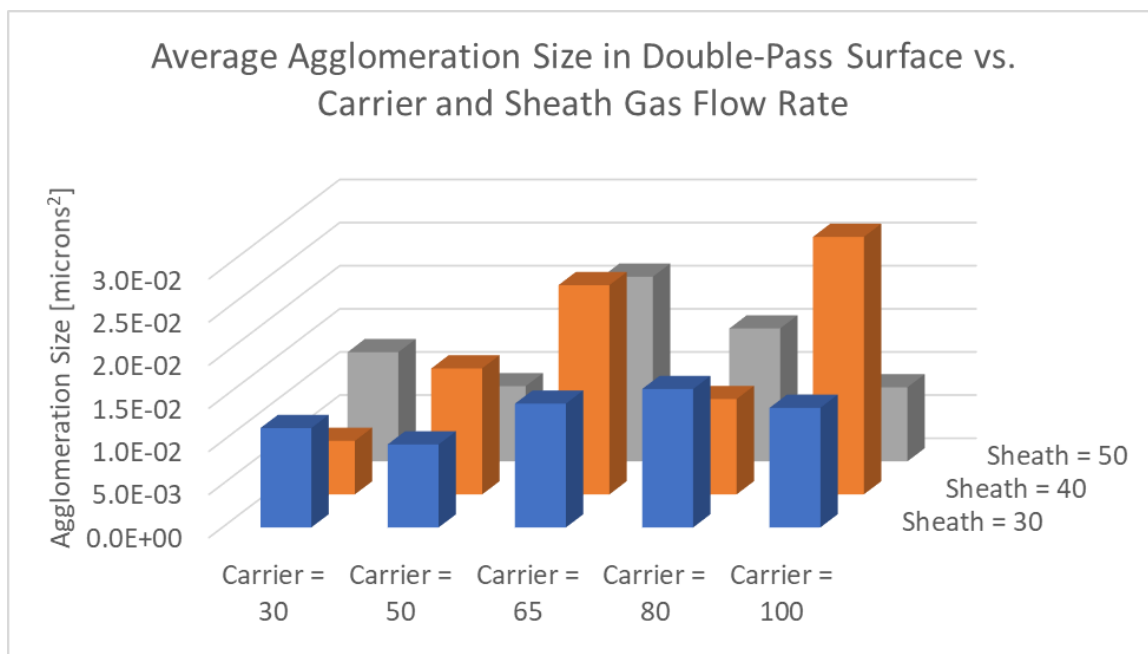


Figure 5.59: Average agglomeration size in double-pass trace on the surface as a function of carrier and sheath gas flow rate.

	Carrier = 30	Carrier = 50	Carrier = 65	Carrier = 80	Carrier = 100
Sheath = 30	0.0028±0.006	0.0031±0.007	0.0038±0.003	0.0005±0.024	0.0146±0.020
Sheath = 40	0.0015±0.001	0.0067±0.069	0.0029±0.045	0.0087±0.019	0.0024±0.20
Sheath = 50	0.0009±0.002	0.0022±0.016	0.0040±0.004	0.0014±0.091	0.0009±0.002

Table 5.12: Average agglomeration size in single-pass trace in the bulk.

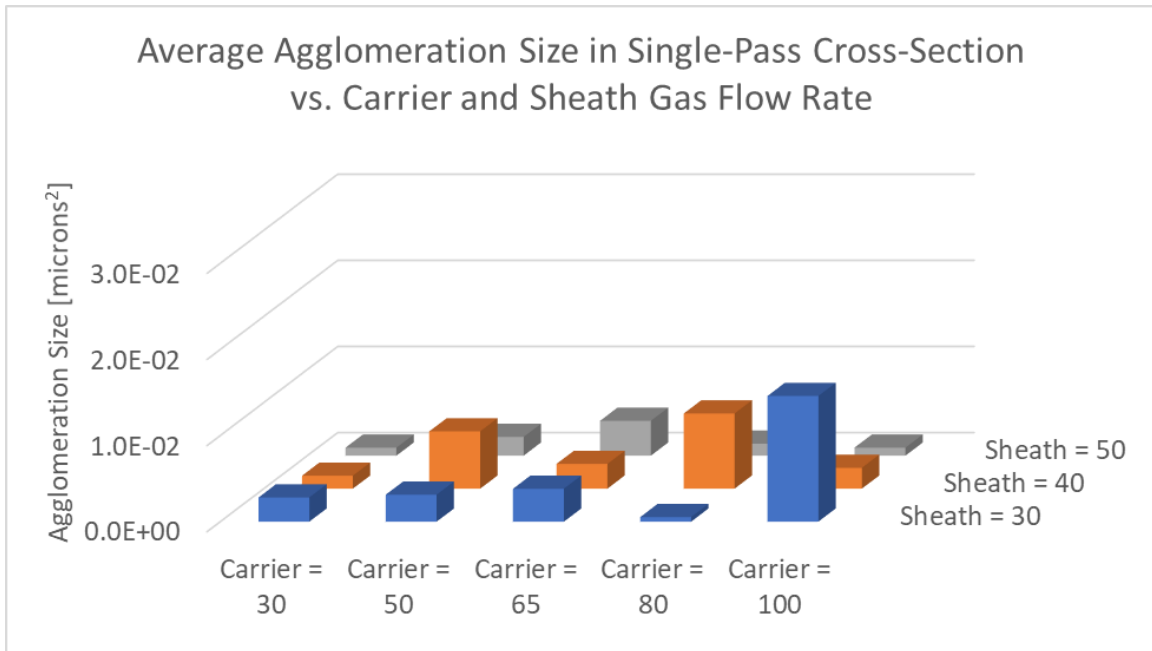


Figure 5.60: Average agglomeration size in single-pass trace in the bulk as a function of carrier and sheath gas flow rate.

	Carrier = 30	Carrier = 50	Carrier = 65	Carrier = 80	Carrier = 100
Sheath = 30	0.0022±0.007	0.0074±0.030	0.0105±0.007	0.0045±0.003	0.0010±0.010
Sheath = 40	0.0009±0.004	0.0026±0.019	0.0024±0.011	0.0084±0.044	0.0004±0.011
Sheath = 50	0.0008±0.002	0.0111±0.007	0.0118±0.013	0.0029±0.002	0.0039±0.008

Table 5.13: Average agglomeration size in double-pass trace in the bulk.

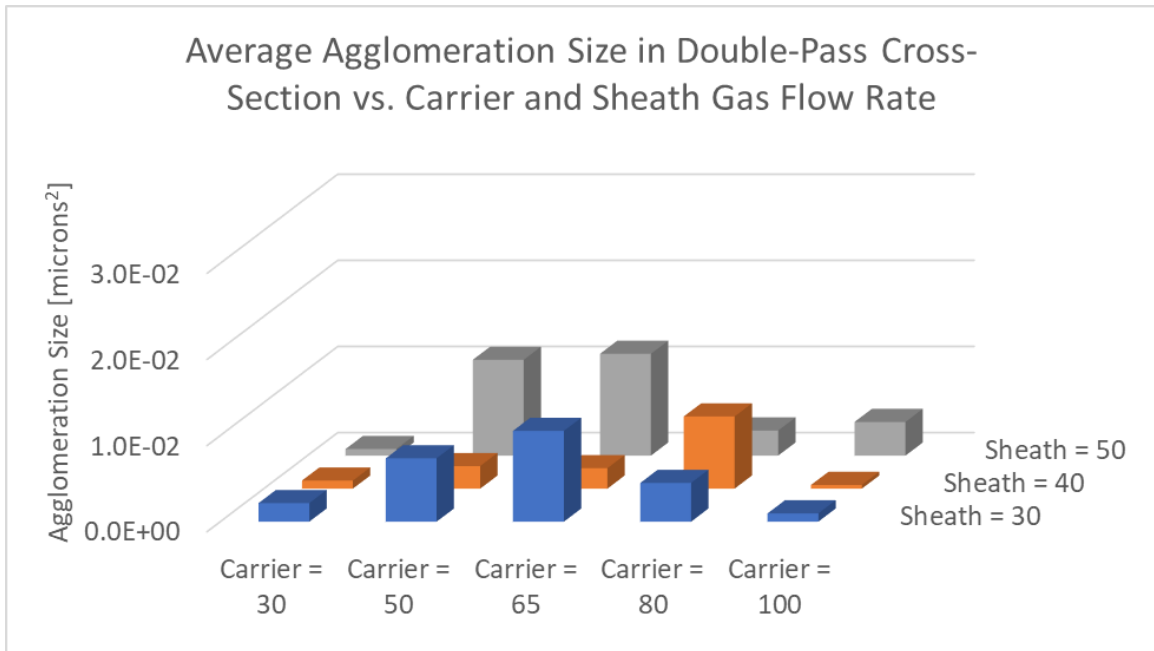


Figure 5.61: Average agglomeration size in double-pass trace in the bulk as a function of carrier and sheath gas flow rate.

	Carrier = 30	Carrier = 50	Carrier = 65	Carrier = 80	Carrier = 100
Sheath = 30	0.044±0.043	0.054±0.046	0.062±0.039	0.030±0.032	0.070±0.059
Sheath = 40	0.029±0.032	0.041±0.028	0.057±0.047	0.050±0.037	0.046±0.042
Sheath = 50	0.036±0.036	0.040±0.028	0.040±0.034	0.039±0.031	0.068±0.058

Table 5.14: Average agglomeration spacing in single-pass trace on the surface.

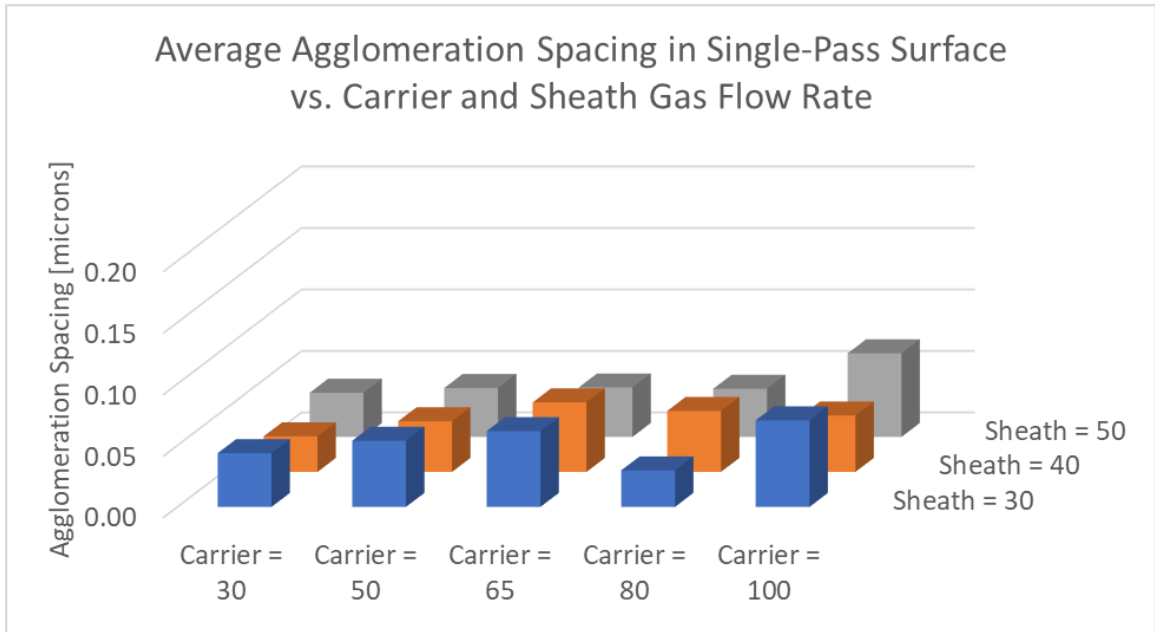


Figure 5.62: Average agglomeration spacing in single-pass trace on the surface as a function of carrier and sheath gas flow rate.

	Carrier = 30	Carrier = 50	Carrier = 65	Carrier = 80	Carrier = 100
Sheath = 30	0.071±0.058	0.026±0.024	0.048±0.049	0.062±0.067	0.067±0.061
Sheath = 40	0.026±0.030	0.035±0.022	0.070±0.055	0.064±0.053	0.073±0.051
Sheath = 50	0.077±0.069	0.079±0.067	0.086±0.048	0.084±0.048	0.028±0.036

Table 5.15: Average agglomeration spacing in double-pass trace on the surface.

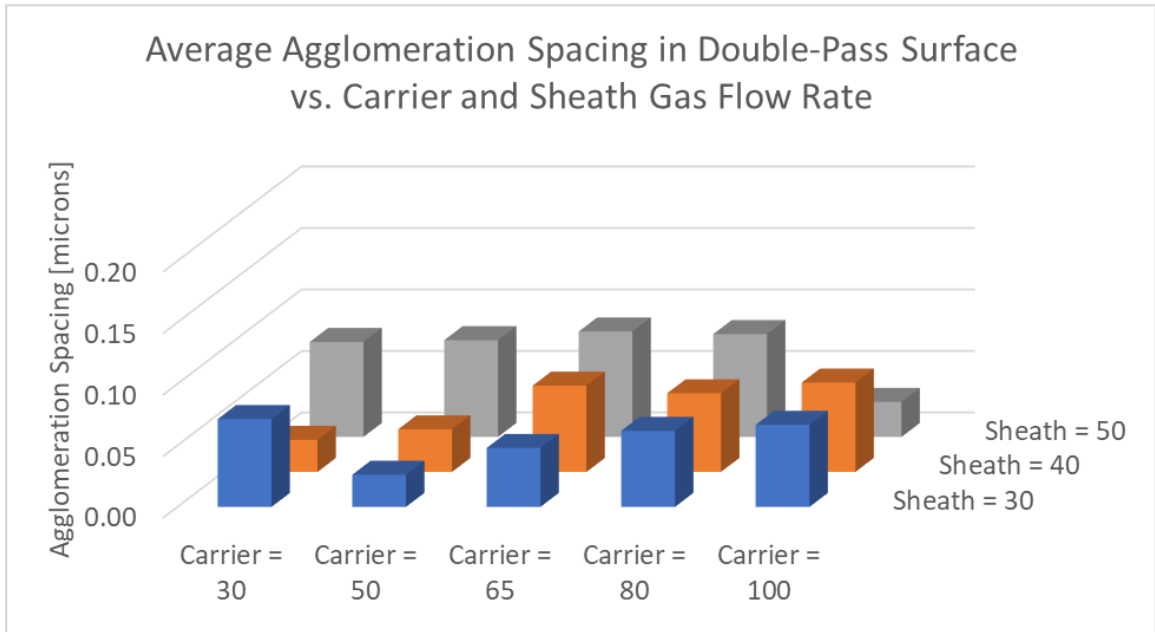


Figure 5.63: Average agglomeration spacing in double-pass trace on the surface as a function of carrier and sheath gas flow rate.

	Carrier = 30	Carrier = 50	Carrier = 65	Carrier = 80	Carrier = 100
Sheath = 30	0.026±0.032	0.021±0.057	0.054±0.026	0.043±0.031	0.051±0.062
Sheath = 40	0.023±0.136	0.025±0.028	0.014±0.020	0.063±0.028	0.022±0.026
Sheath = 50	0.038±0.039	0.019±0.031	0.015±0.032	0.040±0.015	0.103±0.168

Table 5.16: Average agglomeration spacing in single-pass trace in the bulk.

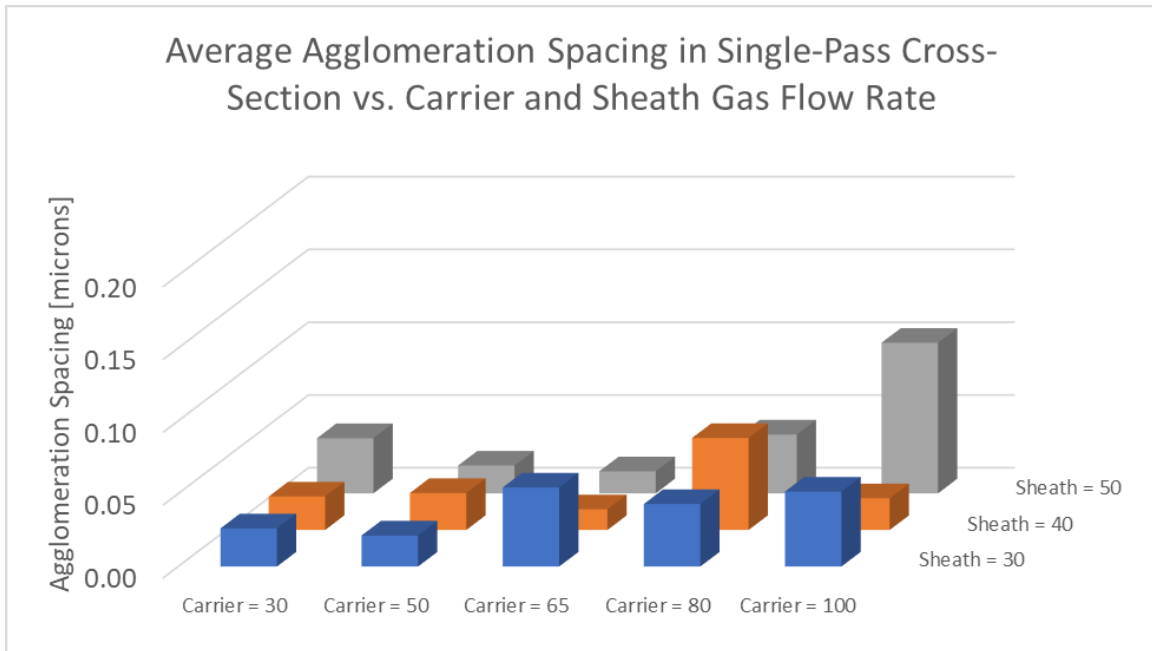


Figure 5.64: Average agglomeration spacing in single-pass trace in the bulk as a function of carrier and sheath gas flow rate.

	Carrier = 30	Carrier = 50	Carrier = 65	Carrier = 80	Carrier = 100
Sheath = 30	0.028±0.032	0.041±0.052	0.016±0.063	0.038±0.085	0.156±0.203
Sheath = 40	0.012±0.028	0.073±0.036	0.022±0.015	0.026±0.057	0.014±0.022
Sheath = 50	0.067±0.069	0.029±0.025	0.030±0.010	0.020±0.041	0.040±0.041

Table 5.17: Average agglomeration spacing in double-pass trace in the bulk.

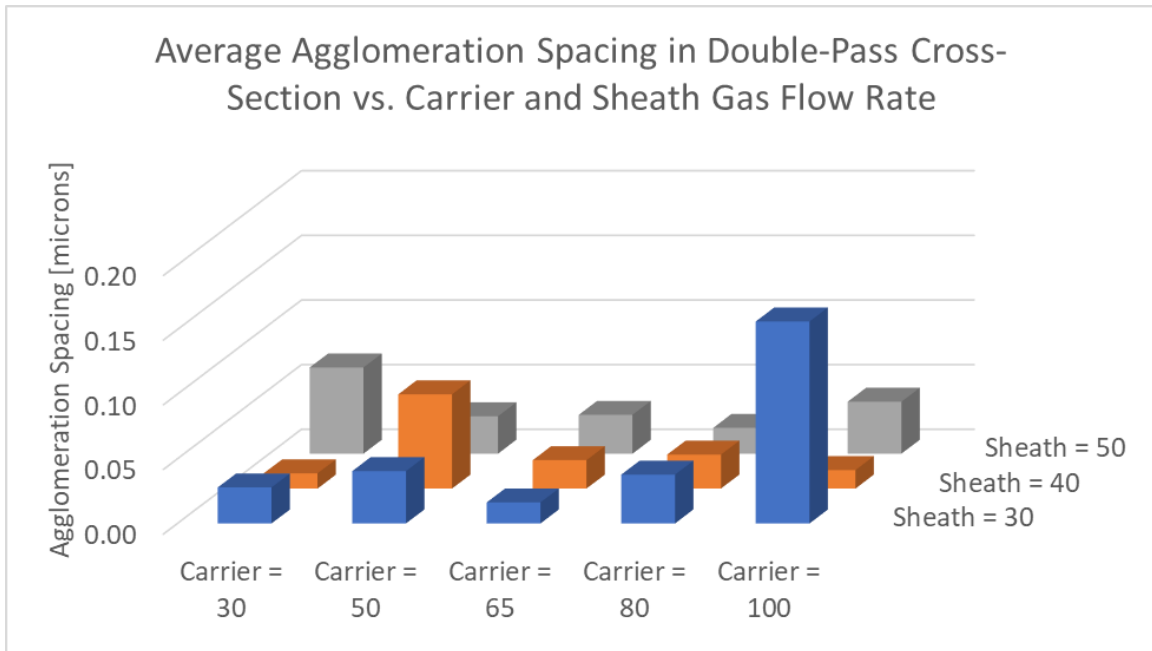


Figure 5.65: Average agglomeration spacing in double-pass trace in the bulk as a function of carrier and sheath gas flow rate.

A7.6: Standard Deviation of Agglomerate Size and Spacing as a Function of Flow Rate

From the image processing of high magnification images for 15 serpentine traces with varying flow rate combinations, an agglomeration size and spacing distribution was produced. The 3D bar charts below plot the standard deviation of the agglomerate size and spacing on the z-axis and lays out the 15 different flow rate combinations corresponding to the 15 different serpentine traces printed in the x-y plane. Furthermore, there is a figure distinguishing between single and double-pass traces as well as surface or cross-section images.

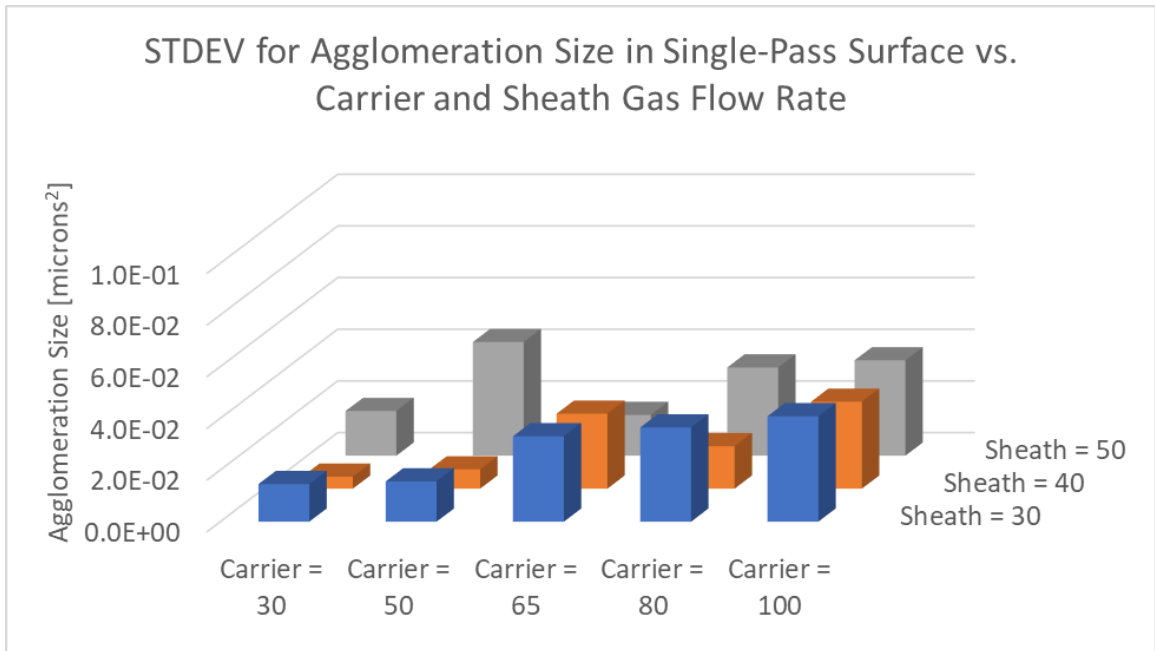


Figure 5.66: Standard deviation of agglomeration size in single-pass trace on the surface as a function of carrier and sheath gas flow rate.

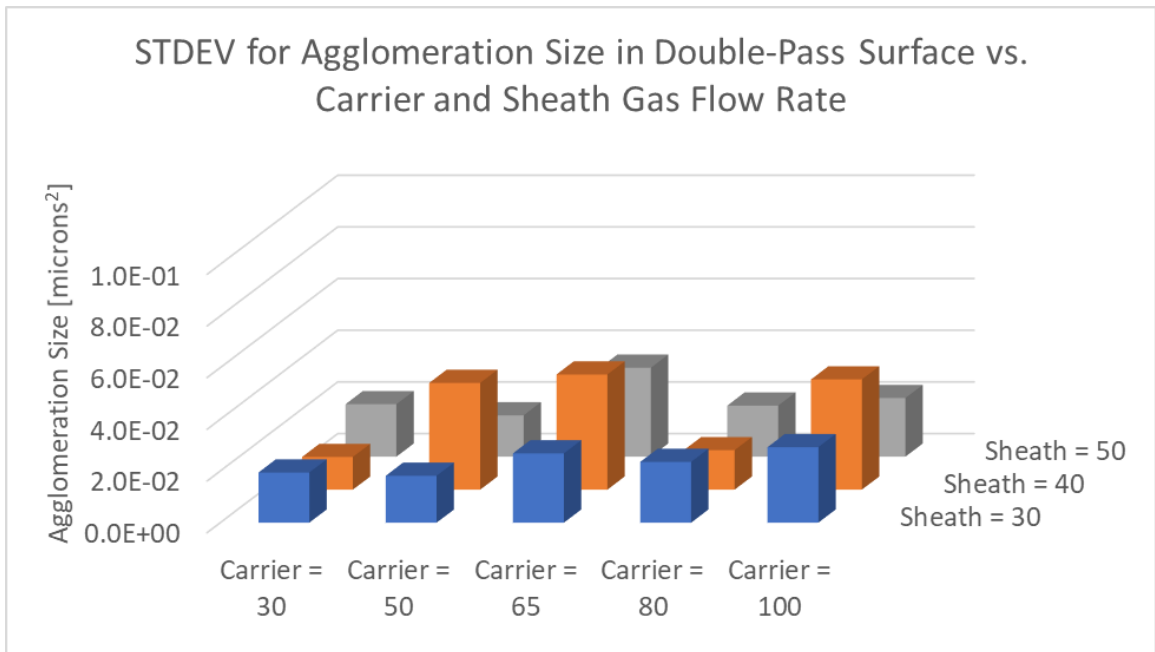


Figure 5.67: Standard deviation of agglomeration size in double-pass trace on the surface as a function of carrier and sheath gas flow rate.

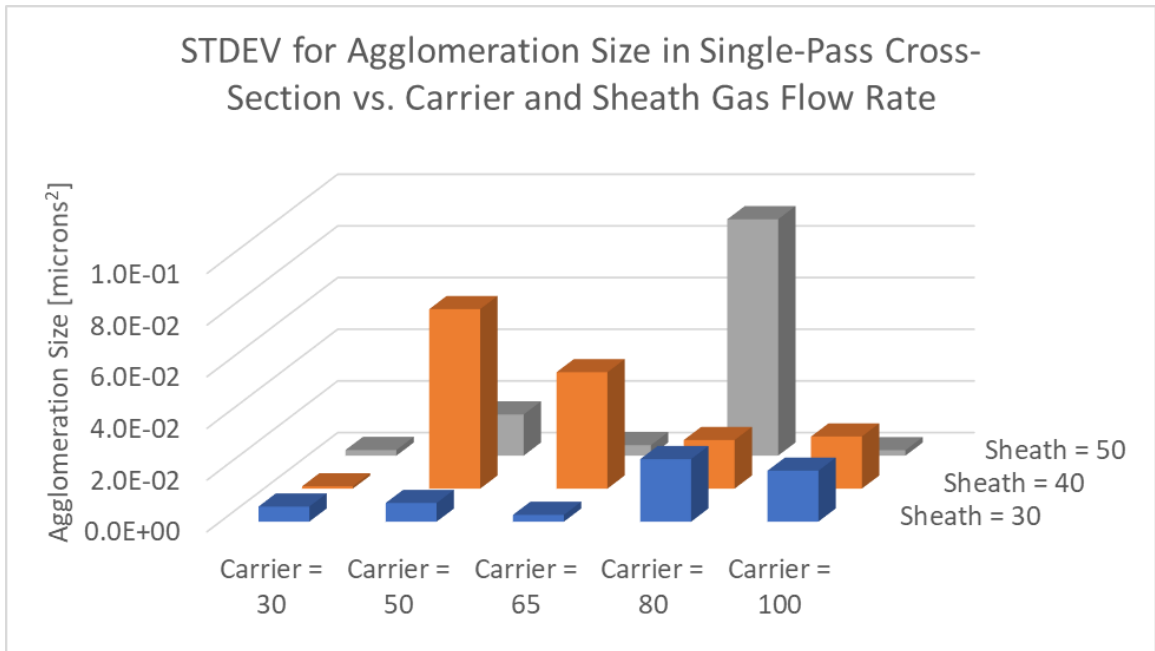


Figure 5.68: Standard deviation of agglomeration size in single-pass trace in the bulk as a function of carrier and sheath gas flow rate.

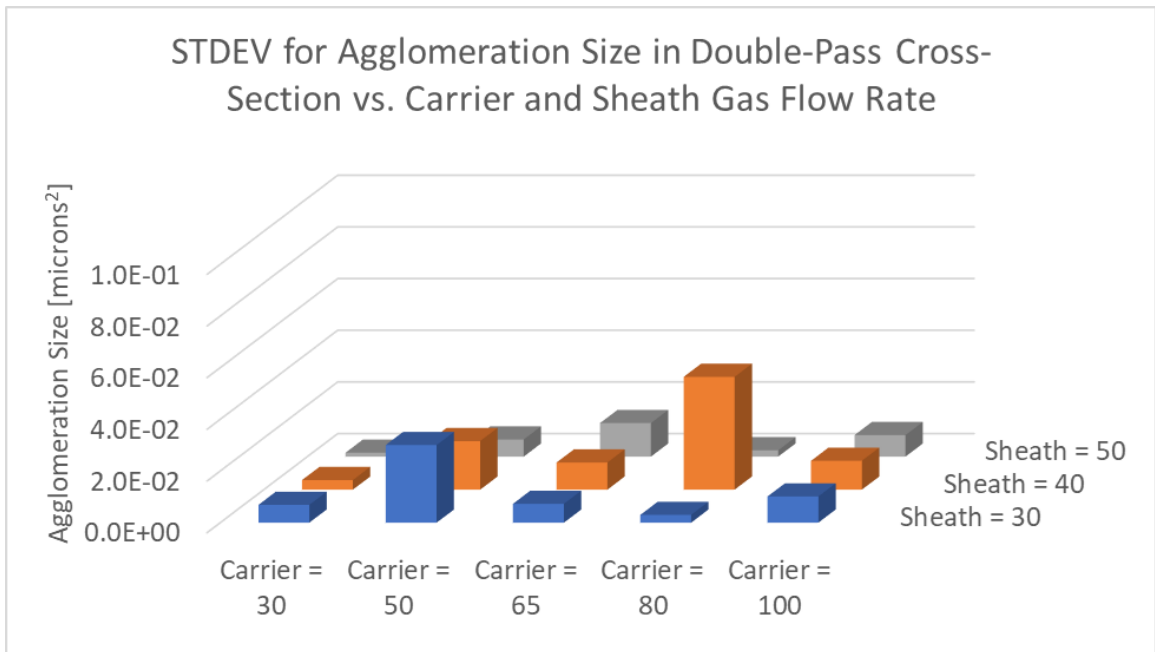


Figure 5.69: Standard deviation of agglomeration size in double-pass trace in the bulk as a function of carrier and sheath gas flow rate.

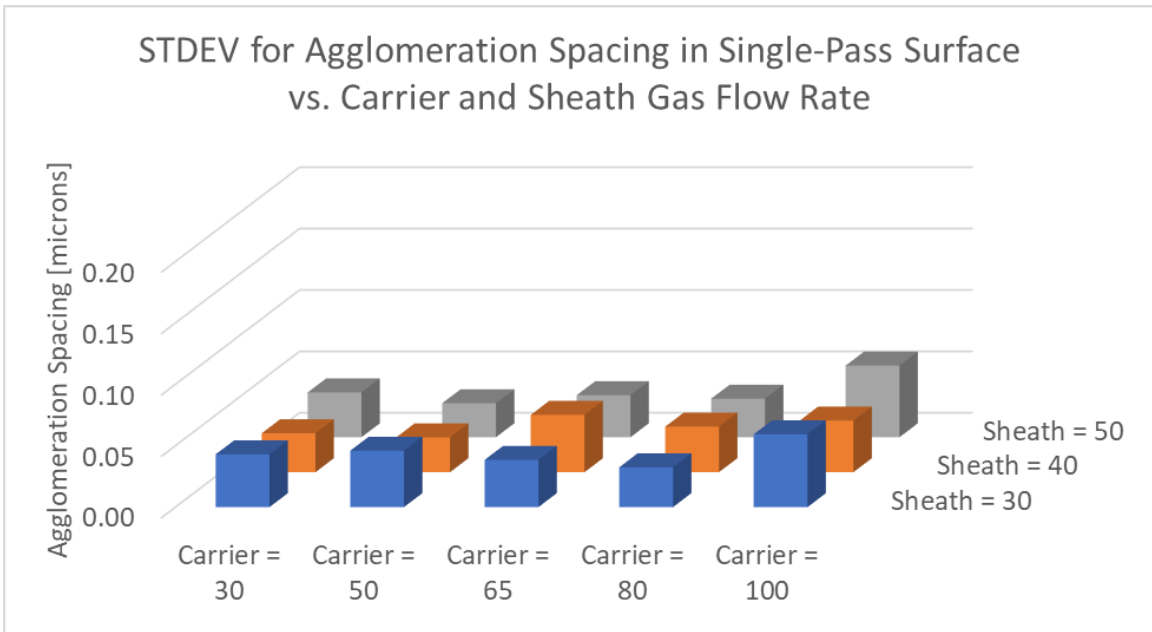


Figure 5.70: Standard deviation of agglomeration spacing in single-pass trace on the surface as a function of carrier and sheath gas flow rate.

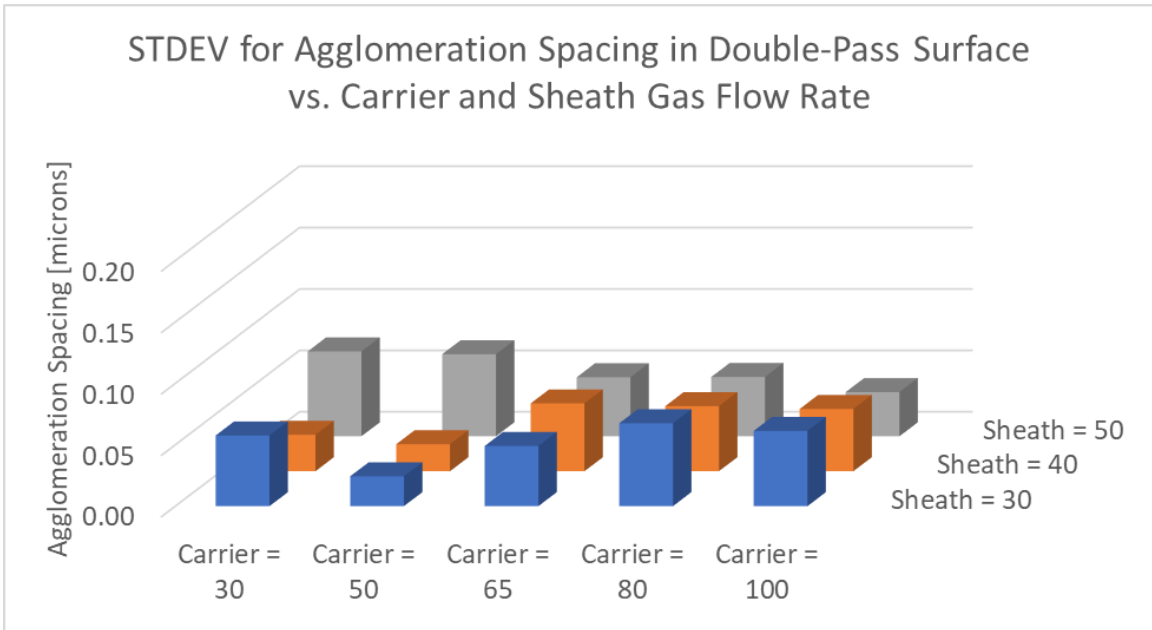


Figure 5.71: Standard deviation of agglomeration spacing in double-pass trace on the surface as a function of carrier and sheath gas flow rate.

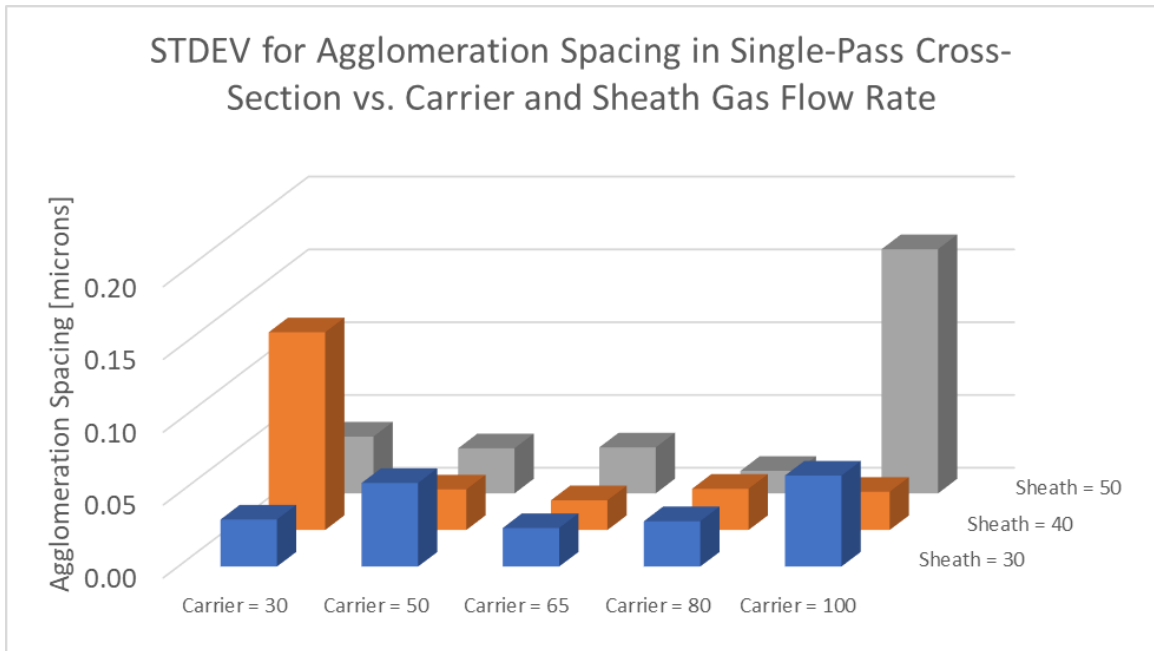


Figure 5.72: Standard deviation of agglomeration spacing in single-pass trace in the bulk as a function of carrier and sheath gas flow rate.

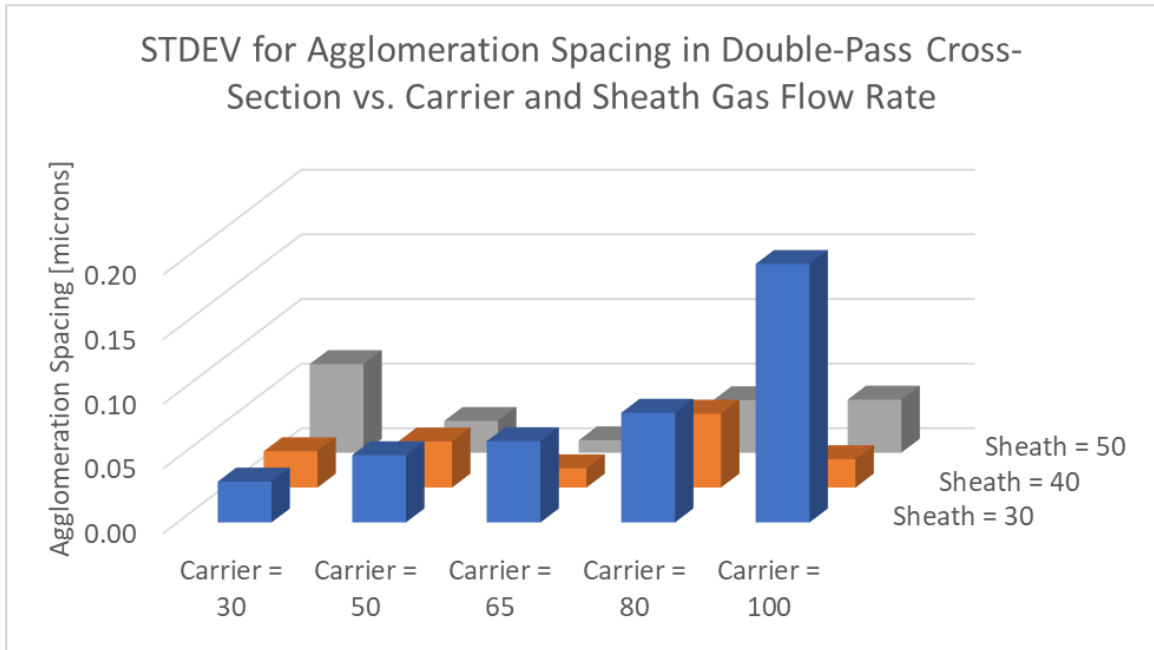


Figure 5.73: Standard deviation of agglomeration spacing in double-pass trace in the bulk as a function of carrier and sheath gas flow rate.

A7.7: Skewness of Agglomerate Size and Spacing as a Function of Flow Rate

From the histograms presented in A7.3, a skewness factor can be calculated based on the log-scale based binning for the five serpentine traces with multiple image data averaged together. The more positive the skewness value, the more skewed right the histogram data is. The 3D bar charts below plot the skewness of the agglomerate size and spacing on the z-axis and lays out the 5 different flow rate combinations corresponding to the 5 different serpentine traces printed in the x-y plane. Furthermore, there is a figure distinguishing between single and double-pass traces as well as surface or cross-section images. The data from the 3D bar charts are provided in tabular form first.

Size		Spacing	
Surface		Surface	
Trace	Skewness	Trace	Skewness
B5S1 SP	0.593	B5S1 SP	2.478
B5S3 SP	0.026	B5S3 SP	2.688
B3S2 SP	0.314	B3S2 SP	0.198
B4S1 SP	0.297	B4S1 SP	0.085
B4S3 SP	0.405	B4S3 SP	0.944
B5S1 DP	0.233	B5S1 DP	0.050
B5S3 DP	0.072	B5S3 DP	0.221
B3S2 DP	0.549	B3S2 DP	0.052
B4S1 DP	0.682	B4S1 DP	2.822
B4S3 DP	0.634	B4S3 DP	2.790
Cross-Section		Cross-Section	
Trace	Skewness	Trace	Skewness
B5S1 SP	0.255	B5S1 SP	3.254
B5S3 SP	1.325	B5S3 SP	1.127
B3S2 SP	-0.302	B3S2 SP	2.790
B4S1 SP	1.552	B4S1 SP	1.942
B4S3 SP	0.449	B4S3 SP	3.016
B5S1 DP	0.951	B5S1 DP	2.585
B5S3 DP	0.628	B5S3 DP	2.653
B3S2 DP	2.487	B3S2 DP	1.500
B4S1 DP	1.113	B4S1 DP	3.182
B4S3 DP	0.572	B4S3 DP	0.768

Table 5.18: Skewness values for agglomeration size and spacing histograms for different flow rates, number of passes (SP – single pass or DP – double pass), and type of image (surface of cross-section).

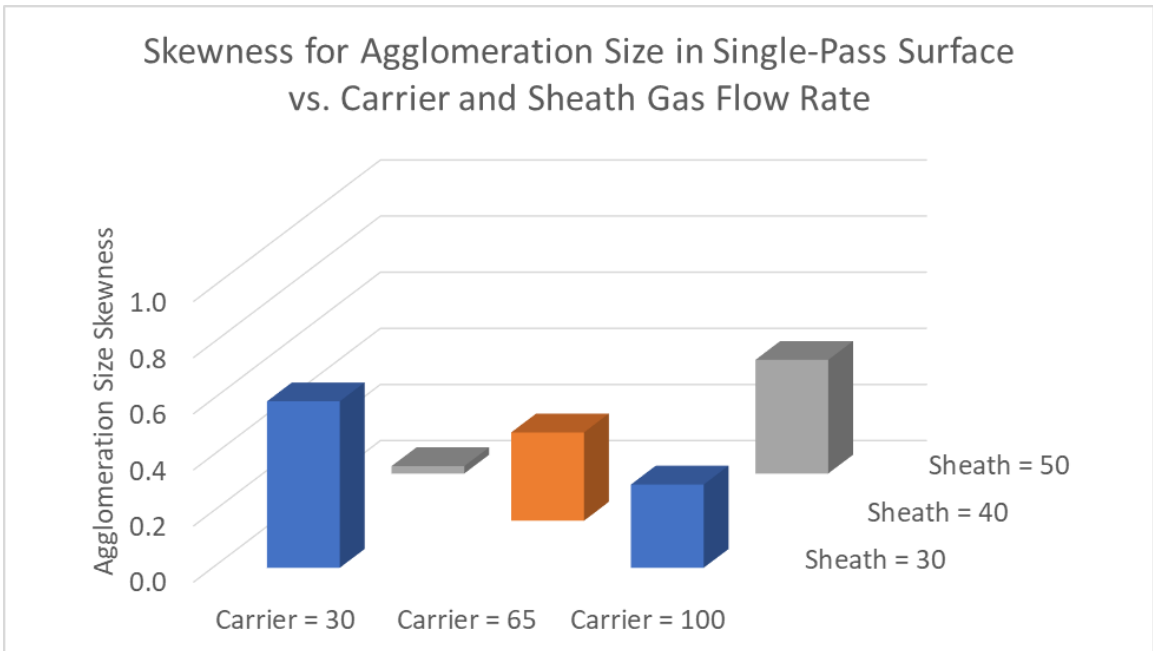


Figure 5.74: Skewness of agglomeration size in single-pass trace on the surface as a function of carrier and sheath gas flow rate.

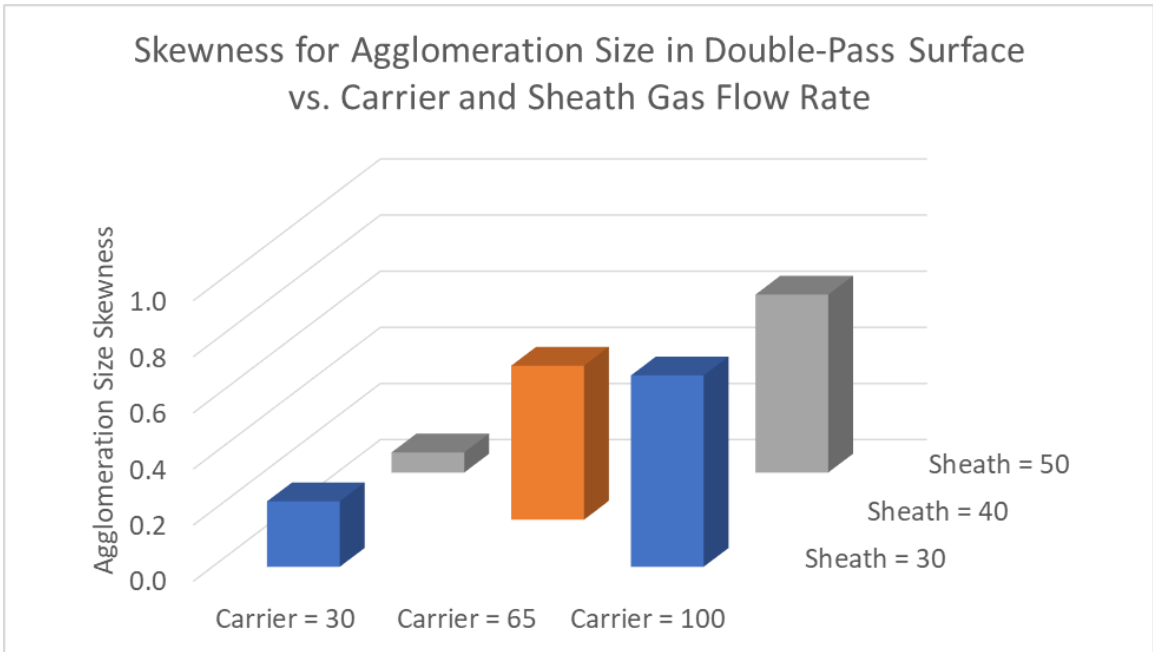


Figure 5.75: Skewness of agglomeration size in double-pass trace on the surface as a function of carrier and sheath gas flow rate.

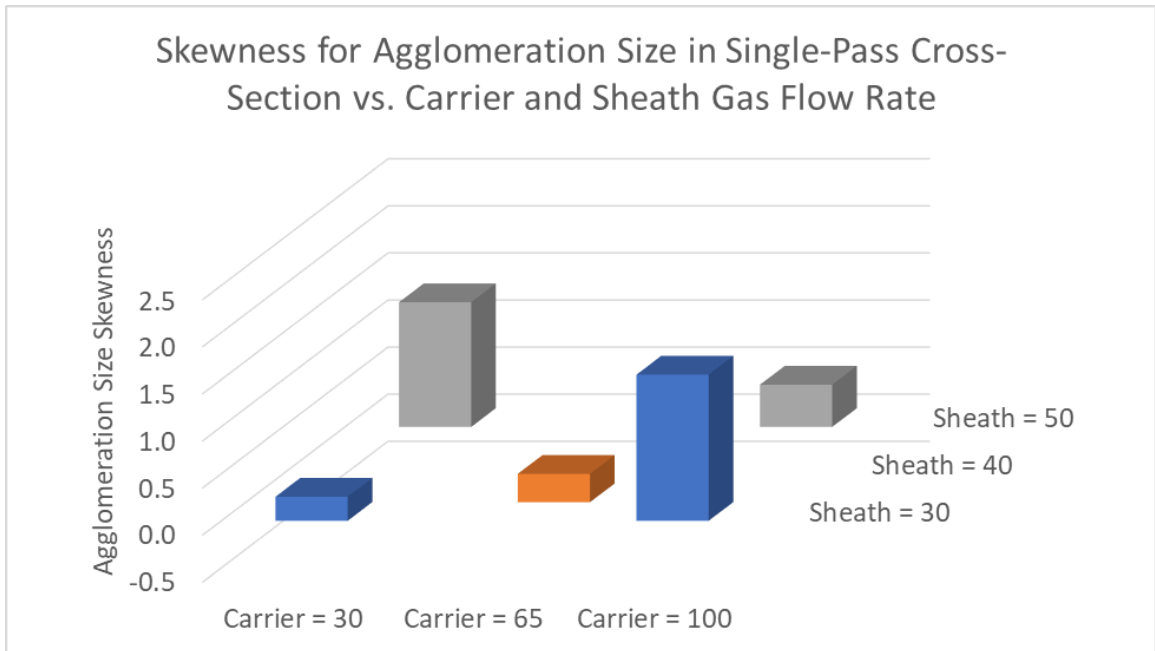


Figure 5.76: Skewness of agglomeration size in single-pass trace in the bulk as a function of carrier and sheath gas flow rate.

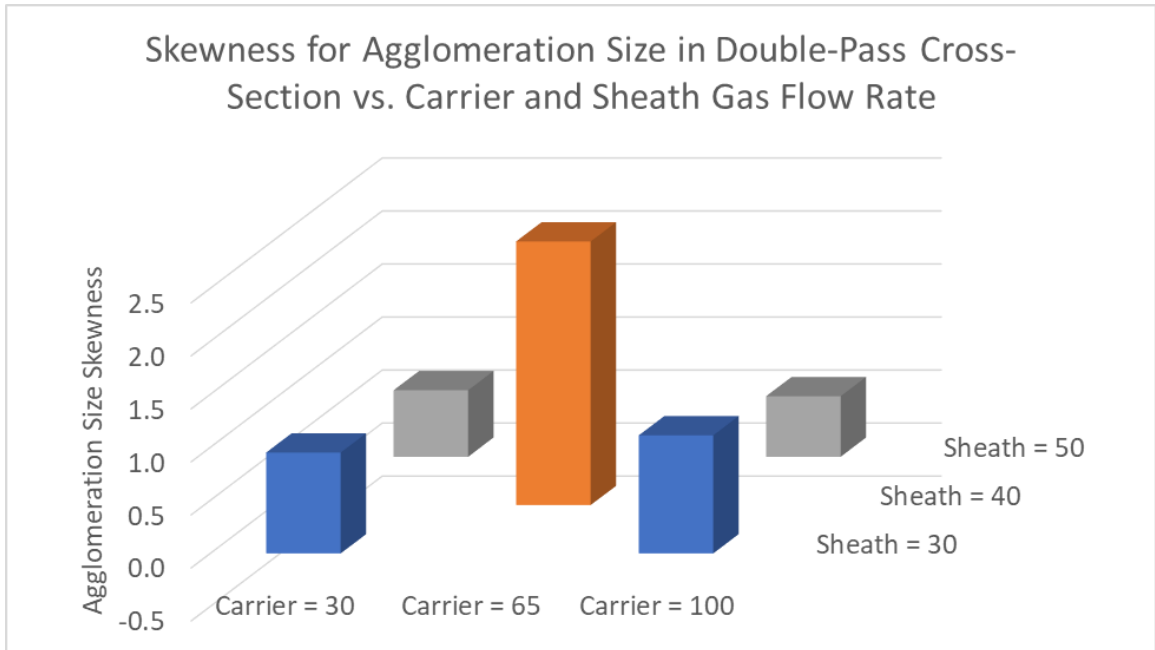


Figure 5.77: Skewness of agglomeration size in double-pass trace in the bulk as a function of carrier and sheath gas flow rate.

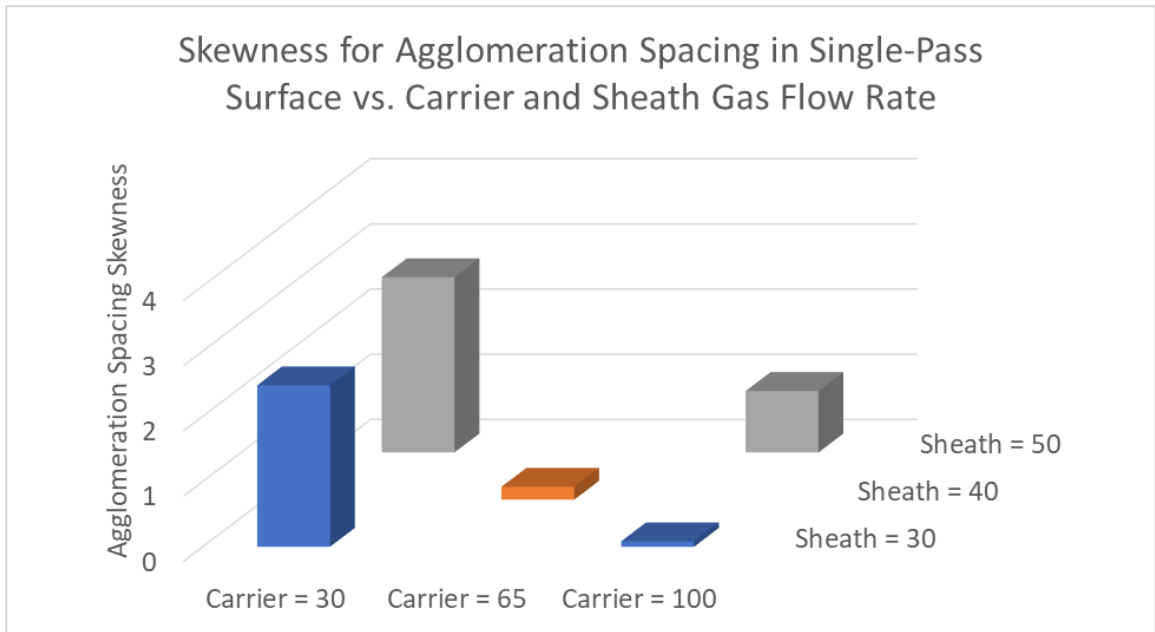


Figure 5.78: Skewness of agglomeration spacing in single-pass trace on the surface as a function of carrier and sheath gas flow rate.

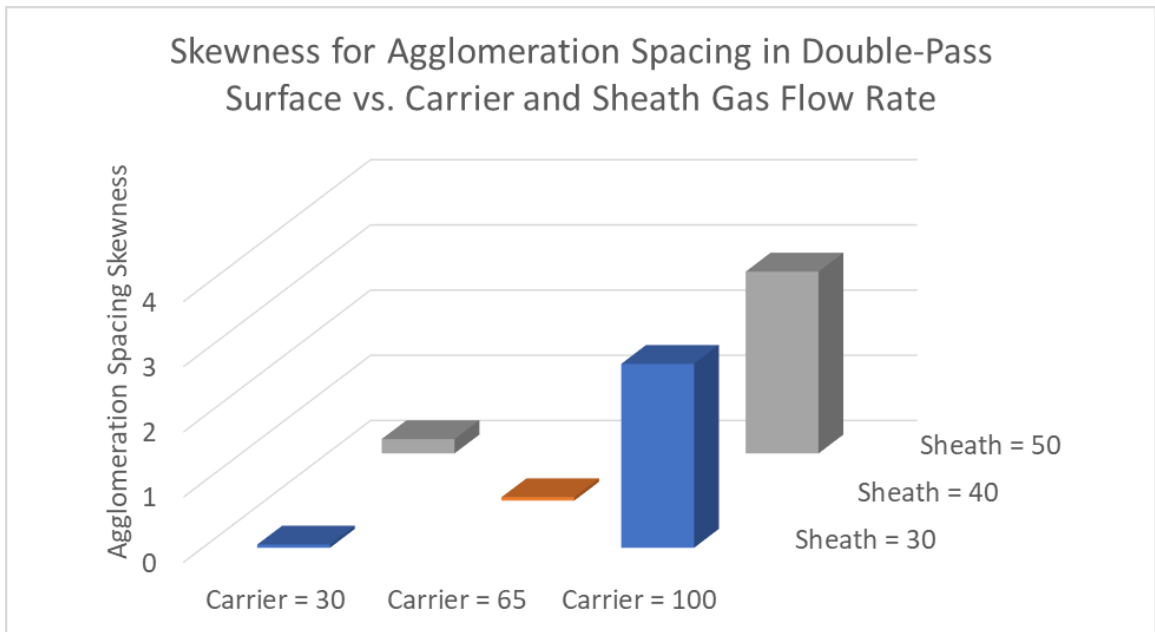


Figure 5.79: Skewness of agglomeration spacing in double-pass trace on the surface as a function of carrier and sheath gas flow rate.

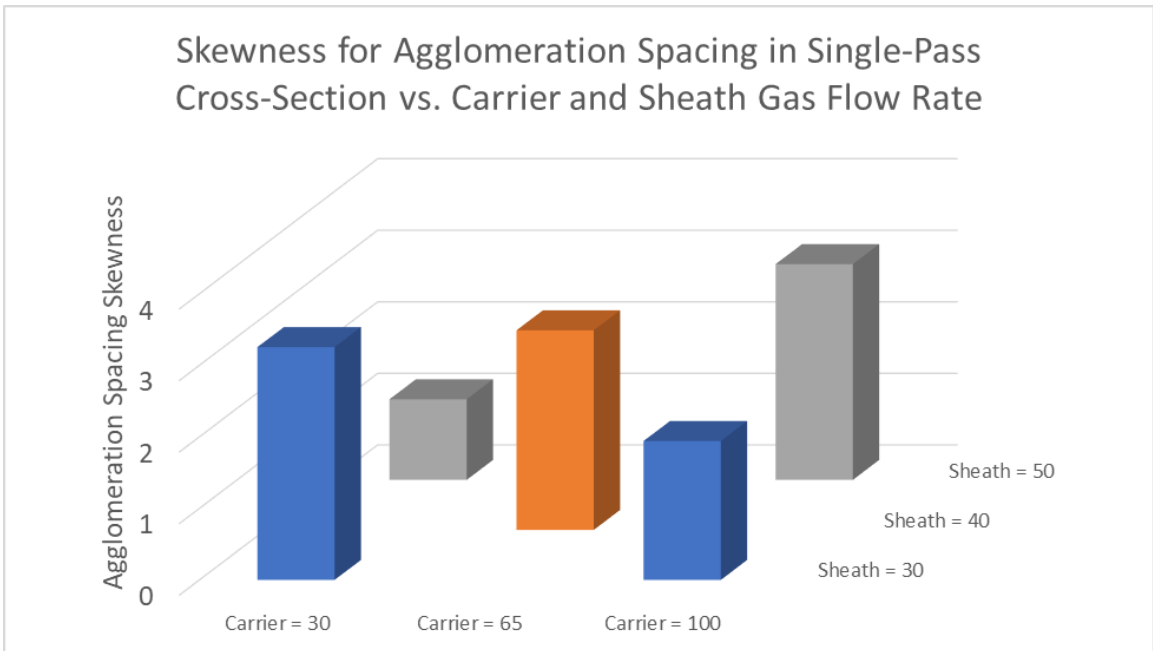


Figure 5.80: Skewness of agglomeration spacing in single-pass trace in the bulk as a function of carrier and sheath gas flow rate.

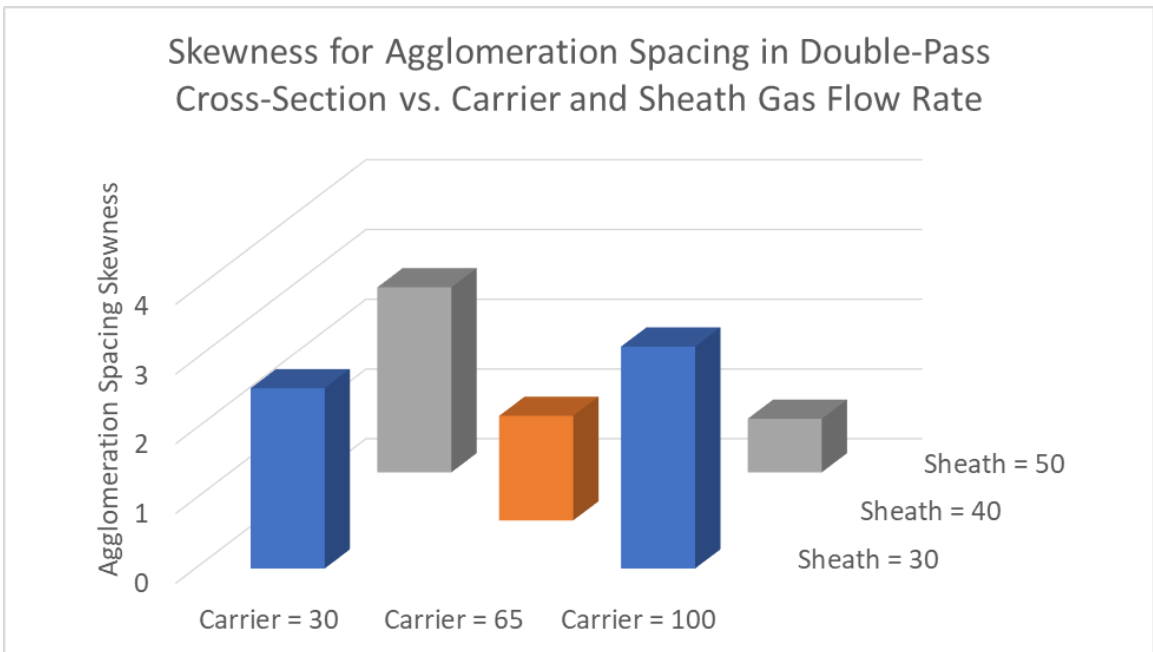


Figure 5.81: Skewness of agglomeration spacing in double-pass trace in the bulk as a function of carrier and sheath gas flow rate.

A8: Finite Element Analysis on Shrinkage Stress

In Section 3.3.6, we discussed a possible driving force for the microcracking reported in this study via capillary pressure gradients caused by escaping solvent volatiles during the sintering process. These pressure gradients can potentially cause separation between nanoparticle clusters before the sintering is completed, thus initiating the reported microcracks. There could also be other potential microcrack drivers, due to gradients of volumetric strain caused by the shrinkage as the solvent volatiles are depleted. This shrinkage is termed ‘chemical’ shrinkage in this discussion. Depending on the degree to which the material has already sintered during this chemical shrinkage, the local volume-averaged stiffness may be sufficient to generate non-trivial amounts of hydrostatic stress gradients in response to this volumetric chemical shrinkage. There is further thermo-mechanical shrinkage that occurs as the printed specimen is cooled from the sintering temperature of 150 °C to room temperature.

To assess the possible role of these volumetric shrinkage strains in the microcracking process, a simplified two-dimensional finite element model was constructed to compare the stresses generated in a thin trace versus a thick trace. Based on laser profilometry conducted at different print conditions, the thinnest trace was modeled with a width of 0.0685 mm and height of 0.0029 mm, while the thickest trace was modeled with a width of 0.1674 mm and height of 0.0165 mm. Both traces were created with a three-point arc that had fillet edges, as shown in Figure 9. Both traces were placed on top of a substrate of Polymer N with a width of 0.75 mm and a thickness of 0.1 mm.

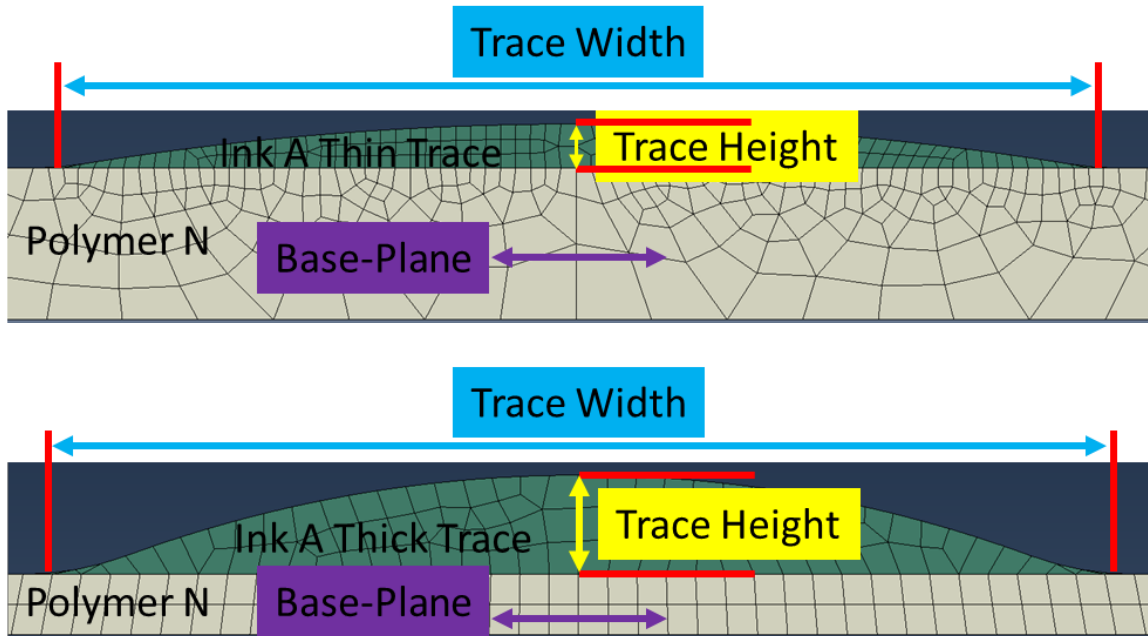


Figure 5.82: Zoomed-in model geometry for a) thin and b) thick trace.

Several simplifications and approximations were made to simplify the analysis.

The results therefore are to be used only for the purposes of finding approximate bounds and qualitative trends in the estimated stresses. All materials were modeled as linear elastic isotropic materials. The FR4 substrate was modeled to have near-infinite stiffness compared those of the Polymer N and of the conductor Ink A. The evaporation (shrinkage) rate was assumed to be uniform throughout the cross-section. The silver trace material was assumed to progressively gain stiffness (due to progressive sintering) and the percentage gain in stiffness was assumed to be linearly proportional to the percentage loss of volatile volume. The chemical shrinkage problem was mimicked by an equivalent thermo-mechanical shrinkage problem, by using the material's coefficient of thermal expansion as a surrogate for chemical shrinkage. Thus, cooling temperature was used as a proxy for the chemical shrinkage and associated sintering process.

Polymer N was modeled as an isotropic elastic solid with $E = 1.1$ GPa and $\nu = 0.43$. Ink A had shrinkage-dependent (temperature-dependent) material properties of $E = 1$ GPa and $\nu = 0.47$ at $T = 1$ and $E = 25$ GPa and $\nu = 0.37$ at $T = 0$. As discussed above, these values for Ink A were guided by the approximation that initially the trace ‘material’ behaved as an incompressible nanoparticle suspension with zero modulus progressively sintered to a nano-porous solid state with a modulus given in the literature and Poisson’s ratio of bulk silver (Long et al., 2017). The relative difference in coefficient of thermal expansion (CTE) between the trace material and Polymer N was set to appropriate value to capture the differences in both chemical shrinkage during the sintering as well as the thermo-mechanical shrinkage during the subsequent cool down. Since the equivalent pseudo thermo-mechanical problem was modeled with a unit change in temperature, the printed trace was given an equivalent pseudo-CTE $\alpha = 0.0886$. This was estimated from the known solvent content of the ink (26.6 percent) before sintering. The resulting volumetric change was divided by three to obtain the corresponding rectilinear shrinkage coefficient. As discussed above, subjecting this model to a simple temperature drop from $T = 1$ to $T = 0$ °C provided an approximate estimate of the resulting stress fields expected throughout the trace during the sintering and cool down.

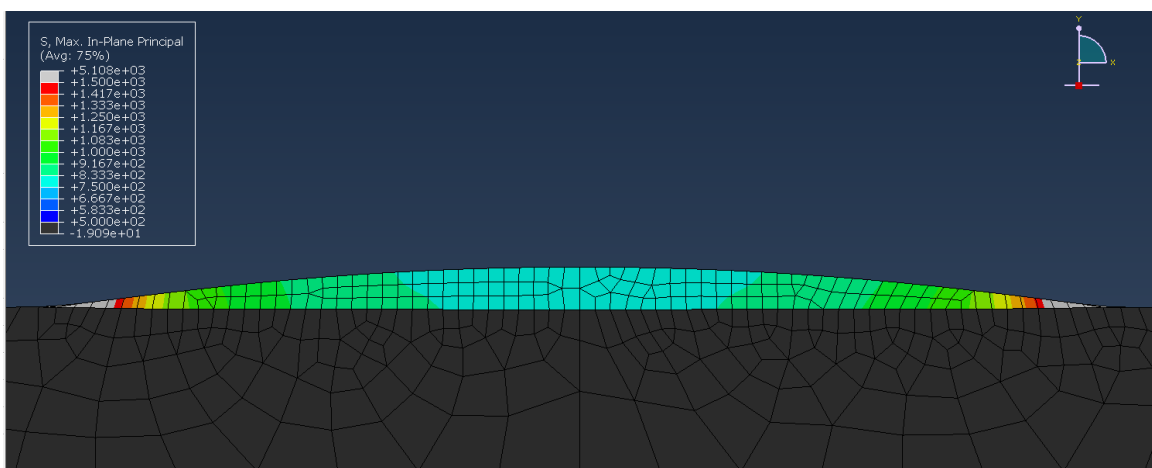
The maximum principal stress fields were then examined for qualitative insights into the possible influence of shrinkage stresses on the reported microcracking. The FEA results showed two counterintuitive trends:

- (i) The maximum principal stress was found to be higher in the thin trace than in the thick trace (Figure 10), thus suggesting that vulnerability to shrinkage driven microcracking could be inversely related to trace thickness. However, as

discussed earlier in Section C, the empirical evidence from this study suggests the opposite.

- (ii) Moreover, the maximum principal stress direction is predominantly parallel to the base-plane of the trace (Figure 11), thus implying that shrinkage-driven microcracking should have mostly been along planes orthogonal to the base-plane. Once again, as discussed earlier in Section C, the empirical evidence in this study contradicts this inference and shows the microcracking predominantly parallel to the base-plane.

Both of these results suggest that the stress from the chemical and thermo-mechanical shrinkage during sintering and subsequent cool down of the printed trace are not the predominant cause of the horizontal microcracking observed in the thicker traces. By a process of elimination, we therefore infer that the more likely driver for the observed microcracking may have been nanoparticle separation caused prior to sintering by the capillary pressure gradients generated during evaporation of the volatiles in the solvent.



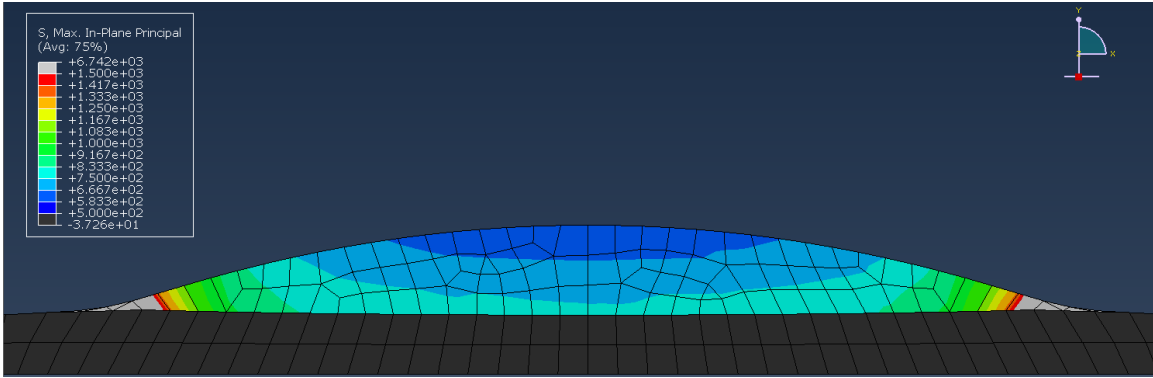


Figure 5.83: Maximum in-plane principal stress contours for the a) thin and b) thick trace.

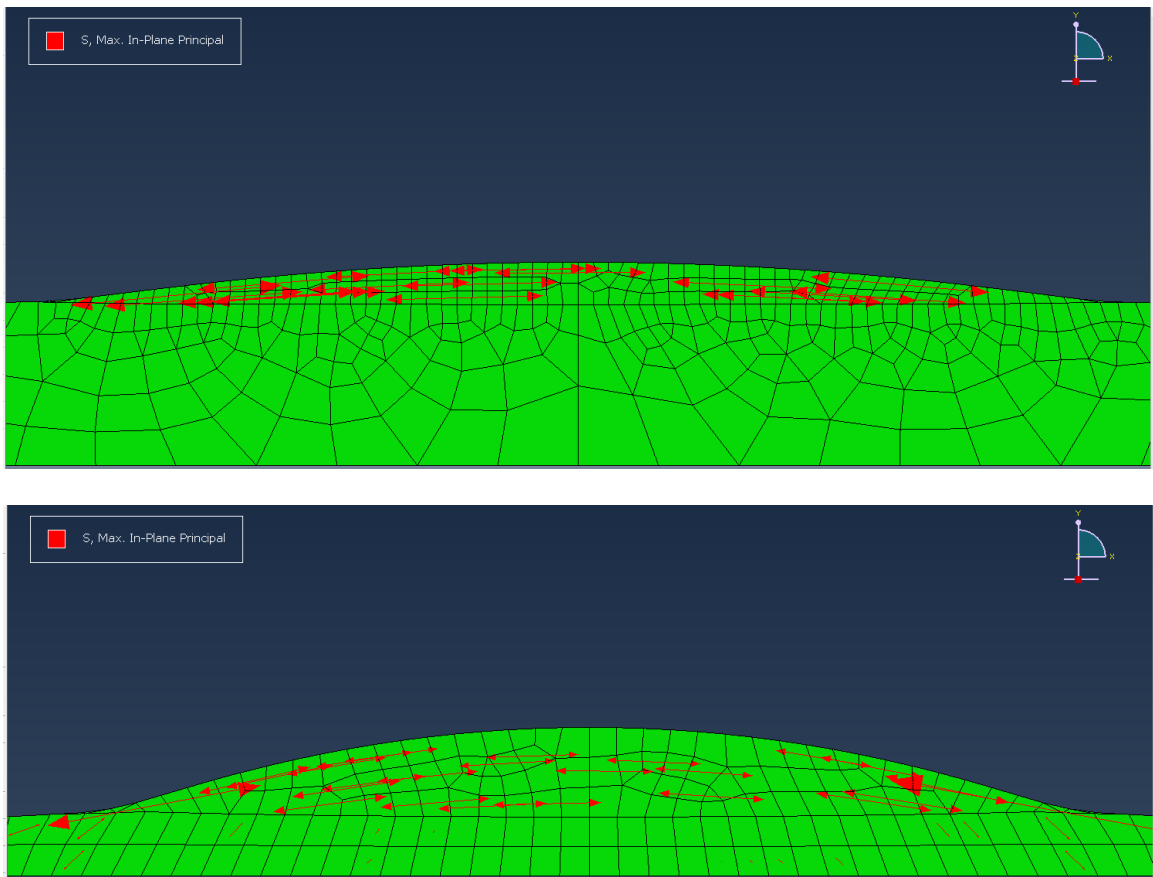


Figure 5.84: Maximum in-plane principal stress direction for the a) thin and b) thick trace.

References

- Agarwala, S., Goh, G. L., & Yeong, W. Y. (2017). Optimizing aerosol jet printing process of silver ink for printed electronics. *IOP Conference Series: Materials Science and Engineering*, 191, 012027.
- Binder, S., Glatthaar, M., & Rädlein, E. (2014). Analytical Investigation of Aerosol Jet Printing. *Aerosol Science and Technology*, 48(9), 924-929.
doi.org/10.1080/02786826.2014.940439
- Chen, G., Gu, Y., Tsang, H., Hines, D. R., & Das, S. (2018). The Effect of Droplet Sizes on Overspray in Aerosol-Jet Printing. *Advanced Engineering Materials*, 20(8), 1701084. doi:10.1002/adem.201701084
- Chou, J., McAllister, M., & Schottland, P. (2014). Aerosol Jet Printable Metal Conductive Inks, Glass Coated Metal Conductive Inks and UV-Curable Dielectric Inks and Methods of Preparing and Printing the Same. *U.S. Patent No. 2014/0035995A1*.
- Christenson, K. K., Paulsen, J. A., Renn, M. J., McDonald, K., & Bourassa, J. (2011). Direct Printing of Circuit Boards Using Aerosol Jet. *27th International Conference on Digital Printing Technologies (NIP27) & Digital Fabrication Conference*, St. Paul, MN.
- Cook, A. (2013). Mechanical and electrical fatigue of aerosol jet printed conductors. M.S. Thesis advised by Tariq Khraishi at *University of New Mexico Department of Mechanical Engineering*.

- Gu, Y., Gutierrez, D., Das, S., & Hines, D. R. (2017). Inkwells for on-demand deposition rate measurement in aerosol-jet based 3D printing. *Journal of Micromechanics and Microengineering*, 27(9), 097001. doi:10.1088/1361-6439/aa817f
- Gu, Y., Hines, D. R., Yun, V., Antoniak, M., & Das, S. (2017). Aerosol-Jet Printed Fillets for Well-Formed Electrical Connections between Different Leveled Surfaces. *Advanced Materials Technologies*, 2(11), 1700178.
doi:10.1002/admt.201700178
- Hackler, D. R., Chaney, R. L., Meek, B. N., Leber, D. E., Leika, S. D., DeGregorio, K. J., Wald, S. F., Wilson, D. G. (2017). Advances in Flexible Hybrid Electronics Reliability. IEEE Workshop on Microelectronics and Electron Devices (WMED).
doi: 10.1109/WMED.2017.7916924
- Happeonen, T. (2016). Reliability studies on printed conductors on flexible substrates under cyclic bending. Ph.D. Dissertation advised by Juha Hakkinen at Technology and Natural Sciences of the University of Oulu.
- Hedges, M., & Marin, A. B. (2012). 3D Aerosol Jet Printing-Adding Electronics Functionality to RP/RM. *The Fraunhofer Direct Digital Manufacturing Conference (DDMC)*, Berlin, Germany.
- Hoey, J. M., Lutfurakhmanov, A., Schulz, D. L., & Akhatov, I. S. (2012). A Review on Aerosol-Based Direct-Write and Its Applications for Microelectronics. *Journal of Nanotechnology*, 2012, 324380.
- Hon, K., Li, L., & Hutchings, I. M. (2008). Direct writing technology—Advances and developments. *CIRP Annals*, 57(2), 601-620.
doi:doi.org/10.1016/j.cirp.2008.09.006

- Kitching, S. & Donald, A. M. (1998). Beam damage of polypropylene in the environmental scanning electron microscope: an FTIR study. *Journal of Microscopy*, 190(3), 357-365. doi:10.1046/j.1365-2818.1998.00346.x
- Liu, M. & Xian, A.P. (2009). Tin Whisker Growth on the Surface of Sn-0.7Cu Lead-Free Solder with a Rare Earth (Nd) Addition. *Journal of Electronic Material*, 38, 2353-2361. <https://doi.org/10.1007/s11664-009-0926-9>
- Long, X., Tang, W., Xia, W., Wu, Y., Ren L., & Yao Y. (2017). Porosity and Young's modulus of pressure-less sintered silver nanoparticles. *2017 IEEE 19th Electronics Packaging Technology Conference (EPTC)*, 1-8.
- Mahajan, A., Frisbie, C. D., & Francis, L. F. (2013). Optimization of Aerosol Jet Printing for High-Resolution, High-Aspect Ratio Silver Lines. *ACS Applied Materials & Interfaces*, 5(11), 4856–4864.
- Park, S., Jang, S., Lee, D., Oh, J., & Kim, H. (2013). Two-step flash light sintering process for crack-free inkjet-printed Ag films. *Journal of Micromechanics and Microengineering*, 23, 015013. doi:10.1088/0960-1317
- Roberson, D. A., Wicker, R. B., Murr, L. E., Church, K., & MacDonald, E. (2011). Microstructural and Process Characterization of Conductive Traces Printed from Ag Particulate Inks. *Materials*, 4, 963-979. doi:10.3390/ma4060963
- Salam, B., Lok, B. K. (2008). Solderability and reliability of printed electronics. 15th International Symposium on the Physical and Failure Analysis of Integrated Circuits. doi: 10.1109/IPFA.2008.4588211
- Salary, R., Lombardi, J. P., Samie Tootooni, M., Donovan, R., Rao, P. K., Borgesen, P., & Poliks, M. D. (2017). Computational Fluid Dynamics Modeling and Online

- Monitoring of Aerosol Jet Printing Process. *ASME. Journal of Manufacturing Science and Engineering*, 139(2), 021015-1-021015-21. doi:10.1115/1.4034591
- Serway, R. A. (1994). *Principles of Physics*. Fort Worth: Saunders College Pub.
- Secor, E. B., et al. (2018). Guided Ink and Process Design for Aerosol Jet Printing Based on Annular Drying Effects. *Flexible and Printed Electronics*. doi: 10.1088/2058-8585
- Singh, K. N., & Tirumkudulu, M. S. (2007). Cracking in Drying Colloidal Films. *Physical Review Letters*, 98(21), 218302-218305.
doi:10.1103/PhysRevLett.98.218302
- Smith, M., Choi, Y. S., Boughey, C., & Kar-Narayan, S. (2017). Controlling and assessing the quality of aerosol jet printed features for large area and flexible electronics. *Flexible and Printed Electronics*, 2, 015004.
- Stoukatch, S., Laurent, P., Dricot, S., Axisa, F., Seronveaux, L., Vandormael, D., Beeckman, E., Heusdens, B., & Destin e, J. (2012). Evaluation of Aerosol Jet Printing (AJP) Technology for Electronic Packaging and Interconnect Technique. *4th Electronic System-Integration Technology Conference (ESTC)*, Amsterdam, The Netherlands.
- Wadhwa, A. (2015). Run-time Ink Stability in Pneumatic Aerosol Jet Printing Using a Split Stream Solvent Add Back System. M.S. Thesis advised by Denis Cormier at *Rochester Institute of Technology Department of Industrial and Systems Engineering*.